

Characterization and Application of Photoswitchable Fluorescent Proteins for Nanoscopy

Zur Erlangung des akademischen Grades eines
DOKTORS DER NATURWISSENSCHAFTEN
von der Fakultät für Physik des
Karlsruher Instituts für Technologie (KIT)

genehmigte

DISSERTATION

von

Dipl. Phys. Jochen Fuchs
aus Ellwangen/Jagst

Tag der mündlichen Prüfung 20. Mai 2011

Referent: Prof. Dr. Gerd Ulrich Nienhaus

Korreferent: Prof. Dr. Wolfgang Wenzel

Contents

1. Introduction	1
2. Fluorescent Proteins	3
2.1. Structure and Chromophore Formation	3
2.2. Red Fluorescent Proteins	4
2.3. Photoactivatable Fluorescent Proteins (PAFPs)	5
2.3.1. Photoconvertible Fluorescent Proteins	5
2.3.2. Photoswitchable Fluorescent Proteins	7
3. Light Microscopy	15
3.1. Diffraction	15
3.1.1. Diffraction Limit	16
3.2. Alternative Microscopy Techniques	18
3.2.1. Fluorescence Resonance Energy Transfer (FRET)	19
3.2.2. Near-field Techniques	19
3.2.3. Confocal Microscopy	19
3.2.4. 4Pi and I ⁵ M Microscopy	20
3.2.5. Stimulated Emission Depletion Microscopy (STED)	20
3.2.6. Structured Illumination Microscopy (SIM)	21
3.3. Photoactivation Localization Microscopy (PALM)	21
3.3.1. Single Molecule Localization	22
3.3.2. Localization Precision	23
3.3.3. PALM Scheme	24
3.4. Resolution in PALM Images	25
3.5. PALM Applications	26
3.6. Markers for High Resolution Imaging	27
3.7. Cellular Structures	27
3.7.1. Cytoskeleton	27
3.7.2. Actin and Lifeact	28
3.7.3. α -actinin	29
3.7.4. Microtubules	29
3.7.5. RITA	30
3.7.6. Paxillin and Focal Adhesions	31

4. Materials and Methods	33
4.1. Spectroscopic Characterization of the Fluorescent Proteins	33
4.1.1. Absorption Spectra	33
4.1.2. Fluorescence Excitation and Emission Spectra	33
4.1.3. pH	33
4.1.4. Photoswitching	33
4.1.5. Thermally Activated Recovery	34
4.2. Extinction Coefficient and Quantum Yield	34
4.3. SVD-MLS Analysis	34
4.4. Single Molecule Measurements	36
4.5. PALM Setup	37
4.5.1. General Considerations	37
4.5.2. Setup	38
4.6. Intensity to Photon Conversion	40
4.7. Stability and Correction	40
4.8. Data Evaluation	40
4.9. Localization Algorithm	43
4.9.1. FluoroBancroft	43
4.10. Localization Statistics	46
4.10.1. Presentation	47
4.11. Cell Preparation	47
4.11.1. Cellular Transfection	48
4.12. PALM Data Acquisition Conditions	48
5. The Photoswitchable Red Fluorescent Protein (psRFP)	49
5.1. pH dependent Spectral Properties	50
5.2. Extinction coefficients and Quantum Yield	57
5.3. Photoswitching	58
5.3.1. Off-switching	59
5.3.2. On-switching	63
5.4. Kindling and Photobleaching	67
5.5. Single Molecule Experiments	70
6. Discussion psRFP	75
7. PALM Developments	81
7.1. Evaluation of Fluorescent Proteins as PALM Markers	81
7.1.1. psRFP	81
7.1.2. mcavRFP	87
7.1.3. mRubyN143C	89
7.1.4. d2EosFP	93
7.1.5. IrisFP PALM	93
7.2. Imaging Protein Movements with Superresolution	98
7.3. LivePALM	108

7.4. Nyquist-Shannon sampling theorem	111
7.5. Light perturbation and cell vitality	112
8. Discussion PALM	115
8.1. Improvements of the PALM Method	115
8.2. Evaluation of new FPs as PALM Markers in Living Cells	116
8.3. Live Cell Imaging	118
8.4. Low Intensity PALM	119
8.5. Resolution	119
9. Conclusion and Outlook	121
A. Publications	141
B. Acknowledgements	143
C. Curriculum Vitae	145

1. Introduction

The last century in physics was dominated by the theory of relativity and quantum theory, which have revolutionized our thinking. At the dawn of the new millennium the interest of many physicists has shifted towards living matter and a century of biology is approaching. Scientists from different disciplines are working together to discover new exciting phenomena. As Richard Feynman once mentioned, nature is not interested in our separations (into physics, biology or chemistry) and many interesting phenomena bridge the gaps between these fields¹. To gain a deeper understanding of living matter we need to observe life on its different length scales from single molecules to whole organisms. A central role in the observation of biological processes is taken by fluorescent proteins (FPs) that have become an inherent part in life sciences research over the last two decades. The first FP was discovered accidentally in the 1960s by Osamu Shimomura when trying to purify aequorin from the jelly fish *Aequorea victoria*². Because the protein solution looked slightly greenish in the sunlight and exhibited very bright green fluorescence under UV illumination, Shimomura named the new protein green fluorescent protein (GFP). After its discovery it took thirty more years for the next step to follow. In 1992 Doug Prasher cloned the gene for GFP and published the amino acid sequence³. Prasher passed on the GFP gene to Martin Chalfie who had the idea to use GFP as a genetically encoded highlighter. Chalfie's group was the first to show expression of GFP in prokaryotes (*Escherichia coli*) and eukaryotes (touch neurons of *C. elegans*)⁴ thereby establishing that this protein with its unique properties could be used as a fluorescent marker in-vivo. At the same time, Roger Tsien started to study and biochemically engineer the protein. He revealed the autocatalytic chromophore formation and by 1994, his group had produced a blue variant of GFP⁵. This was the beginning of the development of a vast array of fluorescent proteins that span the visible spectrum from blue to deep red. For their achievements, the Nobel Prize in chemistry was awarded to Shimomura, Chalfie and Tsien in 2008. Their discoveries stimulated the field and shortly thereafter fluorescent proteins were discovered in anthozoa animals^{6, 7, 8}. During the last 20 years, FPs have become popular tools in life science research due to the fact that, after introducing the artificial FP gene into the cell, the encoded polypeptide chain is synthesized by the cell machinery itself and the fluorescent chromophore is produced without need of cofactors or substrates. By adding a short targeting peptide sequence, a fusion protein or a tissue-specific promoter to the FP sequence, cellular structures or particular tissues can be selectively labeled and protein localization, movement and interactions can be studied in living cells. Furthermore, FPs have applications as engineered biosensors for the measurement of ion concentration and pH in living cells⁹. Most exciting for physicists, the discovery of photoswitchable FPs has led to the development of novel high resolution microscopy techniques¹⁰. For

1. Introduction

the use of photoswitchable FPs in such advanced applications and the development of new FPs with improved properties, a deep understanding of the photophysics and the structure dynamics relationship in FPs is required.

2. Fluorescent Proteins

2.1. Structure and Chromophore Formation

All fluorescent proteins (FPs) share a characteristic barrel-like structure (Fig.2.1a) which is roughly 40 Å long and 30 Å wide and consists of 220–240 amino acids that fold into β -sheets. For most FPs, especially from anthozoa, four of those barrels are arranged in a tetrameric quaternary structure. A central helix runs along the axis of the barrel and stabilizes the chromophore that is formed autocatalytically inside the barrel from three amino acids without additional cofactors (Fig.2.1b). The chromophores found in all nat-



Figure 2.1. Structure of fluorescent proteins. (a) All FPs share a barrel-like structure. (b) The light-emitting chromophore (red) is protected by a barrel formed from β -sheets. (c) Chromophore structure of psRFP. The chromophore extends from the p-hydroxybenzyl ring of the tyrosine to the imidazolinone ring. In orange and red fluorescent proteins (DsRed or eqFP611) the single bond between the amide nitrogen and $C\alpha$ of the first of the three chromophore-forming amino acids is oxidized to an acylimine group in the same plane as the p-HBI chromophore.

ural FPs consist of three amino acids X-Tyr-Gly, where the first amino acid, X, can be arbitrary, but the other two are strictly conserved. The chromophore of the green fluorescent protein, 4-(p-hydroxybenzylidene)-5-imidazolinone (p-HBI), is generated with characteristic time scales ranging from minutes to hours. Starting with a peptide cyclization initiated by nucleophilic attack of the Gly67 amide nitrogen on the carbonyl carbon of Ser65 to create a five-membered imidazolinone ring, followed by oxidation-dehydration steps to form the conjugated π -electron system that extends from the p-hydroxybenzyl ring of the tyrosine to the imidazolinone ring (Fig.2.1c)¹¹. The cyclization reaction is promoted by the electrostatic catalyst Arg96, and subsequent removal of the Tyr66 α -proton is likely facilitated by the acid-base catalyst Glu222^{12, 13}. The two rings of

2. *Fluorescent Proteins*

the chromophore are stabilized in a coplanar conformation by the protein environment, which is essential for a high fluorescence quantum yield¹⁴. However, missing interactions of the chromophore with the surrounding protein matrix in solution lead to fast radiationless decay by internal conversion¹⁵. The absorption spectrum of GFP displays two distinct bands at 395 (A band) and 475 nm (B band), which are associated with the neutral phenol and anionic phenolate of the chromophore, respectively. Most FPs exhibit a protonated (neutral) and a deprotonated (anionic) form of the tyrosine moiety in different ratios over the whole pH range. In general, the excitation of the anionic form leads to bright fluorescence emission and the excitation of the neutral form induces only weak, blue-shifted fluorescence or no emission at all. An exception are FPs that show excited state proton transfer (ESPT)^{16, 17, 18, 19, 20}. In this case, the excitation of the neutral form results in an acidification of the phenol, the phenolic proton is released and emission from the anionic chromophore can be observed.²¹.

2.2. Red Fluorescent Proteins

An extension of the conjugated π -electron system of the p-HBI chromophore in green fluorescent proteins leads to red emission. Currently known red fluorescent proteins (RFPs) share two types of chromophores, the DsRed-like chromophore²² or the Kaede/EosFP-like chromophore²³. The orange/red emission in DsRed or eqFP611 arises from an acylimine extension of the two-ring π -system of the GFP-like chromophore. It was generally believed that the green emitting GFP-like chromophore is an on-pathway intermediate during formation of the red emitting chromophore. But a recent publication proposed a branched pathway model with the green and the red chromophore as two different end products²⁴. Cyclization of the protein backbone is followed by an initial oxi-

dation step to form an intermediate mixture of a cyclic imine and a hydroxylated cyclic imine. Dehydration of the hydroxylated form yields the neutral GFP chromophore. But, depending on the oxygen concentration, instead of dehydration an oxidation step can occur that generates an acylimine bond between the chromophore and the preceding polypeptide residue which extends the π -electron system. At that stage, the conjugated system does not yet include the tyrosine because the bond between the imidazolinone and the phenol remains unoxidized, therefore, the conjugated species produces blue fluorescence. This blue emitting intermediate serves as a template for the red emitting chromophore. After hydroxylation, the chromophore loses its blue fluorescence and serves as a substrate for dehydration to the neutral red chromophore that will form an equilibrium with the anionic chromophore according to the pH value. A similar model for chromophore formation in red emitting proteins was suggested based on structural analyses^{25, 26}. The key feature here is that the formation of the N-acylimine C=N bond precedes the oxidation of the C α -C β bond in the Tyr64 side chain. The discovery of red fluorescent proteins (RFPs) provided researchers with advantageous fluorescent markers for deep-tissue imaging and permits the observation of biological processes inside living tissues and cells. Beneficial are the reduced cellular autofluorescence background

in the red spectral region as well as the reduced scattering at longer wavelength which increases the light penetration in the sample and of course the less cytotoxic, longer-wavelength excitation light^{27, 28, 29}. Besides, red FPs are excellent fluorescent resonance energy transfer (FRET) partners for bright green and yellow emitting FPs^{30, 31, 32} and perfectly suited for colocalization experiments^{33, 34}.

2.3. Photoactivatable Fluorescent Proteins (PAFPs)

Photoactivatable FPs are a new class of fluorescent proteins. A change of their emission properties in response to irradiation in a specific wavelength range renders them interesting for many applications. Protein tracking in living cells³⁵, data storage³⁶ and superresolution microscopy^{37, 38, 39} are only a few examples. Photoactivatable FPs can be divided into photoconvertible FPs and photoswitchable FPs. Photoconvertible FPs are irreversibly converted from one state to another, whereas photoswitchable FPs can be switched between two different states for many times.

2.3.1. Photoconvertible Fluorescent Proteins

Under light of a specific wavelength, one sort of photoconvertible FPs show an increase of fluorescence emission which results from the irreversible photoconversion of the neutral chromophore to the anionic chromophore that exhibits bright fluorescence. The photoconversion mechanism of these PAFP consists of a decarboxylation of the Glu215 residue, resulting in reorganization of the hydrogen bond network inside the protein, followed by chromophore deprotonation. This mechanism is supported by the crystal structure of PA-GFP⁴⁰, the first photoconvertible FP. Apart from PA-GFP⁴¹, PS-CFP⁴² and PAmRFP1⁴³ belong to this FP subclass. PA-GFP was created from *Aequorea* GFP by introducing the substitution of Thr203 to histidine, which leads to the production of mostly neutral chromophores. With almost no chromophores in the anionic state, no fluorescence upon 480-nm excitation was observed. Intense illumination around 400 nm leads to a decarboxylation of Glu222, which results in the reorganization of the hydrogen bond network and chromophore deprotonation, accompanied by an up to 100-fold increase in green fluorescence. Another photoconvertible FP with the same underlying mechanism is PS-CFP⁴². In contrast to PA-GFP, PS-CFP shows a significant level of cyan fluorescence ($\lambda_{em} \sim 470$ nm) in the non-activated state. Intense irradiation with light around 400 nm switches the emission from predominantly cyan to green ($\lambda_{em} \sim 510$ nm). Photoconversion with violet light has also been observed for PAmRFP1 which has initially a weak cyan fluorescence, but during irreversible photoactivation at 380 nm, red fluorescence with an emission maximum at 605 nm increases. A second red emitting photoactivatable FP is PA-mCherry that can also be photoconverted from a non-fluorescent to a stable red fluorescent state with 400-nm irradiation and features a contrast ratio up to 3000–5000 fold⁴⁴. However, the mechanism that leads to the fluorescence enhancement is different from the previous ones. A Kolbe-type radical mechanism was proposed for the phototransformation. The light activation induces the photochem-

2. Fluorescent Proteins

ical decarboxylation of the Glu215 residue which leads to the chemical oxidation, with a double bond formation between the p-hydroxybenzyl ring of the tyrosine to the imidazolinone ring. The resulting extended π -electron system forms the red fluorescent chromophore⁴⁵.

Characteristic for the photoconvertible FPs EosFP⁴⁶, mcavRFP⁴⁷, Kaede⁴⁸, Dendra2⁴⁹, rfpRFP⁴⁷ and KikGR⁵⁰ is the change in emission from green to red in response to violet light. Initially, proteins of this group mature to a green-emitting state with a GFP-like chromophore. However, UV-violet light at approximately 350–450 nm efficiently converts them into red fluorescent proteins. The structural basis for the photoconversion is a light-induced cleavage of the His62-N α -C α bond. The thereby extended conjugated π -electron system, which includes the imidazole ring of histidine or at least the newly formed conjugated double bond, causes a redshift in emission^{51, 52}. Details of the photoconversion process are discussed for EosFP.

EosFP

EosFP was cloned from the coral *Lobophyllia hemprichii* and is named after the Greek goddess of the dawn. This FP emits strong green fluorescence (Fig.2.2a) that changes to red emission (Fig.2.2b) under \sim 400 nm illumination⁴⁶. The green chromophore consists

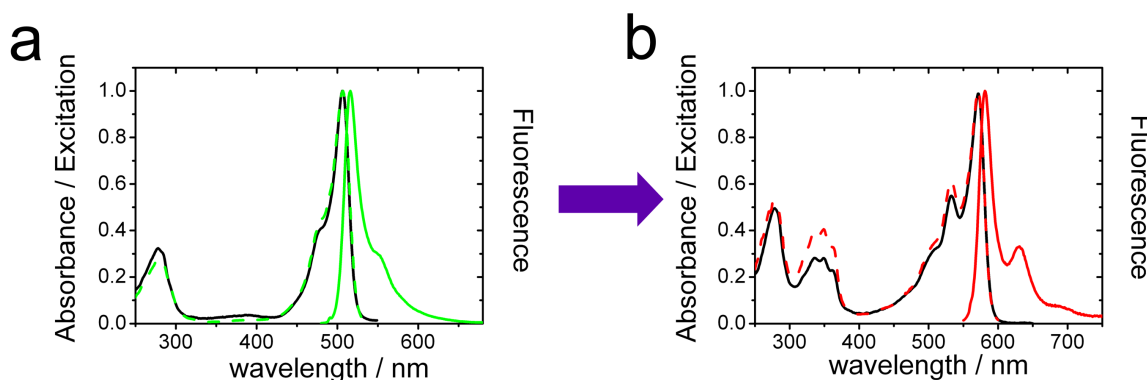


Figure 2.2. (a) Emission (green), excitation (green, dashed) and absorption spectra (black) of the green form of EosFP. The green EosFP chromophore can be photoconverted to a red emitting chromophore with intense violet/blue illumination. (b) Emission (red), excitation (red, dashed) and absorption spectra (black) of the red form of EosFP.

of a 4-(p-hydroxybenzylidene)-5-imidazolinone moiety, formed from the tripeptide His-Tyr-Gly. Structural studies have revealed that the formation of the red, elongated chromophore π -conjugation is accompanied by the irreversible cleavage of the peptide backbone in a β -elimination reaction (Fig. 2.3)⁵¹. The backbone between the N α and the C α of His62 breaks and the His62 imidazole ring joins the delocalized π -electron system via an all-trans-alkenylene structure. Further details of the photoconversion have been described in two publications^{51, 53}. EosFP forms a tetramer that can be separated into two dimeric subunits, by introducing the mutation Thr158Val which breaks up the AC

2.3. Photoactivatable Fluorescent Proteins (PAFPs)

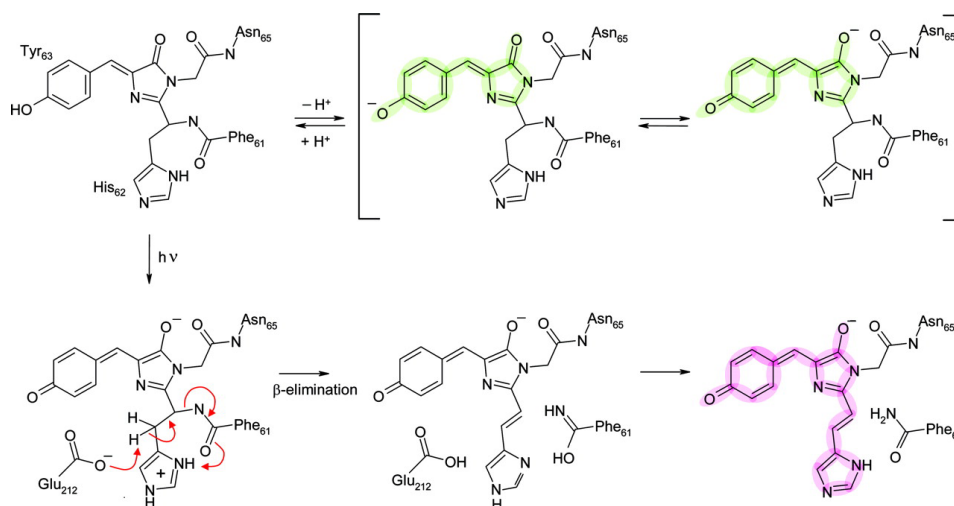


Figure 2.3. Reaction mechanism suggested for the chromophore extension and backbone cleavage. Details are discussed in the text. Scheme from Nienhaus et al.⁵¹.

interface. The resulting dimer was named d2EosFP and can be further split into the monomeric variant mEosFP with the additional Val123Thr mutation⁵⁴. The potential of EosFP as a valuable tool for protein tracking and regional optical marking of protein subpopulations has been demonstrated in living cells and tissue⁵⁴. Due to its outstanding properties EosFP has also become one of the most used fluorescent proteins in the new and fast developing field of high resolution microscopy^{55, 37, 56}. An improved variant of mEosFP for high resolution microscopy has recently been reported⁵⁷.

mcavRFP

The fluorescent protein mcavRFP was found in the ectodermal tissue of the coral *Montastrea cavernosa*⁵⁸. The protein, like EosFP, changes its emission from green to red upon irradiation with light of wavelengths around 400 nm. Although the conversion mechanism for mcavRFP is not known in detail, a similar or even identical mechanism as found in EosFP can be assumed. Interestingly, mcavRFP is found as a natural protein dimer, whereas most of the anthozoa FPs exhibit a tetrameric structure. This fact facilitates the generation of a monomeric mcavRFP protein.

2.3.2. Photoswitchable Fluorescent Proteins

Photoswitchable FPs can be reversibly switched between a non-fluorescent (dark) and a fluorescent (bright) state, controlled by external irradiation. In contrast to photoconvertible and photoactivatable FPs that are limited to a single irreversible photoconversion or activation, photoswitchable FPs are capable of many on-off switching cycles. FPs exhibiting this peculiar feature are found in the green spectral region (Dronpa⁵⁹, Padron⁶⁰) as well as in the red spectral range (KFP⁶¹ and its advanced variant KFP1⁶², rsCherry⁶³ and rsCherryRev⁶³). They can be further subdivided into photoswitchable FPs with

2. Fluorescent Proteins

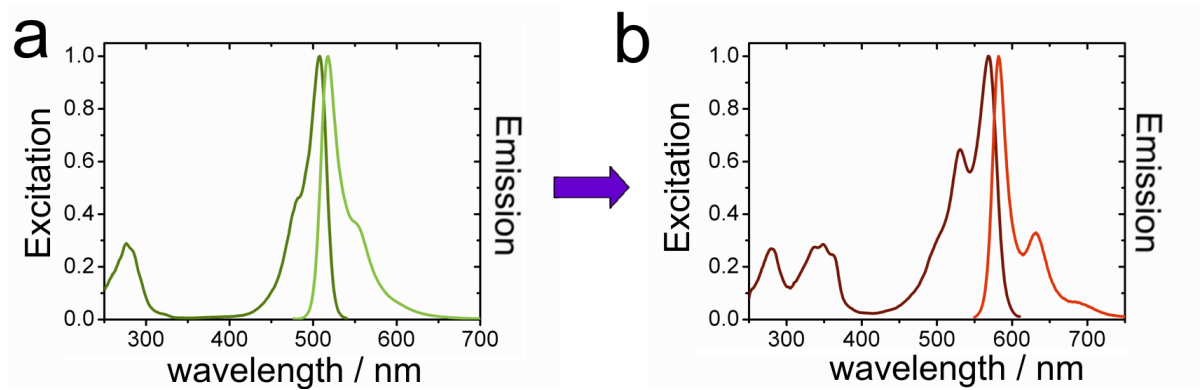


Figure 2.4. (a) Excitation (dark green) and emission (light green) spectra of the green form of mcavRFP. (b) Excitation (dark red) and emission (light red) spectra of the red form of mcavRFP obtained after illumination of the green form with 405 nm light.

positive or negative switching mode. FPs that are switched to their fluorescent state with the same wavelength that excites the fluorescence are called positive switchers and FPs that are switched to the non-fluorescent state with the excitation light are termed negative switchers⁶³. The positive switching mode is in general preferable over the negative switching mode for super-resolution applications, because the fluorescence signal can be read without the undesired off-switching side effect, which results in higher localization accuracy. The mechanism for reversible photoswitching is based on light driven isomerization between a planar cis chromophore and a non-planar trans conformation, often accompanied by a change in chromophore protonation^{64, 65}. The chromophore in bright fluorescent FPs generally adopts a planar cis conformation whereas the non or weakly fluorescent trans chromophore commonly found in chromoproteins offers non-radiative de-excitation pathways due to enhanced chromophore flexibility. There is only one exception, the highly fluorescent planar trans chromophore in the red FP eqFP611⁶⁶. The photoisomerization can efficiently be driven by light, so that FP fluorescence can be arbitrarily switched on or off by external irradiation. When the FP is switched to the non-equilibrium state and afterwards left in the dark, the chromophore thermally relaxes back to the equilibrium state.

psRFP

The red fluorescent FP asRFP was cloned from *Anemonia sulcata* var. *rufescens* and showed weak photoswitching characteristics under blue illumination (~450 nm). Analysis of the amino acid sequences of asRFP revealed a sequence identity of ~90 % with asFP595⁶¹, the first photoswitchable FP. The structure of asRFP shows the tetrameric quaternary arrangement typical of anthozoa FPs. The four monomers are arranged as dimers of dimers with identical monomeric subunits (Fig. 2.5). By following a similar route as in asFP595, the interesting photoswitching properties of asRFP could be further improved. Ser143 was replaced by a glycine during site-directed mutagenesis and

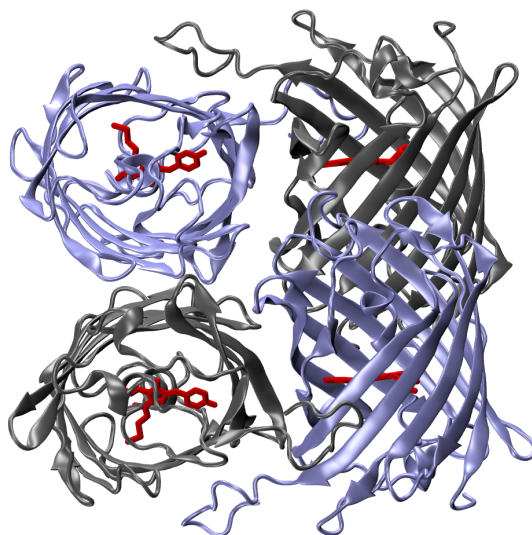


Figure 2.5. The monomeric subunits of psRFP are arranged in a tetrameric quaternary structure, consisting of dimers of dimers.

the resulting protein was named psRFP. In this new variant, already weak illumination with light around 450 nm leads to a considerable loss in fluorescence, which recovers after a short time without illumination. The x-ray structure of psRFP is almost identical to the structure of KFP1⁶², an improved version of asFP595. The chromophore in both proteins is derived from the tripeptide Met-Tyr-Gly and an acylimine extension to the well known GFP chromophore shifts the emission into the red spectral region to around 600 nm. The backbone between Cys62 and the chromophore is cleaved during the autocatalytical formation which gives the chromophore more conformational freedom. Interestingly, in the fluorescent ground state, the structure of psRFP exhibits mainly a planar cis chromophore, in contrast to the structurally similar KFP1, which is found to be predominantly in the non-fluorescent trans state. After 450-nm irradiation, an increased population of the trans chromophore and a concomitant decrease of fluorescence was observed. The direct chromophore environment critically influences the chromophore properties. The carbonyl oxygen of the imidazolinone ring hydrogen-bonds with the side chain of Arg92 (Fig. 2.6). The amino acids Glu214, His197 and Glu195 form a hydrogen bond network beneath the chromophore. Lys67 can form salt bridges with Glu145 and Glu195. The trans conformation of the chromophore is stabilized by hydrogen bonds from the tyrosine oxygen atom to the Ser158 oxygen and a water molecule that forms a hydrogen bond to Glu145. Ser158, Glu195 and Glu214 were found in two different conformations depending on the chromophore conformation.

IrisFP

Further improvements of EosFP yielded IrisFP, the first FP that combines irreversible green-to-red photoconversion with reversible photoswitching between a fluorescent and

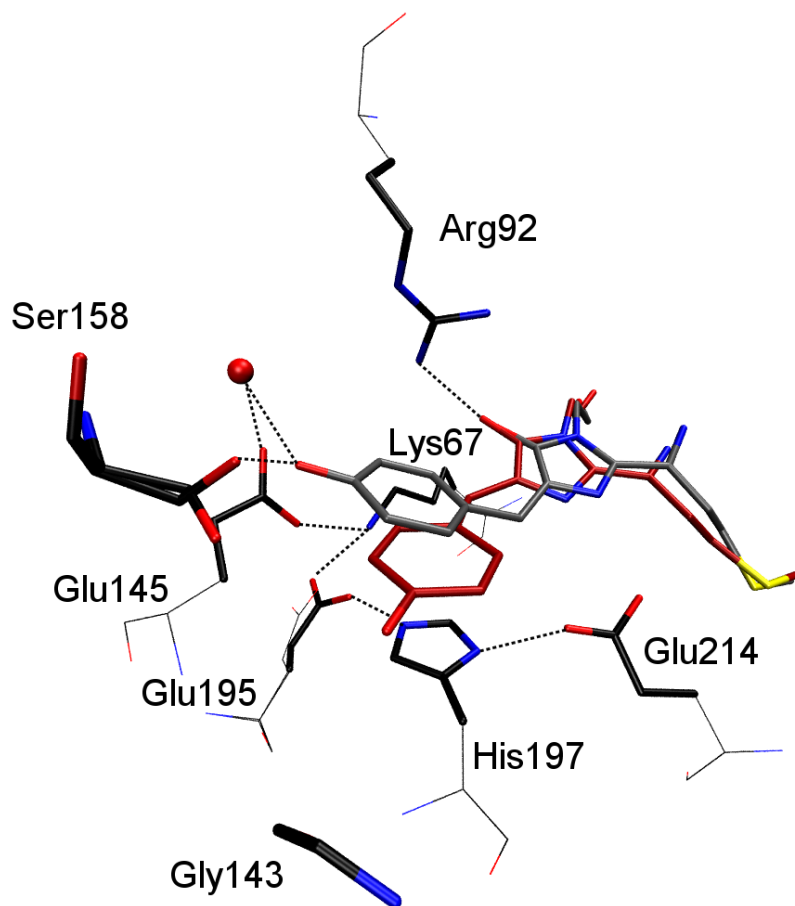


Figure 2.6. The cis (red) and the trans (gray) chromophore of psRFP together with important amino acids in the direct chromophore environment are displayed. Color coding for surrounding residues: black = carbon; red = oxygen; blue = nitrogen. Water molecules are represented by red spheres, hydrogen bonds by dashed lines.

a non-fluorescent state⁶⁷. The green-to-red conversion that changes the emission from ~516 nm to ~580 nm, is achieved by intense 405-nm illumination. The same structural modification that was earlier identified in EosFP also leads to an extension of the emitting π -electron system in IrisFP, which results in a shift of the emission to longer wavelengths. This is not surprising because IrisFP, named after the Greek goddess Iris that personifies the rainbow, was derived from EosFP. More interesting is the fact that, in addition to photoconversion, IrisFP exhibits a reversible on-off switching mode based on cis-trans isomerization, in both its green and red forms. IrisFP was generated by replacing Phe173 with a serine in EosFP. The smaller sidechain of serine provides open space that allows cis-trans isomerization and leads to reversible photoswitching. IrisFP displays a negative switching mode, the same wavelength that excites the fluorescence switches the protein to a dark state. Excitation with 473 nm/561 nm excites the emission at 516 nm/580 nm and induces a transition to the non-fluorescent trans state at

2.3. Photoactivatable Fluorescent Proteins (PAFPs)

the same time. Illumination with weak 405-nm light, on the other hand, turns the green emission (Emission peak at $\lambda_{em} = 516$ nm) back on by switching the chromophore from the trans to the fluorescent cis state. The same effect can be observed under 473-nm illumination for the red chromophore. IrisFP is an interesting marker for live cell experiments due to its remarkable properties. However, its tetrameric nature might perturb the function and localization of the labeled proteins. Therefore, an advanced monomeric variant, mIrisFP, was developed⁶⁸ by Susan Gayda and Maik Krause. The mutations A69V, K145I, and Y189A yielded a monomeric, bright and photostable marker protein with spectroscopic and photoswitching properties similar to those of IrisFP (Fig. 2.7).

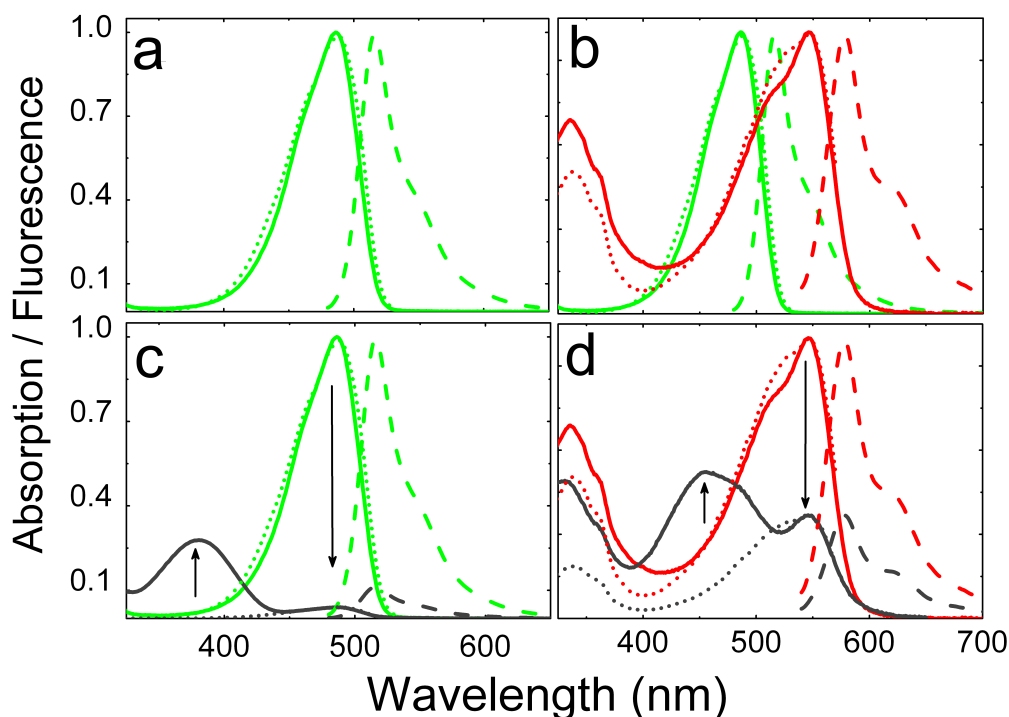


Figure 2.7. Spectroscopic characterization of mIrisFP. Absorption, excitation, and emission spectra scaled to equal peak amplitudes are displayed by solid, dotted, and dashed lines, respectively. Emission spectra of green (red) mIrisFP were recorded with 473 (532) nm excitation. Excitation spectra of green (red) IrisFP were measured for 540 (580) nm emission. (a) Spectra of green mIrisFP. (b) Spectra of green mIrisFP before (green lines) and after (black lines) illumination with 473-nm light for off-switching. (c) Spectra of red mIrisFP (red lines) after photoconversion of green mIrisFP (green lines) with intense 405-nm light. (d) Spectra of red mIrisFP before (red lines) and after (black lines) illumination with 532-nm light for off-switching (corrected for background). Spectra measured by Susan Gayda, image taken from⁶⁸.

mRubyN(N143C)

The red FP mRuby is a monomeric variant of eqFP611 found in the sea anemone *Entacmaea quadricolor*⁶⁹. With excitation and emission maxima at 558 nm and 605 nm, mRuby combines bright red emission with a large Stokes shift of 47 nm⁷⁰. The chromophore in eqFP611, 2-iminomethyl-5-(4-hydroxybenzylidene)-imidazolinone, forms autocatalytically from the tripeptide Met63-Tyr64-Gly65 and assumes a fluorescent coplanar trans configuration. For the dimeric variant d1eqFP611, a red-shifted species was observed after intense 532-nm illumination and attributed to a trans-cis isomerization⁷¹. Spectroscopic and structural studies of dimeric variants of eqFP611 identified a fluorescent trans conformation with 611-nm emission and a fluorescent cis species with 639-nm emission. The replacement of Asn143 by serine yielded a mixture of cis and trans chromophores with an overall emission maximum at 630 nm. The asparagine at position 143 forms a hydrogen bond with the trans chromophore and thereby stabilizes the trans conformation. With the goal of destabilizing this interaction in mRuby and generate a switching FP, the mutation Asn143Cys was introduced. The absorption spectrum of the N143C mutant shows a prominent shoulder towards longer wavelength on the anionic band at 560 nm and the emission band is shift about 10 nm towards lower wavelength in the mutant compared to mRuby (Fig. 2.8). The prominent shoulder in the absorp-

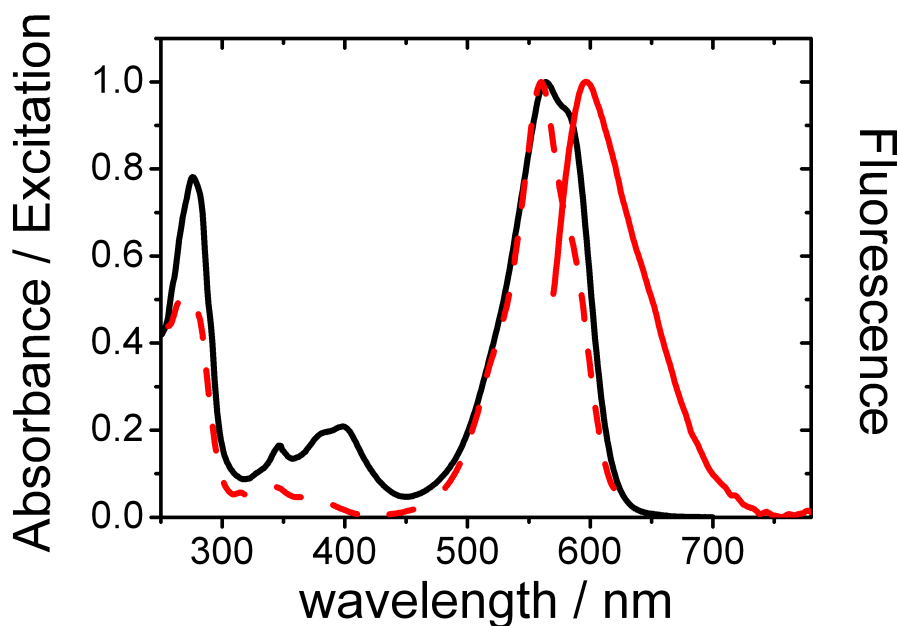


Figure 2.8. Spectroscopic characterization of mRuby(N143C). Absorption, excitation, and emission spectra scaled to equal maximum amplitudes are depicted by red, red dashed, and black lines, respectively.

tion spectrum results most probably from a second chromophore conformation (cis and trans). Unfortunately mRuby(N143C) displayed no switching under 450-nm activation,

2.3. Photoactivatable Fluorescent Proteins (PAFPs)

as expected; instead, the FP showed a remarkable bleaching behavior, similar to psRFP (Fig. 2.9).

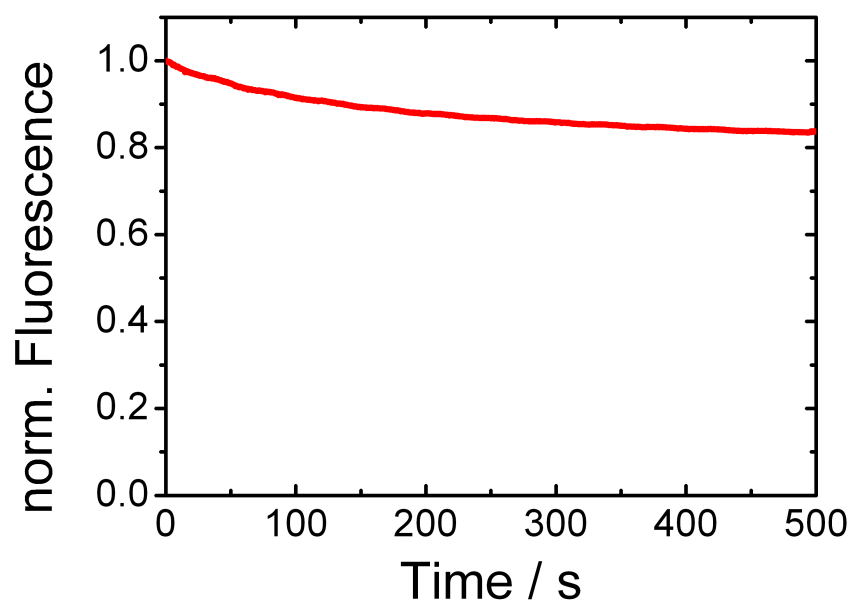


Figure 2.9. Bleaching curve of mRuby(N143C) (561-nm irradiation with 250 W cm^{-2}).

3. Light Microscopy

Light microscopy is by far the most widespread microscopy technique used in the life sciences because the noninvasive nature of light allows the investigation of biological processes in living cells and organisms with minimal disturbance of the cellular environment. Especially popular is fluorescence microscopy, which permits the selective tagging of molecules and organelles combined with a wide variety of readout modes such as fluorescence lifetime, anisotropy, color and intensity. Fluorescence microscopy has the unique capability to probe dynamic processes, linking molecular components and their localization with function and permits the identification of multiple specific components. However, fluorescence microscopy has a major drawback. The limited resolution of visible light due to diffraction makes it impossible to study structures smaller than $\approx \lambda/2$. In other words, light microscopy cannot provide a detailed picture of many interesting cellular processes such as protein complex formation, structural dynamic details and reorganization on the lower nanometer scale.

3.1. Diffraction

When light hits an obstacle, the amplitude and phase of a part of the wavefront is changed leading to the general phenomenon known as diffraction. Diffraction describes the apparent bending of waves around small obstacles and the spreading out of waves past small openings. The propagation of the wavefront after an obstacle can be explained by the Huygens-Fresnel principle. Every point on the wavefront is considered as a point source for a secondary radial wave. The subsequent propagation and addition of all resulting radial waves form the new wavefront past an obstacle or aperture. The sum of all wave contributions is determined by the relative phases and the amplitudes of the individual waves. The intensity distribution of the wavefront can be observed as an interference pattern or diffraction pattern with minima and maxima on a distant screen. Diffraction occurs in all lens-based optical setups such as telescopes, microscopes and many others. The objective of a microscope can be simplified as a single lens that focuses the diverging light from a source onto the detector (Fig. 3.1a). This lens represents a circular aperture that causes diffraction. Light waves emitted isotropically from a point source do not interfere at a single point after propagating through the lens. Instead a setup dependent intensity pattern, called point spread function (PSF), emerges around the point (Fig. 3.1b). The PSF of a circular aperture is given by the Airy function,

$$I = I(0) \left[\frac{2J_1(kaq/R)}{kaq/R} \right]^2, \quad (3.1)$$

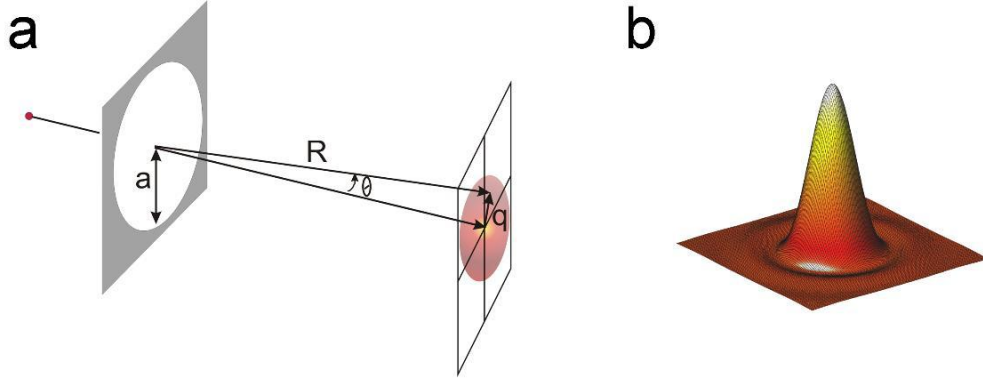


Figure 3.1. (a) The emitted light from a point source is diffracted by a circular aperture (lens) and the diffraction pattern (b) is detected on a distant screen. (b) Airy intensity distribution detected after light emitted from a point source passed through a circular aperture.

where $I(0)$ is the maximum intensity of the pattern at the airy disc center, J_1 is the Bessel function of the first kind of order one, $k = 2\pi/\lambda$ is the wavenumber, a is the radius of the aperture, q is the radial distance from the optical axis in the observation plane and R is the distance between the lens and the observation plane. The equation can also be written as a function of the angle θ , with $\sin \theta = q/R$,

$$I = I(0) \left[\frac{2J_1(ka \sin \theta)}{ka \sin \theta} \right]^2, \quad (3.2)$$

where θ is the angle of observation. The minima of the intensity distribution are given by the zeros of the Bessel function $J_1(x)$, at $x = ka \sin \theta \approx 0, 3.83, 7.02, \dots$. It follows that the first ring of minimal intensity occurs at

$$\sin \theta \approx \frac{3.83}{ka} = \frac{3.83\lambda}{2\pi a} = 1.22 \frac{\lambda}{2a} = 1.22 \frac{\lambda}{d}. \quad (3.3)$$

The radius q of the first ring of minimal intensity is given by

$$q = R \sin \theta = 1.22 \frac{R\lambda}{d}. \quad (3.4)$$

If the light is focused by a lens with the focal length f on the screen, $f \approx R$, and the equation becomes

$$q = R \sin \theta \approx 1.22 \frac{f\lambda}{d}. \quad (3.5)$$

3.1.1. Diffraction Limit

It is the expanded intensity distribution due to diffraction that limits the ability of a light microscope to resolve fine detail. This can be understood by considering two separated

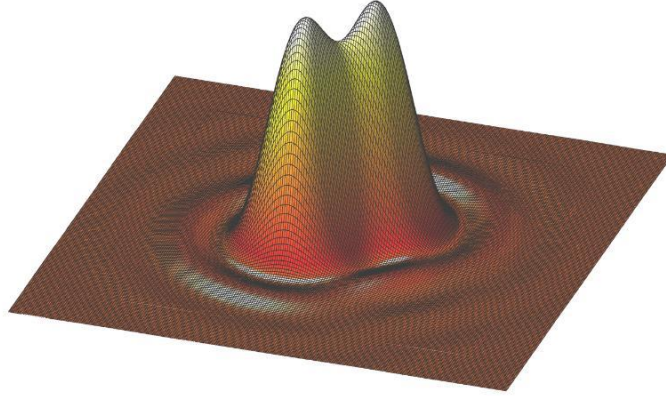


Figure 3.2. Two point sources in close proximity are detected as two Airy patterns and can only be resolved as two separated point sources as long as the maximum of one Airy pattern coincides with the first minimum of the other.

point sources in close proximity. Each point source will produce an Airy pattern on the detector (Fig. 3.2) and, as the point sources move closer together, the pattern will start to overlap, ultimately the two distributions will merge and form a single pattern. In this case, the two point sources can no longer be resolved as separated points. According to Lord Rayleigh, two point sources can still be resolved, if the maximum of one Airy pattern coincides with the first minimum of the other.

$$\Delta x_{\min} = 1.22 \frac{f\lambda}{d}. \quad (3.6)$$

Ernst Abbe formulated his resolution limit for optical microscopes in a similar way: The exact spacing in a specimen can be resolved when the numerical aperture of the objective lens is large enough to capture the first order diffraction pattern produced in a diffraction-limited microscope at a specific wavelength. He derived the lateral and axial resolutions of such an instrument as

$$\Delta x_{\min} = \frac{\lambda}{2 \text{NA}} = \frac{\lambda}{2n \sin \alpha} \quad (3.7)$$

and

$$\Delta z_{\min} = \frac{2\lambda}{n \sin^2 \alpha}, \quad (3.8)$$

respectively. The index of refraction n and the half-angle α of the maximum cone of light that can enter or exit the lens together with the wavelength of light λ determine

3. Light Microscopy

the resolution of a microscope. With a numerical aperture (NA) around 1 to 1.5, the resolution of a microscope operating with visible light is limited to ~ 200 nm. Unfortunately, many cellular processes occur on length scales smaller than 200 nm, which leaves us with a light microscope, excellently suited for non-invasive cell studies but with an insufficient resolution. Both, Rayleigh's criterion and Abbe's diffraction limit were developed at a time when light was still detected with the naked eye. They neglect the stochastic nature of the photon-detection process and hence, do not consider the total photon counts in the acquired data. Therefore, both criteria are not well adapted to current microscope setups, in which highly sensitive photon-counting cameras are used. A fundamental resolution measure (FREM) can be calculated for modern microscopes from a stochastic framework⁷². It gives a bound to the accuracy with which the distance between two point sources can be estimated based on the acquired data as

$$x_{min} = \frac{1}{\sqrt{4\pi\Lambda_0 \cdot (t - t_0)\Gamma_0(d)}} \cdot \frac{\lambda}{NA}, \quad (3.9)$$

where λ denotes the emission wavelength, NA denotes the numerical aperture of the objective, Λ_0 is the number of detected photons per molecule, $[t_0, t]$ is the acquisition time interval and $\Gamma_0(d)$ is given by

$$\Gamma_0(d) = \int_{R^2} \frac{1}{\frac{J_1^2(\alpha r_{01})}{r_{01}^2} + \frac{J_2^2(\alpha r_{02})}{r_{02}^2}} \left(\left(x + \frac{d}{2} \right) \frac{J_1(\alpha r_{01})J_2(\alpha r_{01})}{r_{01}^3} \right. \quad (3.10)$$

$$\left. - \left(x - \frac{d}{2} \right) \frac{J_1(\alpha r_{02})J_2(\alpha r_{02})}{r_{02}^3} \right)^2 dx dy, \quad (3.11)$$

with J_n denoting the n th order Bessel function of the first kind, $\alpha = 2\pi NA/\lambda$; $r_{01} = \sqrt{(x + d/2)^2 + y^2}$ and $r_{02} = \sqrt{(x - d/2)^2 + y^2}$. The FREM depends on the distance d of the two point sources and is well below Rayleigh's criterion (less than 5 nm for 100 nm distance). For distances < 50 nm, however, the FREM deteriorates with decreasing separation. Thus, two point sources can be resolved far better than Abbe's limit in modern microscopes. All resolution criteria are based on the distance between two point sources, however, in labeled biological samples usually the density of fluorescent markers is much higher and the PSF of ten to hundred point sources overlap and cannot be decomposed.

3.2. Alternative Microscopy Techniques

The limited ability of light microscopy to resolve structures smaller than 200 nm gave rise to the development of a series of alternative microscopy techniques for biological applications such as soft X-ray tomography (SXT)⁷³ or electron microscopy⁷⁴. The soft X-ray illuminating photons used in SXT allows imaging of whole specimens with a resolution that is well below the diffraction limit of visible light⁷⁵. Cryogenic electron tomography (cryo-ET) provides even higher resolution (4-5 nm) for 3D imaging that permits detailed

studies of cellular and supermolecular structures⁷⁶. Unfortunately, a harsh treatment of the cells that can cause artifacts, is usually necessary to obtain high resolution images. Additionally, both techniques are limited to static snapshots and cannot capture dynamic processes. Therefore, it was necessary to develop complementary methods based on visible light microscopy for live cell observations.

3.2.1. Fluorescence Resonance Energy Transfer (FRET)

Interesting biological problems including conformational changes, direct protein-protein interaction and binding of proteins to cellular structures can be studied by fluorescence resonance energy transfer (FRET)^{77, 78, 79, 80}. Two molecules are labeled with fluorescent markers emitting in different spectral ranges. If the marker in the lower wavelength range is close to the red-shifted marker, the excitation energy is radiationless transferred and can be emitted in the longer wavelength range. By monitoring the emission from both labels the distance between the two can be calculated. FRET is not a new microscopy technique, but a powerful tool for the study of processes in the 1–10 nm range. Nevertheless, it still leaves a gap between 10–200 nm that can not be resolved by conventional light microscopy techniques.

3.2.2. Near-field Techniques

In principle, near-field techniques such as atomic force microscopy (AFM) and near-field scanning optical microscopy (NSOM) are able to overcome the resolution limit and fill the gap. Both methods have been successfully applied in the investigation of biological macromolecular structures. In NSOM a small subwavelength sized aperture that is used as a light source and/or detector is scanned in close proximity (10–20 nm) over the surface of the sample, thereby generating a point by point image with resolution related to the size of the probe (30–100 nm). The diffraction limit is overcome by removing the lenses and thus eliminating the need for focusing. Although NSOM has been used to study the nanoscale organization of several membrane proteins^{81, 82}, imaging in the nearfield is technically challenging and the imaging speed is slow. In addition, NSOM and AFM are restricted to probing the cell surface and cannot be used for intracellular imaging. These factors have prevented the widespread use of both methods in cell biology. It is possible to speed up the image acquisition by the recently introduced lenses with negative refractive index⁸³ which allow imaging of larger areas. Unfortunately these methods are also limited to surface imaging, due to the reliance on the evanescent light field, which fades exponentially within a distance of $\lambda/2$ from the object. These evanescent waves are converted into propagating waves and a magnified image is formed on a distant screen⁸⁴, however, hyperlens imaging is not a real far-field technique.

3.2.3. Confocal Microscopy

Confocal microscopy is a far-field technique that has especially improved 3D imaging. The sample is illuminated by a diffraction limited, focused spot and the light from the

3. Light Microscopy

sample is detected through a pinhole⁸⁵. By employing pointwise illumination scanning and pointwise detection, only the fluorophores in the shared volume of the illumination and detection point spread functions are detected. The effective PSF of such a microscope is described by the product of the diffraction pattern for illumination and for detection: $I(x, y, z) I_{em}(x, y, z) \approx I^2(x, y, z)$ ^{86, 87}. The multiplication of intensities and the nearly quadratic dependence on the intensity in this formula reduces the full width at half maximum (FWHM) of its central spot by $\sim \sqrt{2}$. In the Fourier domain, the multiplication expands the optical bandwidth of spatial frequencies even by a factor of two. In practice, however, the newly gained higher frequencies are heavily damped and the resolution of confocal microscopy is limited to a FWHM >200 nm in the focal plane and to >450 nm along the optical axis⁸⁸. Nevertheless, confocal microscopy is the basis for point-scanning superresolution techniques such as 4Pi microscopy and stimulated emission depletion microscopy because it improves 3D-imaging and effectively rejects background signals.

3.2.4. 4Pi and I⁵M Microscopy

In the early 1990s, two interference-based far-field optical microscopy techniques emerged, the spot-scanning 4Pi microscopy⁸⁹ and widefield I⁵M⁹⁰ that use juxtaposed objectives to expand the illumination or the detection wavefront. With a more completely collected spherical wavefront, fluorescent markers can be located more precisely. The same holds for the illumination wavefront. Both microscopy techniques coherently add the wavefronts of two large-angle lenses for excitation, detection, or both. I⁵M achieves an improvement in axial resolution by a factor of 3.5 compared to confocal and 7 fold compared to widefield microscopy, 4Pi microscopy improves the lateral resolution ~ 1.5 times and the axial resolution 7 times. However, because the enlarged wavefront is still not close enough to spherical, the focal spot exhibits lobes above and below the focal plane that have to be removed mathematically. After deconvolution, images of the Golgi apparatus and the mitochondrial network with ~ 100 nm axial resolution^{91, 92} were obtained and enzyme localization and transport of secretory cargo was monitored⁹³. Nonetheless, these methods perfected focusing alone and the diffraction barrier remained in place.

3.2.5. Stimulated Emission Depletion Microscopy (STED)

The first far-field method that surpassed the diffraction barrier was stimulated emission depletion (STED) microscopy⁹⁴. In a STED experiment, a focused excitation laser beam, which pumps the fluorophores to their excited state, is overlaid with a red-shifted STED beam (Fig. 3.3). This STED beam, typically with a donut-shaped intensity profile, triggers stimulated emission of the excited fluorophores in a region surrounding the excitation spot, forcing them to the ground state. The size of the PSF is reduced and the resolution increased because the STED beam confines fluorescence emission to a small region in the center of the donut. Due to the nonlinear intensity dependency of the deexcitation, resolutions below the diffraction limit can be achieved, despite the excitation beam and STED beam being diffraction-limited. STED over-

3.3. Photoactivation Localization Microscopy (PALM)

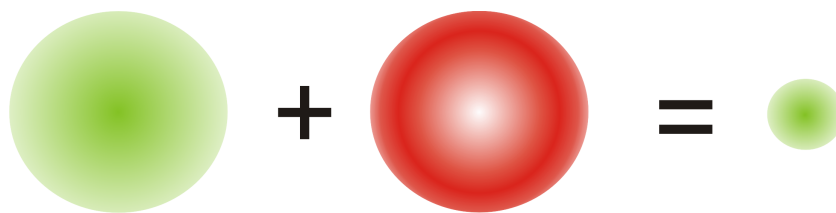


Figure 3.3. A focused excitation laser beam that pumps the fluorophores to their excited state (green), is overlaid with a STED beam (red) that triggers stimulated emission of the excited fluorophores and leaves only molecules in a small region fluorescent.

comes the diffraction barrier by ensuring that any neighboring fluorophores are never simultaneously in the on-state. To obtain a complete high resolution image, the beams are scanned across the sample, thereby achieving resolutions as high as 20 nm in the lateral directions, 30–40 nm in the axial direction, and 40–45 nm in all three dimensions simultaneously in biological samples when lateral and axial STED beams are combined in a 4Pi geometry^{95, 96}. For nitrogen-vacancy color centers in diamond, a resolution below 10 nm has been demonstrated⁹⁷. Video-rate imaging of synaptic vesicles in live hippocampal neurons using STED has been achieved⁹⁸ and nanoscale dynamics of membrane lipids in living cells has been demonstrated through the combined application of fluorescence correlation spectroscopy (FCS) and STED⁹⁹. STED has also been extended to reversibly saturable optical fluorescent transitions (RESOLFT)⁸⁸ a method that utilizes photoswitching instead of stimulated emission.

3.2.6. Structured Illumination Microscopy (SIM)

A different approach to increase the resolution is structured illumination microscopy (SIM)^{100, 101}. The sample is illuminated by a periodic wide-field light pattern that mixes with the spatial information in the sample and thereby shifts high frequency information into the detection range of the microscope. The frequency space that can be detected by the microscope is expanded and the PSF reduced. The resolution can be increased by a factor of two, as the periodicity of the excitation pattern is diffraction limited. Together with the dual objective geometry of I⁵M a 3D resolution of 100 nm is achievable^{102, 101}. When SIM is used with saturating intensities, excitation patterns with arbitrarily high spatial frequencies can be generated, which extends the resolution of saturated structured illumination microscopy (SSIM) significantly beyond the diffraction barrier^{103, 104}.

3.3. Photoactivation Localization Microscopy (PALM)

STED and SIM improve the optical resolution by spatially modulating the excitation light which fundamentally distinguishes them from another, recently introduced class of high resolution techniques including photoactivated localization microscopy (PALM)³⁷, fluorescence photoactivation localization microscopy (FPALM)³⁸ and stochastic optical

3. Light Microscopy

reconstruction microscopy (STORM)¹⁰⁵. These methods rely on two ideas, first, the localization of a single point source with a precision beyond the diffraction limit and second, the isolation of single point sources within a fluorescent ensemble based on consecutive photoactivation and bleaching or deactivation.

3.3.1. Single Molecule Localization

Although the intensity distribution of a single fluorophore in a light microscope is diffraction limited and results in an Airy disc of $\sim 200\text{--}300\text{ nm}$ on the charge-coupled device (CCD) camera (Fig. 3.4a,c), the precision of determining the fluorophore position can be much higher, up to 1 nm and better^{106, 107}. The fluorophore position is estimated

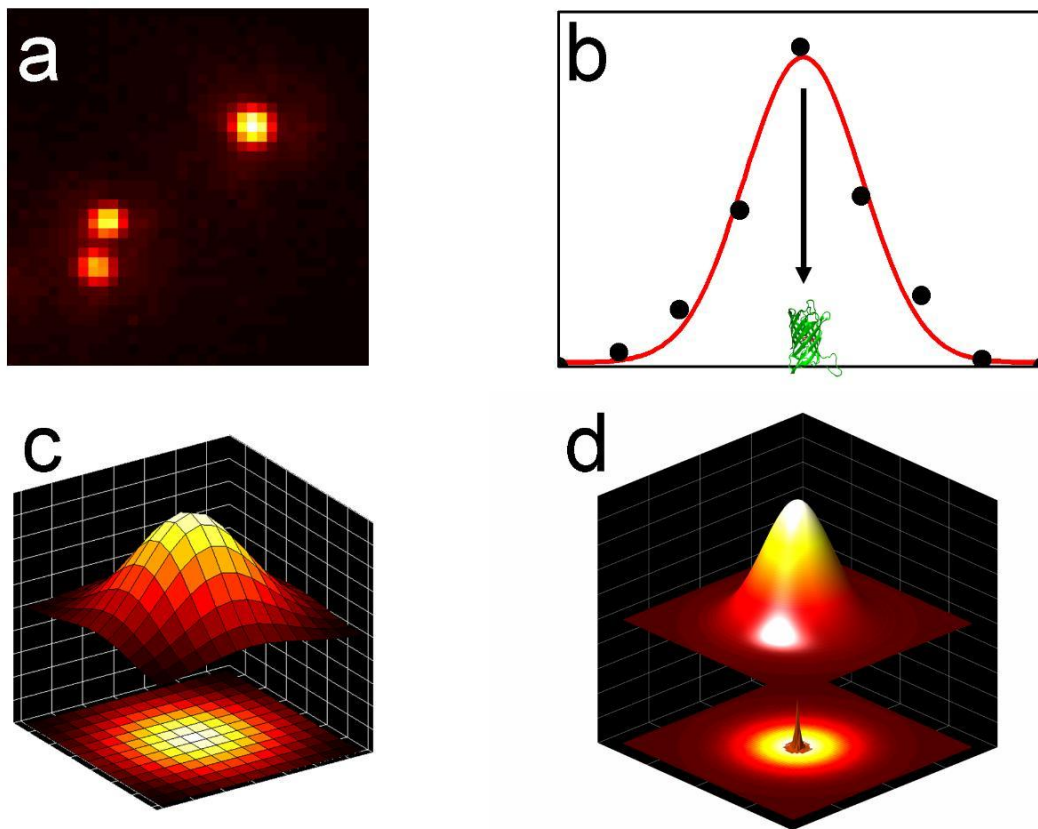


Figure 3.4. (a) Detected PSFs of three fluorophores on a CCD camera. (b) Detected intensity values (black dots) and Gaussian fit that yields the position of the fluorophore. (c) Three dimensional intensity distribution. (d) Two dimensional fit of the detected intensity distribution and position of the fluorophore.

by a statistical fit to the photon distribution which yields the center of the fluorescence emission that coincides with the position of the fluorophore (Fig. 3.4b,d). When the

3.3. Photoactivation Localization Microscopy (PALM)

fluorophore is assumed to be a point source, then the photon distribution is given by the point-spread function (PSF) of the microscope,

$$\text{PSF}(r) = \left(\frac{2J_1(ra)}{r} \right)^2, \quad (3.12)$$

with

$$a = \frac{2\pi\text{NA}}{\lambda}, \quad (3.13)$$

where r is the distance from the origin, NA is the numerical aperture of the objective, λ is the wavelength of light and J_1 is the Bessel function. The detected intensity distribution can be well approximated by a two-dimensional Gaussian distribution¹⁰⁸,

$$I(x, y) = I_0 \cdot \exp \left[-\frac{(x - x_0)^2 + (y - y_0)^2}{2s^2} \right], \quad (3.14)$$

where x_0 and y_0 are the coordinates of the point source, I_0 is a constant and s is the standard deviation. The Gaussian distribution is mathematically more tractable and the differences to the Airy function are minor in practice because the recorded fluorescence images are rarely precise enough to distinguish between the two functions¹⁰⁹.

3.3.2. Localization Precision

Each registered photon from a fluorescent source gives a measure of the position of the source, and the position error for each photon measurement is given by the standard deviation of the point spread function of the microscope. The measured position of the source is then determined by the average of detected photon positions. The error on the mean is calculated as

$$\langle (\Delta x)^2 \rangle = \frac{s^2}{N}, \quad (3.15)$$

with the localization error Δx , the standard deviation of the point spread function s and the number of photons N . Because the photons are detected with a CCD camera that consists of pixels of size a , an additional error resulting from the uncertainty of where the photon arrived in the pixel adds to the uncertainty of each photon measurement,

$$\langle (\Delta x)^2 \rangle = \frac{s^2 + a^2/12}{N}, \quad (3.16)$$

for $s > a$. The factor $a^2/12$ is the variance of a top-hat distribution of size a . The localization precision deteriorates due to background noise b . Common sources of background noise include camera readout noise, dark current noise, and cellular autofluorescence.

$$\langle (\Delta x)^2 \rangle = \frac{8\pi s^4 b^2}{a^2 N^2}. \quad (3.17)$$

3. Light Microscopy

Combining the results for photon-counting noise, pixelation error, and background noise in one equation leads to the localization error in two dimensions¹⁰⁹

$$\langle(\Delta x)^2\rangle = \frac{s^2 + a^2/12}{N} + \frac{8\pi s^4 b^2}{a^2 N^2} \quad (3.18)$$

and in one dimension

$$\langle(\Delta x)^2\rangle = \frac{s^2 + a^2/12}{N} + \frac{4\sqrt{\pi} s^3 b^2}{aN^2}. \quad (3.19)$$

For high photon numbers and low background, the localization precision increases. Especially in biological samples with increased background from autofluorescence, bright fluorophores with high emission are needed to achieve localization accuracies of 20–30 nm.

3.3.3. PALM Scheme

Single fluorophores can be localized with extremely high precision. However, the method can not be applied to densely labeled biological samples because the overlapping PSFs of the numerous labels prevent the accurate localization of single fluorophores. One approach to separate the emission from different fluorophores is to employ spectrally distinct labels which can be detected with different filters this method is termed spectrally assigned localization microscopy (SALM)¹¹⁰. But the visible spectral range is limited and the emission spectra of currently used fluorescent markers restricts the number of separately detectable fluorophores to about ten. A more successful method, applied in PALM imaging, is to separate the emission of the numerous fluorescent markers in time by sequentially switching them on and off (Fig. 3.5). For this approach, photoactivatable fluorescent markers are needed. Possible labels are photoactive FPs or synthetic dyes that are activated by light of a certain wavelength and subsequently photobleached or photoswitched to a non-emitting dark state by light of a second wavelength. During each imaging cycle, most molecules remain undetectable (green molecules) and only a small percentage is stochastically switched to the detectable state (red molecules). The light-induced change can be from non-fluorescent to fluorescent (psRFP, mRubyN143C, mIrisFP) or a change in emission wavelength (EosFP, mcavRFP, mIrisFP). The number of molecules in the detectable state is controlled by the light intensity of the activation light and can be adjusted to minimize the probability of detecting two molecules within a diffraction limited spot. The well separated single fluorescent molecules are then detected and localized by one of the fitting routines described in the experimental section. After emitting sufficient photons for precise localization, the fluorescent molecules are photobleached or switched off, ideally after one image frame and new molecules are activated. Repeating this process over many cycles and combining the detected molecule positions in one data set allows reconstruction of a super-resolution image (Fig. 3.5). Variations of this method have been published under new acronyms, such as PALM with independently running acquisition (PALMIRA)¹¹¹, ground state depletion and individual

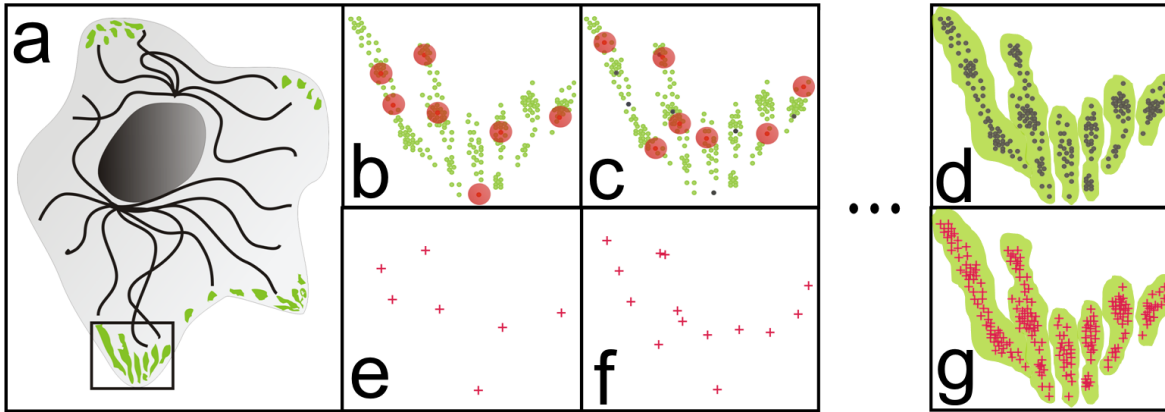


Figure 3.5. (a) Cell with nucleus, microtubuli network and focal adhesion points. Paxillin, a key component of the focal adhesion complex is labeled with a photoconvertible/photoactivatable FP. (b) A sparse subset of FPs is activated/converted (red dots) and detected. The molecule positions are determined (e) from the recorded signals. (c) Molecules detected in (a) are switched off or bleached (black dots) and a new subset of FPs is activated/converted, detected and localized (f). This procedure is repeated for several thousand frames until all FPs are localized (d). (g) The positions of all detected FPs are combined to a high resolution image (red crosses). The green structures indicate a conventional microscopy image.

molecule return (GSDIM)¹¹², point accumulation for imaging in nanoscale topography (Paint)¹¹³ and direct STORM (dSTORM)¹¹⁴ or spectral precision distance measurement (SPDM)¹¹⁵.

3.4. Resolution in PALM Images

The experimental PALM scheme permits localization of single fluorophores with high precision in densely labeled biological samples. But one has to distinguish between localization accuracy which gives a measure of how precisely a single fluorophore can be localized, and the resolution which is classically defined as the minimum distance necessary to distinguish two emitting point sources. In principle, it is impossible to define a resolution for PALM images in the classical sense, because two emitting particles in close proximity are never simultaneously detected. Therefore two fluorophores can be arbitrarily close and still be resolved as two distinct emitters in a PALM experiment. One can only give the localization accuracy for the single emitters. However, the resolution of an image is not solely determined by the localization precision of the individual markers, but rather by the number and spacing of the fluorophores. The Nyquist sampling theorem can be applied to determine the image resolution when the sample features are considered in the domain of spatial frequency rather than object size. The number of objects per spatial unit (the frequency) is the inverse of the object size and emphasizes the importance of the spacing between specimen features in image formation. According

to the Nyquist-Shannon theorem¹¹⁶, the sampling frequency should be at least twice the highest spatial frequency contained in the image. Thus, an average distance of 25 nm between the localized fluorophores allows imaging of two-dimensional structures with a resolution of 50 nm. The image resolution in fluorescence microscopy is generally determined by the label density, which varies locally in biological samples and, therefore, the resolution according to the Nyquist-Shannon theorem is a local property.

3.5. PALM Applications

PALM was first used to visualize the distribution of the lysosomal transmembrane protein CD63, mitochondria and the focal adhesion protein vinculin³⁷. At the same time a second research group imaged DNA constructs with 20 nm resolution using synthetic dyes¹⁰⁵. Soon thereafter, the technique was expanded to two-color applications on microtubuli and clathrin coated pits¹¹⁷, microtubuli networks¹¹⁸, adhesion complexes³⁴, chromosomal proteins H2A and Snf2H¹¹⁹, clusters of transferrin receptor, clathrin light chain⁴⁴ and vertebrate kinetochore components¹²⁰. The method has also been extended from a 2D imaging technique to 3D imaging with subdiffraction accuracy over an imaging depth of a few microns by double-plane detection in biplane (BP) FPALM¹²¹. Introducing astigmatism, as in 3D STORM^{122, 123} allowed imaging with 20–30 nm resolution in the lateral and 50 nm in the axial direction, and engineering a double-helix shaped point spread function¹²⁴ yielded a resolution of 75 nm in axial direction. Axial sectioning can also be achieved by an interferometric design (iPALM)¹²⁵, where two opposing objectives collect the emitted photons, and due to the photons' selfinterference for equal path lengths, the distance of the emitters from the focal plane can be determined with a very high precision of 10-20 nm. Besides the improvement in axial resolution, the lateral resolution is also increased because twice the number of photons are collected. The practical use of this technique has been demonstrated in a detailed study of focal adhesions. Modification with a tilted mirror close to the sample is necessary in virtual volume superresolution microscopy (VVSRM) for an isotropic 3D resolution. This super-resolution technique has been applied for imaging bacteria, bacteria actin homologue MreB and neural dendrites¹²⁶. The greatest potential advantage of high resolution light microscopy is the application to living cells and tissue. So far only a few experiments have demonstrated the ability of PALM in live-cell imaging. The distribution of the membrane protein haemagglutinin from influenza virus was studied in live fibroblasts with 40 nm accuracy¹²⁷, the bacterial actin protein MreB in live *Caulobacter crescentus*¹²⁸, high-density molecular tracks of tso45 vesicular stomatitis virus G particles and HIV-1 Gag membrane proteins were observed³⁵, and adhesion-complex dynamics was imaged with 60 nm resolution¹²⁹. The high resolution microscopy method has also been applied to image hotspots of localized electromagnetic modes on structured metal surfaces with 1.2 nm accuracy¹³⁰. At these hotspots, signals are enhancement by a factor of 10^{15} , therefore, the effect has a broad range of potential applications, such as the detection of weak chemical signals¹³¹.

3.6. Markers for High Resolution Imaging

Photoswitchable or photoconvertible fluorescent proteins are excellent markers for high resolution imaging in living cells. Besides the genetically encoded FPs, a number of other luminescent markers can be employed for high resolution imaging. Organic dyes such as ATTO dyes are used in STED applications^{132, 133} and photochromic probes, including rhodamines, diarylethenes, photoswitchable cyanines and ATTO dyes are employed in PALM related methods^{134, 135, 118, 117, 136}. Caged compounds could also be exploited in superresolution imaging^{137, 138}. During uncaging, irradiation with UV light causes the release of a protective group and results in a large increase in the fluorescence intensity of the dye. Apart from increased brightness and photostability compared with FPs, non-genetically encoded probes have some drawbacks, for example, they have to be targeted to the biomolecule of interest, which can be achieved by using antibody conjugation. Unfortunately, antibodies are not membrane permeable, and hence are not useful for intracellular labeling of living cells. In fixed cells, the labeling efficiency is usually low, and the large size of the antibody adds another ~10–20 nm to the localization uncertainty. Therefore, new and innovative techniques were developed to append chemically synthesized fluorophores to proteins within living cells. Some methods use a peptide sequence fused to the protein of interest to recruit the organic dye^{139, 140, 141, 142} and other methods utilize proteins for labelling with small-molecule probes^{143, 144, 145} or a combination of a peptide recognition sequence and an enzyme that catalyses the covalent attachment of the probe to the peptide is used^{146, 147}. Also chemical tags can be employed for live cell high resolution imaging¹⁴⁸. Another promising class of luminescent markers are nanocrystals, for example, super-resolution optical fluctuation imaging (SOFI) makes use of the fluorescence blinking of semiconductor quantum dots to obtain subdiffraction optical resolution¹⁴⁹. Nanodiamonds with nitrogen vacancies are very robust with regard to photobleaching and provide an extremely high localization accuracy⁹⁷.

3.7. Cellular Structures

The cellular structures that are studied by high resolution microscopy throughout this work are described in the following section.

3.7.1. Cytoskeleton

The cytoskeleton is a cellular scaffold contained within the cytoplasm of the cell that maintains the cell shape, provides mechanical stability and participates in many cellular processes, including cell motility, cell adhesion, cell division, vesicle and organelle movement and cell signaling. The cytoskeleton is formed by actin filaments together with intermediate filaments and microtubules.

3.7.2. Actin and Lifact

Actin is a highly-conserved 42-kDa globular protein¹⁵⁰, that is found in almost all eukaryotic cells. Filaments composed of actin molecules are dynamic structures that are changed by coordinated polymerization and depolymerization. In migrating cells the dynamic assembly/disassembly of the actin network drives cell motility, while in a muscle, a stable actomyosin system forms the contractile apparatus¹⁵¹. Actin filaments are assembled in two general types of structures: bundles and networks. The structures that contribute to cell migration are organized in the lamellipodial actin network, which provides the force for plasma membrane protrusion during cell migration. The contractile actin stress fibers are individual filaments or bundles of numerous actin filaments that can be divided into three classes: ventral stress fibers, dorsal stress fibers and transverse arcs. Ventral stress fibers lie along the base of the cell, attached to the focal adhesions at each end. Dorsal stress fibers are attached to a focal adhesion at one end only and transverse arcs are curved actin bundles, which display a periodic α -actinin myosin distribution, and are typically not directly attached to focal adhesions, but are connected to the substrate via dorsal stress fibers. The different actin structures can be studied with the help of Lifact¹⁵² a short peptide (17 amino acids), which binds to filamentous actin (F-actin) structures in eukaryotic cells and tissues. When fused to fluorescent proteins, Lifact can be used as a marker for imaging actin structures in fluorescence microscopy.

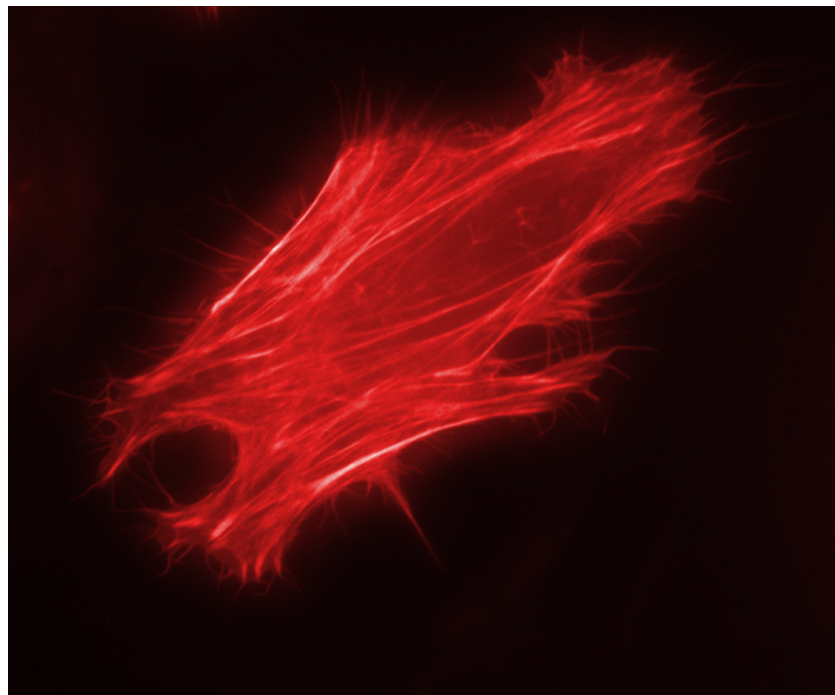


Figure 3.6. Actin filaments visualized with the actin-binding peptide Lifact labeled with mRuby in living cells. Image from F. Oswald, Department of Internal Medicine I, University Medical Center Ulm.

3.7.3. α -actinin

The actin binding protein α -actinin cross-links actin filaments and is a major constituent of diverse actin-based structures, such as stress fibers, focal adhesions, and the peripheral belt of epithelial cells¹⁵³. Apart from its mechanical function, α -actinin plays multiple important roles in the cell. It links the cytoskeleton to different transmembrane proteins in a variety of junctions, regulates the activity of a number of receptors, and serves as a scaffold to connect the cytoskeleton to diverse signaling pathways¹⁵⁴.

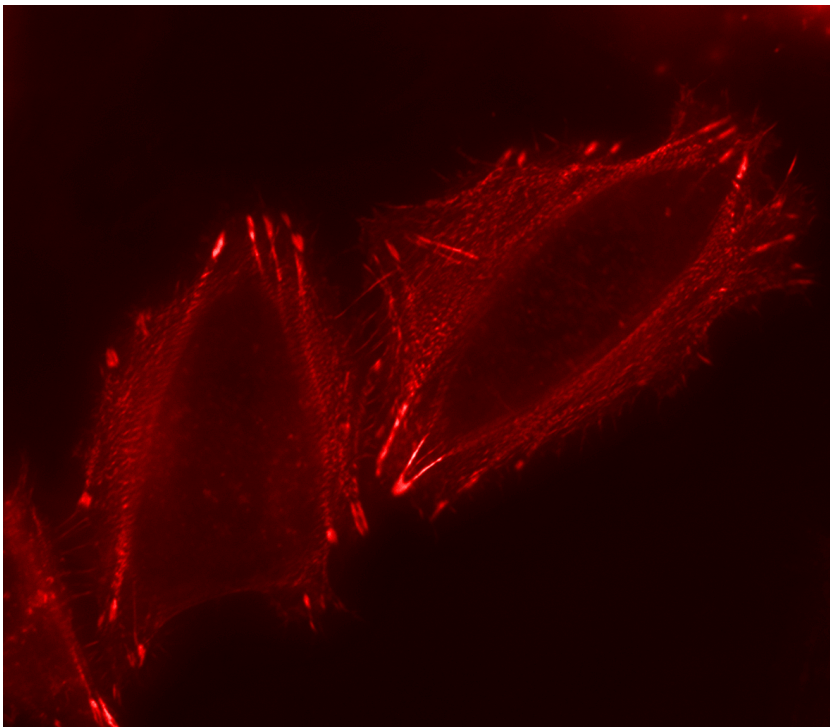


Figure 3.7. α -actinin structures labeled with mRuby in living cells. Image from F. Oswald, Department of Internal Medicine I, University Medical Center Ulm.

3.7.4. Microtubules

Microtubules are cytoskeletal polymers made of repeating α - and β -tubulin heterodimers¹⁵⁵. The tubulin dimers polymerize in protofilaments, which bundle into hollow cylindrical filaments and are present in all eukaryotes. These filaments have a diameter of 25 nm and a length varying from 200 nanometers to 25 micrometers¹⁵⁶ and emerge from the microtubule organizing centers (MTOCs), such as centrioles and basal bodies. Microtubules affect cell shape, transport, motility, cell division. They are required for the assembly of the endoplasmic reticulum and the Golgi apparatus, and are used as highways for organelle transport. During mitosis, microtubules rearrange to form the so-called mitotic spindle. The mitotic spindle orients the plane of cell cleavage and functions as a supramolecular motor to segregate the chromosomes to the cell poles during anaphase.

3. Light Microscopy

Of special interest are motor proteins of the kinesin and dynein families, which use ATP hydrolysis to move cargoes along microtubules or microtubules with respect to each other. Microtubule arrays in cells are generally dynamic, capable of assembly, disassembly and rearrangement on a time scale of seconds to minutes.

3.7.5. RITA

The Notch signaling pathway regulates fundamental cellular processes, including stem cell maintenance, control of cell differentiation, and proliferation¹⁵⁷. Notch signaling is activated via direct cell-to-cell contacts. Upon ligand binding, the proteolytic cleavage and release of the Notch intracellular domain (NICD) is induced which translocates to the nucleus. It activates transcription of Notch target genes in the nucleus through interaction with the DNA binding protein RBP-J (Recombination signal sequence-Binding Protein $J\kappa$). The recently discovered protein RITA (RBP-J Interacting and Tubulin Associated) is a highly conserved, 36 kDa protein that interferes with Notch- and RBP-J-mediated transcription¹⁵⁸. It induces nuclear export of RBP-J and thereby functions as a negative modulator of the Notch signaling pathway via shuttling of RBP-J to tubulin fibers. RITA is excellently suited to visualize the microtubuli network, due to its tubulin-binding ability.

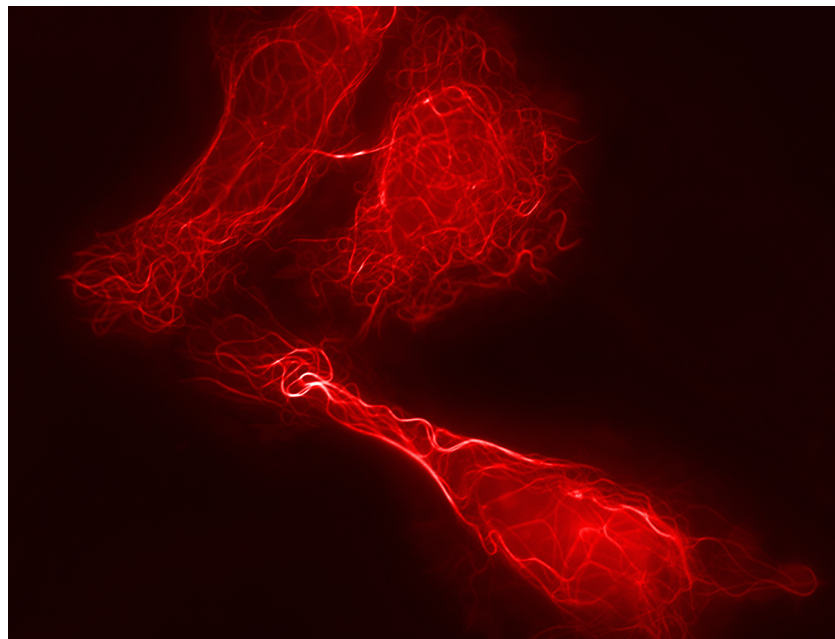


Figure 3.8. Microtubule fibers visualized with the microtubuli binding protein RITA labeled with mRuby. Image from F. Oswald, Department of Internal Medicine I, University Medical Center Ulm.

3.7.6. Paxillin and Focal Adhesions

Cells adhere to underlying substrates through discrete regions of the plasma membrane, referred to as adhesion plaques, focal contacts, or focal adhesions. This interaction of a cell with its microenvironment regulates numerous processes such as embryonic development, wound healing, immune surveillance and tissue homeostasis through the modulation of migration, differentiation and proliferation. The transmembrane proteins responsible for regulating the binding of a cell to components of the external environment are the integrins. They serve as bridges between the extracellular matrix (ECM), the intracellular signaling machinery and the actin cytoskeleton. Interaction with the ECM leads to integrin clustering and recruitment of a wide variety of intracellular proteins. These macromolecular foci contain more than 125 individual proteins, and many of these proteins exhibit multi protein-protein interactions^{159, 160}. Unfortunately, most of the interactions that govern focal adhesion function, regulation of the multiple interactions and their role in coordinating bidirectional signaling are still unknown. One of the important proteins that has already been studied to some extent is paxillin, a protein that serves as a platform for recruitment of numerous regulatory and structural proteins¹⁶¹. Paxillin, together with other proteins, controls the dynamic changes in cell adhesion, cytoskeletal reorganization and gene expression that are necessary for cell migration and survival. The name paxillin is derived from the term paxillus (a peg or stake) and suggests a function that is analog to a tent peg which tethers actin stress-fiber cables to the adhesion site because, initially, focal adhesions were believed to function solely as passive structural links between the ECM and the actin cytoskeleton. It has now been recognized that adhesion contacts are dynamic structures^{162, 163, 164, 165} that assemble, disassemble or mature at the extending leading edge and disassemble at the retracting cell rear during cell migration. Paxillin is one of the earliest proteins to be detected in forming adhesions at the leading edge of the cell, where it is rapidly organized¹⁶⁶, which suggests that paxillin plays an important role in promoting the assembly of adhesions and in defining their molecular composition. Upon application of tensile force, some focal complexes mature and provide a physical link to the contractile actomyosin machinery that is required for cell translocation. It is also of note that the adhesion disassembly does not occur homogeneously within adhesion contacts, but rather in a punctate manner¹⁶⁷.

3. *Light Microscopy*

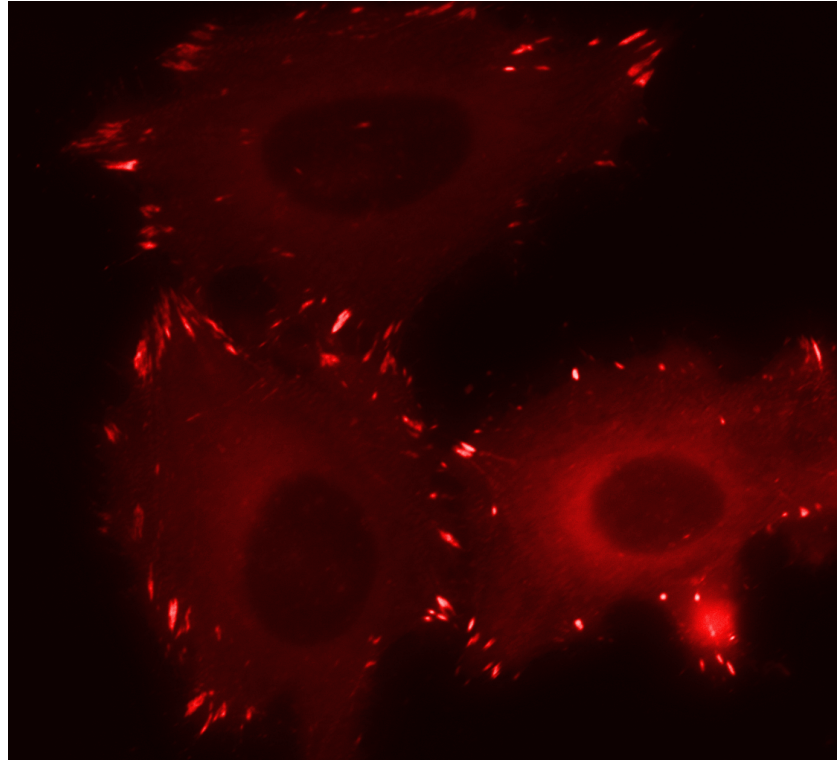


Figure 3.9. Paxillin labeled with mRuby accumulates in focal adhesions. Image from F. Oswald, Department of Internal Medicine I, University Medical Center Ulm.

4. Materials and Methods

4.1. Spectroscopic Characterization of the Fluorescent Proteins

4.1.1. Absorption Spectra

Absorption spectra were recorded on a Cary 1 spectrometer (Varian, Darmstadt, Germany) with a resolution of 1 nm. The protein solution was centrifuged for 10 min at 13,400 rpm, filled into a quartz cuvette and left in the spectrometer for 10 min in the dark. Subsequently, three absorption spectra were taken in 5 min time intervals to ensure that the sample was in thermal equilibrium.

4.1.2. Fluorescence Excitation and Emission Spectra

Fluorescence excitation and emission spectra were measured on a SPEX Fluorolog II spectrofluorometer (Spex Industries, Edison, NJ). Emission spectra were recorded with 2.1-nm resolution and 550-nm or 580-nm excitation. For excitation measurements, the emission was monitored at 630 nm and the resolution was 2.1 nm. Both measurements were corrected for the wavelength dependence of the detector efficiency. Prior to the fluorescence measurements, the concentration of the protein solution was determined in an absorption measurement and adjusted to an optimal value.

4.1.3. pH

For pH dependent data collection, a few microliters of concentrated protein stock solution were added to sodium citrate/phosphate, sodium phosphate, sodium carbonate buffer systems (pH 4.2–10). The final ionic strength was adjusted with sodium chloride to 150 mM.

4.1.4. Photoswitching

Photoswitching was induced by illuminating the sample solution with 473-nm laser light (LSR473-200-T00, Laserlight) at 20–800 mW cm⁻² (off switching) and with 561-nm laser light (GCL-150-561, CrystaLaser) at 20–500 mW cm⁻² (on switching). Special care was taken to illuminate the complete sample solution. Emission and absorption spectra were recorded during photoswitching. Low excitation light intensity at 580 nm compared to the switching intensities minimized the influence of the probe light on the sample. For

kinetic experiments, light-induced changes of the fluorescence intensity at 610 nm were recorded as a function of time.

4.1.5. Thermally Activated Recovery

For thermal recovery measurements and Arrhenius analysis, a psRFP sample was illuminated with 473-nm light until no further decrease in fluorescence was observed. The fluorescence recovery was monitored at 610 nm with the lowest possible 580-nm excitation intensity. For the Arrhenius analysis, the temperature of the sample was controlled and adjusted from 5°C to 40°C in 5°C steps. All other measurements were performed at room temperature.

4.2. Extinction Coefficient and Quantum Yield

The extinction coefficient was determined from the Beer-Lambert law

$$\epsilon = A/cl, \quad (4.1)$$

with the measured absorption A , the concentration c and the path length l (in our case 1 cm). The quantum yield QY was calculated according to the following equation¹⁶⁸, by using cresyl violet as reference

$$QY_{psRFP} = QY_{ref} \frac{I_{psRFP}}{I_{ref}} \frac{A_{ref}}{A_{psRFP}}. \quad (4.2)$$

The absorption A of the fluorescent form at pH 7 was obtained from the fitting procedure to the pH dependent absorption spectra, described in the results section. The emission intensity I was measured for both psRFP in buffer at pH 7 and the reference cresyl violet (SigmaAldrich, Steinheim, Germany) in methanol at equal optical densities. Usually, the refractive index of water (1.33) and methanol (1.33) has to be included in equation (4.2) but in our case the values for both solutions are the same.

4.3. SVD-MLS Analysis

The measured absorption spectra are a superposition of at least two or more absorption spectra at each pH value. The underlying ‘pure’ absorption spectra can be extracted with singular value decomposition based on matrix least squares fitting (SVD-MLS)^{169, 170}. Data obtained from thermal recovery experiments after 473-nm illumination are arranged in a matrix \mathbf{D} , of m different wavelengths and n different time points. This matrix can be decomposed as

$$\mathbf{D} = \mathbf{S}\mathbf{F}^T(\mathbf{p}) + \mathbf{E}, \quad (4.3)$$

where the rows of \mathbf{S} contain the absorption spectra of the different protein conformations (basis spectra). \mathbf{F}^T is the transpose matrix \mathbf{F} , which contains the time dependent

amplitudes of the basis spectra that depend on a set of fit parameters \mathbf{p} and the error matrix \mathbf{E} that contains random errors. The amplitudes of the basis spectra given as rows in \mathbf{F} are proportional to the concentration of the different protein states according to Beer's law. A model for trans(T)-cis(C) isomerization allows one to decompose the matrix \mathbf{D} and determines the population matrix $\mathbf{F}(\mathbf{p})$. During illumination with 473-nm light, the entire chromophore population of psRFP is switched from the cis state to the trans state. After the illumination is stopped, the chromophore relaxes back to a cis-trans equilibrium state. The changes in populations of the chromophore conformations are described by the following differential equations:

$$\frac{d[T]}{dt} = -k_{tc}[T] + k_{ct}[C], \quad (4.4)$$

$$\frac{d[C]}{dt} = k_{tc}[T] - k_{ct}[C], \quad (4.5)$$

with the rate coefficients k_{tc} for trans-cis isomerization and k_{ct} for cis-trans isomerization. The solution of the differential equations for the trans population describes the change in chromophore population:

$$[T](t) = \Delta[T]_0 e^{-t/\tau} + [T]_{eq}, \quad (4.6)$$

with

$$\frac{1}{\tau} = k_{tc} + k_{ct}, \quad (4.7)$$

and the equilibrium concentration $[T]_{eq}$ and $\Delta[T]_0 = [T] - [T]_{eq}$ at time $t = 0$. The population of the cis conformation $[C]$ is given by $[\text{total}] - [T]$. The best parameter set is determined by minimizing the error function

$$\phi = \|\mathbf{E}\| = \|\mathbf{D} - \mathbf{S}\mathbf{F}^T(\mathbf{p})\|. \quad (4.8)$$

For a fixed model matrix $\mathbf{F}(\mathbf{p})$, ϕ can be minimized by choosing $\mathbf{S} = \mathbf{D}(\mathbf{F}^T(\mathbf{p}))^+$, with the pseudo-inverse $(\mathbf{F}^T)^+$ of the matrix \mathbf{F}^T . This method is called matrix least-squares (MLS) method. Unfortunately, the MLS method is quite computer intensive, but it can be combined with singular value decomposition (SVD) for faster computation. SVD decomposes the matrix \mathbf{D} into

$$\mathbf{D} = \tilde{\mathbf{U}}\tilde{\mathbf{S}}\tilde{\mathbf{V}}^T. \quad (4.9)$$

The columns of $\tilde{\mathbf{U}}$ contain the basis spectra, and the matrix $\tilde{\mathbf{V}}$ consists of amplitude vectors. Only the first few basis spectra are above the noise level, the number of significant contributions can be identified by the diagonal elements s_r of the matrix $\tilde{\mathbf{S}}$ that are called singular values. The experimental data matrix \mathbf{D} with effective rank r can be well approximated by the first r columns of the SVD matrices,

$$\mathbf{D} = \tilde{\mathbf{U}}\tilde{\mathbf{S}}\tilde{\mathbf{V}}^T \approx \tilde{\mathbf{U}}_r\tilde{\mathbf{S}}_r\tilde{\mathbf{V}}_r^T. \quad (4.10)$$

4. Materials and Methods

The best parameter set $\hat{\mathbf{p}}$ of the model is then determined by minimizing the error function

$$\tilde{\phi} = \| \tilde{\mathbf{S}}_r (\tilde{\mathbf{V}}_r^T - \tilde{\mathbf{V}}_r^T (\mathbf{F}^T(\hat{\mathbf{p}}))^+ \mathbf{F}^T(\mathbf{p})) \| . \quad (4.11)$$

4.4. Single Molecule Measurements

For the single-molecule and surface layer experiments on psRFP, a sandwich cell was fabricated from two glass coverslips and double-sided sticky tape. The glass coverslips were coated with 1 mg/ml BSA solution containing biotinylated BSA (bovine serum albumin, Sigma-Aldrich) at a ratio 1:10 that formed a dense layer on the surface and prevented psRFP adsorption to the surface. After 10 min, the sandwich was first washed with water. Then with a 10 $\mu\text{g}/\text{ml}$ streptavidin solution (Sigma-Aldrich) was applied for 10 min, followed by another washing step. Streptavidin binds specifically with high affinity to the biotin labels on BSA. Finally, biotinylated psRFP molecules that bind to the fixed streptavidin on the surface was added in picomolar concentrations. After the sample was washed again to remove the unbound psRFP molecules it was ready to be imaged. In order to immobilize the psRFP molecules, the proteins were labeled with biotin NHS that reacts with free amino groups of the protein. The sample solution was incubated with a 2:1 molar excess of biotin NHS in phosphate buffer for 4 h at room temperature.

4.5. PALM Setup

4.5.1. General Considerations

PALM relies on single molecule detection with a good signal to noise ratio and low background fluorescence to achieve a high localization precision. Therefore, background suppression techniques such as total internal reflection fluorescence (TIRF)¹⁷¹ are employed or the exposure time of a fast CCD camera is matched to the average on-time of the fluorescence emitter to reduce background fluorescence¹⁷². In a TIRF setup, the sample is excited by an exponentially decaying evanescent field which is produced by an excitation light beam traveling in a solid glass coverslip incident at a high angle upon the solid/liquid surface at which cells adhere (Fig. 4.1a). The angle must be large enough for the beam to be totally internally reflected rather than refracted through the interface (Fig. 4.1b), a condition that occurs above the critical angle

$$\theta_c = \arcsin(n_2/n_1), \quad (4.12)$$

where n_1 and n_2 are the refractive indices of the solid (~ 1.5 , glass slide) and the aqueous solution (1.33), respectively. For incidence angles $\theta < \theta_c$, most of the light propagates through the interface but for $\theta > \theta_c$, all of the light reflects back into the solid. Some of the incident energy, however, penetrates through the interface and propagates parallel to the surface in the plane of incidence. The field in the liquid, called the evanescent field, is capable of exciting fluorescent molecules that might be present near the surface. For an infinitely wide beam, the intensity of the evanescent wave decays exponentially with perpendicular distance z from the interface:

$$I(z) = I(0)e^{-z/d}, \quad (4.13)$$

with

$$d = \frac{\lambda_0}{4\pi}(n_2^2 \sin^2\theta - n_1^2)^{-1/2}. \quad (4.14)$$

λ_0 is the wavelength of the incident light in vacuum. The penetration depth d decreases with increasing θ and is usually in the range of 100 nm. A TIRF setup can be realized with different optical arrangements, a prism can be used to direct the light towards the TIR interface¹⁷³ or a high numerical aperture (NA > 1.4) microscope objective itself can be employed for this purpose¹⁷⁴. We decided to build an objective-type TIRF which is better suited for single molecule detection in cells and offers more flexibility than the prism-based version, for example it can be combined with an atomic force microscope (AFM) or a patch-clamp setup. To achieve an incident angle that is higher than the critical angle, the incident beam must be constrained to pass through the periphery of the objective's pupil and must emerge with only a narrow spread of angles. This can be accomplished by setting the parallel incident beam to be focused off-axis at the objective's back focal plane. For internal reflection to occur at the interface with

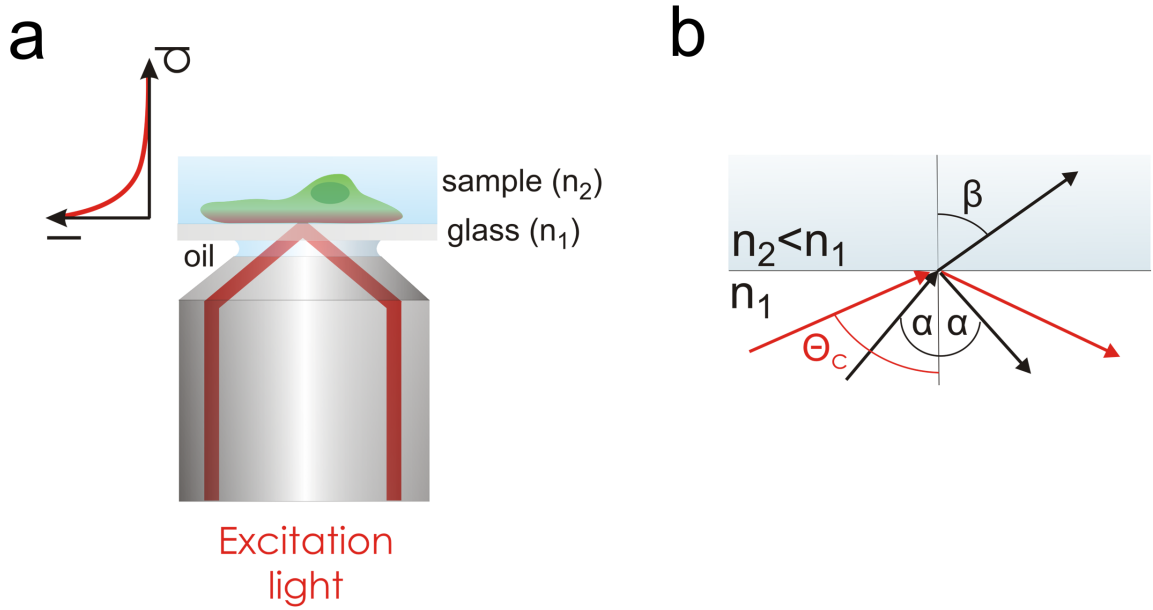


Figure 4.1. TIRF excitation scheme. **(a)** The excitation light is reflected at the glass/water interface and penetrates only about 100 nm into the sample. **(b)** The excitation light above the critical angle (red) is reflected at the glass/water interface. Excitation light with incidence angles below the critical angle (black) can propagate deep into the sample.

an aqueous medium of refractive index of water, $n_2 = 1.33$, the objective numerical aperture (NA) must be greater than n_2

$$n_2 = n_1 \sin \theta_c = NA. \quad (4.15)$$

For viewing the interior of a cell with a variable refractive index $n_2 \sim 1.38$, an objective with NA higher than 1.4 is needed.

4.5.2. Setup

Our objective TIRF setup (Fig. 4.2) is based on a Zeiss Axiovert microscope (Axiovert 200, Zeiss, Jena, Germany). Samples can be illuminated by three diode-pumped solid-state lasers, with emission wavelengths of 561 nm (GCL-150-561, CrystalLaser, Reno, NV), 405 nm (CLASII 405-50, Blue Sky Research, Milpitas, CA) and 473 nm (LSR473-200-T00, Laserlight, Berlin, Germany). The individual beams are combined using mirrors M1 - M4 and dichroic beamsplitters DM1 and DM2. Two reflecting parts per laser are necessary to couple the different laser wavelength effectively into a single fiber. The intensities and illumination schemes are controlled via an acousto-optic tunable filter (AOTF) (AOTFnC-400.650, A-A Opto-Electronic, Orsay Cedex, France). After coupling into the microscope with the optical fiber, the excitation beam is widened by a telescope consisting of the lenses L1 and L2 and focused into the back focal plane of

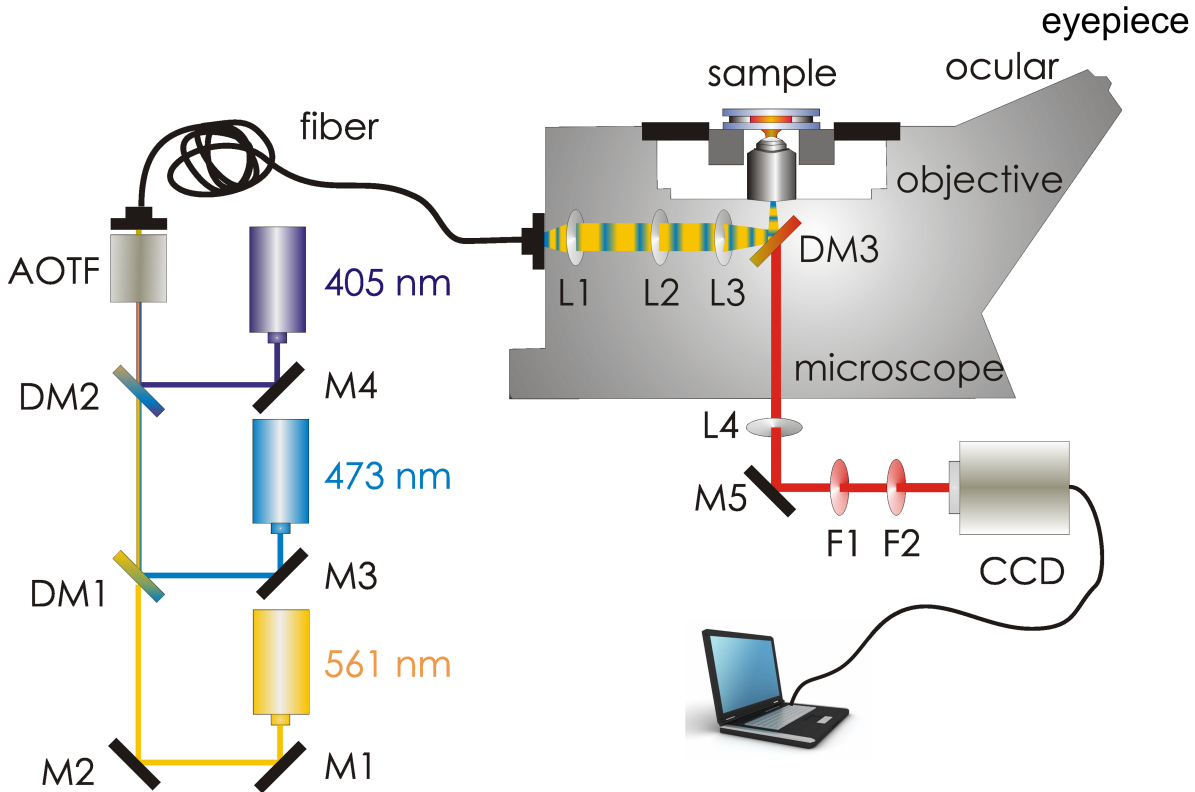


Figure 4.2. PALM setup based on a TIRF microscope.

an oil immersion objective (PlanApo N 60 /1.45, Olympus, Hamburg, Germany) by lens L3. The fluorescence emission is collected by the same objective and separated from the illumination light by a triple line dichroic mirror DM3 (λ 405/473/561, AHF, Tübingen, Germany), filtered with a band pass F1 (Brightline HC 617/73, AHF, Tübingen, Germany) and a second band pass F2 (HQ 610/75, AHF) for fluorescence in the red spectral region and with two filters (Chroma HQ 535/70 and Semrock razor edge LP 488, AHF) for the green spectral region. Two filters are necessary to block the excitation light that is reflected back from the sample due to the objective TIRF excitation scheme. The fluorescence light is detected by a CCD camera (Ixon DV887ECS-BV, Andor, Belfast, Northern Ireland) via the mirror M5 and the magnification is adjusted by lens L4 in the detection path to yield optimal single molecules localization conditions. The optimal sample area per pixel can be calculated as

$$\left(\frac{a}{s}\right)^4 = \frac{96\pi b^2}{N}, \quad (4.16)$$

with the standard deviation s of the PSF, the edge length a of the area imaged per pixel, the background photons b and the signal photons N . The sample area imaged per pixel has to be chosen with care. If the PSF of a single molecule spreads over too many pixels, the detector noise degrades the signal-to-noise ratio and the localization deteriorates. On the other hand, if most of the intensity is detected in one or very

few pixels, only very few values are available for the localization fitting procedure. It turns out that the optimal value is about 130 nm^{109} , so that an area of 5 times 5 pixels accommodates virtually the entire intensity emitted by an individual fluorophore.

4.6. Intensity to Photon Conversion

The detected intensity is given in analog to digital units (ADUs) which need to be converted into the corresponding number of photons N . The conversion is determined by the gain factor $g = ADUs/N$ and can be calculated by applying Poisson statistics. The expectation value and the variance are the same, $\langle N \rangle = \text{var}(N)$ for a Poisson distribution which leads to the relation¹⁷⁵

$$\frac{\text{var(ADUs)}}{\text{ADUs}} = \frac{g^2 \cdot \text{var}(N)}{g \cdot N} = g. \quad (4.17)$$

By plotting the variance of the intensity values, measured for a series of inhomogeneously illuminated images, against the expectation value, the gain factor can be obtained by linear regression. It is then possible to calculate the photon numbers with a known gain factor from the measured intensities in ADUs.

4.7. Stability and Correction

The microscope has to be placed on a vibration isolated table to minimize environmental vibrational influences. We also replaced the microscope stage by a new computer controlled stage that contains threads with smaller clearance. This leads to excellent stability characteristics. Nevertheless, it was necessary to add gold beads (40 nm gold colloid, BBInternational, Cardiff, UK) or fluorescent beads (FluoSpheres (red) 20 nm and TetraSpeck microspheres 100 nm, Invitrogen GmbH, Darmstadt, Germany) to the sample to correct for small stage drifts during data acquisition. The stage drift leads to an undesired broadening of the observed structures, which can be corrected with continuously emitting beads that are added to the sample. The positions of the luminescent particles are calculated for each frame and the offset compared with the starting position is used to shift the image and compensate for the sample drift (Fig. 4.3).

4.8. Data Evaluation

Data acquisition and image processing was performed on a personal computer (Intel Core 2 Quad 3.0 GHz, Arlt, Ulm, Germany) running Windows XP. The images acquired by the CCD camera are continuously streamed to a file on the computer hard disk. The data are saved as image stacks with ~ 100 images per stack. In this way, the first image stacks can already be accessed by the image analysis software while data are being collected. Data acquired from the sample are analyzed by a custom written software. The steps

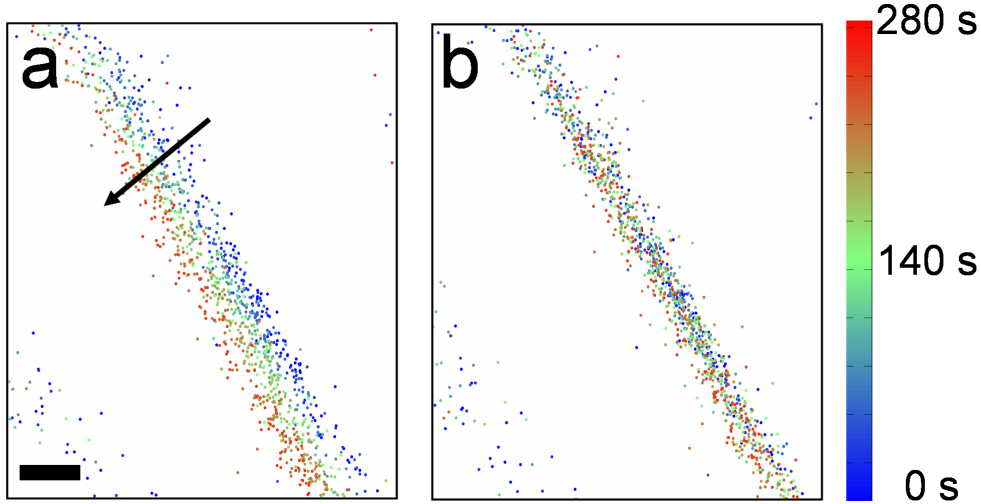


Figure 4.3. Color coded positions of psRFP labeled RITA molecules. (a) Molecule positions without drift correction. The microtubule fiber is broadened by the sample drift. (b) Molecule positions after drift correction. The actual width of the fiber is correctly displayed. Scale bar 200 nm.

of the following PALM image analysis routine are shown in different colors (Fig. 4.4). First, emission patterns from single molecules need to be identified. The raw image is corrected for the camera dark offset and the intensity values are converted from ADUs into photon counts. The criterion for a first identification of a single molecule is the emission intensity value. The single molecule detection was accomplished by creating two subsequent images, one by applying a discoidal averaging filter of a diameter of three pixels, another one by applying an annular averaging filter of a width of one pixel and a diameter of five pixels to the original image. The difference of the two, $I_{\text{difference}}$, is analyzed for values above a threshold, $I_{\text{source,image}}$, specifying a minimum number of photons, $I_{\text{source,theory}}$, emitted by a single molecule. The relation is given by

$$\frac{I_{\text{source,image}}}{I_{\text{difference,image}}} \geq \frac{I_{\text{source,theory}}}{I_{\text{difference,theory}}}, \quad (4.18)$$

for which the theoretical intensities are calculated based on the known width of the point spread function. This procedure efficiently rejects features not associated with single fluorophores, e.g., multiple fluorophores with overlapping point spread functions or cellular autofluorescence. Starting with the position of the brightest pixel, the intensities within a 5 by 5 pixel fitting window are taken from the original image frame. In this way, 80 % of the intensity is captured and the localization yields good results even with inhomogeneous cellular background due to autofluorescence, organelle transparency and labeling densities. The background correction is performed either by subtracting the median of the current frame or by using a local background, depending on the uniformity of the background. The local background subtraction employs the average of a one-pixel

4. Materials and Methods

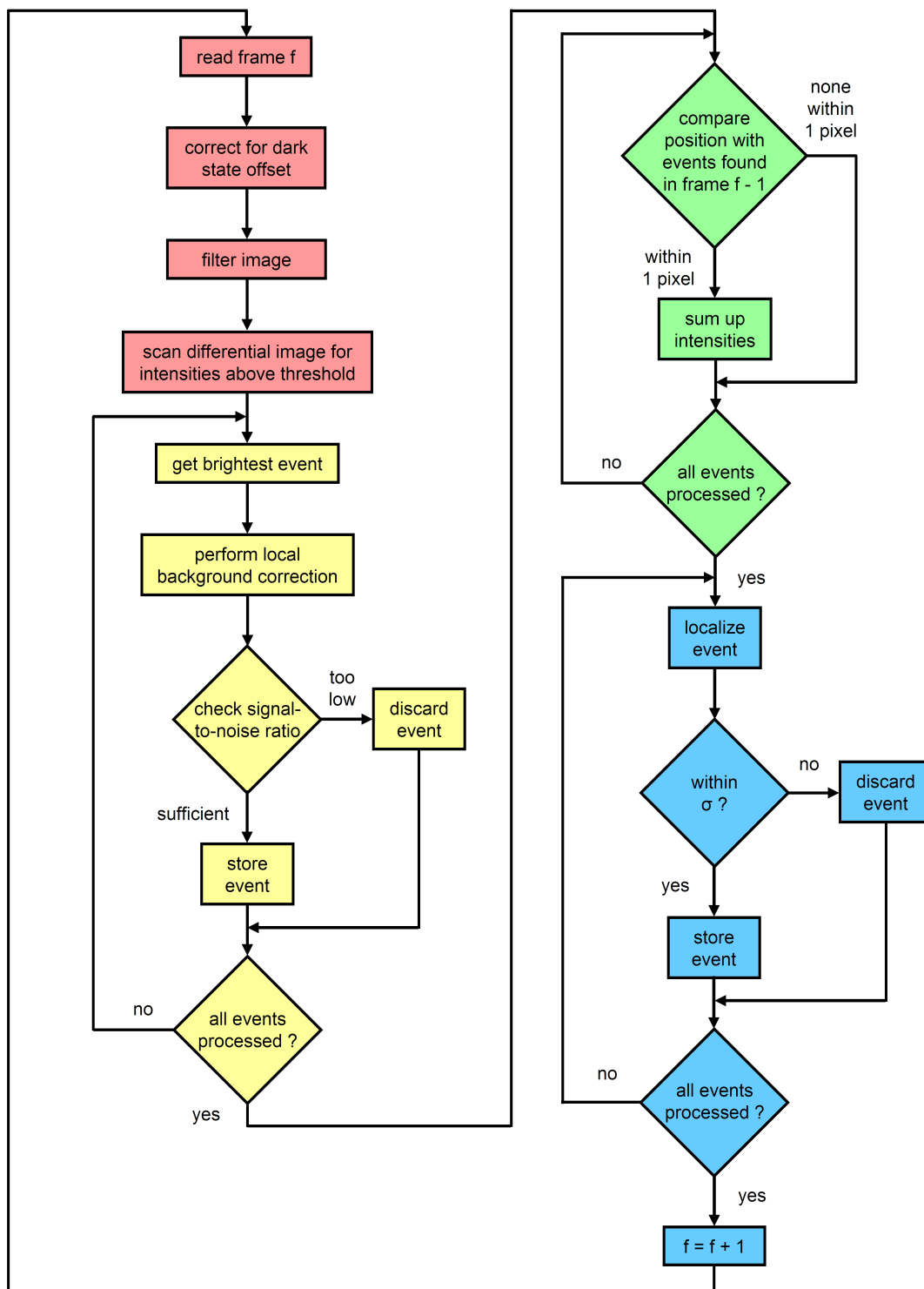


Figure 4.4. Flow chart of the PALM image analysis routine. Identification of single molecules emission patterns (red), background correction (yellow), combination of the intensities originating from the same molecule (green), localization step (blue). Flow chart taken from⁵⁶.

wide frame around the fitting window in the original image. The photon counts after background correction are compared to the shot noise of the peak, i.e., the square root of the overall background intensity inside the fitting window. If the photon counts of the signal are significantly higher than the shot noise (typically > 5 -fold), the event is stored. After all events above the threshold have been processed, the positions of the fit windows within the image are compared to those of the preceding frame. Intensity peaks appearing at the same position ± 1 pixel are taken to arise from the same molecule and are subsequently added up. For all other events of the preceding frame, single fluorophores are localized by applying either the fluoroBancroft algorithm⁵⁶ or a least squares fit. If the distance between the location computed and the center of the window is less than the standard deviation of the point spread function, the event is registered, otherwise discarded. The algorithm then continues with the next frame.

4.9. Localization Algorithm

The signal emitted from a point source will be detected as a diffraction broadened PSF that can be described by an Airy function. The measured PSF is deteriorated by background, photon and pixelation noise and can be well approximated by a Gaussian function. It turned out that the direct least-squares Gaussian fit to the intensity distribution is the most favorable algorithm in terms of precision and accuracy. It is also most robust at a low signal-to-noise ratio¹⁰⁸. Therefore, we used this fitting algorithm throughout this work unless stated otherwise. Although the direct Gaussian fit seems to be the superior, it has one drawback, the fitting routine is not very fast. A less time consuming alternative is the fluoroBancroft algorithm¹⁷⁶.

4.9.1. FluoroBancroft

The fluoroBancroft algorithm¹⁷⁶ is derived from Bancroft's algorithm that is known as a solution to the position estimation problem in the Global Positioning System (GPS)¹⁷⁷. The algorithm uses the fact that the measured intensity at a certain point of the PSF is related to the distance from the source particle (Fig. 4.5). For a known form of the PSF the fluorescence intensity measurement can be converted to the distance between the fluorescent particle and the position at which the measurement was taken. For a CCD camera the position is given by the center of the pixel in which the intensity is measured. The determination of the distance to the source leads to a circle of possible locations. The size of the area imaged on a single pixel was chosen in such a way that the PSF spreads over a number of pixels. The distance obtained from the evaluation of the intensity of a second pixel yields a second circle. The position of the source is now restricted to two points at the intersection of the two circles. With a third distance, the position is precisely given by the intersection of the three circles. If the measured data include noise, the position is no longer determined by the intersection of the three circles but by an intersection area which approximates the exact position. The approximation can be improved by including more intensity measurements. An analytical solution to

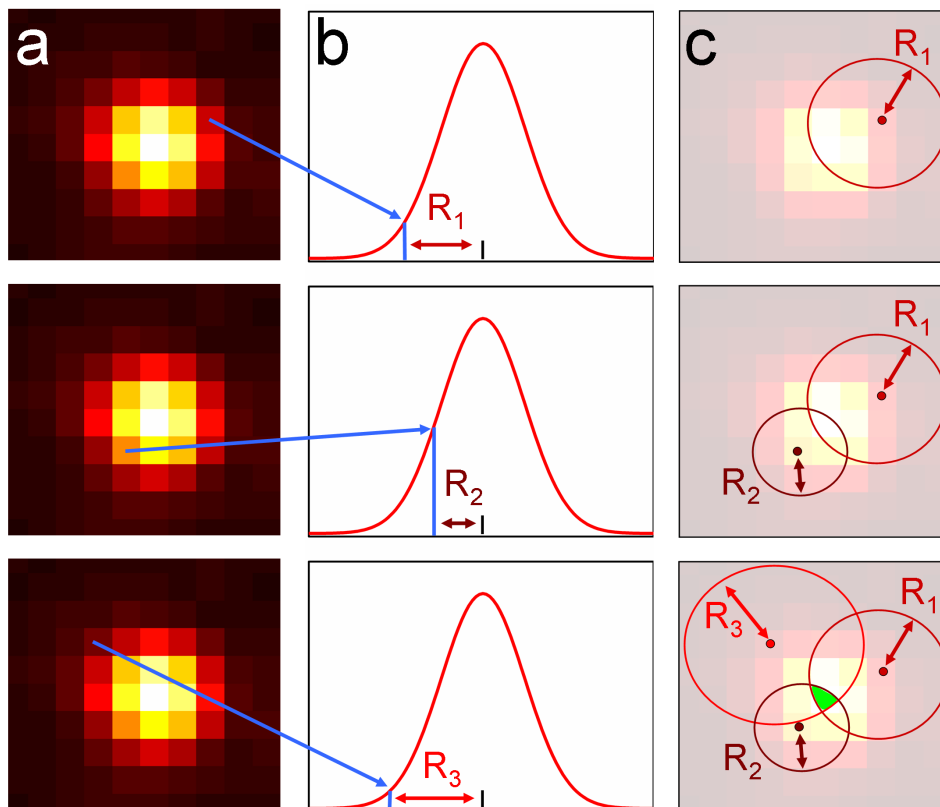


Figure 4.5. Column (a) Diffraction broadened intensity distribution of a single fluorophore detected on the CCD camera. Column (b) The fluorescence intensity measurement can be converted to the distance between the fluorophore, at the center of the Gaussian intensity distribution (red), and the position at which the measurement was taken. Column (c) A circle with radius R , calculated from the Gaussian distribution, can be drawn around the detection position. This procedure is repeated for all measured intensity values, shown for two additional measurements (second, third row). The position of the fluorophore is determined by the intersection of at least three circles. The green area represents the uncertainty of the calculated position due to noise.

the linear system of the range estimates can be obtained through the Moore-Penrose generalized inverse. The intensity profile of a fluorescent emitter located at (x_0, y_0) is modeled as a Gaussian profile

$$I(x, y) = m e^{-\frac{(x-x_0)^2}{2\sigma_x^2} - \frac{(y-y_0)^2}{2\sigma_y^2}} + \eta_B + \eta_{shot}. \quad (4.19)$$

m is a scaling factor that is determined by the photon emission intensity of the fluorescent emitter and the integration time of the measurement, background and shot noise are described by η_B and η_{shot} , respectively, the width of the two dimensional Gaussian profile is given by σ_x and σ_y that are determined by setting the e^{-1} point of the intensity model

to be equal to the Rayleigh radius:

$$\sigma_x = \sigma_y = \frac{0.6\lambda}{\sqrt{2}NA}. \quad (4.20)$$

where NA is the numerical aperture of the objective and λ the wavelength of the emitted light. If the width in x-direction is not equal to the width in y-direction, then the y-coordinate is scaled by defining $\tilde{y} = (\sigma_y/\sigma_x)$

$$I(x, y) = m e^{-\frac{(x-x_0)^2}{2\sigma_x^2} - \frac{(\tilde{y}-\tilde{y}_0)^2}{2\sigma_x^2}} + \eta_B + \eta_{shot} \quad (4.21)$$

$$= m e^{-\frac{r^2}{2\sigma_x^2}} + \eta_B + \eta_{shot}, \quad (4.22)$$

with distance r between the detection position (x, y) and the position of the molecule

$$r = \sqrt{(x - x_0)^2 + (\tilde{y} - \tilde{y}_0)^2}. \quad (4.23)$$

The range to the source particle can be obtained by rearranging (4.22)

$$r^2 = 2\sigma_x^2 \ln(m) - 2\sigma_x^2 \ln(\langle I \rangle - N_B). \quad (4.24)$$

For a collection of measurements from the positions (x_i, y_i) , which we denote with I_i , we define

$$b = 2\sigma_x^2 \ln(m), \quad (4.25)$$

$$P_i^2 = 2\sigma_x^2 \ln(I_i - N_B), \quad (4.26)$$

$$\alpha_i = \frac{1}{2}(x_i^2 + \tilde{y}_i^2) + P_i^2, \quad (4.27)$$

$$\Lambda = \frac{1}{2}(x_0^2 + \tilde{y}_0^2). \quad (4.28)$$

Then (4.24) can be written as

$$0 = \alpha_i + \Lambda - \begin{pmatrix} x_i & \tilde{y}_i & 1 \end{pmatrix} \begin{pmatrix} x_0 \\ \tilde{y}_0 \\ b \end{pmatrix}. \quad (4.29)$$

Stacking together N such measurements and rearranging yields

$$B \begin{pmatrix} x_0 \\ \tilde{y}_0 \\ b \end{pmatrix} = \alpha + \Lambda e, \quad (4.30)$$

with

$$\alpha = \begin{pmatrix} \alpha_1 \\ \vdots \\ \alpha_n \end{pmatrix}, e = \begin{pmatrix} 1 \\ \vdots \\ 1 \end{pmatrix}, B = \begin{pmatrix} x_1 & \tilde{y}_1 & 1 \\ \vdots & \vdots & \vdots \\ x_n & \tilde{y}_n & 1 \end{pmatrix}. \quad (4.31)$$

4. Materials and Methods

The linear system is overdetermined and, therefore, does not have an exact solution, in general. But an approximation of the solution that minimizes the Euclidean norm of the residual error,

$$\delta = B \begin{pmatrix} x_0 \\ \tilde{y}_0 \\ b \end{pmatrix} - (\alpha + \Lambda e), \quad (4.32)$$

is given by the Moore-Penrose pseudo-inverse of B ,

$$\begin{pmatrix} x_0 \\ \tilde{y}_0 \\ b \end{pmatrix} = B^\dagger (\alpha + \Lambda e), \quad (4.33)$$

with $B^\dagger = (B^T B)^{-1} B^T$ and the following proposition,

$$B^\dagger e = \begin{pmatrix} 0 \\ \vdots \\ 0 \\ 1 \end{pmatrix}, \quad (4.34)$$

the position of the fluorescent particle can be solved by defining the matrix Q ,

$$Q = \begin{pmatrix} 1 & 0 & 0 \\ 0 & \frac{\sigma_x}{\sigma_y} & 0 \end{pmatrix}. \quad (4.35)$$

Equation (4.33) is pre-multiplied by Q , which yields, together with the proposition the fluoroBancroft solution:

$$\begin{pmatrix} x_0 \\ y_0 \end{pmatrix} = Q B^\dagger \alpha. \quad (4.36)$$

For practical calculations, the vector α and the matrix B are built. Then the Moore-Penrose inverse B^\dagger is determined and the matrix multiplication (4.36) is performed.

4.10. Localization Statistics

The position of the fluorescent molecule is obtained from a direct Gaussian fit to the acquired data. The fit also provides information about the number of signal photons per molecule and the width of the PSF. From the background correction, the number of background photons and readout noise can be estimated. This information allows the calculation of the localization error and helps in judging the image quality.

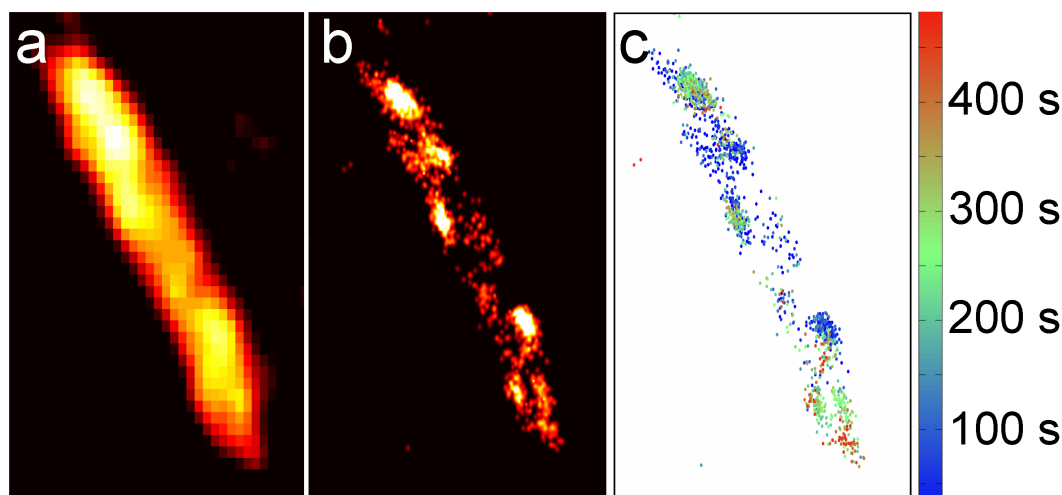


Figure 4.6. Different representations of the acquired data. (a) Sum of the acquired frames yield the TIRF image. (b) The PALM image is constructed from single molecule positions convoluted with a Gaussian distribution to account for localization accuracy. (c) The calculated single molecule positions are given in a color code corresponding to the detection time of the individual signals.

4.10.1. Presentation

The data acquired during PALM imaging can be presented and evaluated in different ways (Fig. 4.6). Simply adding up all frames yield the TIRF image. The corresponding PALM image can be constructed based on the parameters determined during localization. A Gaussian intensity distribution, scaled with the number of detected photons and the position error σ is plotted for each detected molecule around the obtained center coordinates. The molecules given in a rendered PALM image can be selected by their localization precision, number of detected signal photons, detected background photons per molecule and variance of the detected PSF. These parameters help to sort out undesired signals or provide images with a certain localization accuracy. The software also permits plotting of the positions obtained from the data fit with a color code corresponding to the time of detection. This representation allows the visualization of organelle and structural changes over time on the nanometer scale.

4.11. Cell Preparation

All PALM experiments were performed on HeLa cells. This cell line was derived from cervical cancer cells taken from Henrietta Lacks and is one of the oldest and most commonly used human cancer cell lines. HeLa cells have been used for cancer and AIDS research, the effects of radiation and toxic substances, gene mapping and many other experiments. More than 60,000 scientific articles have been published about research involving HeLa cells.

4.11.1. Cellular Transfection

HeLa cells (American Type Culture Collection) were grown at 37 °C under 5% CO₂ in Dulbecco's Modified Eagle Medium (DMEM, Gibco; Invitrogen) supplemented with 10% fetal calf serum. For imaging, cells were cultured on fibronectin covered coverslips (Nunc) at a density of 10⁵ cells cm⁻². After 16 h, cells were transfected with 500 ng of expression plasmids using the Nanofectin transfection reagent (PAA Laboratories GmbH, Cölbe, Germany). The medium was replaced after 48 h by colorless DMEM to minimize fluorescent background for imaging and fluorescent beads were added for drift correction. Subsequently, cells were imaged for live cell experiments or fixed with 4 vol. % paraformaldehyde followed by 15 min incubation in 50 nM ammonium chloride. Finally, samples were washed with PBS buffer and covered with fixation medium Pro-Long Gold antifade reagent p36930 (Invitrogen GmbH, Darmstadt, Germany) before the samples had to harden for 24 h. All cell preparations were done in the group of Franz Oswald (Department of Internal Medicine I, University Medical Center Ulm)

4.12. PALM Data Acquisition Conditions

PALM images were taken at 25–28°C and under ambient conditions, unless stated otherwise, on the PALM setup including lasers and filters described earlier.

5. The Photoswitchable Red Fluorescent Protein (psRFP)

The fluorescent protein psRFP is an interesting marker for high resolution microscopy due to the favorable red emission and the possibility to reversibly switch the protein between a fluorescent on-state and a nonfluorescent off-state (Fig. 5.1). For better understanding of the photophysical processes we performed spectroscopic studies and tried to link the photophysical processes to structural changes within the protein matrix. Illumination with yellow and blue light can trigger a number of different events in psRFP such as photoisomerization, photobleaching and changes in the chromophore protonation states. Protein structures of psRFP obtained by X-ray diffraction have shown that the

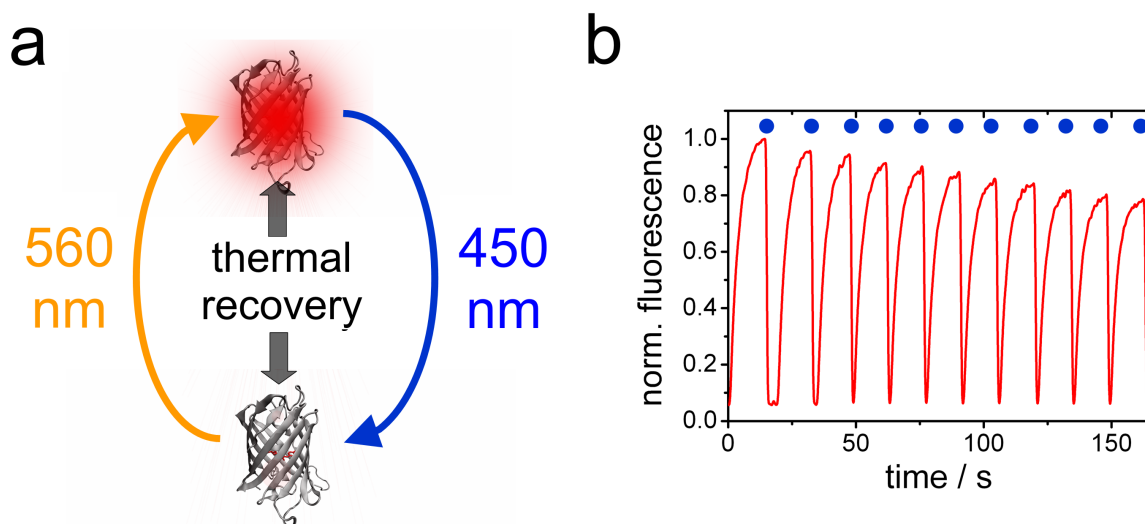


Figure 5.1. (a) Switching modes in psRFP. Off-switching is accomplished by irradiation with blue light (450 nm) and on-switching occurs during illumination with yellow light (560 nm); alternatively, the protein returns thermally activated to its initial state ground state equilibrium. (b) Fluorescence signal from a purified psRFP solution, which was repeatedly switched off and subsequently returned thermally to the fluorescent state.

chromophore of the protein can adopt either the cis or the trans conformation (Fig. 5.2). In each conformation, the hydroxyphenyl ring of the chromophore can be neutral (protonated) or anionic (deprotonated), which leads to spectrally different bands in the absorption spectrum, generally referred to as A and B band, respectively. Thus, altogether four contributions, cis neutral (CH), cis anionic (C⁻), trans neutral (TH) and

5. The Photoswitchable Red Fluorescent Protein (psRFP)

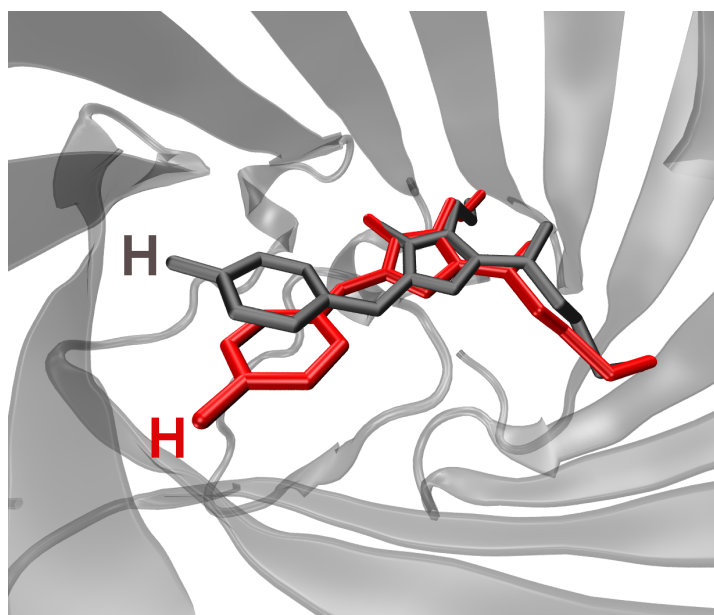


Figure 5.2. The chromophore in psRFP can adopt either the cis (red) or the trans (gray) conformation. In each conformation, the hydroxyphenyl ring of the chromophore can be neutral (protonated, H) or anionic (deprotonated) which leads to four different absorption spectra.

trans anionic (T^-), are expected to contribute to the absorption spectrum at pH 7, but only two main bands are apparent in the spectrum at ~ 450 nm and ~ 562 nm (Fig. 5.3). The 450-nm band (A band) decreases with increasing pH and can, therefore, be assigned to the neutral chromophores. As the pH dependent studies in the following section will show, the contributions of the neutral cis (CH) and the neutral trans (TH) chromophore conformations to the absorption spectrum cannot be determined from a single spectrum due to an almost perfect overlap of their absorption spectra. The band peaking at 562 nm (B band) represents a mixture of the anionic cis (C^-) and the anionic trans (T^-) chromophores. A single excitation band with maximum at 583 nm ($\lambda_{em} = 630$ nm) was detected at pH 7. The unexpected shift between the absorption and excitation band implies already that the anionic species, contributing mostly to the B band at 562 nm, is not the fluorescent species at pH 7. If the 562-nm band is excited at 550 nm, fluorescence emission with maximum intensity at 603 nm was recorded. The lack of a 450-nm band in the excitation spectrum suggests that the neutral chromophores present at pH 7 are non-fluorescent. Indeed, no fluorescence from the neutral chromophores was detected under 450-nm excitation.

5.1. pH dependent Spectral Properties

Fluorescence emission and photoswitching depend on the chromophore conformation and the protonation state. To obtain insight into the ground state protonation equilibria of

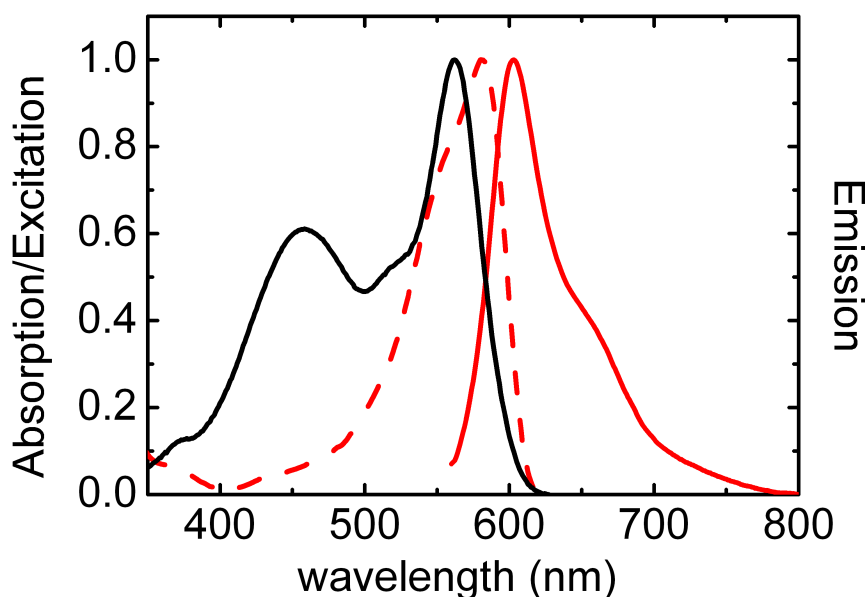


Figure 5.3. Absorption (black), excitation (dashed, red line) and emission (solid red line) spectra of psRFP at pH 7. All spectra are scaled to unity for better comparison.

the cis and trans chromophores, $C^- + H^+ = CH$ and $T^- + H^+ = TH$, and to identify the fluorescent species, we have measured the absorption, excitation and emission spectra as a function of pH. Simple inspection of the absorption spectra (Fig. 5.4a) revealed a two-step increase of the signal at ~ 562 nm at the expense of the 450-nm band. The first step is complete at \sim pH 6 and the second exchange occurs above pH 7. For a more accurate analysis of the protonation equilibria, we have decomposed the absorption spectra in the range pH 4.2 to pH 10, using the absorption spectra of the neutral (~ 450 nm) and the anionic (~ 562 nm and 583 nm) chromophore species given in figure 5.4b as basis spectra. The band shapes of the 450-nm and the 562-nm bands were obtained from SVD analysis (Fig. 5.5) and the 583 nm band was modeled to match the excitation spectrum. In figure 5.4c, we plot the normalized concentration of the different species as a function of pH. The concentrations were calculated for the separated absorption spectra of the different conformations. Due to the almost identical band shape, the fit cannot distinguish between the A bands of the cis and trans chromophores. Therefore we show the combined concentration of both, the cis and the trans form, in figure 5.4c. The first drop in the population of the species represented by the A band and the concomitant increase of the absorption band at ~ 562 nm can be modeled according to the Henderson-Hasselbalch relation with $pK_a = 4.7 \pm 0.1$. We assigned the change in both bands to the deprotonation of the nonfluorescent trans chromophore. Switching experiments presented later did confirm our assignment (Fig. 5.13, 5.25). The nearby Glu145, which forms a water mediated hydrogen bond with the trans chromophore, can act as a proton

5. The Photoswitchable Red Fluorescent Protein (psRFP)

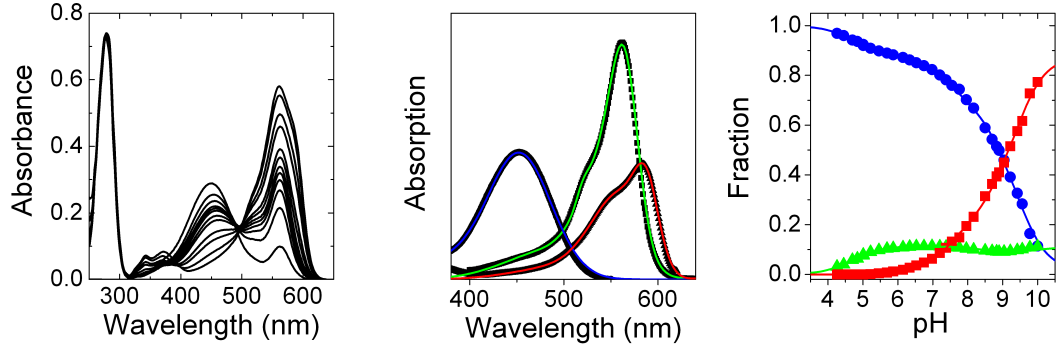


Figure 5.4. pH dependence of the absorption spectra of psRFP in the pH range 4.2–10. **(a)** Selected spectra. **(b)** Basis spectra of the identical cis and trans neutral forms (~ 450 nm, blue), the anionic trans form (~ 562 nm, green) and the anionic cis form (~ 583 nm, red). The Spectra obtained from experimental data by SVD analysis (~ 450 nm and ~ 562 nm) and the excitation spectrum (~ 583 nm) are plotted as black symbols. **(c)** Normalized concentrations over the measured pH range for species represented by the basic spectra. A Henderson-Hasselbalch relation describes the low pH increase ($pK_a = 4.7$) and a two-site protonation model fits the pH changes in the pH range above pH 7. The experimental data for the neutral bands (blue dots), the anionic trans absorption (green triangles) and the anionic cis band (red squares) are shown together with the theoretical fits (same colors).

acceptor (Fig. 5.6). There was no proton acceptor found in close proximity to the cis chromophore, which supports our assignment of the first deprotonation step to the trans chromophore and the deprotonation at higher pH to the cis chromophore. The second exchange between the decaying 450-nm band and the increasing 583-nm band cannot be modeled by a single protonation reaction, suggesting that the deprotonation of the cis chromophore is coupled to the deprotonation of a neighboring amino acid. A two-site protonation model¹⁷⁸ (Fig. 5.7) describes the pH dependence of the neutral (CH) and anionic cis (C^-) chromophore population together with the population of the protonated (XH) and deprotonated (X^-) amino acid in the chromophore environment,

$$f_{CHXH}(pH) = 1/(1 + 10^{x_1} + 10^{x_3} + 10^{x_1+x_2}), \quad (5.1)$$

$$f_{C^-XH}(pH) = 10^{x_1}/(1 + 10^{x_1} + 10^{x_3} + 10^{x_1+x_2}), \quad (5.2)$$

$$f_{CHX^-}(pH) = 10^{x_3}/(1 + 10^{x_1} + 10^{x_3} + 10^{x_1+x_2}), \quad (5.3)$$

$$f_{C^-X^-}(pH) = 10^{x_1+x_2}/(1 + 10^{x_1} + 10^{x_3} + 10^{x_1+x_2}), \quad (5.4)$$

with $x_i = pH - pK_{ai}$. The entire neutral and anionic cis populations are given by,

$$f_{CH}(pH) = f_{CHXH}(pH) + f_{CHX^-}(pH), \quad (5.5)$$

$$f_{C^-}(pH) = f_{C^-XH}(pH) + f_{C^-X^-}(pH), \quad (5.6)$$

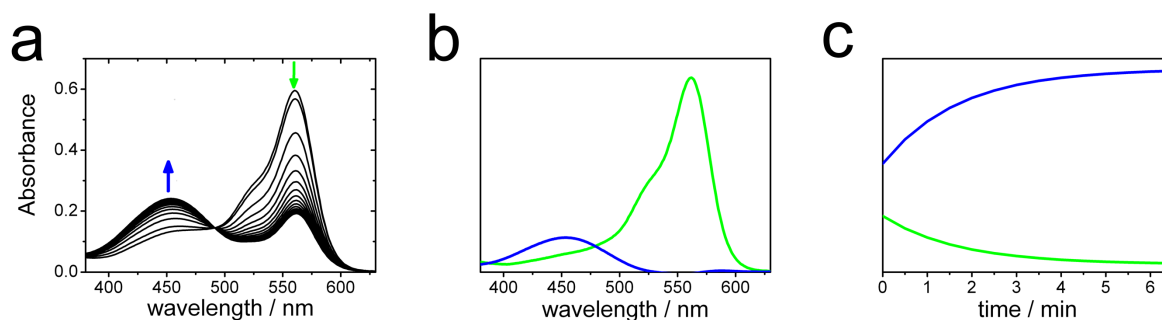


Figure 5.5. (a) Absorption spectra of the thermal recovery after illumination with 473-nm light. (b) Basic spectra of the neutral (blue) and anionic (green) chromophore calculated from the SVD analysis. (c) Time course of the thermal recovery obtained from the SVD analysis.

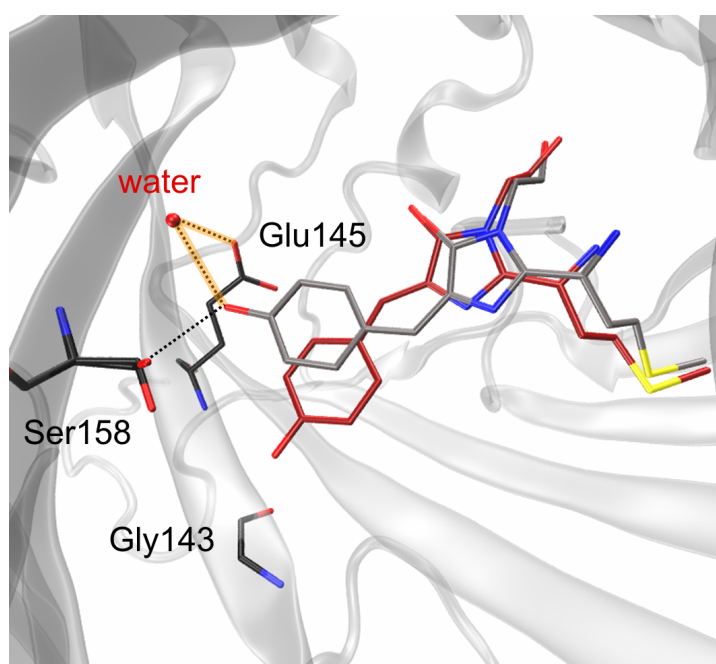


Figure 5.6. The chromophore environment in psRFP. The Glu145 forms a hydrogen bond with the trans chromophore via a water molecule and can act as proton acceptor for the proton released from the trans chromophore. On the other side, there is no proton acceptor in close proximity to the cis chromophore.

respectively. It should be also noted that $pK_{a1} + pK_{a2} = pK_{a3} + pK_{a4}$. A fit of the data with this model model yielded $pK_{a1} = 7.9 \pm 0.1$, $pK_{a2} = 8.4 \pm 0.1$, $pK_{a3} = 7.5 \pm 0.1$, $pK_{a4} = 8.8 \pm 0.1$. The deprotonation of the cis chromophore next to a protonated and deprotonated amino acid is described by pK_{a1} and pK_{a4} , respectively, and the deprotonation of the amino acid next to an anionic and a neutral chromophore is characterized by pK_{a2} and pK_{a3} , respectively. The deprotonation of the nearby amino acid induces a change in the electrostatic environment of the chromophore, which causes peak shifts of

5. The Photoswitchable Red Fluorescent Protein (psRFP)

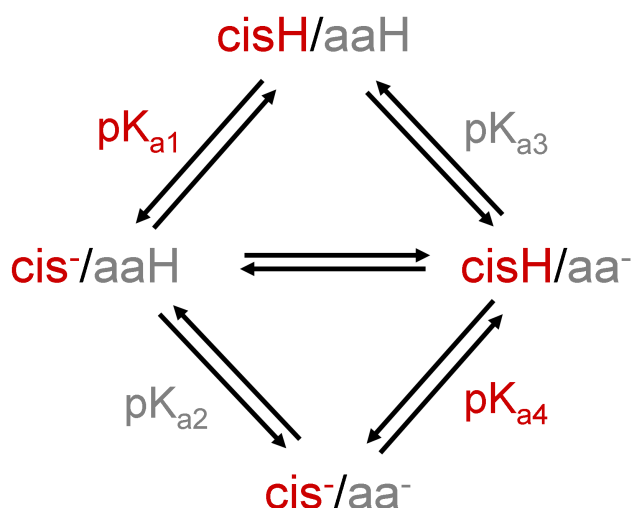


Figure 5.7. Two-site protonation model describing the pH dependence of the cis chromophore (cis) deprotonation with simultaneous deprotonation of a neighboring amino acid (aa). The deprotonation of the cis chromophore next to a protonated and deprotonated amino acid is described by pK_{a1} and pK_{a4} , respectively, and the deprotonation of the amino acid next to an anionic and a neutral chromophore, which can be seen as a peak shift in the absorption spectra, is characterized by pK_{a2} and pK_{a3} . It should be also noted that $pK_{a1} + pK_{a2} = pK_{a3} + pK_{a4}$.

the A and B bands in the absorption spectrum. The measured peak shifts (Fig. 5.8) of the anionic chromophore, which could be fitted with $pK_a = 8.3 \pm 0.1$, and the neutral chromophore, with a $pK_a = 7.5 \pm 0.1$, coincide with the values obtained from the two-site protonation model, which confirms the applied model. The excitation and emission bands (Fig. 5.9) display only a minor shift with increasing pH. However, both show an simultaneous increase in band area, in parallel with the absorption band of the anionic cis chromophore with $pK \sim 8$. Concomitantly, we note an increase in the emission intensity (recorded for 550 nm excitation)(Fig. 5.10), confirming that the anionic species with the more red-shifted band is the fluorescent form. In analogy to other photoswitchable FPs, we propose that the fluorescent chromophore adopts the planar anionic cis form. Overall, $\sim 90\%$ of the molecules are in the cis conformation and $\sim 10\%$ in the trans conformation, independent of pH. At pH 7, only $\sim 6\%$ of all molecules have an anionic cis chromophore and are thus fluorescent. This fraction increases to $\sim 50\%$ at pH 9. It is interesting to see that in the almost identical protein KFP1 the chromophore exclusively adopts the trans conformation^{179, 180}. We tried to identify the amino acids that selectively stabilize the cis conformation of the chromophore in psRFP. Surprisingly, no difference between the two molecules was found in the direct chromophore environment. Hence, we examined amino acids that could influence the direct protein environment and we found Met13

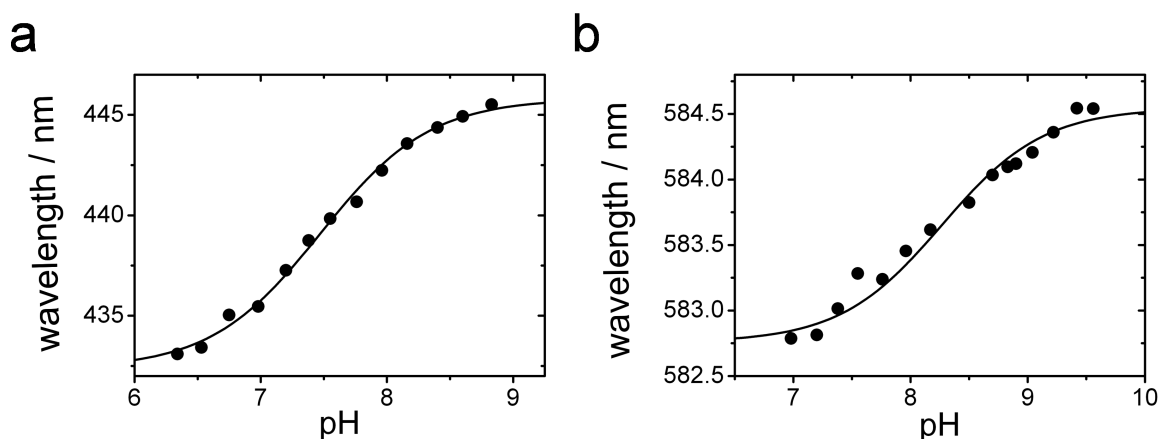


Figure 5.8. (a) Peak position of the neutral cis band after subtraction of the absorption spectrum at pH 6 (black dots). The fit to the data with a Henderson-Hasselbalch model yields a $pK_a = 7.5$. (b) Peak position of the anionic cis band after subtraction of the absorption spectrum at pH 6 (black dots). The fit of a Henderson-Hasselbalch model to the data yields a $pK_a = 8.3$.

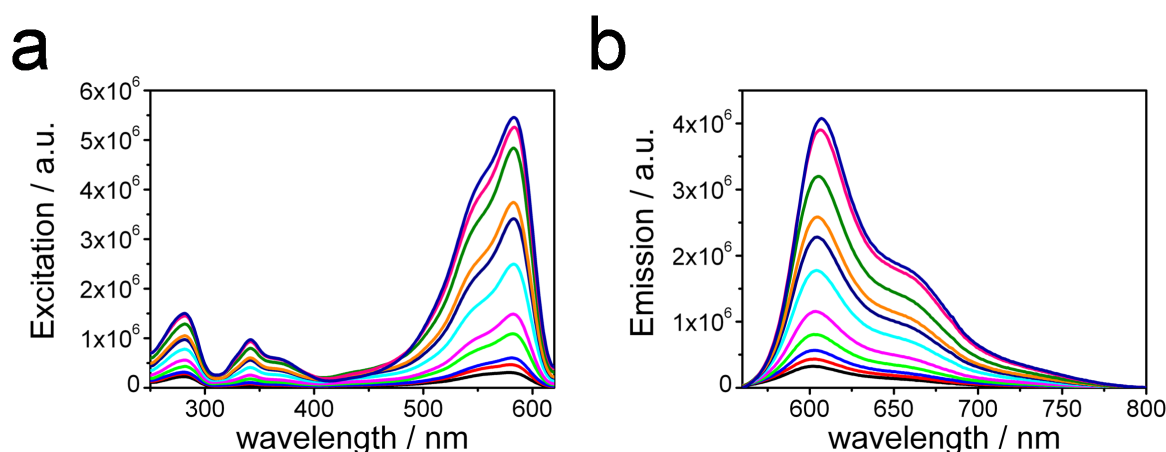


Figure 5.9. (a) The excitation spectra of psRFP increase in amplitude and band area from pH 6.3 (black) to pH 10 (blue). (b) The emission spectra of psRFP from increase in amplitude and band area from pH 6.3 (black) to pH 10 (blue).

(psRFP) / Thr13(KFP1) and Leu147 (psRFP) / Val147 (KFP1). During the evolution of psRFP from the chromoprotein asCP562, Met13 was identified as a key residue responsible for its bright fluorescence. We assume that Met13 pushes Cys62 towards the chromophore and thereby stabilizes the cis conformation in psRFP. The influence of Leu147 that was not recognized during the evolution process was studied in more detail, by mutating the leucine at position 147 to a valine in psRFP. We expected that the mutant psRFP(L147V) showed a higher trans chromophore population than psRFP. To verify our assumption, we measured the absorption spectra of psRFP(L147V) from pH

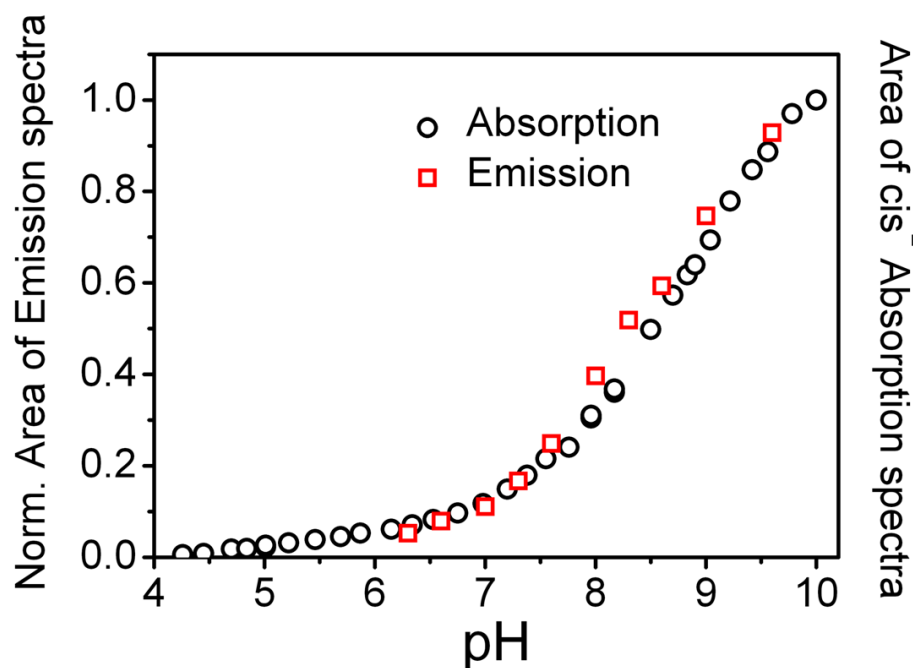


Figure 5.10. The fluorescence emission increases parallel with the absorption band area of the anionic cis chromophore.

4.4 to pH 9.8 and fitted the absorption spectra with basis spectra (Fig. 5.11) obtained in the same way as described before. The 450-nm band that is composed of trans and cis anionic chromophore absorption decays in two steps (Fig. 5.12a), similar to that of psRFP. The trans chromophore deprotonates during the first step with a $pK_a = 4.2 \pm 0.1$ (psRFP $pK_a = 4.7$) and the neutral cis chromophore is depopulated in a second step with $\sim pK 9$. The pK_a value of the trans chromophore is shifted compared to psRFP, and, indeed, the pH series of psRFP(L147V) also revealed that the cis/trans ratio changes from 90 %/10 % in psRFP to 50 %/50 % in psRFP(L147V) (Fig. 5.12c) for the same ratio of cis and trans extinction coefficients within the measurement accuracy. We compared the crystal structures of psRFP and KFP1 to identify the interaction that stabilizes the trans chromophore in psRFP(L147V). The longer sidechain of leucine in psRFP compared to valine in KFP1 and psRFP(L147V) pushes Glu195, which forms a hydrogen bond with His193 in KFP1, towards His197. As a result, His197 hydrogen bonds to Glu195 in psRFP instead of forming a hydrogen bond with Glu145, as seen in the KFP1 structure. Thereby His197 slightly shifts its position. In KFP1, the interaction with His197 pushes the hydroxyphenyl ring of the chromophore out of the plane of the imidazolinone ring and stabilizes the trans conformation. On the other hand, in psRFP, the imidazole ring of the histidine is shifted and stabilizes the cis conformation.

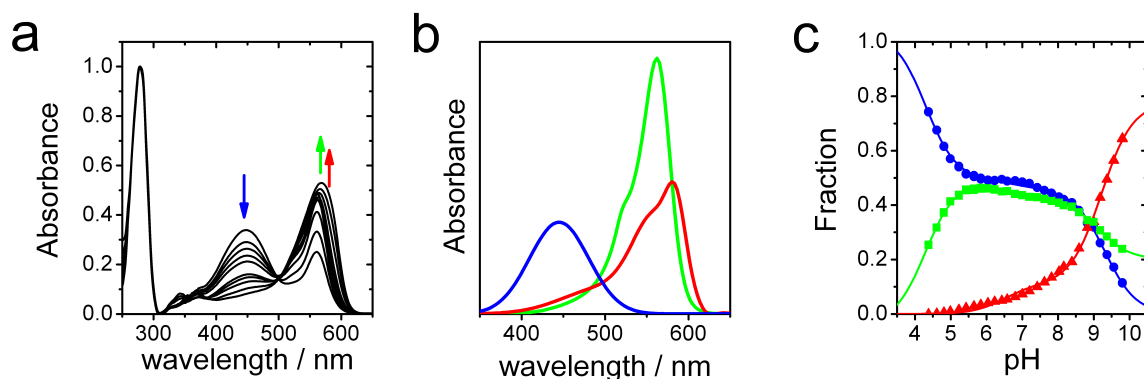


Figure 5.11. pH dependence of the absorption spectra of psRFP(L147V) in the pH range 4.4–9.8. (a) Selected spectra are shown for easier inspection. (b) Basic absorption spectra of the identical cis and trans neutral forms (~450 nm, blue), the anionic trans form (~562 nm, green) and the anionic cis form (~583 nm, red). (c) Change in band areas with pH of the three basic spectra. The experimental data for the neutral bands (blue dots), the anionic trans absorption (green squares) and the anionic cis band (red triangles) are given together with the theoretical fits (same colors).

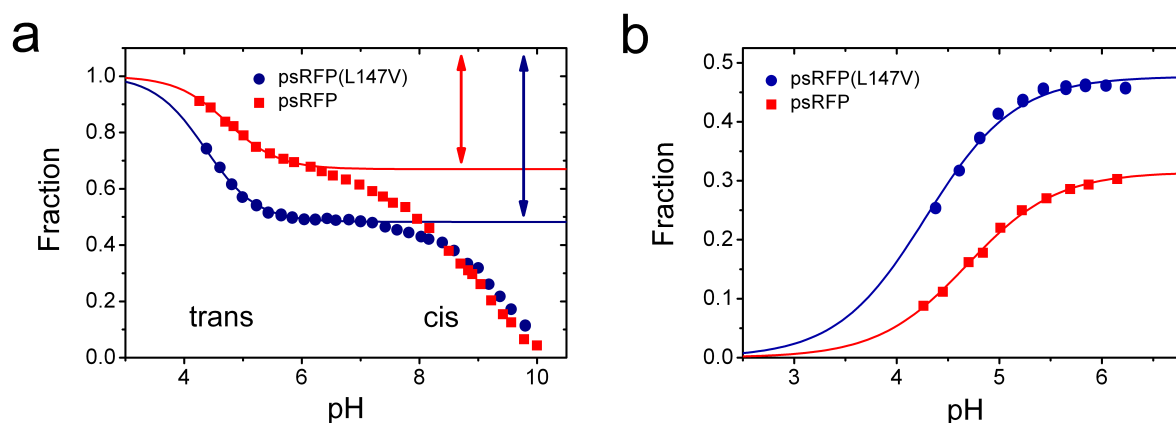


Figure 5.12. Comparison of the deprotonation of psRFP and psRFP(L147V). (a) Change in band area over pH of the neutral trans and cis bands of psRFP (red) and psRFP(L147V) (blue). (b) Simultaneously with the decrease of the neutral trans absorption bands, an increase of the anionic trans absorption bands of psRFP (red) and psRFP(L147V) (blue) was observed.

5.2. Extinction coefficients and Quantum Yield

It is challenging to estimate the molar extinction coefficients of a protein ensemble with diverse chromophore conformations and protonation states. We determined the overall amount of matured psRFP chromophore by alkaline denaturation¹⁸¹ and compared the 450-nm absorption to the absorption of the denatured chromoprotein asCP562. Since asCP562 includes only mature proteins with a functional chromophore, the chromophore

5. The Photoswitchable Red Fluorescent Protein (psRFP)

concentration for the psRFP sample could be deduced. Due to imperfect chromophore formation and impurities in the sample, the protein concentration could be determined with an error of 20 %. With the known concentration of matured chromophores in the psRFP sample, we were able to calculate the extinction coefficients and quantum yield for the different chromophore conformations. By switching the complete chromophore population to the anionic trans form at pH 6.4 under 450-nm illumination, the extinction coefficient of the anionic trans form with an absorption maximum at 562 nm could be calculated as $\epsilon_{562} = 47,000 \pm 12,000 \text{ M}^{-1}\text{cm}^{-1}$. Overall the extinction coefficient could be determined with an error of about 25 %. From the ratio calculated for the loss in the neutral 450-nm band and the increase in the 562-nm band during deprotonation of the trans chromophore ($\text{pK}_a = 4.7$), the extinction coefficient of the neutral trans chromophore could be estimated as $\epsilon_{450} = 19,000 \pm 5,000 \text{ M}^{-1}\text{cm}^{-1}$. The extinction coefficient of the neutral cis form was determined to $\epsilon_{450} = 13,000 \pm 3,000 \text{ M}^{-1}\text{cm}^{-1}$ from the change in population during thermally activated recovery after off switching with 473-nm light. For this experiment, the pH value was adjusted to pH 6.4. At this pH, only anionic trans and neutral cis chromophores are present in the sample and, with the known extinction coefficient of the anionic trans chromophore, the extinction coefficient of the neutral cis band at 450 nm can be estimated. Finally, the extinction coefficient of the anionic cis conformation, the fluorescent form, was deduced from the pH transition of the cis chromophore ($\text{pK}_a \sim 8$) to $\epsilon_{583} = 27,000 \pm 6,000 \text{ M}^{-1}\text{cm}^{-1}$. With the known extinction coefficient, the quantum yield of the fluorescent form could be determined to 0.61 ± 0.2 by comparison to cresyl violet¹⁶⁸. The error resulted mainly from determination of the absorbance of the anionic cis conformation. This value cannot be directly measured, but it is obtained from a fit of the basis absorption spectra of the different chromophore conformations to the measured absorption spectrum. A variation of the fit parameters such as peak positions and width allowed the estimation of a maximum error.

Chromophore conformation	Extinction coefficient ($\text{M}^{-1}\text{cm}^{-1}$)	Fluorescence Quantum Yield
neutral trans	19,000	-
neutral cis	13,000	-
anionic trans	47,000	-
anionic cis	27,000	0.61

Table 5.1. Extinction coefficients and quantum yield for the different chromophore conformations of psRFP. The extinction coefficients were determined with an error of about 25 % and the quantum yield with an error of about 30 %.

5.3. Photoswitching

psRFP can be switched either from a fluorescent state to a non-fluorescent state (off-switching) or from a non-fluorescent to a fluorescent state (on-switching), depending on

the irradiation wavelength.

5.3.1. Off-switching

Illumination with light around 450 nm leads to a reduction of fluorescence emission. This effect can only be observed for a sufficiently high population of the fluorescent anionic cis chromophore ($>pH6$). However, light-induced changes in the relative fractions of the various chromophore species can be seen in the absorption spectra at any pH. After 3

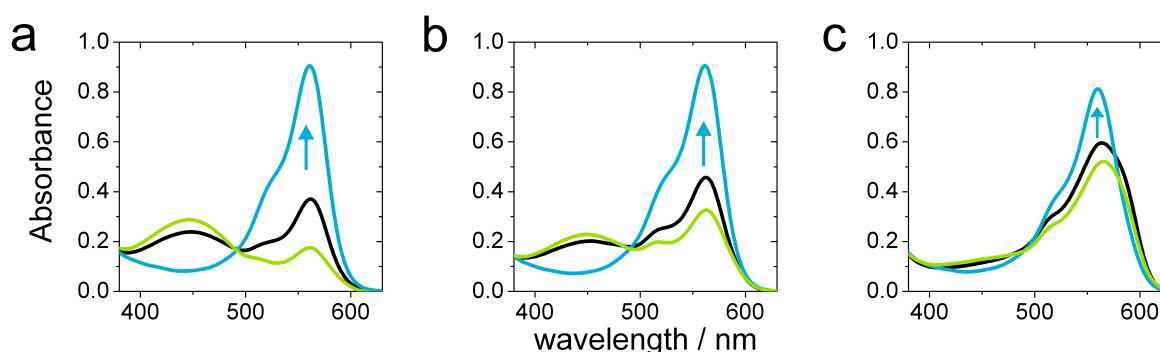


Figure 5.13. Absorption spectra at pH 4.8 (a), pH 7 (b) and pH 9.5 (c) before illumination (black line) are shown together with the absorption spectra after 3 min 473-nm irradiation (cyan) for off-switching and absorption spectra after 20 min 561-nm illumination (green) for on-switching.

min of 473-nm irradiation (0.5 W cm^{-2}), the absorption band of the neutral cis chromophore (450-nm band) disappeared completely at pH 7 and, concomitantly, the anionic trans absorption (562 nm band) increased (Fig. 5.13b). Excitation of the neutral cis chromophore (CH) caused photoisomerization and deprotonation of the chromophore, which yields the anionic trans form (T^-). At pH 4.8, both the neutral cis (CH) and trans (TH) conformations are populated (450 nm band) and can be excited. The neutral cis chromophores (C^-) undergo the same isomerization/deprotonation process as for pH 7 to yield the anionic trans form (T^-). As a result of the pH-dependent ground state equilibrium of TH and T^- , one would still expect to observe a fraction of neutral trans chromophores after illumination. However, the absorption band at 450 nm has completely disappeared (Fig. 5.13a). Therefore, we suggest that excitation of the neutral trans chromophore with 473-nm light causes deprotonation of the hydroxyphenyl oxygen, most likely in the excited state, which is coupled to a still unknown process rendering the reprotonation in the ground state very slow. At pH 9.5, the T^- band gains at the expense of the absorption bands of both CH and C^- under 473-nm excitation. The loss of CH leads to a readjustment of the ground state equilibrium and hence to a concomitant depletion of C^- . Compared to the spectra at pH 4.8 and 7 after illumination, the cis chromophores did not completely disappear, which is due to the compensation of the light induced off-switching by increased thermal recovery from the trans to the cis ground state at pH 9.5. The changes induced by illumination with blue

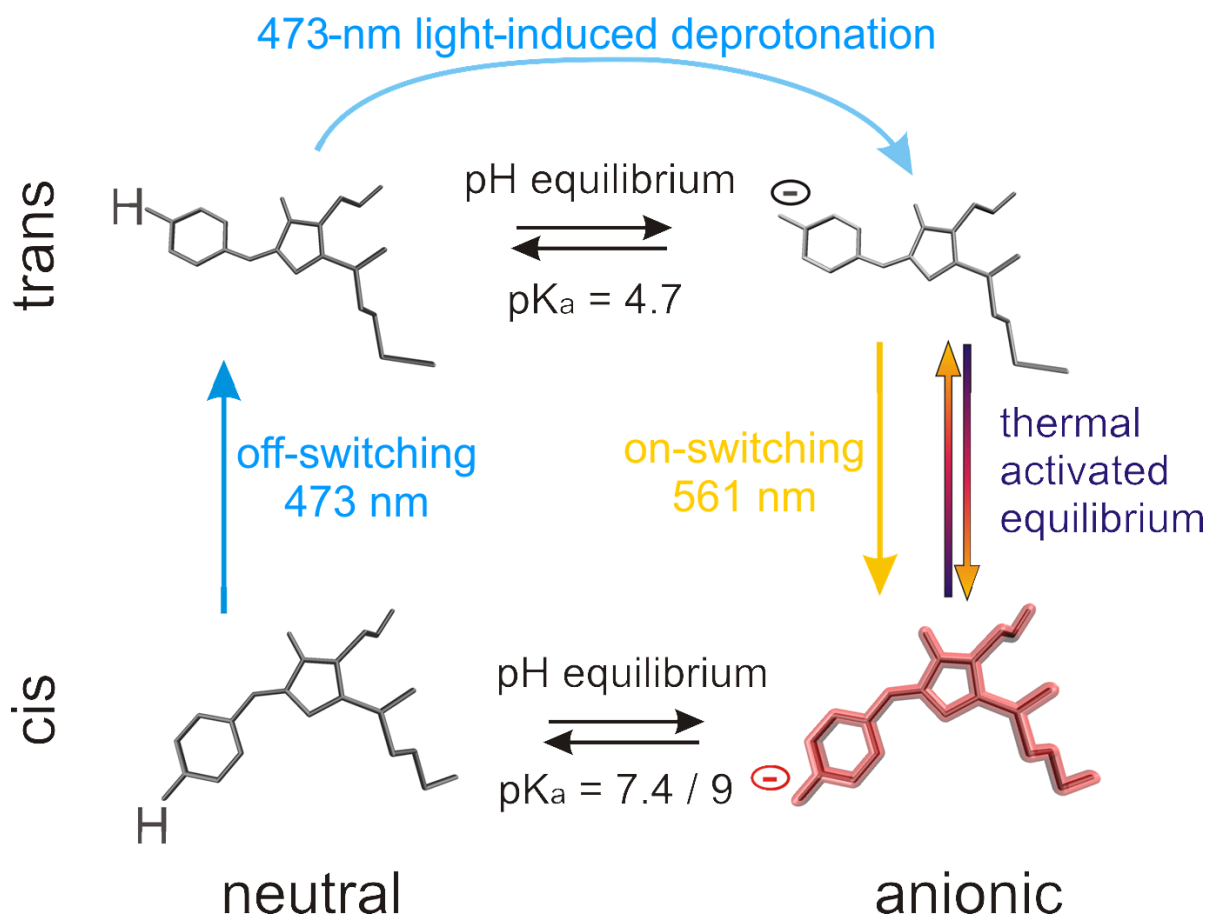


Figure 5.14. Isomerization and protonation pathways in psRFP. Illumination with 473-nm light leads to a net cis-trans isomerization of the neutral chromophore and deprotonation of the neutral trans chromophore. Illumination with 561-nm illumination causes trans-cis isomerization. The chromophore can also recovery to the initial state during a thermally activated process. The populations of the different states is furthermore determined by the pH equilibria of the cis and trans chromophores.

light (473 nm) are indicated in blue in figure 5.14). Switching is reversible as can be seen from a series of absorption spectra taken before 473-nm irradiation, after illumination and after 30 min recovery in the dark (Fig. 5.15). For many applications of photo-switchable FPs, in particular high resolution microscopy, the intensity contrast between the fluorescent state and the non-fluorescent state is an important parameter. We illuminated an FP solution with 473-nm light to switch as many FPs to the non-fluorescent off-state as possible and measured the residual fluorescence (Fig. 5.16a) which is, for psRFP, determined by the equilibrium of the light driven off-switching and the thermally activated recovery rates (Fig. 5.14). A 20-fold decrease in intensity and resulting a 5 % residual fluorescence could be observed after 473-nm irradiation with power densities $< 1 \text{ W cm}^{-2}$, which is well below the power densities used in PALM microscopy. The light induced reduction of the fluorescent anionic cis population leaves overall only 0.3 % of

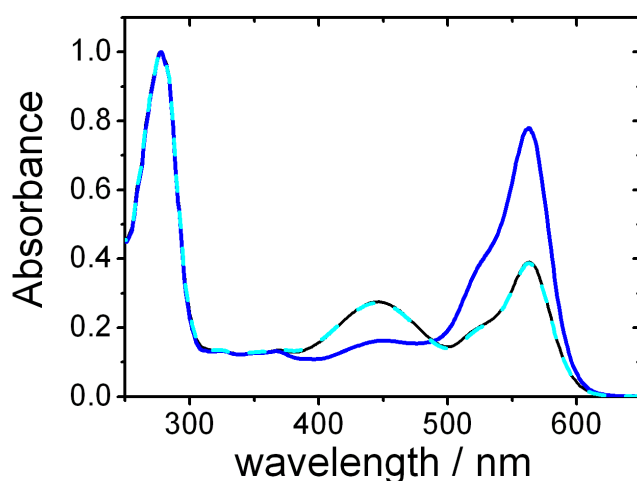


Figure 5.15. Reversible switching of psRFP. Absorption spectrum before 473-nm illumination (solid black), after illumination (solid green) and after thermal recovery (dotted green).

all molecules in the fluorescent state and provides ideal conditions for the recently introduced high resolution microscopy techniques (see PALM section), with only a sparse number of fluorescent labels in the emitting state and a large reservoir of dark molecules. The off-switching rate constant is power dependent and cis-trans photoisomerization increases with increasing 473-nm illumination power density (Fig. 5.16b). However, above

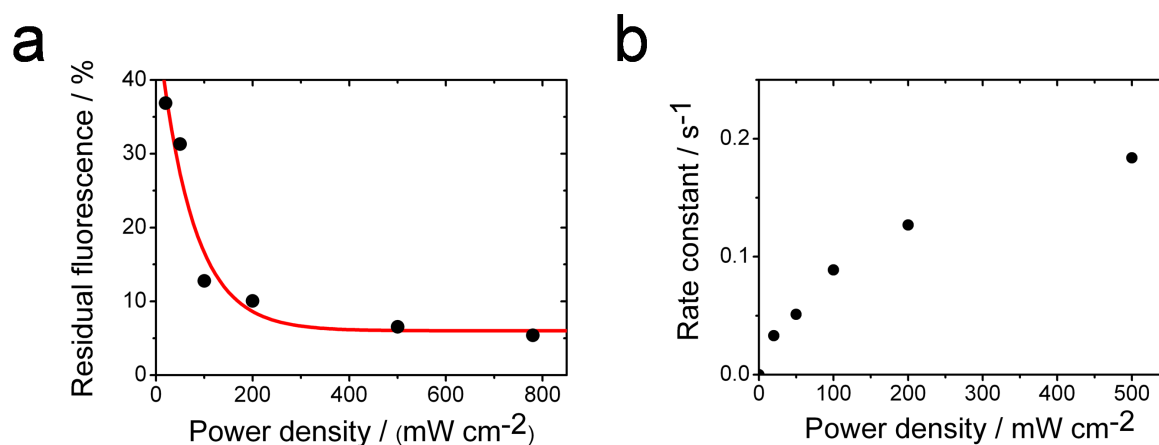


Figure 5.16. Power dependent off-switching properties. **(a)** Residual fluorescence after 473-nm irradiation (black dots) together with an exponential fit (red line). **(b)** Power dependent off-switching rates under 473-nm illumination.

100 mW cm^{-2} , saturation of the transition can be observed. To further understand the influence of illumination intensity and pH on the switching process we examined the

5. The Photoswitchable Red Fluorescent Protein (psRFP)

off-switching kinetics. The fluorescence time traces display a biphasic decay that can be explained by taking all isomerization and protonation reactions into account (Fig. 5.17). The switching kinetics at pH 7 depend on several processes, the protonation equilibrium

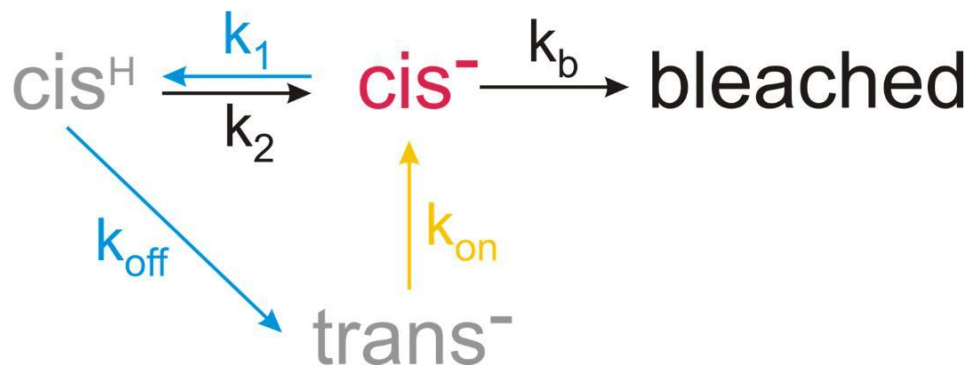


Figure 5.17. Light driven switching scheme at pH 7. Illumination with 473-nm light causes cis-trans isomerization of the neutral cis chromophores leading to a readjustment of the pH equilibrium between the neutral and the anionic cis chromophores and a depopulation of anionic cis chromophores. The neutral trans chromophore is not populated at pH 7 and, therefore, only the anionic trans chromophore can be excited with 561-nm irradiation and switched to the cis conformation. Excitation with the same wavelength leads to bleaching of the anionic cis form.

of the neutral and the anionic cis chromophore described by the rate constants k_1 , k_2 , the photo-induced cis-trans isomerization of the excited neutral cis chromophore (k_{off}) and the thermally activated trans-cis back isomerization as well as the weak photoinduced trans-cis isomerization due to weak excitation of the anionic trans chromophore at 473 nm. We combined the last two processes to a single rate constant for back-isomerization, k_{on} , because their contributions are very small. The populations of the anionic cis chromophore (C^-), the neutral cis chromophore (CH) and the anionic trans chromophore (T^-) are then described by the following set of differential equations

$$\frac{d[C^-]}{dt} = -k_1[C^-] + k_{\text{on}}[T^-], \quad (5.7)$$

$$\frac{d[CH]}{dt} = -k_2[CH] - k_{\text{off}}[CH] + k_1[C^-], \quad (5.8)$$

$$\frac{d[T^-]}{dt} = -k_{\text{on}}[T^-] + k_{\text{off}}[CH]. \quad (5.9)$$

The neutral trans chromophore is not populated at pH 7. Fits of the fluorescence decays at pH 7 with this model describe perfectly the measured data for different off-switching intensities (Fig. 5.18a). The off-switching rate constant for cis-trans isomerization increases from 0.04 s^{-1} (20 mW cm^{-2}) to 0.18 s^{-1} (500 mW cm^{-2}) (Fig. 5.16b) with increasing illumination intensity. The evolution of the chromophore populations under 473-nm illumination are given in figure 5.18b for 20 mW cm^{-2} excitation. The fluorescent anionic and the neutral cis states decrease over time in favor of the anionic trans

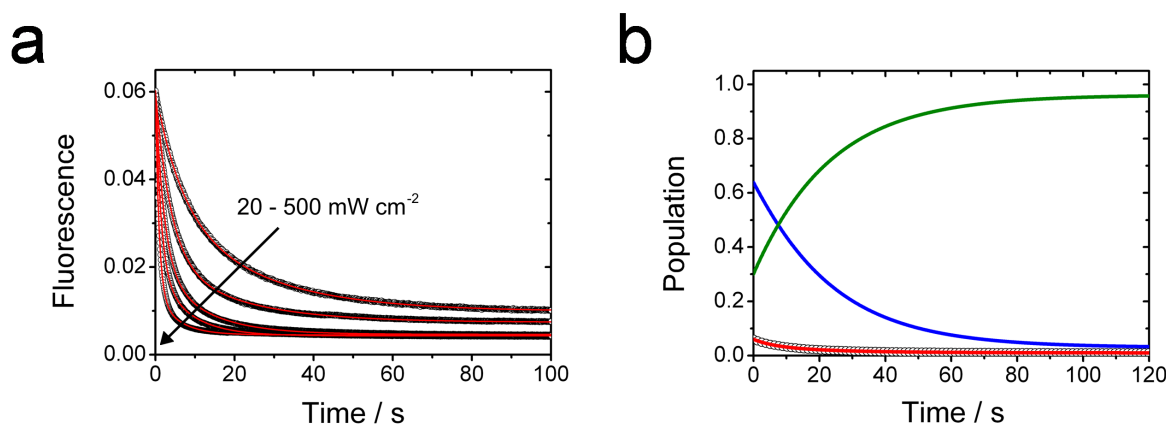


Figure 5.18. Power dependent off-switching kinetics. (a) Fluorescence time traces with 20 mW cm⁻² to 500 mW cm⁻². 473-nm illumination intensities (open circles). The decrease of the anionic cis chromophore (C⁻) can be described by equation 5.7 (red lines). The off-switching rate coefficients increase with increasing intensity. (b) Calculated time course under 20 mW cm⁻² 473-nm illumination for the fraction of the neutral cis conformation (blue), the anionic trans conformation (green) and the anionic cis conformation (red) together with the measured fluorescence values (open circles).

state. An equilibrium state under 473-nm illumination is reached after a few minutes, the cis conformation is almost completely depopulated and the anionic trans state is the dominant chromophore conformation. The population distribution under 473-nm irradiation is confirmed by the absorption spectrum measured after 473 nm illumination (Fig. 5.13b), which displays a dominant trans peak and almost no absorption in the cis bands. Interestingly, the light driven off-switching rate coefficient k_{off} decreases with pH from 0.048 s⁻¹ at pH 7 to 0.033 s⁻¹ at pH 9.5. The pH dependence tracks that of the fraction of neutral cis chromophores. The reaction rate coefficient is thus governed by the supply of reactant, i.e. the neutral cis chromophore CH. This supply, in return, is determined by the ground-state equilibrium, $CH = C^- + H^+$, which shifts with increasing pH towards the anionic form.

5.3.2. On-switching

After illumination with 473-nm light, which induced off-switching, the protein can either revert thermally activated to equilibrium in the dark before irradiation or the process can be accelerated by 561-nm light, which can be monitored as an increase in fluorescence.

Light-driven On-switching

Excitation of the anionic trans chromophore with 561-nm light speeds up the recovery process. The light-driven on-switching kinetics display single exponential behavior with on-switching rate coefficients increasing from 0.006 s⁻¹ at pH 6.5 to 0.06 s⁻¹ at pH 10

5. The Photoswitchable Red Fluorescent Protein (*psRFP*)

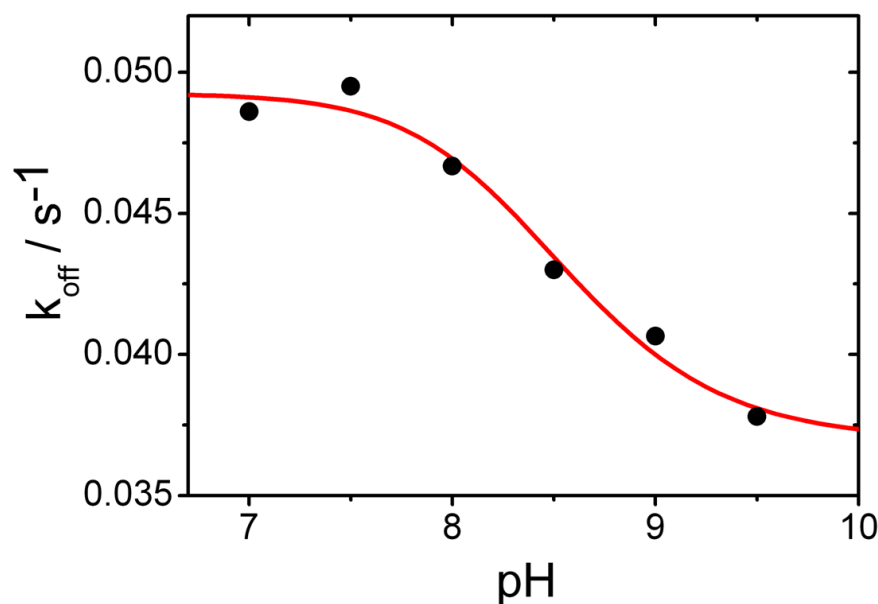


Figure 5.19. pH dependence of the off-switching rate coefficient (black dots) measured under 473-nm illumination (50 mW cm^{-2}). The fit curve that describes the pH-dependent population of the neutral cis chromophore (Fig. 5.4c) is scaled to the data for comparison (red line).

(Fig. 5.20a). At first view, one might assume that the pH dependence of the on-switching follows that of the anionic cis chromophore fraction. A detailed analysis showed, however, that the rate coefficients follow a trend line for a deprotonation with $\text{p}K_a = 9.2$ (Fig. 5.20b). No deprotonation step with $\text{p}K_a = 9.2$ was found in the analysis of the different chromophore populations, but the inspection of the peak positions of the combined cis and trans anionic absorption bands displayed a blue shift with $\text{p}K_a = 9.2$. The peak shift is first dominated by the anionic cis population that generates a red shift due to the increasing red shifted absorption spectrum of the anionic cis chromophore. At higher pH, a blue shift can be observed that cannot result from a change in chromophore population. Rather, deprotonation of an amino acid in the vicinity of the trans chromophore may explain both the blue shift in the absorption spectrum and the increased switching rate for trans-cis isomerization. A comparison of the crystal structures of KFP1 at pH 5.7¹⁷⁹ (PDB ID 1XQM) and at pH 9.5¹⁸⁰ (PDB ID 1XMZ) displayed only one major difference. His197 is found in a second conformation at pH 9.5 which we assume is due to deprotonation and the concomitant break of the hydrogen bond to Glu145. Since the imidazol ring of the histidine π -stacks to the chromophore hydroxyphenyl ring, deprotonation and a change of position of His197 could induce the observed peak shift and facilitate trans-cis isomerization.

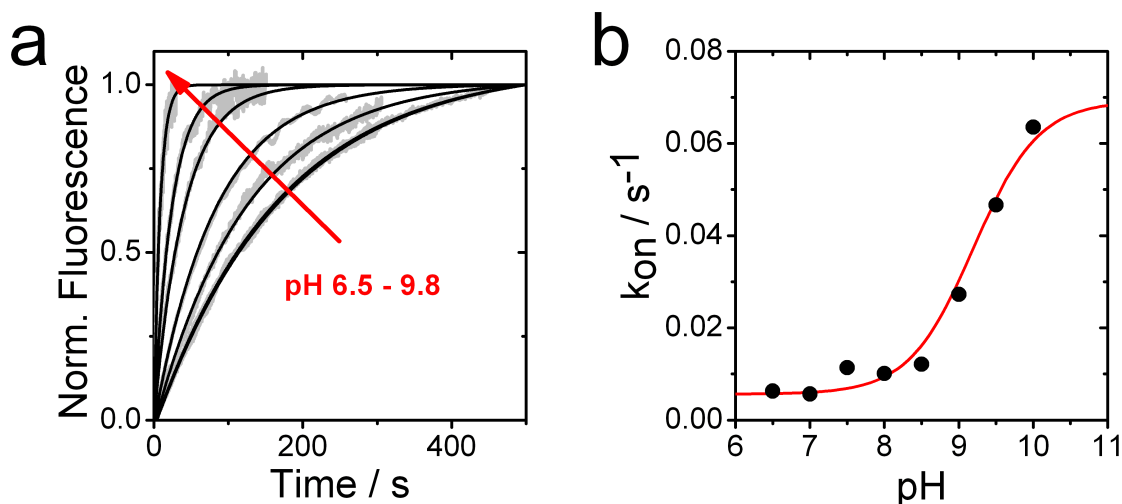


Figure 5.20. Light-driven on-switching kinetics. (a) pH-dependent fluorescence time traces under 561-nm excitation, after exposure to 473-nm illumination (grey) and fits (black). (b) The light-driven recovery rates (black dots) increase with increasing pH. The fit curve that describes the deprotonation of an amino acid, close to the chromophore, according to Henderson-Hasselbalch with $pK_a = 9.2$ is scaled to the data for comparison (red line).

Thermally Activated Recovery

The anionic trans population obtained after 473-nm illumination reverts to the initial cis-trans equilibrium by a thermally activated recovery process. The fluorescence increase follows mono-exponential recovery kinetics (Fig. 5.23a). Special care was taken during these experiments to minimize the influence of the probe light on the recovery kinetics. The pH dependent recovery kinetics, which are affected by the population of the different chromophore conformations offer valuable clues to the switching mechanism. We could observe an increasing relaxation rate (Fig. 5.23) that is directly related to a decrease of the energy barrier between the trans and cis ground states. A comparison of the pH-dependent changes of the rate coefficients with the band shift of the combined absorption spectrum (Fig. 5.21) show, that both changes are caused by the deprotonation of an amino acid with $pK_a = 9.2$. Such a change was also observed for light-driven on-switching and attributed to deprotonation of His197 that could explain the lower energy barrier for isomerization at high pH. After photosactivation with 473-nm illumination the complete chromophore population is switched to the anionic trans state at pH 7. For this reason, the rate coefficient k for trans-cis isomerization is observed for the recovery process and the rate coefficient for cis-trans isomerization can be neglected. The height of the energy barrier separating the anionic trans and cis ground states can be obtained from temperature dependent measurements of the fluorescence recovery through a fit of the rate coefficients k (Fig. 5.24). After photosactivation with 473-nm illumination the complete chromophore population is switched to the anionic trans state at pH 7. For

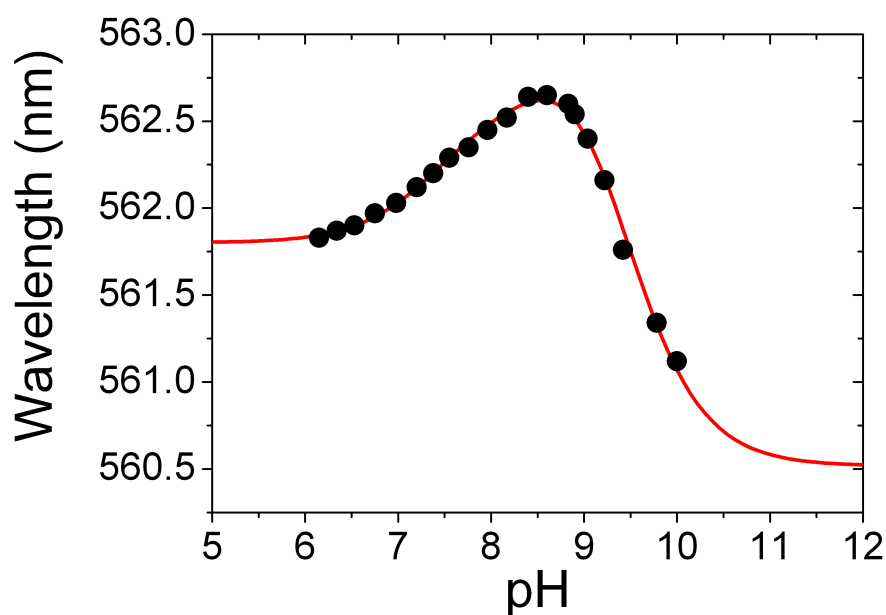


Figure 5.21. The peak position of the combined anionic trans and cis absorption bands (black dots) shifts first from pH 6 to longer wavelength, which can be explained by the deprotonation of the cis chromophore. The increasing the anionic cis chromophore with maximum absorption at 583 nm causes an the red shift of the combined absorption. This shift is described by the two-site protonation model equation 5.5, (Fig. 5.4c). But for higher pH values, the peak position shifts to lower wavelength again. This shift of the peak can only be explained by a change in the electrostatic environment of the trans chromophore, which is cause by the deprotonation of a nearby amino acid according to the Henderson-Hasselbalch equation with a $pK_a = 9.2$. The red line is fit of the sum of both contributions to the measured peak shift.

this reason, the rate coefficient k for trans-cis isomerization is observed for the recovery process and the rate coefficient for cis-trans isomerization can be neglected. The rate coefficients are given in an Arrhenius plot and the energy barrier for thermal relaxation was determined by a fit of equation 5.10 to the data.

$$k = A e^{-\frac{E_a}{RT}}. \quad (5.10)$$

The rate coefficient k depends on the pre-exponential factor A , the activation energy E_a , the gas constant R and the temperature T . Arrhenius analysis showed that, for trans-cis isomerization, the chromophore has to overcome an energy barrier of $E_a = 89 \text{ kJ mol}^{-1}$ at pH 7 and the fit yielded a pre-exponential factor of $A = 2.2 \cdot 10^{13} \text{ L mol}^{-1} \text{ s}^{-1}$. The value for the barrier is slightly higher than the value determined for cis-trans isomerization in KFP1 (71 kJ mol^{-1})¹⁸⁰ or the 55 kJ mol^{-1} reported for cis-trans isomerization of a green model chromophore in solution¹⁸².

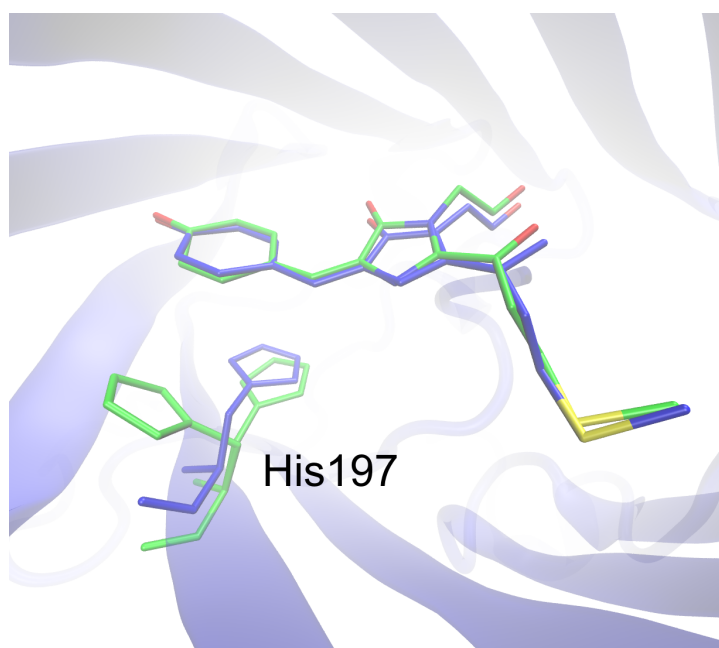


Figure 5.22. Structure of KFP1. The trans chromophore and His197 in the low pH (pH 5.7, blue) and the high pH (pH 9.5, green) structures are shown. His197 was found in a single conformation at pH 5.7 and in an additional second conformation at pH 9.5. The second conformation that does not π -stack to the chromophore is only possible if the hydrogen bond network that stabilizes His197 below the chromophore is ruptured.

5.4. Kindling and Photobleaching

Illumination of the initial ground state with 561-nm light caused a fluorescence increase as observed earlier for KFP1⁶², termed kindling. Excitation of the anionic trans chromophore causes trans-cis isomerization and the absorption band of the anionic trans chromophore decreased in favor of the the neutral and anionic cis chromophore absorption bands (Fig. 5.25). After 30 min irradiation with intense 561-nm light (40 mW cm^{-2}), the absorption spectra showed thermally activated back-isomerization towards the trans-cis equilibrium. However, the initial state before irradiation was not reached due to photobleaching and irreversible kindling (Fig. 5.26). The spectra, after recovery in the dark, exhibit a higher cis population that could not be switched back to the initial state. Irreversible kindling after 561-nm illumination, which results in a non-switchable fluorescent form, was earlier reported for KFP1⁶², PA-GFP⁴⁰ and PAmCherry1⁴⁴. The decarboxylation of Glu215 was identified as the process causing irreversible kindling in these proteins. It seems that the hydrogen bond between the imidazolinone nitrogen of the chromophore and the carboxyl side chain of Glu215 is obviously necessary to stabilize the trans conformation. Decarboxylation of Glu215 leads to the rupture of this hydrogen bond. The chromophore can no longer be stabilized in the trans conformation but is instead irreversible switched to the cis conformation.

5. The Photoswitchable Red Fluorescent Protein (psRFP)

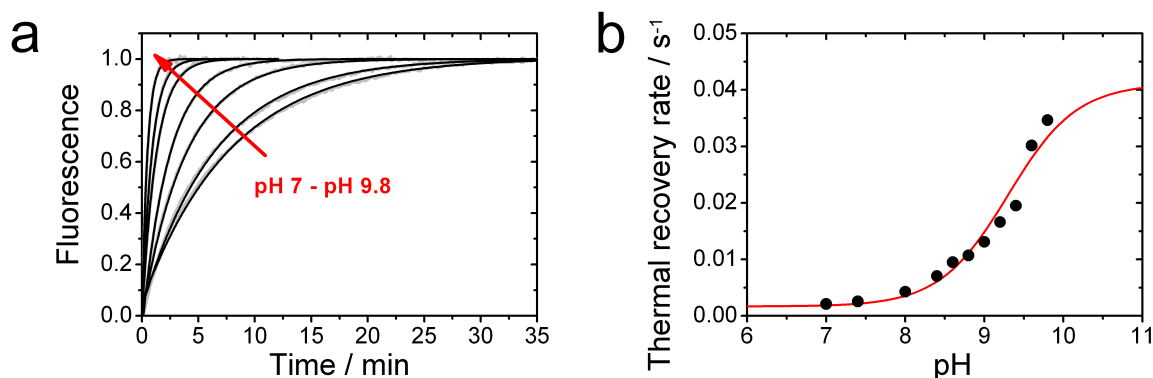


Figure 5.23. Thermally driven on-switching kinetics. (a) pH-dependent fluorescence time traces after exposure to 473-nm illumination (grey) and fits (black). (b) The thermal recovery rates (black dots) increase with increasing pH. The fit curve, that describes the pH-dependent deprotonation of an amino acid with $pK_a = 9.2$ according to the Henderson-Hasselbalch equation, is scaled to the data for comparison (red line).

The fluorescence activation kinetics, starting from the ground state, show two competing processes, photoactivation from the anionic trans to the anionic cis state and photobleaching of the molecules in the anionic cis state, i.e., irreversible destruction of the light emitting chromophore (Fig. 5.27). The observed fluorescence time traces depend on the excitation intensity and on the population of the anionic cis (C^-) and trans (T^-) states,

$$\frac{d[C^-]}{dt} = -k_{bleach}[C^-] + k_{on}[T^-]. \quad (5.11)$$

At short times, the activation process dominates the fluorescence time traces at pH 7. Due to a higher population of the anionic trans (30%) conformation as compared to the anionic cis conformation (6%), the number of activated molecules exceeds the bleached molecules. The number of molecules in the dark states decreases with increasing time and more molecules are bleached than activated. Therefore, the bleaching process becomes more prominent. Higher excitation intensities increase both the bleaching and the activation rate coefficients and thereby shift the protein population faster from the anionic trans to the anionic cis and finally to the bleached state. Bleaching is governed by the excitation intensity and relies on the population of the anionic cis state, which is only weakly populated at pH 7 (6 %). With increasing pH, the population of the fluorescent anionic cis chromophore increases and, thus, bleaching becomes more dominant (Fig. 5.28). Furthermore, the ground state pH equilibrium between neutral cis (CH) and the anionic cis (C^-) chromophore determines the amount of anionic cis chromophore (Fig. 5.17). In contrast to most other fluorescence proteins, which show mono-exponential bleaching kinetics, the interplay of the different processes in psRFP leads to a slow bleaching rate. For properly chosen excitation intensity, live cell samples

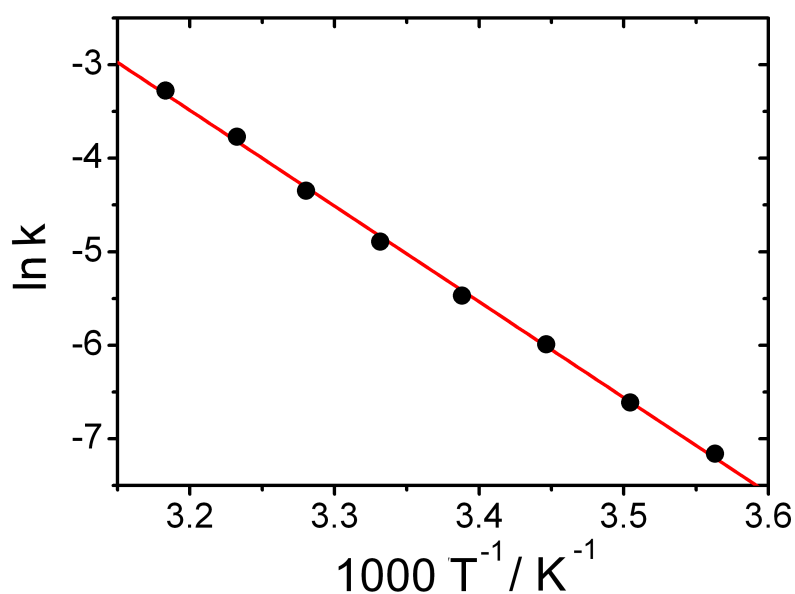


Figure 5.24. Arrhenius analysis for thermally driven relaxation from the anionic trans ground state to the cis ground state conformation. The experimental data (black dots) are well described by the Arrhenius model, eq. 5.10 (red line).

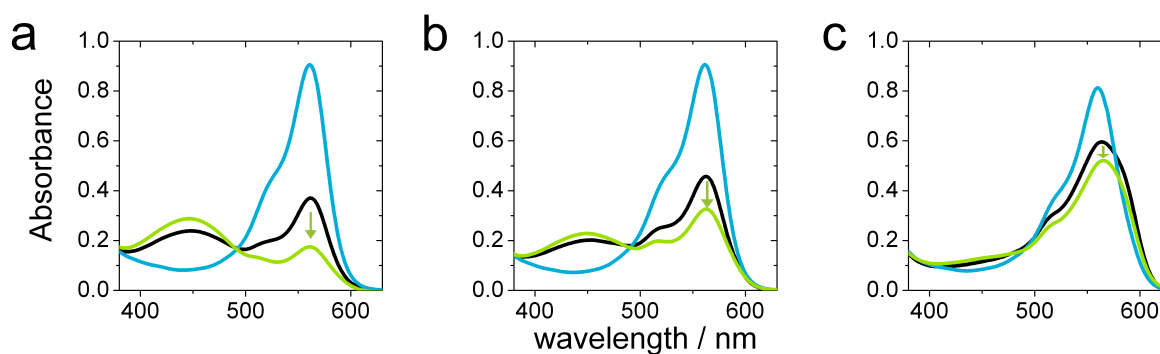


Figure 5.25. Absorption spectra at pH 4.8 (a), pH 7 (b) and pH 9.5 (c) before illumination (black line), after 3 min 473-nm irradiation (cyan) for off-switching and after 20 min 561-nm illumination (green) for on-switching.

can be observed with almost constant brightness over long time periods. At increased excitation intensities, psRFP is excellently suited for high resolution microscopy with a constant low number of molecules in the fluorescent state over a long period of time (30 min).

5. The Photoswitchable Red Fluorescent Protein (psRFP)

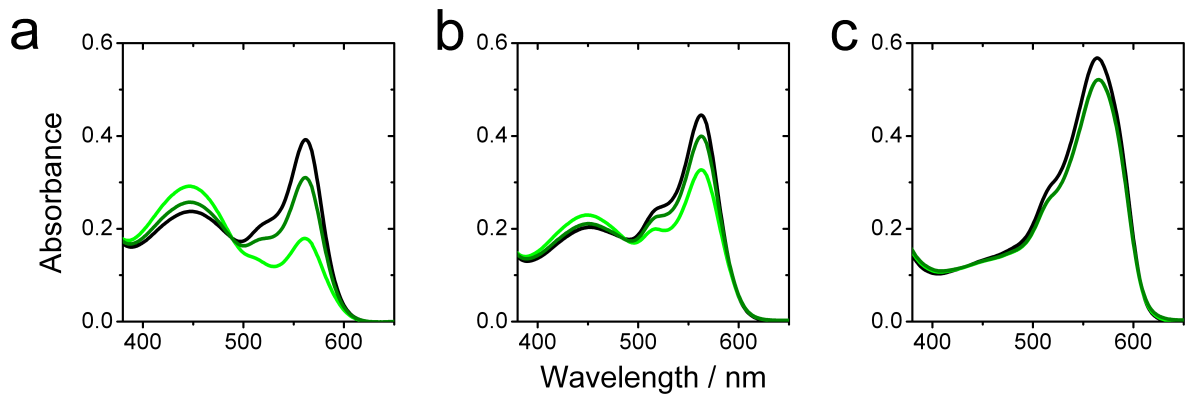


Figure 5.26. Absorption spectra before 561-nm irradiation (black line) at pH 4.8 (a), pH 7 (b) and pH 9.5 (c) are plotted together with the absorption spectra after 30 min illumination with intense 561-nm light (40 mW cm^{-2}) (light green) and absorption spectra after thermal recovery in the dark for 12 h (dark green).

5.5. Single Molecule Experiments

For single molecule experiments, purified proteins were sparsely immobilized on a bovine serum albumin (BSA) surface to characterize their single molecule emission properties. The molecules were localized with the PALM software and the total number of emitted photons per molecule was determined together with the localization error (Fig. 5.29). psRFP is a bright fluorescent FP with 1300 (mean) and 661 (median) detected photons per molecule. The high photon number and the low background fluorescence on the BSA surface led to an excellent localization error of 11 nm. We also immobilized a thin film of psRFP molecules on the BSA and examined the switching properties under intensities typically used for light microscopy (4 kW/cm^{-2}). The protein layer was excited with 532-nm light (4 kW/cm^{-2}) and, for off-switching, the sample was exposed to additional 488-nm illumination (4 kW/cm^{-2}). Under these conditions, typically used for single molecule confocal microscopy, the off-switching was only limited by the mechanical shutter reaction time of 20 ms. The on-switching (4 kW/cm^{-2}) took about 3 seconds (Fig. 5.30). More than ten on/off switching cycles were measured without considerable bleaching of the thin protein layer.

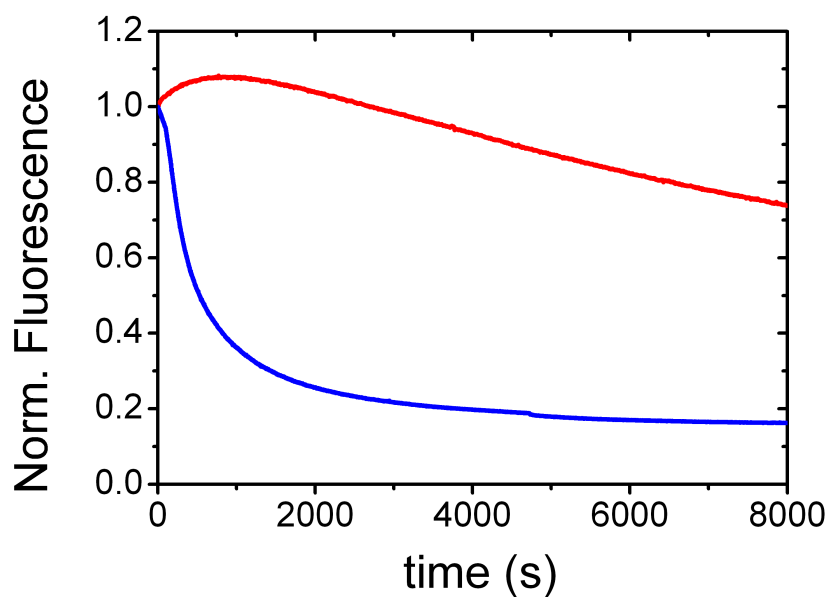


Figure 5.27. Bleaching curve of psRFP under 561-nm illumination at 2 W cm^{-2} (red), 30 W cm^{-2} (blue). Two main processes are visible in the fluorescence kinetics, photoactivation from the dark (anionic trans) state to the fluorescent (anionic cis) state and photobleaching of the fluorescent molecules. At higher illumination intensity, the bleaching process becomes more dominant.

5. The Photoswitchable Red Fluorescent Protein (psRFP)

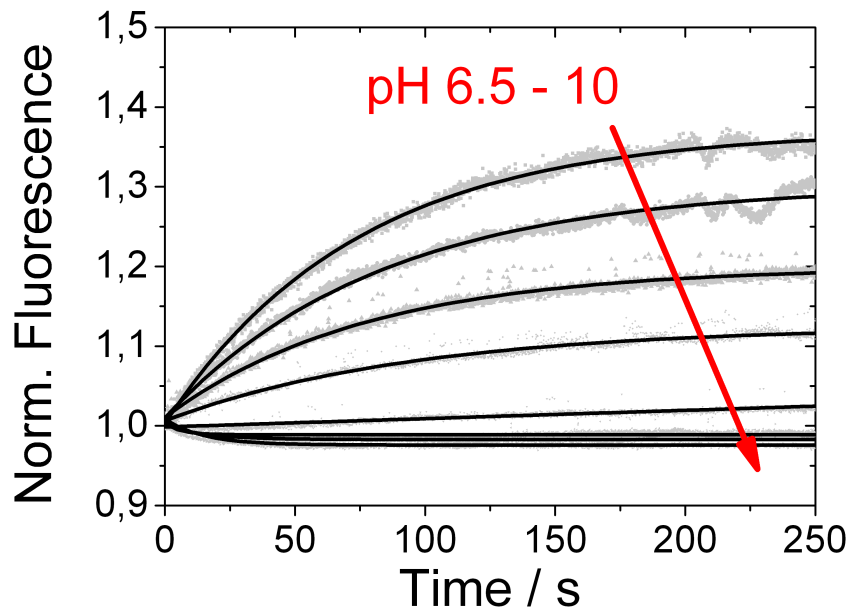


Figure 5.28. Normalized pH dependent (pH 6.5 to pH 10 in 0.5 pH steps) fluorescence kinetics under 561-nm (100 mW cm^{-2}) illumination (grey) and fits (black). Photoactivation is higher at low pH and decreases with increasing population of the anionic cis conformation.

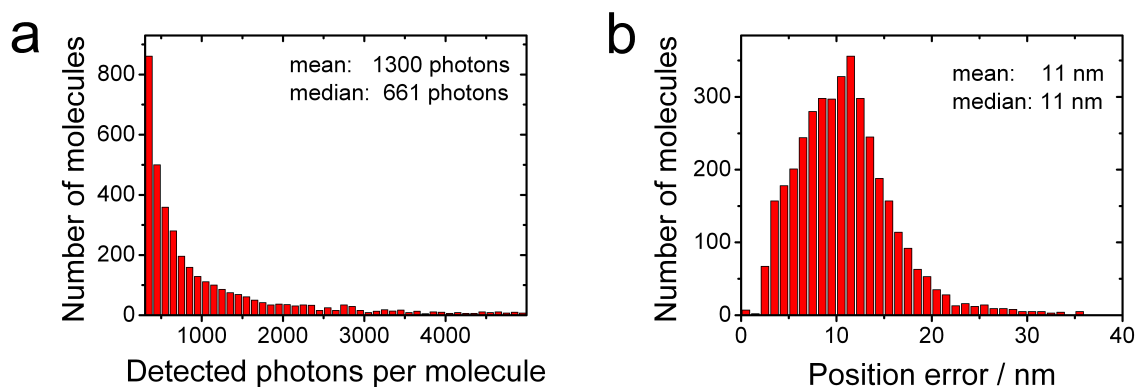


Figure 5.29. Localization properties of psRFP molecules immobilized on a BSA surface. (a) The detected number of photons per molecule (mean: 1300, median: 661). (b) The localization accuracy (mean: 11 nm, median: 11 nm)

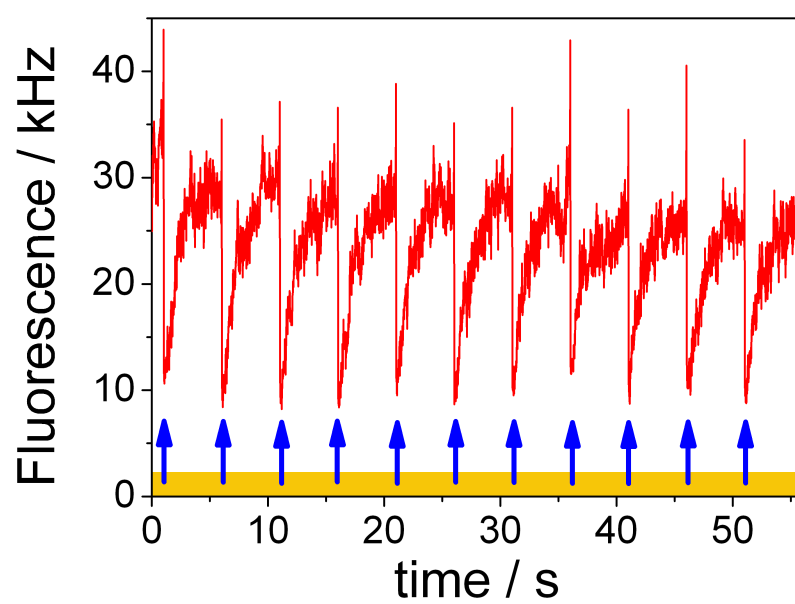


Figure 5.30. Switching of a psRFP layer immobilized on a BSA surface. The proteins were excited with 532-nm light and additionally exposed to 488-nm irradiation for off-switching.

6. Discussion psRFP

We have studied the interaction of the chromophore with the protein environment. The protein environment affects important properties such as emission and photoswitching of fluorescent proteins. This knowledge is essential for new imaging applications and further improvement of the optical properties of FPs in general. In psRFP, the protein environment influences the cis and trans chromophore conformations and the protonation states. For all switchable FPs described so far, either the cis or trans conformation is stabilized by the protein matrix. Our pH dependent studies show contributions of both conformations (90 % cis and 10 % trans) in psRFP over the whole measurable pH range. The ratio of the two chromophore conformations can be shifted towards the trans conformation (50 % trans, 50% cis) by introducing the Leu147Val mutation. This mutation leads presumably to a rearrangement of the hydrogen bond network in the chromophore environment around His197 to a configuration similar to that seen in KFP1^{180, 179}. The resulting configuration stabilizes the trans conformation (Fig. 6.1). We can change a FP, which is initially in the fluorescent state and can be switched off (psRFP) towards a FP, that is initially in the dark state and has to be activated (KFP1). This knowledge will be helpful to design future FPs with a defined chromophore conformation.

Furthermore, we observed the interaction of the chromophore with a second amino acid in the environment. The deprotonation of this amino acid with a $pK_a = 9.2$ causes a blue shift of the trans chromophore absorption spectrum and an increase in the thermal and light driven trans-to-cis back isomerization in psRFP. To identify the amino acid, we compared the psRFP structure to the KFP1 structure with the trans chromophore at high pH (9.5)¹⁸⁰ and low pH (5.7)¹⁷⁹. The two structures show an obvious difference for His197. The electron density of His197 displays a single conformation at low pH, whereas, at high pH, two conformations were found. The second His197 conformation can only be explained by a deprotonation of His197 and a rupture of the hydrogen bond network with the surrounding residues. This deprotonation influences the trans chromophore and can also be seen in the presence of the cis chromophore in psRFP. It is consistent with the two-site deprotonation behavior observed in the pH dependent measurements. However, the deprotonated His197 cannot adopt the same position in psRFP as in KFP1 because it would block the cis conformation. Nevertheless the deprotonation of His197 explains all observed effects.

For imaging applications, it is essential to understand the switching mechanisms in psRFP. The chromophore is switched to a non-fluorescent state with irradiation around 450 nm. With illumination in this wavelength range both the neutral cis and the neutral trans chromophore are excited and can isomerize to the alternative conformation. We observed an effective cis-trans isomerization together with light-induced deprotonation of the trans conformation. This leads to a shift in population from the cis conformation

6. Discussion *psRFP*

to the anionic trans conformation. Our observation is supported by molecular dynamics simulations that predicted a higher probability for cis-trans isomerization of the neutral chromophore of asFP595¹⁸³. The light-induced proton transfer with long recovery times for the trans chromophore additionally prevents direct re-isomerization to the cis state. This mechanism leads to efficient switching from the neutral cis to the anionic trans conformation. The cis-trans isomerization coupled with the pH equilibrium of the cis chromophore results in fluorescence off-switching above pH 6, which is facilitated by the absence of the neutral trans population at physiological pH. Worth mentioning is that no light-induced deprotonation was observed for the cis chromophore, most probably due to the absence of a proton acceptor in the chromophore environment.

Efficient on-switching is achieved by exciting the anionic trans chromophore. Light-induced trans-to-cis isomerization under 561-nm irradiation was observed over the whole pH range. This observation excludes the neutral trans form as the key conformation for on-switching because the neutral trans chromophore is not populated above pH 6. Therefore the model suggested for asFP595¹⁸³, which assumes on-switching based on the excitation of the neutral trans chromophore, does not fit for *psRFP*. The increase of the rate coefficient for light-induced on-switching with increasing pH is coupled to the deprotonation of His197 and rupture of the hydrogen bond network below the chromophore. The missing interaction between the hydroxyphenyl ring of the chromophore and the π -stacked His197 leads to facilitated trans-cis isomerization. The same effect is also visible in the thermally driven ground state recovery and confirms the importance of His197 for the switching mechanism.

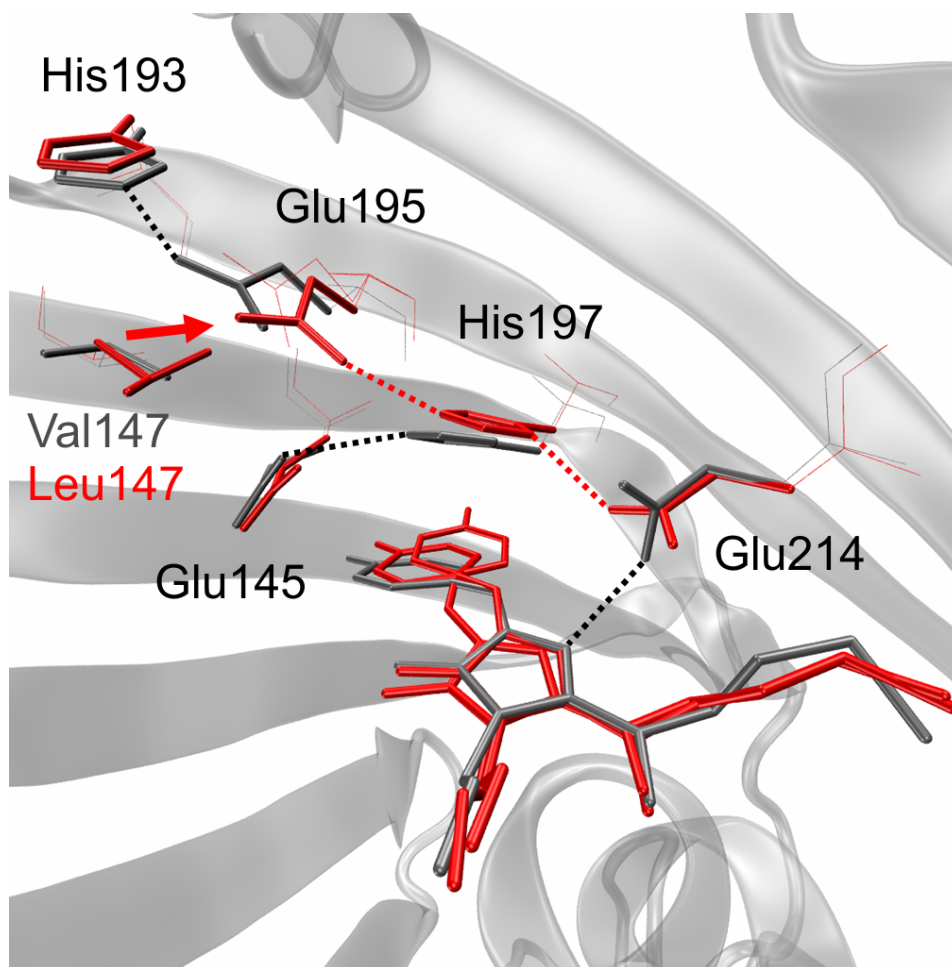


Figure 6.1. Comparison of the chromophore environment in psRFP (red) with both chromophore conformations and KFP1 (gray) with the chromophore in the trans conformation. The longer sidechain of Leu147 in psRFP compared to Val147 in KFP1 pushes Glu195 towards His197 and thereby changes the hydrogen bond network around the chromophore

Photoswitching in psRFP is affected by different factors. The population of the chromophore conformations and protonation states play an important role. Only the neutral cis chromophore can be excited with 450-nm light at physiological pH because the trans population is completely shifted to the anionic form. Therefore, light-driven trans-cis isomerization under 450-nm illumination is excluded above pH 6. psRFP shares a chromophore population distribution with other positive switchers such as KFP1 and Padron, that exhibits only a neutral cis chromophore around pH 7. Excitation in the neutral band causes cis-trans isomerization and thereby a depopulation of the fluorescent anionic cis form. On the other hand, excitation of the anionic forms yields trans-cis isomerization due to the predominant population of the anionic trans chromophore. The excitation wavelength of the fluorescent form shifts the chromophore population from the non-fluorescent trans to the fluorescent cis form. The chromophore population is important

6. Discussion *psRFP*

for the photoswitching of *psRFP* but it does not solely determine the switching behavior. Additional processes such as light-induced deprotonation influence the switching behavior. The light-induced deprotonation of the neutral trans chromophore prevents back isomerization after light-driven cis-trans isomerization in *psRFP* and makes off-switching more effective.

The population of the different chromophore states also influences photobleaching. A large amount of FPs in the dark state, which can be slowly activated, causes slow bleaching of *psRFP*. An almost constant number of molecules are detected over a long period of time. This number is determined by the on-switching rate, the pH-dependent equilibrium of the cis conformation and the bleaching rate. The resulting slow bleaching under moderate illumination intensity renders *psRFP* an excellent marker for continuous long-term studies. Similar non-exponential slow bleaching curves have been observed for EGFP, several orange and red FPs¹⁸⁴ and for mRuby(N143C) and might cause by a non-fluorescent dark chromophore fraction in these proteins.

Furthermore the excellent optical properties of *psRFP* make this FP an interesting marker for imaging applications. Red switchable FPs, in general, exhibit a rather high variation in extinction coefficients ranging from 18,000 to 85,000 M⁻¹cm⁻¹ (Table 6.1). The value of the fluorescent form of *psRFP* (27,000 M⁻¹cm⁻¹) is a little bit lower than the values for KFP1 and the red forms of mEos2 and tdEosFP. The high fluorescence quantum yield of *psRFP* is particularly interesting, because the determined quantum yields for reversibly photoswitchable red FPs so far have been very low, three orders of magnitude lower than for irreversible and non-switchable FPs. According to our analysis, *psRFP* is the first reversibly switchable red FP with a comparable quantum yield (0.61) to state-of-the-art red FPs such as PAmCherry1, PATagRFP or tdEosFP. The high quantum yield and extinction coefficient make *psRFP* a bright, reversibly switchable FP capable of competing with other state-of-the-art FPs. In addition, *psRFP* offers the functionality of a reversibly switchable FP, that can be switched on and off for many times. This is essential for applications such as data storage³⁶ or background suppressing microscopy¹⁸⁵ and many other new exciting applications. However, it should be mentioned that the low quantum yield measured for KFP1, rsCherry and rsCherryRev could be due to incomplete switching, which results in an underestimation of the true value⁶³. Only after intense irradiation with 514 nm light (~1kW), which resulted in irreversible kindling, a comparable quantum yield of 0.5 was observed for asFP595¹⁸⁶, which is closely related to KFP1 and *psRFP*.

The fast switching behavior of *psRFP* under high excitation intensities provides the basis for the potential use of *psRFP* in high-resolution microscopy applications such as RESOLFT and SSIM. We show in the next chapter that *psRFP* is an excellent marker for PALM, due to its the high molecular brightness and good single molecule localization properties.

Fluorescent Protein	Excitation / Emission (nm)	Extinction coefficient ($M^{-1}cm^{-1}$)	Fluorescence Quantum Yield	Brightness x 1000	Photo-activation mode
psRFP	583/603	27,000	0.61	16.5	reversible
KFP1 ⁶²	580/600	59,000	0.07	4.1	reversible
rsCherry ⁴⁴	572/610	81,000	0.02	1.6	reversible
rsCherryRev ⁴⁴	572/608	85,000	0.005	0.4	reversible
PAmCherry1 ⁴⁴	564/595	18,000	0.46	8.3	irreversible
mCherry ⁴⁴	587/615	72,000	0.22	15.8	-
tdEosFP(red) ⁶⁸	569/582	33,000	0.6	19.8	irreversible
mEos2 ⁶⁸	573/584	46,000	0.66	30.4	irreversible
PATagRFP ¹⁸⁷	562/595	66,000	0.38	25.1	irreversible
TagRFP ¹⁸⁷	555/584	100,000	0.48	48	-

Table 6.1. Comparison of switchable red FPs

7. PALM Developments

7.1. Evaluation of Fluorescent Proteins as PALM Markers

PALM imaging requires fluorescent proteins with excellent photoactivation contrast over background, great photostability and high single-molecule brightness. In addition, the fluorescent marker protein should not disturb the function or localization of the protein of interest and the labeling density has to be high enough to achieve an image resolutions far beyond the diffraction limit (see Nyquist-Shannon sampling theorem).

7.1.1. psRFP

The red emitting psRFP showed an encouraging localization and switching performance in in vitro experiments. Therefore, we tested psRFP for its performance as fluorescent marker in human HeLa cells. The fusion constructs of psRFP with paxillin, Lifeact and Rita displayed bright fluorescence and did not affect cell viability. Reversible switching of the fluorescence was achieved by irradiating the living cells with blue light (473 nm) for off-switching and yellow light (561 nm) for on-switching. To ensure that psRFP did not interfere with the function of the fusion partner due to its tetrameric nature, we confirmed the proper localization of the paxillin, Rita and Lifeact fusion constructs (Fig. 7.1, 7.2, 7.3). The image of the paxillin fusion displayed the typical paxillin-rich adhesion complexes in the cell periphery, the Lifeact and the Rita fusions localized along the cytoskeletal actin filaments and microtubuli. No unexpected fluorescence signal from protein clusters or from improperly incorporated proteins was observed. To demonstrate the utility of psRFP for subdiffraction imaging, a PALM image of the paxillin fusion was constructed from data acquired with 100 ms dwell time, 561 nm excitation (60 W/cm^2) and 473 nm ($0\text{--}4 \text{ W/cm}^2$) irradiation. A comparison between the TIRF and PALM image shows the substantially higher resolution of the PALM image (Fig. 7.1). Details hidden in the TIRF image can be clearly distinguished in the PALM images. What appears to be a single, $5 \mu\text{m}$ long focal adhesion in the TIRF image actually consists of several separated subclusters, which are 100 nm to 500 nm in diameter (Fig. 7.1d,e). Comparable small paxillin patches were also observed close to ventral actin fibers³⁴. We confirmed the localization results by transfecting cells with psRFP fused to the microtubule-binding protein Rita, which permits observing of the microtubule-network close to the cell surface (Fig. 7.2). Data for the reconstruction of the PALM image were taken at 100 ms per frame, excitation with 561-nm illumination (100 W/cm^2) and 473-nm light (0.6 W/cm^2) for off-switching. Because single molecules are detected and

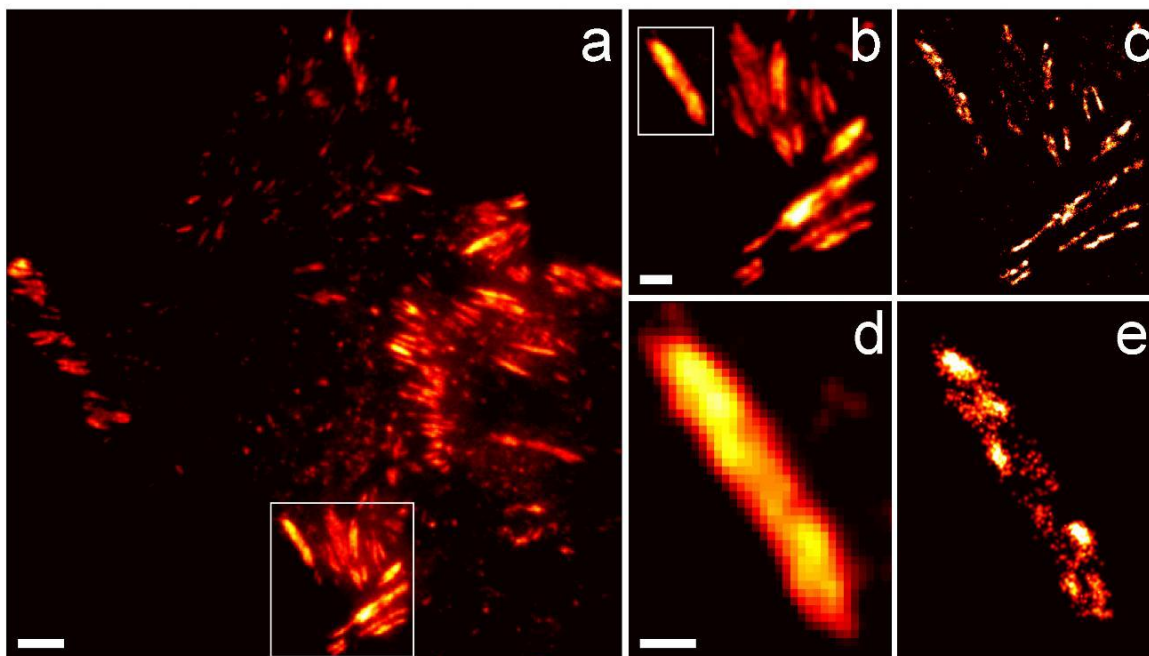


Figure 7.1. Superresolution PALM and TIRF images of a living HeLa cell expressing a psRFP-paxillin construct. (a) TIRF image of the whole cell with psRFP located in the focal adhesions. (b) Close-up of the white marked region in (a). (c) PALM image of the same region in (a). (d) TIRF image of a single adhesion complex marked by a white frame in (b). (e) PALM image of the same adhesion complex with increased resolution. Scale bars, 5 μm (a), 2 μm (b,c), 1 μm (d,e).

localized during data acquisition of PALM images, information about signal photons, background and localization precision are available for each molecule. The information is given in histograms (Fig. 7.4). On average, 623 (mean), 250 (median) signal photons per psRFP molecule were detected. At the same time, 56 (mean), 35 (median) background photons per molecule and pixel were recorded. The theoretical 2D position error was calculated to 28 nm (mean), 28 nm (median). Single fluorophores can be localized with an average accuracy of 28 nm. To continue that this high localization accuracy also translates into an image that represents the recorded structures accurately, we estimated the width of microtubules that can be characterized as long hollow cylinders with a fixed outer diameter of 25 nm¹⁵⁶. Thus, they are excellently suited to verify the resolution of in vivo imaged cellular structures. The 1D localization error across the microtubule fiber profile is 18 nm (mean), 17 nm (median), instead of the 2D position error used to estimate the width of a microtubule fiber. The cross section of a psRFP-Rita labeled microtubule segment is projected onto a plane and convoluted with a Gaussian function with $\sigma = 17$ nm (Fig. 7.5). The resulting distribution can be compared to the molecule distribution of three differently labeled filament segments in figure ???. The positions of all detected molecules were projected along the contour line and are given in histograms (Fig. 7.8). The full width half maximum (FWHM) was calculated to be 48 nm for the

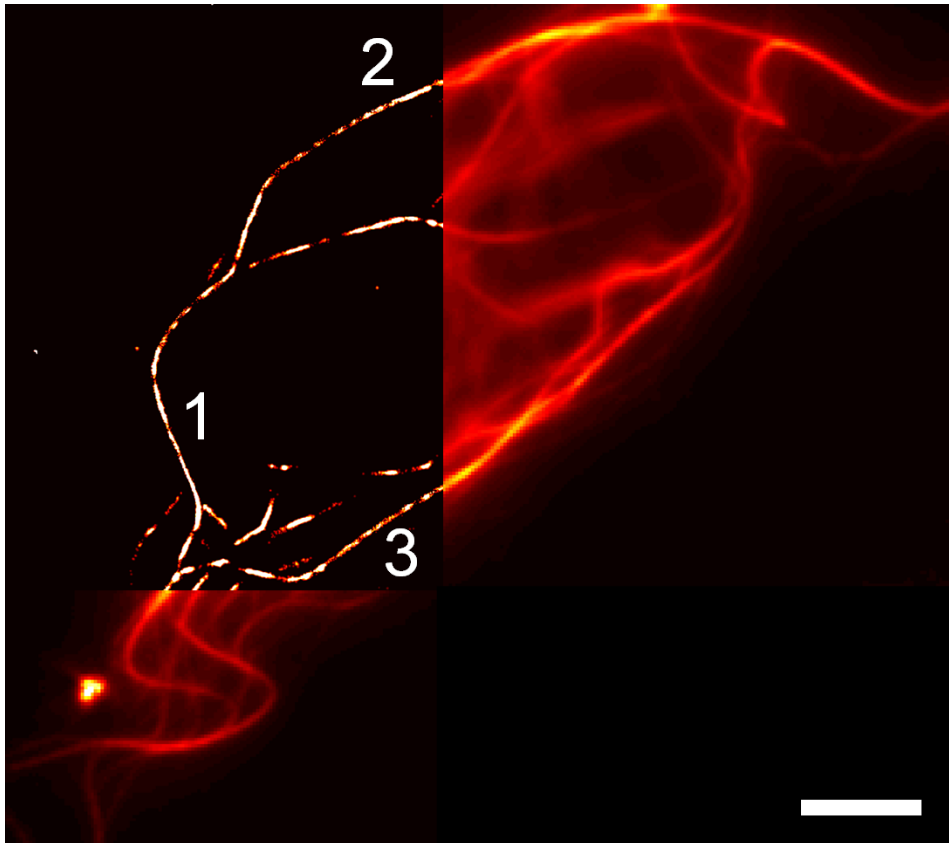


Figure 7.2. Combined superresolution PALM and TIRF image of a living HeLa cell expressing a microtubuli binding psRFP-Rita construct. The width of the microtubuli filaments marked with 1, 2 and 3 are analyzed in detail. Scale bar $5\mu\text{m}$.

theoretical distribution and experimentally determined to 63 nm (1), 52 nm (2) and 50 nm (3) for the microtubuli segments. The experimental values are in very good agreement with the calculated average value.

In previous experiments, the sample was illuminated with low intensities of 473-nm light for the first few hundred frames to ensure a small number of fluorescent molecules in the beginning of the data acquisition. After a few hundred frames, the 473-nm illumination was switched off because the number of molecules in the fluorescent state had decreased to a level that was excellently suited for PALM imaging. After this observation, we tried to image cells, transfected with the actin binding peptide Lifeact, simply by exciting the FPs with 561-nm irradiation (100 W/cm^2). No phototoxic irradiation in the blue/violet (405 nm/473 nm) region was necessary at all for high-resolution imaging (Fig. 7.3). Frames with a dwell time of 100 ms were taken for 275 s and, during the entire acquisition time, the equilibrium between photobleaching of the fluorescent molecules and photoactivation of the non-fluorescent molecules kept the number of molecules in the on-state constant in a range suitable for PALM experiments (Fig. 7.7).

The PALM images of the labeled actin filaments prove that a sufficiently large number of molecules was localized to image the structures with high resolution (Fig. 7.8 a,b).

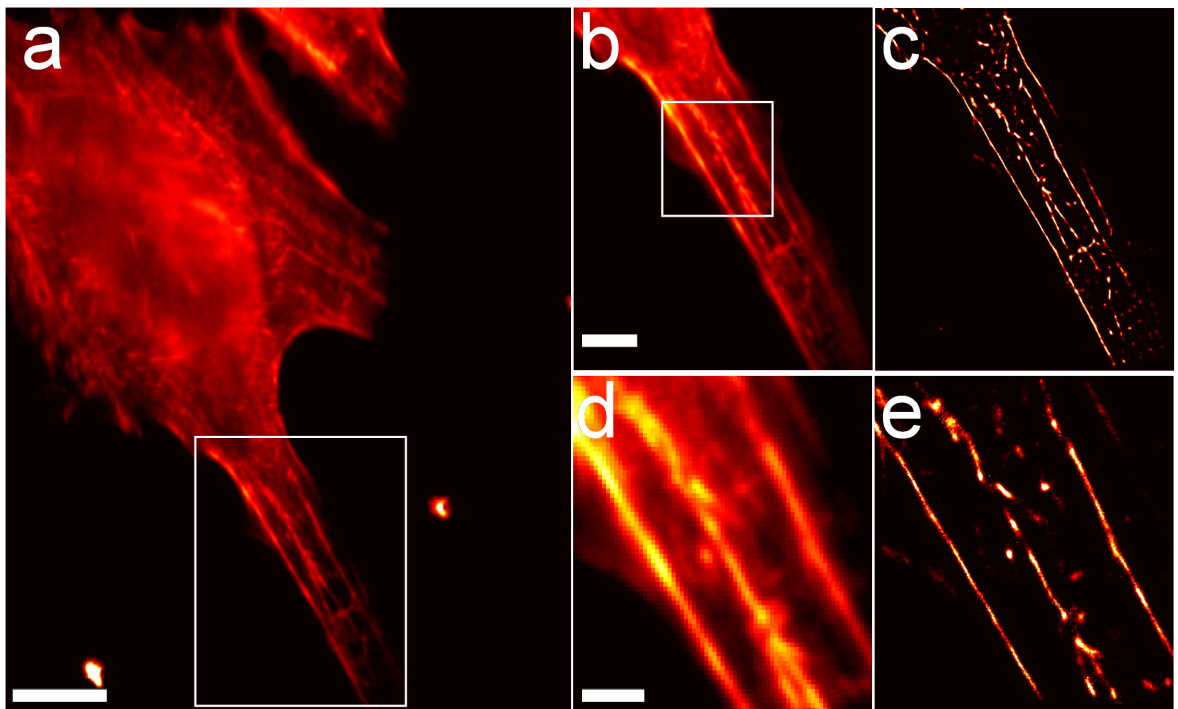


Figure 7.3. Superresolution PALM and TIRF images of a live HeLa cell expressing a psRFP-Lifeact construct. (a) TIRF image of the whole cell with labeled actin stress fibers. (b) Close-up of the white marked region in (a). (c) PALM image of the same region in (a). (d) TIRF image of a close up of three stress fibers. (e) PALM image of the same stress fibers with increased resolution. Scale bar, 10 μm (a), 5 μm (b,c) and 2 μm (d,e).

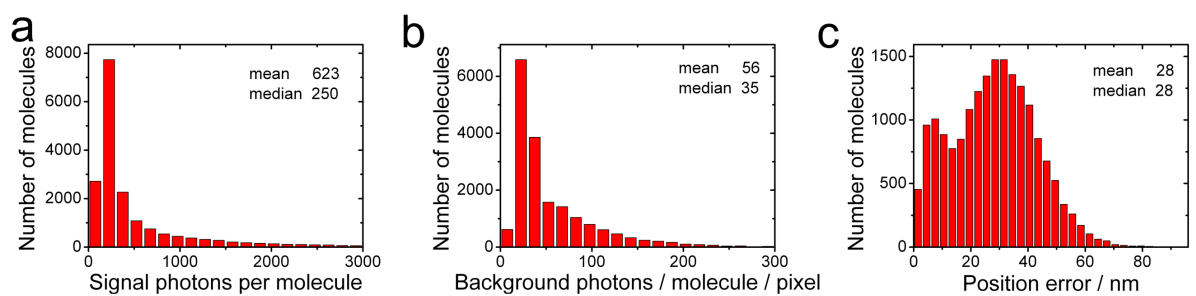


Figure 7.4. Statistics of the PALM analysis of Fig. ??. (a) The distributions of the detected number of photons per psRFP molecule, (b) the number of background photons per molecule and pixel and (c) the 2D position error are given.

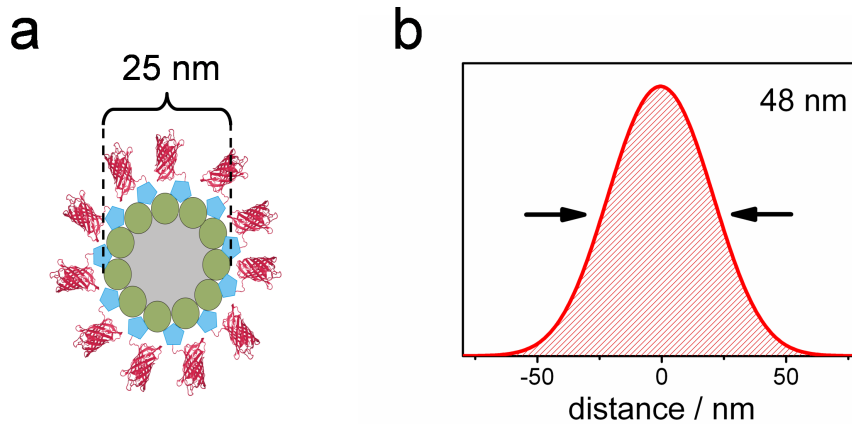


Figure 7.5. Cross section of a microtubule filament cross section. (a) Rita molecules labeled with psRFP bind to the microtubule filament. A width of 5 nm was assumed for the psRFP–Rita construct. Finally, the total diameter of the fiber with the bound labels is about 35 nm. (b) Projection of the psRFP model positions onto a plane perpendicular to the filament and convolution of each possible molecule position with the 1D Gaussian error function yield a broadened marker distribution with a full width at half maximum (FWHM) of 48 nm.

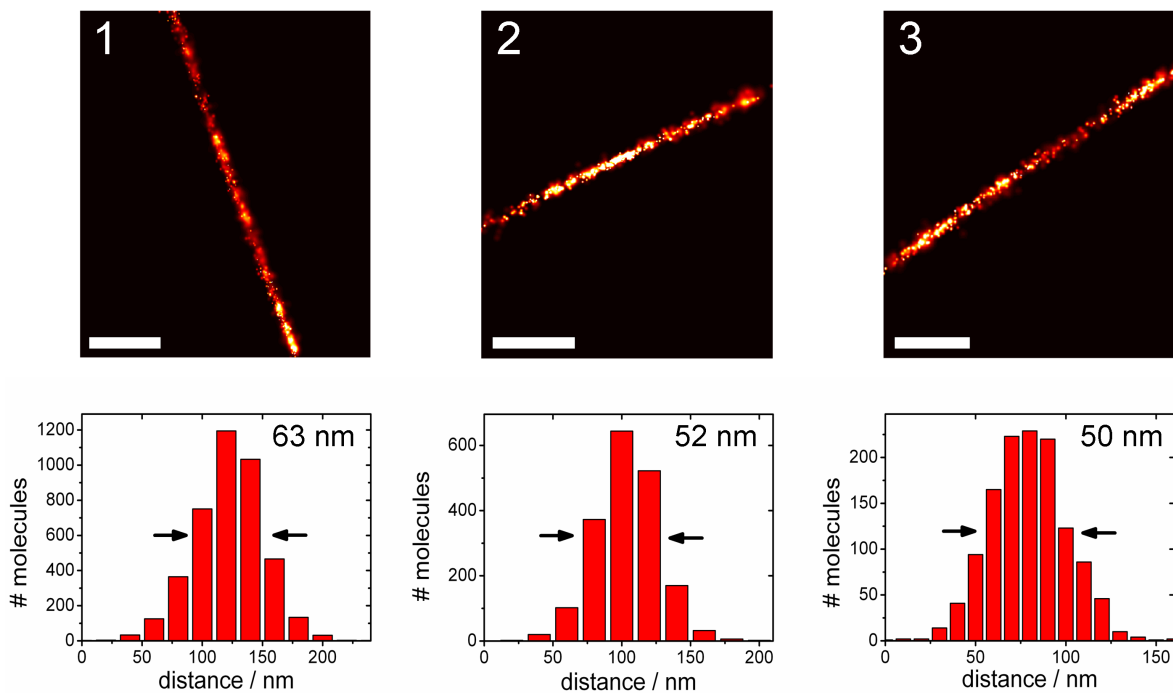


Figure 7.6. Distribution of molecules bound to the three filament segments marked in Fig.7.2. The positions of all detected molecules were projected along the contour line and are given in histograms. The full width at half maximum (FWHM) of the experimentally determined distributions are 63 nm (1), 52 nm (2) and 50 nm (3) for the microtubuli segments. Scale bars 500 nm.

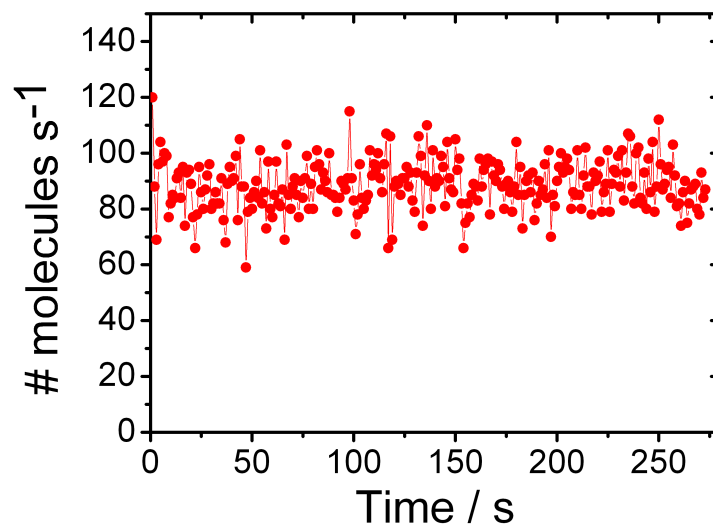


Figure 7.7. The number of molecules detected per second in the cell region given in Fig.7.3d,e is constant for the acquisition time.

The stress fibers close to the cell surface can be seen particularly well due to the TIRF illumination that penetrates only a few hundred nanometers into the cell. The exponentially decaying illumination even gives a crude of the z-position. Brighter regions of the fibers are closer to the surface than the dimmer regions of the fibers, that extend further into the cell. After plotting the molecule position along the contour line in a histogram (Fig. 7.8c), the FWHM of the distribution was determined to be 49 nm.

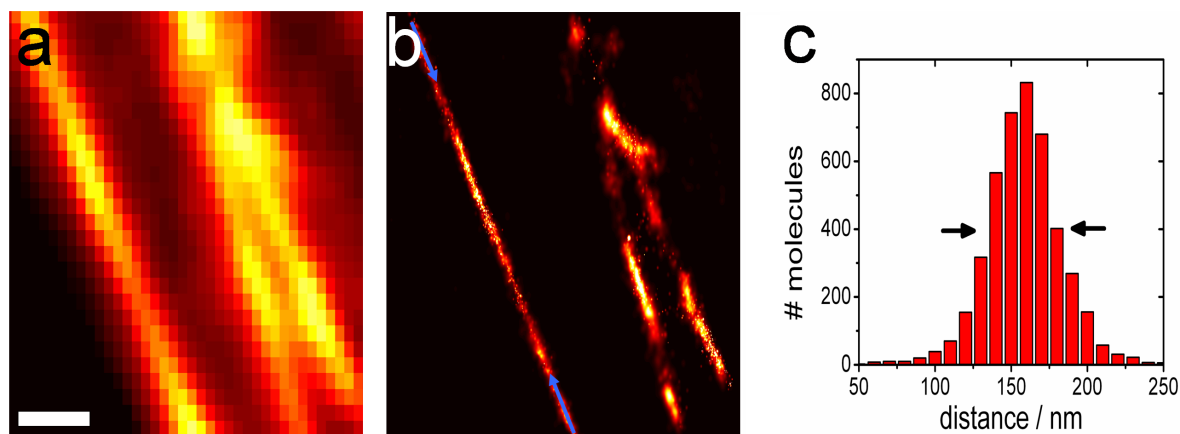


Figure 7.8. PALM image of a stress fiber in a live HeLa cell labeled with the psRFP-Lifeact construct. (a) TIRF image of the stress fiber. (b) PALM image of the same region. The width of the stress fiber segment labeled with two blue arrows is given as a projection along the contour line in (c). The FWHM of the distribution is 49 nm. Scale bar, 1 μm .

7.1.2. mcavRFP

FPs with a high contrast ratio of emitted fluorescence over background are well suited for high localization accuracy in PALM applications. This condition is fulfilled particularly well by FPs that change their emission wavelength under illumination. Excellent results have already been obtained with dimeric d2EosFP⁵⁶ and pseudo-monomeric tdEosFP³⁴. However, true monomeric FPs are preferred to minimize the influence of the marker on the studied protein. With mEos2, a promising monomeric photoconverter was developed, but it still shows some dimerization tendency at low protein concentrations⁵⁷. We have studied mcavRFP, a monomeric photoconvertible FP that could be a potential alternative. The evaluation of Lifeact and Rita fusions with mcavRFP showed promising results. Both fusions displayed excellent localization along the cytoskeletal fibers (Fig. 7.9, 7.11) due to the monomeric nature of the protein. PALM images were recorded with 561-nm excitation (100-125 W/cm²) and weak 405-nm irradiation (0.1 W/cm²) for constant photoconversion and a dwell time of 100 ms per frame. Actin filaments that are 500 nm apart are almost undistinguishable in the TIRF recording but the two filaments can easily be resolved in the PALM image (Fig. 7.10). The increased resolution also becomes apparent for cells transfected with a mcavRFP-Rita fusion construct. The FWHM of a single labeled microtubule fiber could be determined to be 64 nm, in good agreement with the localization error of 35 nm (mean), 32 nm (median) calculated from 686 (mean), 349 (median) detected photons per molecule and the background in the sample of 120 (median), 87 (mean) photons per molecule and pixel.

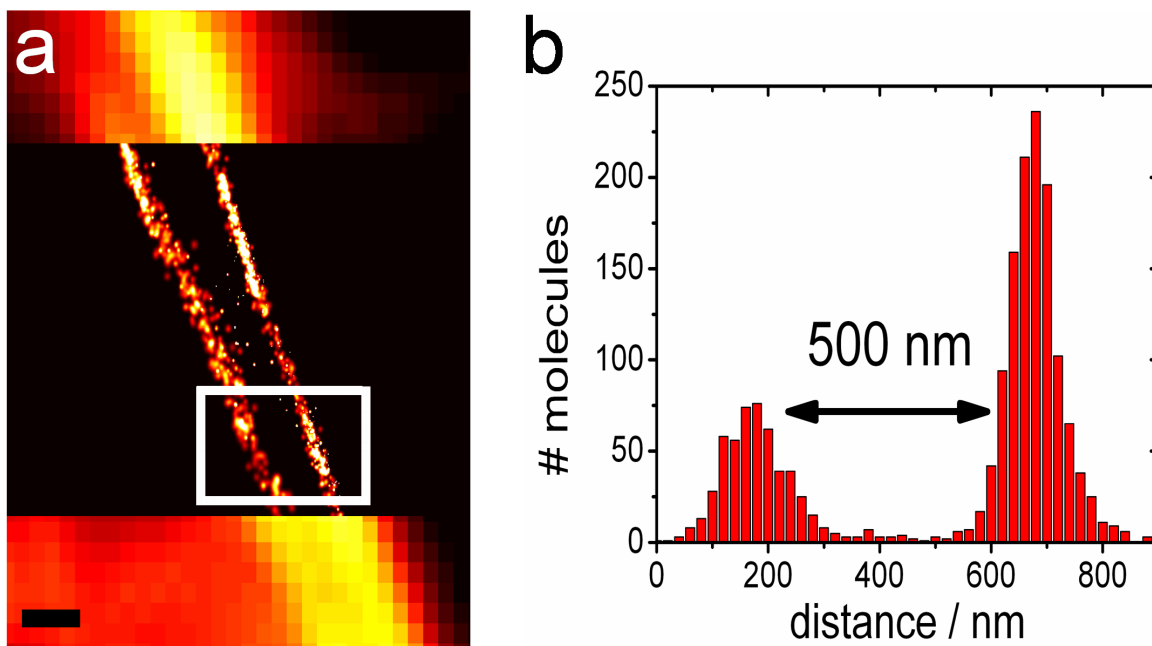


Figure 7.10. (a) Combined TIRF and PALM (middle) image of two actin fibers in Fig.7.9.(b)The distribution of mcavRFP molecules along the stress fibers in the white frame is given as a projection along the contour lines. Scale bar, 500 nm.

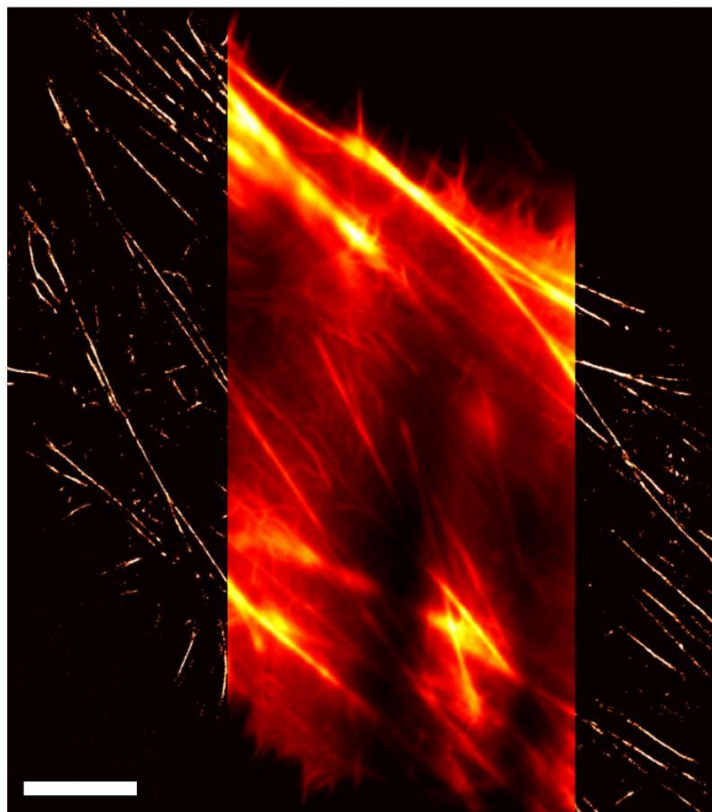


Figure 7.9. Combined superresolution and TIRF(middle) image of a live HeLa cell expressing a mcavRFP-Lifeact construct. Scale bar, 10 μm .

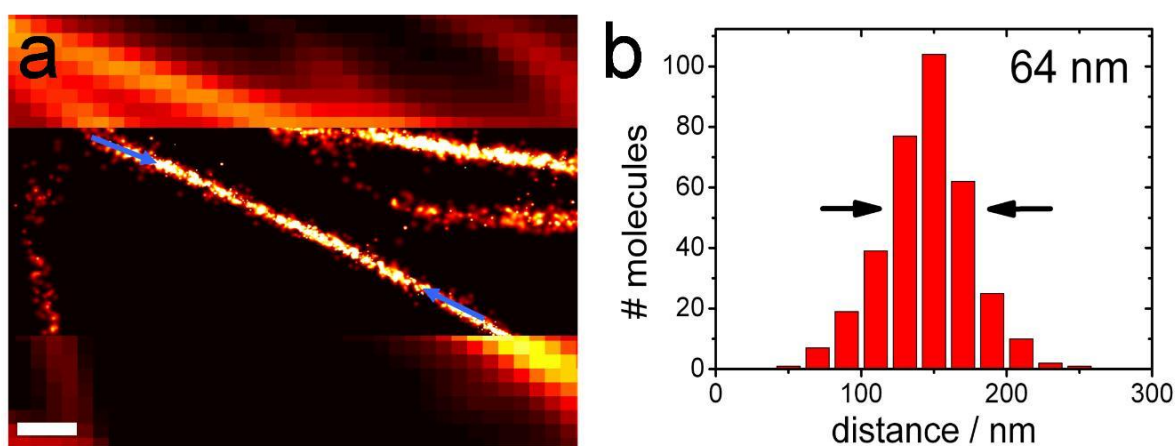


Figure 7.12. (a) Combined TIRF and PALM (middle) image of microtubules in Fig.7.11. (b) The distribution of mcavRFP molecules along the cytoskeletal fiber segment marked with blue arrows is given as a projection along the contour line. The FWHM of the fiber was estimated as 64 nm. Scale bar, 500 nm.

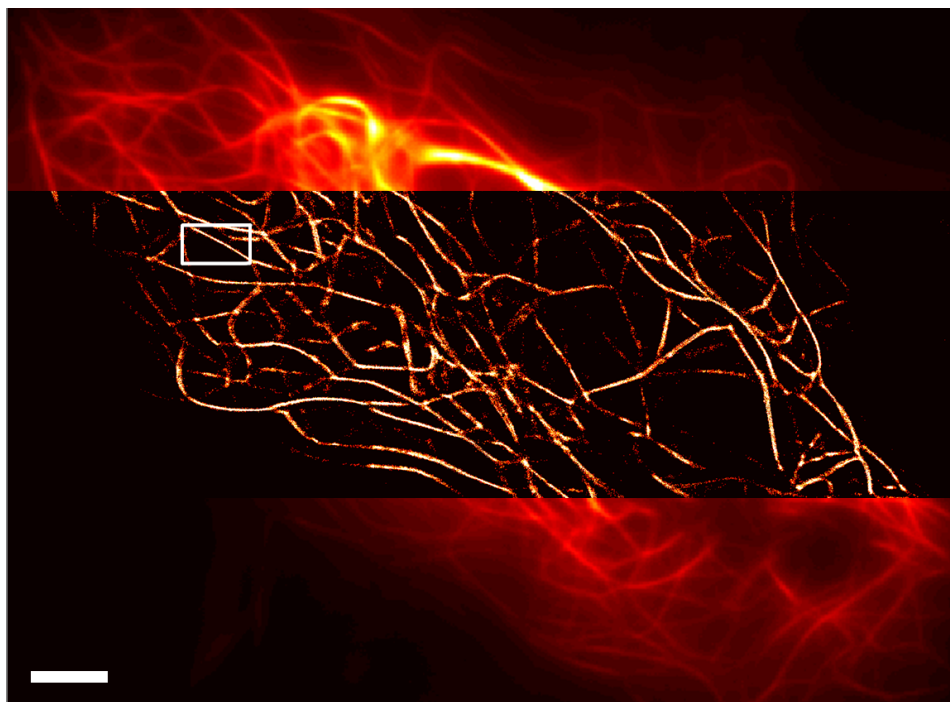


Figure 7.11. Combined TIRF and PALM (middle) image of a live HeLa cell expressing a mcavRFP-Rita construct. Scale bar, 5 μm .

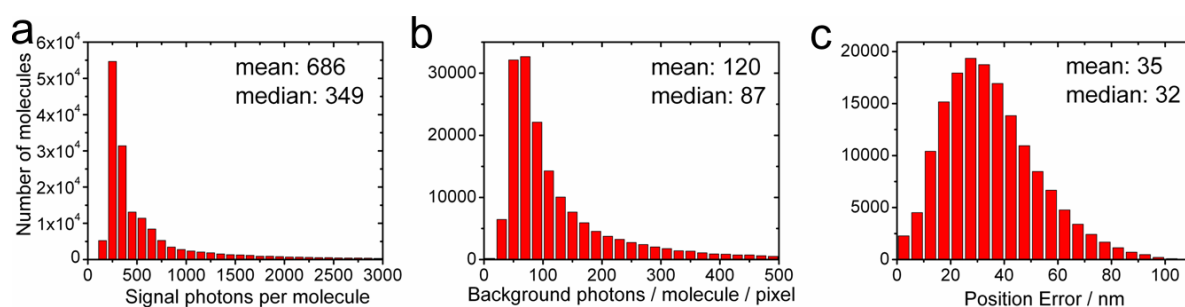


Figure 7.13. Statistics of the PALM image in Fig. 7.11. (a) The number of emitted photons per molecule, (b) the number of background photons per molecule and pixel and (c) the 2D position error are given.

7.1.3. mRubyN143C

The bright red fluorescent FP mRuby has been successfully used in conventional microscopy⁷⁰. An improved variant of mRuby with the asparagine at position 143 replaced by a cysteine (N143C) displayed slow bleaching kinetics similar to psRFP. This observation motivated us to investigate the application of mRuby(N143C) in high resolution microscopy. Although this FP showed no sign of photoswitching under 450-nm illumination, it turned out that mRuby(N143C) is well suited for PALM. The absorption of mRuby(N143C) displays a shoulder that is not visible in the excitation spectrum (Fig. 2.8). It is assumed that this shoulder represents a non-fluorescent chromophore confor-

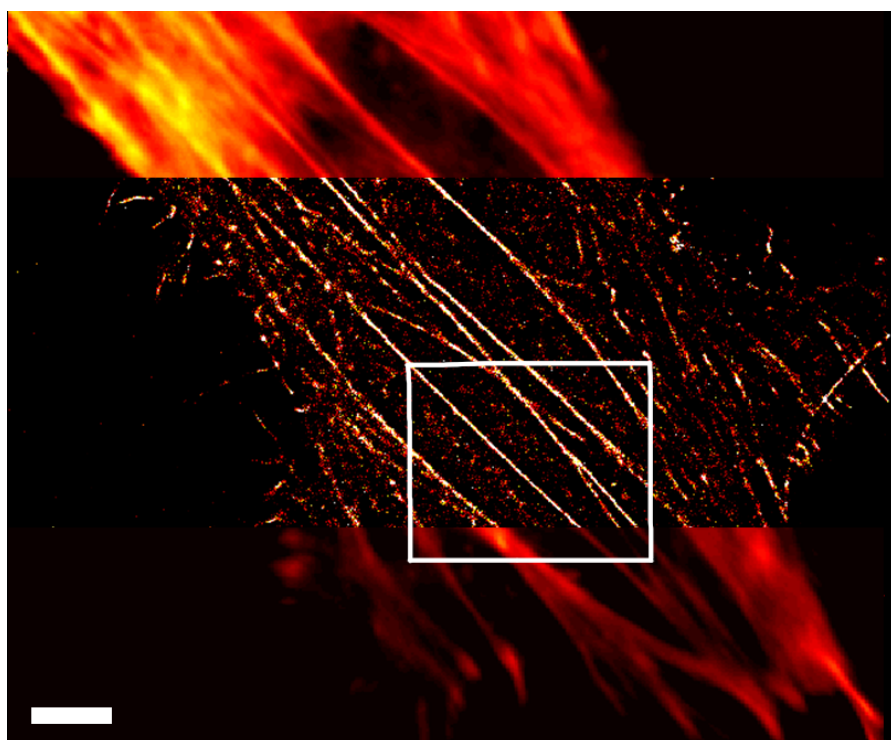


Figure 7.14. Combined TIRF and PALM (middle) image of actin stress fibers in a live HeLa cell expressing the mRuby(N143C)-Lifeact construct. Scale bar, 5 μm .

mation that can be successively activated to the fluorescent state, similar to psRFP. The properly chosen excitation/activation intensity, allows the detection of separate signals from single molecules. However, a detailed understanding of exact mechanism requires further inspection. Nevertheless, under 561-nm (250 W cm^{-2}) illumination and with 50 ms acquisition time per frame single molecules were registered and actin stress fibers labeled with a Ruby-Lifeact construct could be imaged with a PALM resolution comparable to state of the art FPs after a short time of pre-bleaching (Fig. 7.14, 7.15). Equally good results were observed for mRuby fused to Rita. The microtubule network was efficiently labeled, and images could be obtained with high resolution (Fig. 7.16). The FWHM of a single microtubule fiber was determined as 60 nm. From the single molecule information, the 2D position error was calculated to be 29 nm (mean) and 27 nm (median) from 610 (mean) and 312 (median) signal photons per molecule and 102 nm (mean) and 72 (median) background photons per molecule and pixel. Presumably high resolution imaging of mRuby(N143C) in cells is effected by a large fraction of dark molecules that are slowly activated during the imaging process. The exact underlying molecular processes require further inspection.

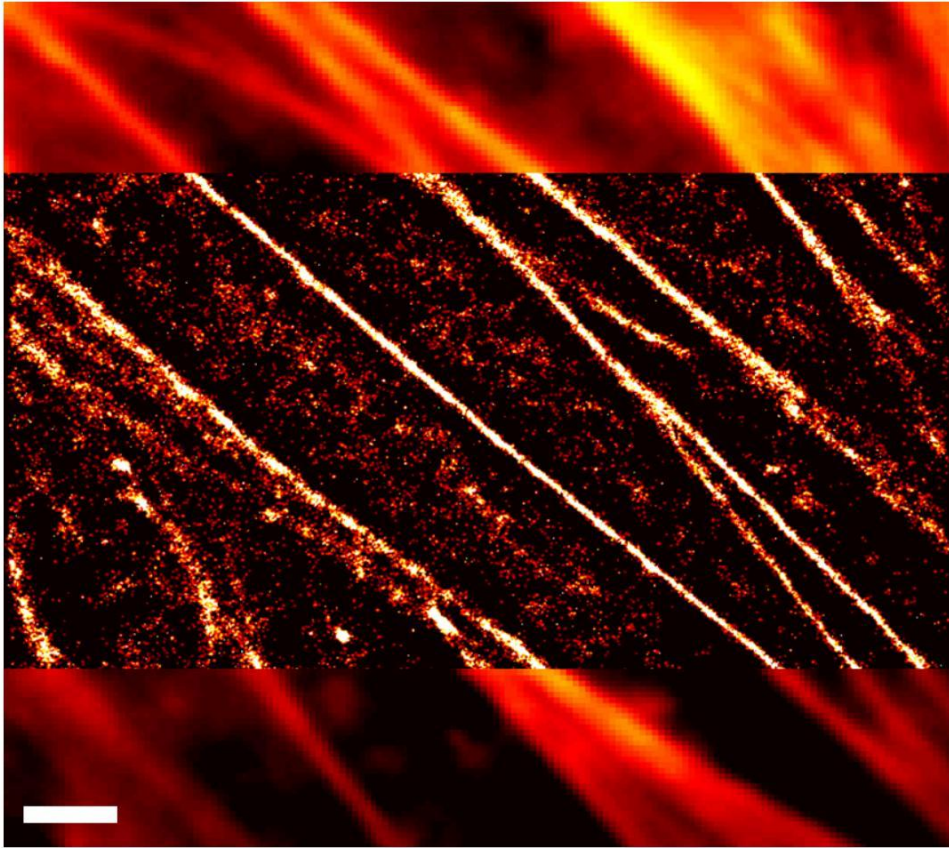


Figure 7.15. Combined TIRF and PALM (middle) image of actin stress fibers. Close-up of the region marked with a white frame in Fig.7.14. Scale bar, 2 μm .

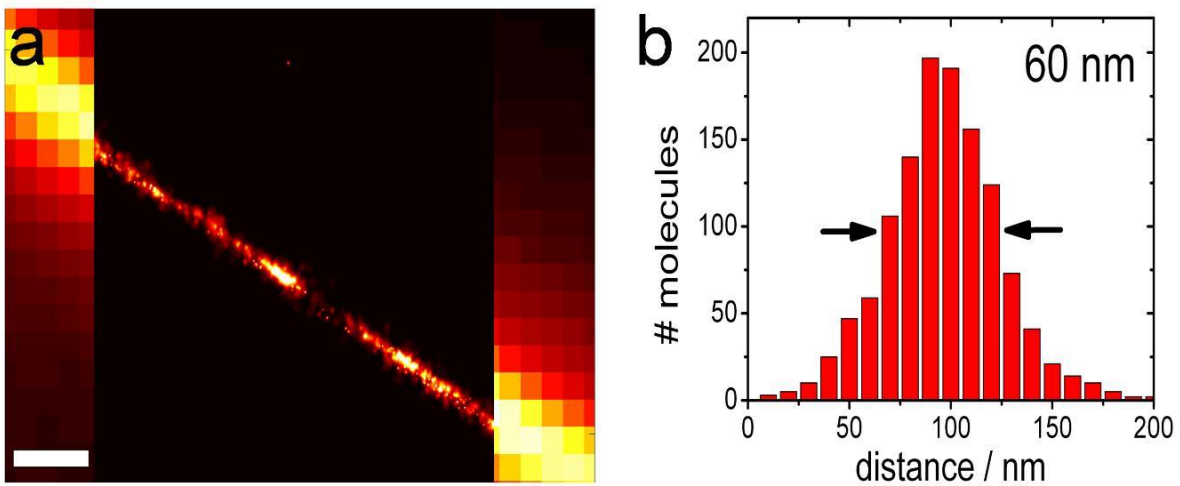


Figure 7.18. Combined TIRF and PALM (middle) image of microtubuli in Fig. 7.16.(b) The distribution of mRuby(N143C) molecules along the cytoskeletal fiber segment in (a) is given as a projection along the contour line. The width of the fiber was estimated to 60 nm. Scale bar, 500 nm.

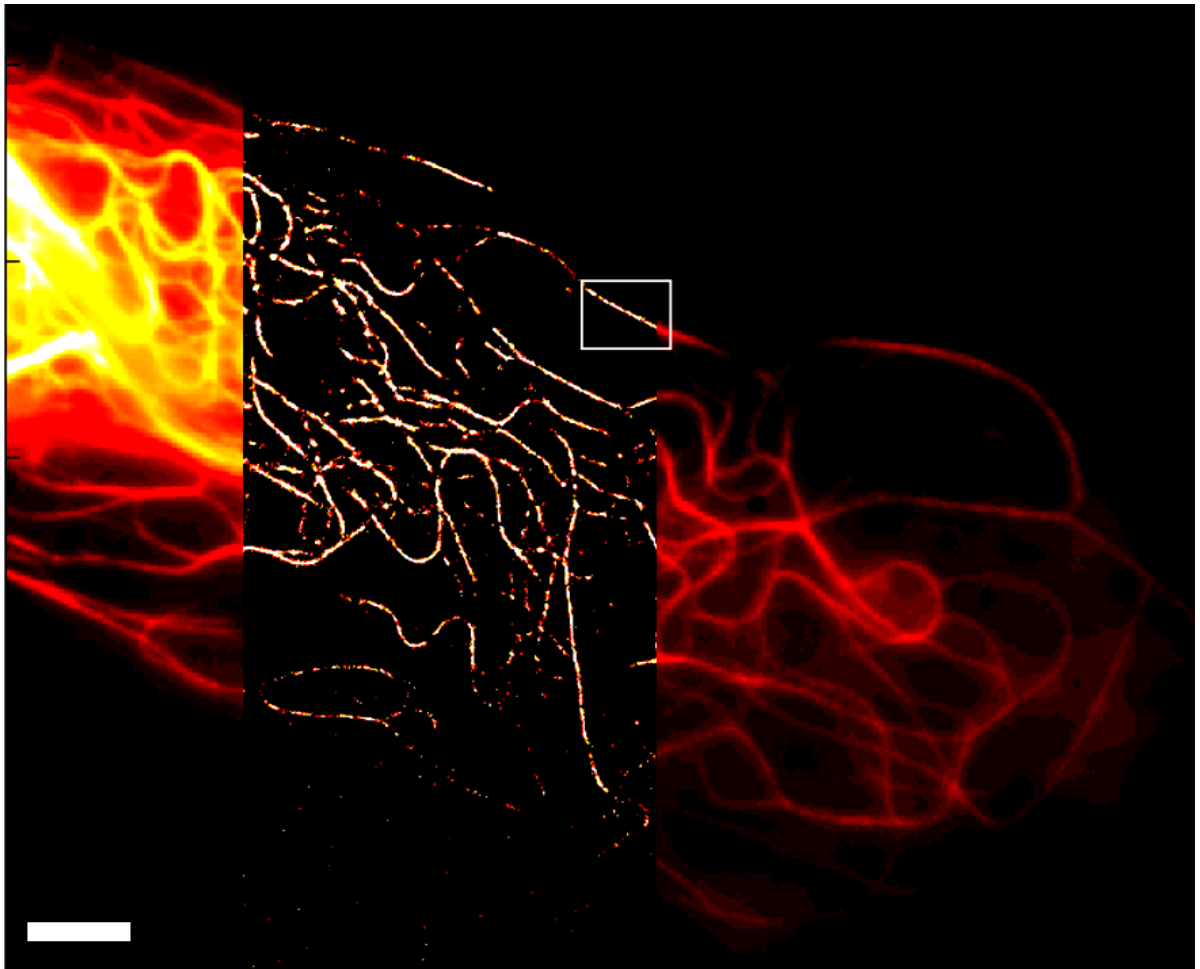


Figure 7.16. Combined TIRF and PALM (middle) image of microtubules in a live HeLa cell expressing the mRuby(N143C)-Rita construct. Scale bar 5 μm .

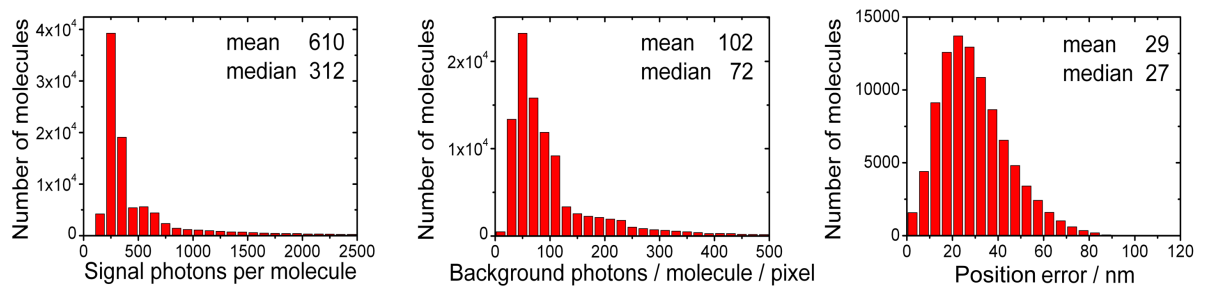


Figure 7.17. Statistics of the PALM image in Fig. 7.16. The number of emitted photons per molecule, the number of background photons per molecule and pixel and the 2D position error are given.

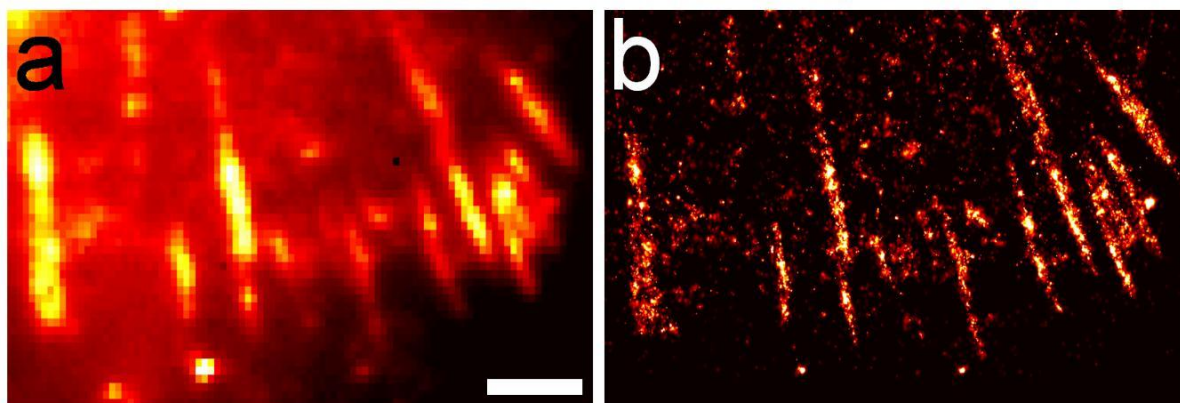


Figure 7.19. TIRF image (a) and PALM image (b) of focal adhesions in a fixed HeLa cell expressing the d2Eos-paxillin construct.

7.1.4. d2EosFP

We also briefly characterized d2EosFP, a dimeric variant of EosFP, which we later used to analyze the performance of our livePALM imaging software. In a paxillin fusion (Fig. 7.19), the FPs display high brightness; 492 (mean), 256 (median) signal photons per molecule and low background 48 photons (mean) and 30 (median) due to the green-to-red conversion were detected in fixed cells (Fig. 7.20), resulting in an excellent localization with a 2D position error of only 21 nm (mean) and 19 nm (median) under 561-nm illumination (340 W cm^{-2}) and 100 ms dwell time per frame. Green-to-red photoconversion was accomplished with 405-nm irradiation ($0.05 - 500 \text{ mW cm}^{-2}$).

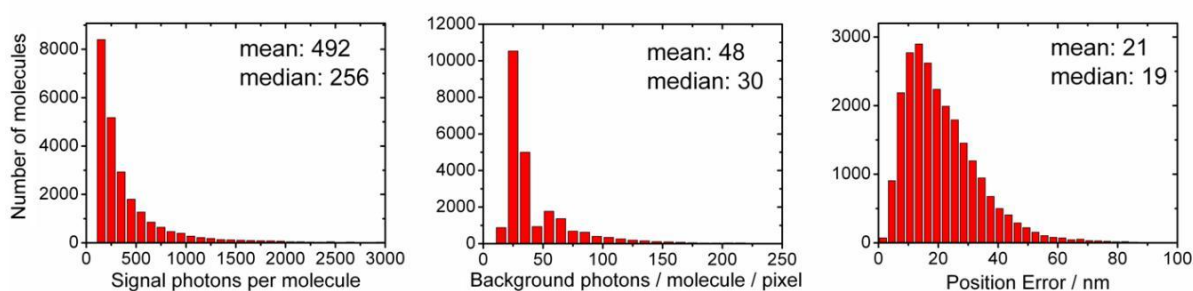


Figure 7.20. Statistics of the PALM image in Fig. 7.19. The number of emitted photons per molecule, the number of background photons per molecule and pixel and the 2D position error are given.

7.1.5. IrisFP PALM

mIrisFP adds a new dimension to PALM microscopy with its multiple photoswitching modes that offer new experimental schemes and more flexibility. In cells with a high autofluorescent background in the green spectral range, mIrisFP can simply be switched to its red form and imaged with lower background and scattering light. Furthermore,

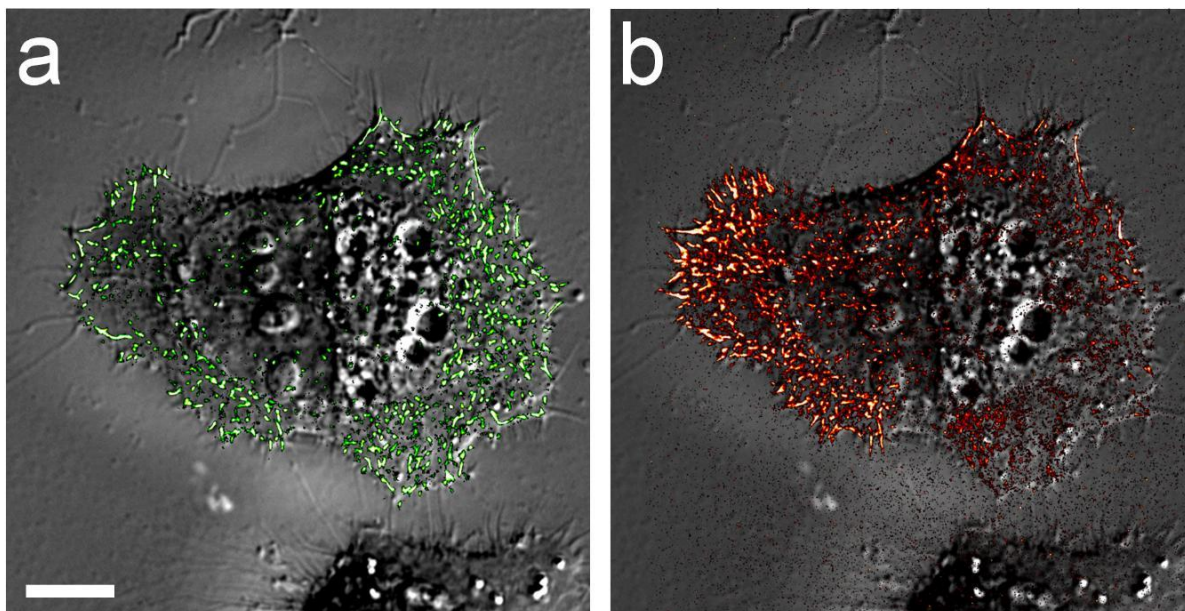


Figure 7.21. Overlay of a differential interference contrast (DIC) image with (a) a PALM image obtained with the green form of mIrisFP and (b) after photoconversion with the red form of mIrisFP. PALM images were recorded by on- and off-switching of mIrisFP in its the green and red forms, respectively.

the green-red photoconverter mIrisFP can be combined with either green or red photoswitchable FPs for two-color high-resolution experiments. We tested mIrisFP for the first time as a cellular marker and verified the correct localization of α -actinin labeled with mIrisFP before and after photoconversion by overlaying a PALM image with a differential interference contrast (DIC) image of the same cell (Fig. 7.21). The α -actinin molecules are located in the focal adhesions and the peripheral belt of the cell, as expected. We also showed that mIrisFP can be successfully photoconverted in living cells without disruption of cellular processes by illuminating the left part of the cell with 405-nm light, thereby inducing the green to red photoconversion. During data acquisition for the PALM image, red molecules had already migrated into the right half of the cell and were integrated into existing focal adhesions, proving that the cellular machinery was still intact. The DIC image demonstrated that the illumination did not cause the cell to retract (Fig. 7.21b). Next, the ability to produce high resolution images with both, the green and the red form of mIrisFP was demonstrated by imaging actin stress fibers in living HeLa cells (Fig. 7.22). The actin filaments were labeled with a mIrisFP-Lifeact fusion construct. A PALM image of the green form of mIrisFP was first taken with 473-nm excitation (20 W cm^{-2}). Subsequently, the complete sample was irradiated with 405-nm light (50 W cm^{-2}) for 30 s to achieve a complete green-to-red conversion of the mIrisFP molecules. Finally, the red form was imaged with 561-nm excitation (200 W cm^{-2}) and 473-nm light (30 mW cm^{-2}) for on-switching. A detailed inspection of the images revealed excellent resolution for PALM images in both spectral ranges (Fig. 7.23). Histograms of the distribution of green and red molecules around the

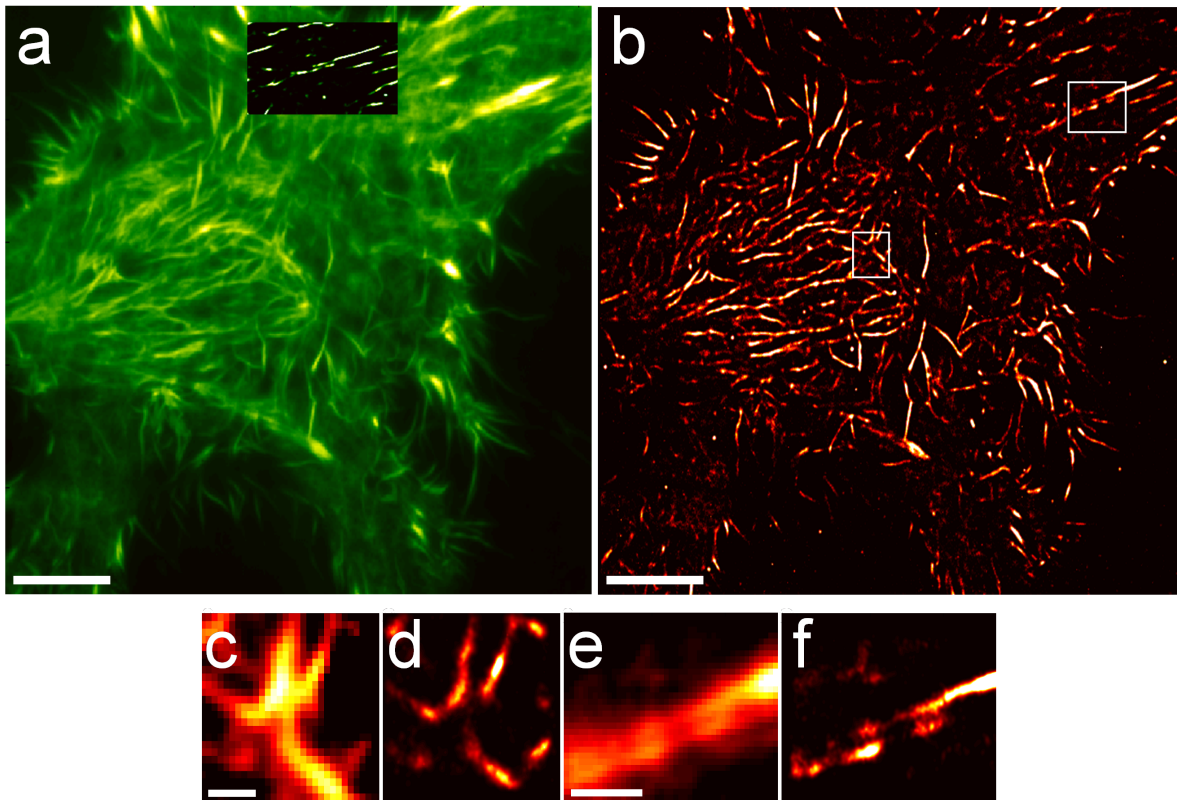


Figure 7.22. HeLa cells were transiently transfected with a Lifeact-mIrisFP construct. The red form of mIrisFP was generated by 405-nm laser irradiation. (a) TIRFM and (inset) PALM overlay images imaged with the green form of mIrisFP. (b) PALM image of the same cell, imaged with the red form of mIrisFP after photoconversion. Expanded views of the regions marked by the white frames in panel (b) are shown as ((c) and (e)) TIRF microscopy images and ((d) and (f)) PALM images. Scale bar, 10 μm (a,b), 1 μm (c-f).

contour line of the stress fiber demonstrate a slightly narrower distribution for the green molecules (69 nm) than for the photoconverted red molecules (82 nm) (Fig. 7.23b,c). 2D error histograms for a paxillin-mIrisFP fusion construct show that the green form of mIrisFP can be localized with an error of 48 nm (mean), 47 nm (median), and the red form with 41 nm (mean), 40 nm (median) in living cells (Fig. 7.24). The higher localization precision for the red fluorophores is determined by the higher number of collected photons, 354 photons (mean), 217 photons (median) compared to 176 photons (mean), 111 photons (median) from the green fluorophores. The background photons per molecule and pixel were, however, lower for green emitting molecules, 18 photons (mean), 13 photons (median), than for the red emitting molecules, 60 photons (mean), 44 photons (median). We performed PALM imaging of HeLa cells expressing a paxillin-mIrisFP construct to ensure that mIrisFP can be used as a fluorescent marker in living human cancer cells. The red form of mIrisFP was generated by 405-nm laser irradiation for 30 s (50 W cm^{-2}) prior to image acquisition with 561-nm (200 W cm^{-2}) and 473-nm

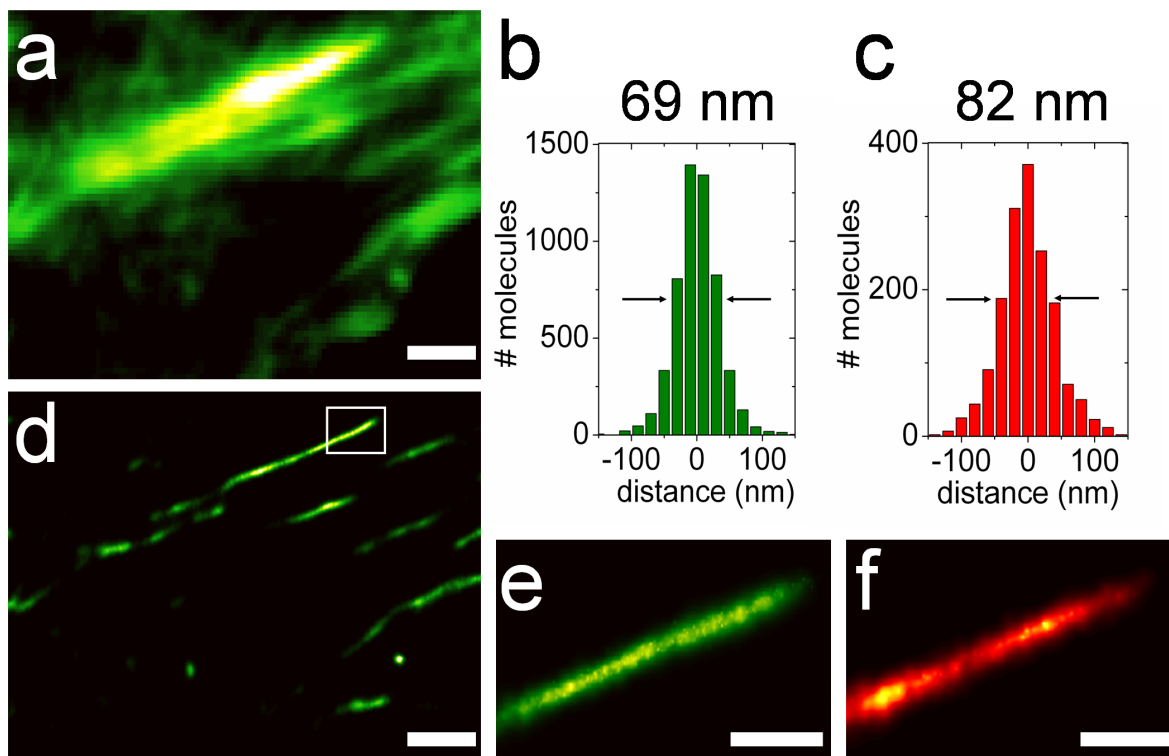


Figure 7.23. Comparison of the same actin fiber labeled with the green and the red form of mIrisFP. (a) TIRFM and (d) PALM images of green mIrisFP. (b,c) Histograms of the distributions of green and red fluorophores around the contour line of the stress fiber depicted in (e) and (f), respectively. Panels (e) and (f) show an expanded view of the region marked by the white frame in panel (d). Scale bar, $2 \mu\text{m}$ (panels a,d), 500 nm (panels e,f).

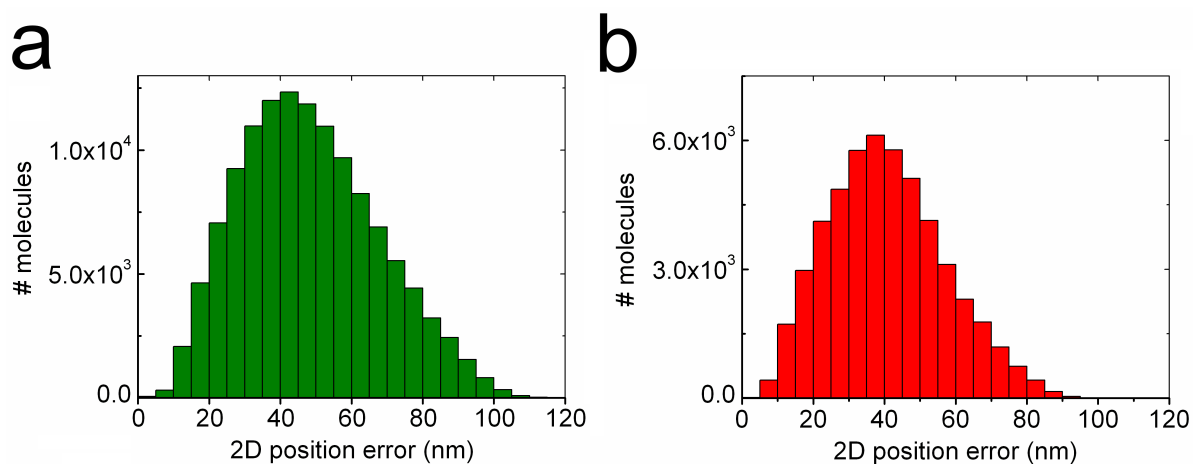


Figure 7.24. (a) Two-dimensional localization error histograms of the green form and (b) the red form of mIrisFP fused to paxillin. Obviously, the precision can be further increased by selecting only molecules with the desired localization precision.

7.1. Evaluation of Fluorescent Proteins as PALM Markers

(30 mW cm^{-2}) laser light. 12,000 camera frames were collected with a dwell time of 50 ms. Neither expression of the construct nor switching or photoconversion was negatively influenced at 37°C . On the contrary, the increased temperature was even beneficial for high resolution imaging because thermal recovery was found to fully replace the light activation process with 473-nm illumination (Fig. 7.25).

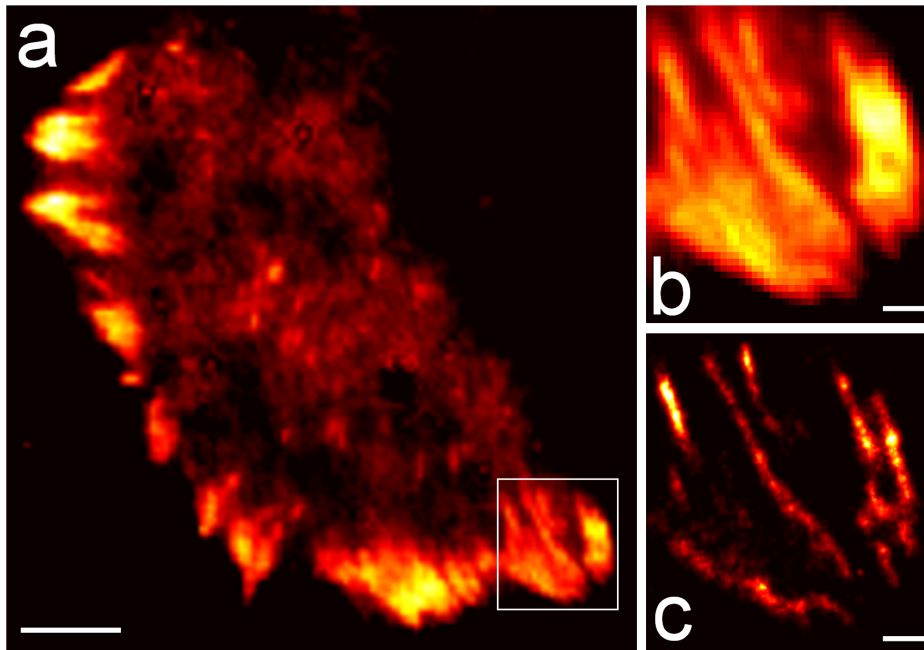


Figure 7.25. HeLa cells were transfected with a paxillin-mIrisFP construct. The red form of mIrisFP was generated by 405-nm laser irradiation. (a) TIRFM image. Expanded view of the region marked by the white frame in panel (a) is shown as (b) TIRFM and (c) PALM image. Scale bar, $5 \mu\text{m}$ (panel a), $1 \mu\text{m}$ (panels b and c).

7.2. Imaging Protein Movements with Superresolution

Due to its unique properties, mIrisFP offers the outstanding possibility of imaging protein localization, trafficking and redistribution with high resolution. This can provide valuable information about protein activation, function and biochemical signaling. In so-called pulse-chase experiments, a subpopulation of photoconvertible/photoswitchable FPs are converted or switched and this subpopulation is monitored over time. This technique offers an elegant way for the visualizing protein movement in a cellular environment. The photoconversion/photoswitching is also exploited to obtain high resolution images. With known photoconvertible/photoswitchable markers, one had the choice to either gain information about cellular dynamics or obtain a superresolution image. In many cases, it is desirable to have both high-resolution structural information combined with knowledge about dynamic changes within living cells. Only the multiple light-induced transitions found in IrisFP permit the combination of pulse-chase experiments with superresolution imaging.

To demonstrate this new method, high resolution dynamic data were acquired. First, a PALM image of the cell was taken with the green form of mIrisFP under 473-nm illumination for both excitation and off-switching (Fig. 7.26 a). The light intensity was adjusted such that only a few molecules, which had thermally reverted to their fluorescent state, were detected in each frame. To increase the number of molecules in the fluorescent state, the activation process can be enhanced by weak 405-nm irradiation. However, this was found to be unnecessary in most cases. After acquisition of several thousand frames, a green PALM image was constructed. This green PALM image gives a high resolution overview of the cellular structures. Up to this point, only green mIrisFP molecules were present in the sample because the 405-nm illumination intensity, used for photoactivation, is too weak for noticeable photoconversion. mIris molecules were then photoconverted from green to red in a selected region of the cell by short, intense 405-nm irradiation (Fig. 7.26 b). Directly after photoconversion, mIrisFP molecules with a red emitting chromophore were registered under 561-nm excitation. The fraction of molecules in the fluorescent state was adjusted with weak 473-nm irradiation. Molecules that were originally located in the conversion region spread out due to dynamic processes in the cell and can be imaged with high resolution (Fig. 7.26 c,d). The information in this experiment is obtained by imaging the distribution of the entire photoconverted population and not from tracking single molecules over time. Finally, data for another green PALM image were recorded to give an overview of the green population.

The new capability presented by mIrisFP was demonstrated with an α -actinin-mIris fusion construct in live HeLa cells. Comparison of the green TIRF and PALM images illustrates the resolution enhancement (Fig. 7.26 e,f,g,h). In the following step, mIris molecules in the region marked by the purple frame were green-to-red photoconverted (Fig. 7.26 g) and, directly after photoconversion, the red molecules were registered for 37.5 s. A red PALM image was reconstructed that showed most of the proteins in the conversion region. Only a few molecules migrated in the cell during photoconversion and data acquisition (Fig. 7.26 i). A second red PALM image acquired during a later time interval (100–300 s) displays the new distribution of photoconverted molecules over the

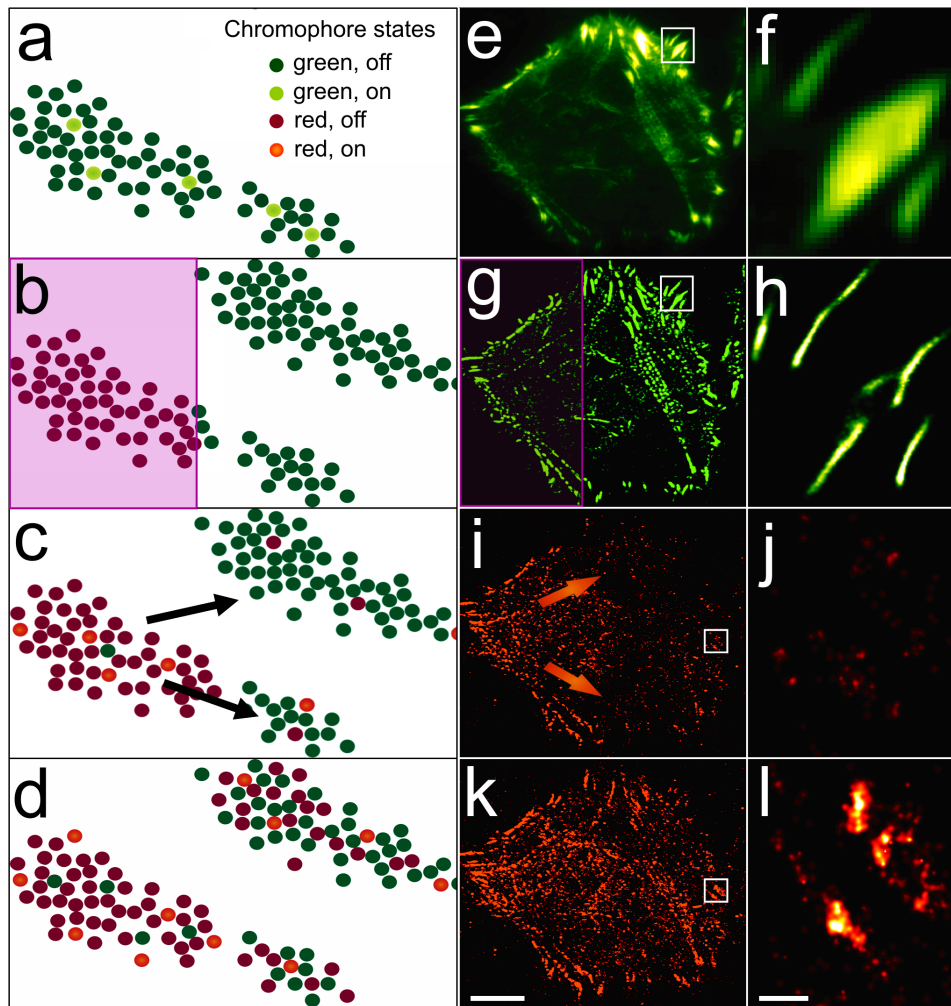


Figure 7.26. Super-resolution imaging of protein movements in a live HeLa cell expressing an α -actinin-mlrisFP fusion protein. (a–d) Schematic of the experiment; (a) a PALM image is acquired using off-on switching of mlrisFP molecules with green chromophores. (b) A subpopulation of mlrisFP molecules in a select region of the cell (marked in violet) are tagged by photoconversion to the red form and (c) migrate to other parts of the cell. (d) Their relocation can be observed with superresolution and as a function of time by acquiring PALM images using off-on switching of mlrisFP molecules with red chromophores. (e) TIRF image of the entire cell and (f) close-up, and the corresponding (g) PALM image and (h) close-up, taken by monitoring fluorescence from green mlrisFP molecules. The violet frame in panel (g) marks the region that was irradiated with 405-nm laser light to induce green-to-red photoconversion of mlrisFP. (i–l) PALM images taken by detecting red-converted mlrisFP, (i) entire cell and (j) close-up, covering the interval 0–37.5 s after the end of photoconversion, and (k) the corresponding image and (l) close-up for the interval 100–300 s. All close-ups are marked by white frames in the full-size images. Scale bar, 10 μm (e, g, i, k), 1 μm (f, h, j, l).

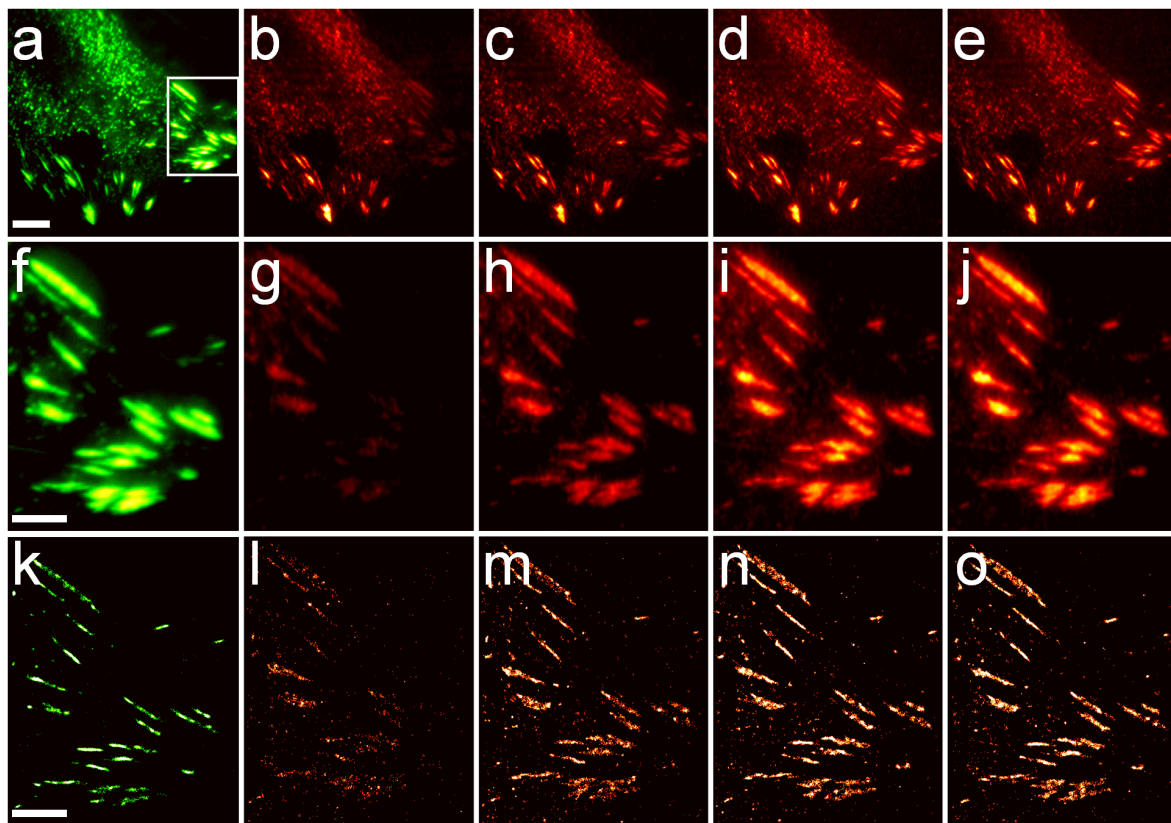


Figure 7.27. Super-resolution imaging of protein movements in a live HeLa cell expressing an α -actinin-mIrisFP(K145I) fusion protein. TIRF images of the green form (a), the photoconverted red form directly after photoconversion (b), 10 min (c), 20 min (d), 30 min (e) after photoconversion. (g–j) Close-up TIRF images of the region marked by a white frame in (a) and the corresponding PALM images (k–o). Scale bar, 10 μm (a), 5 μm (f,k).

entire cell (Fig. 7.26 j). This redistribution of molecules showed that α -actinin molecules are recycled during formation and disintegration of actin-based structures in the cell. It can also be seen that structures which appeared to be static are actually in a dynamic equilibrium.

First, experiments were carried out with a dimeric variant of IrisFP(K145I) fused to paxillin. Paxillin plays a key role in cell adhesion and is permanently redistributed in living cells. A green TIRF (Fig. 7.27 a,f) and PALM (Fig. 7.27 k) image of the cell were acquired with 473-nm (50 W cm^{-2}) illumination and weak 405-nm activation ($50\text{--}500 \mu\text{W cm}^{-2}$) for 5,000 frames of 30 ms. After photoconversion of the left part of the cell with strong 405-nm irradiation (20 W cm^{-2}) for 45 s, high resolution images of the cell with 561-nm excitation (160 W cm^{-2}) and 473-nm activation light (10 mW cm^{-2}) were collected. Four TIRF (Fig. 7.27 g–j) and PALM (Fig. 7.27 l–o) images from 2,000 frames of 50 ms each were constructed directly after photoconversion and at time intervals of 10 min, 20 min and 30 min after photoconversion. The integration of photoconverted

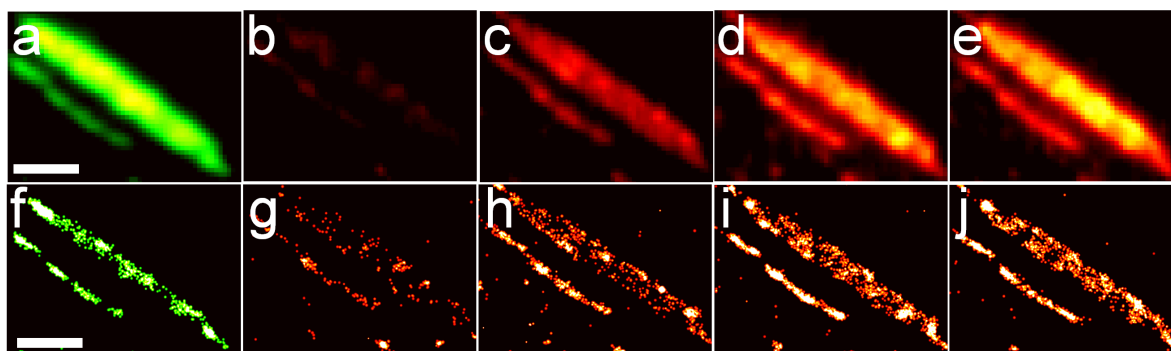


Figure 7.28. Super-resolution imaging of two focal adhesions in a live HeLa cell expressing an α -actinin-mIrisFP(K145I) fusion protein. TIRF images of the green form (a), the photoconverted red form direct after photoconversion (b), 10 min (c), 20 min (d), 30 min (e) after photoconversion and the corresponding PALM images with enhanced resolution (g-j). Scale bar, 2 μ m (a,f)

paxillin into existing and newly forming adhesion contacts in the focal adhesion-rich region marked by the white frame in figure 7.27 can be observed over time with high resolution (Fig. 7.28).

For a detailed study of focal adhesion dynamics in live HeLa cells, an advanced monomeric mIrisFP fusion was developed by Susan Gayda. It is noteworthy to mention that the continuous assembly and disassembly of focal adhesions during cell migration occurs on the time scale of a few hundred seconds, is sufficiently slow to be observed in a series of PALM images without critical image blurring. Again, data were collected for a green PALM image of the whole HeLa cell transfected with paxillin-mIrisFP. The green TIRF (Fig. 7.29 a) and PALM (Fig. 7.29 b) images display the typical distribution of paxillin in focal adhesion complexes, but only the PALM images reveal the fine adhesion complex substructures (Fig. 7.29 d,f) that cannot be seen in the conventionally acquired images (Fig. 7.29 c,e). FP molecules indicated in the blue frame in Fig. 7.29a were green-to-red converted with intense 405-nm laser illumination for 30 s, followed by PALM data acquisition of the red molecules for 600 s. The 12,000 collected frames were binned into 8 images, each covering 75-s intervals. The exchange of paxillin molecules between the conversion region and other cell areas is illustrated as an image series (Fig. 7.30). In the first image (0-75 s, Fig. 7.30a), most paxillin molecules still remain in the conversion region, only a few molecules have migrated to the neighboring cell areas. A further distribution of the red molecules was observed during the following 150 s until an almost even distribution in the cell is reached (Fig. 7.30 b,c). Later, paxillin molecules concentrated in focal adhesions at the lower right edge of the cell (Fig. 7.30 d). A detailed analysis of the two regions marked by white frames (Fig. 7.30) a showed a decrease of red molecules in the conversion region and a delayed increase in the region where the molecules concentrate with increasing time (Fig. 7.31, 7.32).

A magnified image of an adhesion complex in the enriched region showed that finer time binning into 37.5-s intervals still yielded excellent resolution (Fig. 7.33) and proves

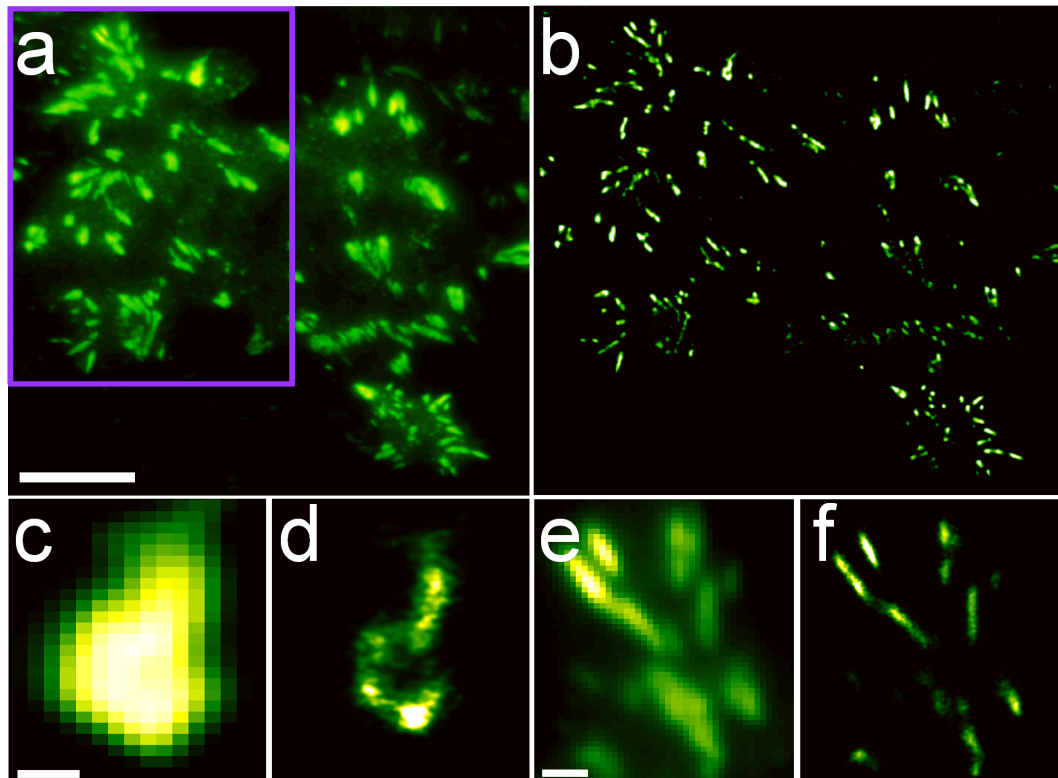


Figure 7.29. Live HeLa cell expressing a mIrisFP-paxillin fusion construct. Corresponding TIRF image (a) and PALM image (b) acquired with the green form of mIrisFP. Molecules in the area marked by the purple frame were later green-to-red photoconverted by 405-nm irradiation. Close up of two regions show the resolution enhancement of the PALM images (d, f) compared to the TIRF images (c, e). Scale bar, 10 μm (a), 500 nm (c,e).

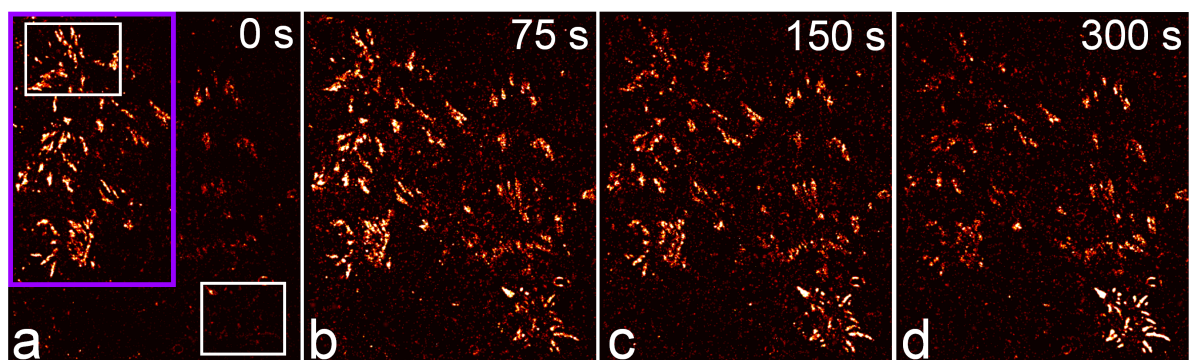


Figure 7.30. PALM images of paxillin-mIrisFP dynamics in a live HeLa cell. (a) Proteins inside the violet frame, also shown in Fig. 7.29, were photoconverted with 405-nm laser light. The PALM images of the red-converted mIrisFP molecules cover the interval 0–75 s (a), 75–150 s (b), 150–225 s (c), 225–300 s (d). Scale bar, 10 μm (a, b), 2 μm (d, k).

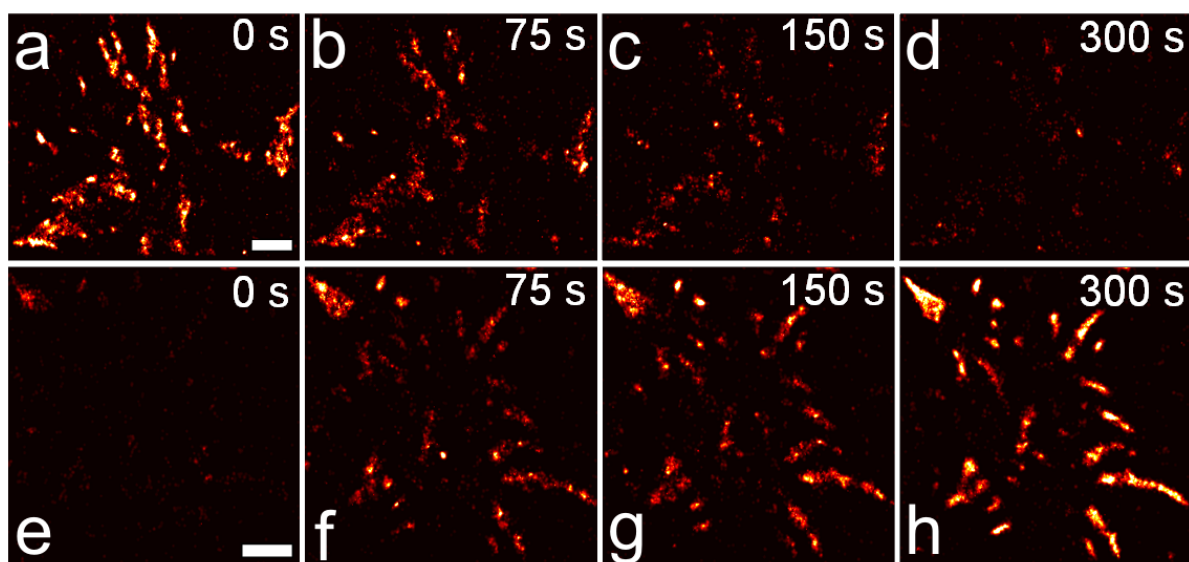


Figure 7.31. PALM images of paxillin-mIrisFP dynamics in a live HeLa cell. Enlarged views of the regions marked by the white frames in Fig.7.30. Adhesions in the conversion region decompose over time (**a–d**) and paxillin molecules migrate to other areas in the cell where the molecules are integrated into already existing focal adhesions or are integrated into new adhesions (**e–h**)

that dynamic processes in the minute time regime can be imaged with PALM. Focal adhesions are highly dynamic structures with permanent protein exchange. An in-depth analysis at high resolution revealed that converted molecules appeared in patches rather than evenly distributed over the adhesion complex. Because PALM imaging is based on the registration of single molecules, it offers the unique possibility of studying the temporal and spatial evolution of individual focal adhesions in a more quantitative way, through analysis of the number of single molecule signals per second in a single adhesion. This quantity is proportional to the entire population of molecules in the site, thereby allowing tracking of the disintegration and growth of single adhesion sites precisely. We studied several focal adhesions (Fig. 7.34) in detail. For a decomposing adhesion complex, a constant rate of 15 green molecules per second was initially recorded. After photoconversion, a rate of 10 red molecules per second was detected. The discrepancy between the number of red and green detected molecules is caused by differing excitation intensities. The excitation and activation irradiation for the red molecules was adjusted to match the timescale for paxillin migration. The intensities for the green molecules were optimized to capture as many molecules as possible in a short time. After photoconversion, the red molecules disappeared within ~ 300 s. This is consistent with the images calculated for the first and second 300-s intervals after photoconversion. The decrease of red paxillin-mIrisFP molecules may have different reasons: either the number of molecules in the adhesion site is constant and the red molecules are replaced by green molecules, or the decrease could be due to disassembly of the focal adhesion. The green image constructed from data collected 600–700 s after photoconversion and

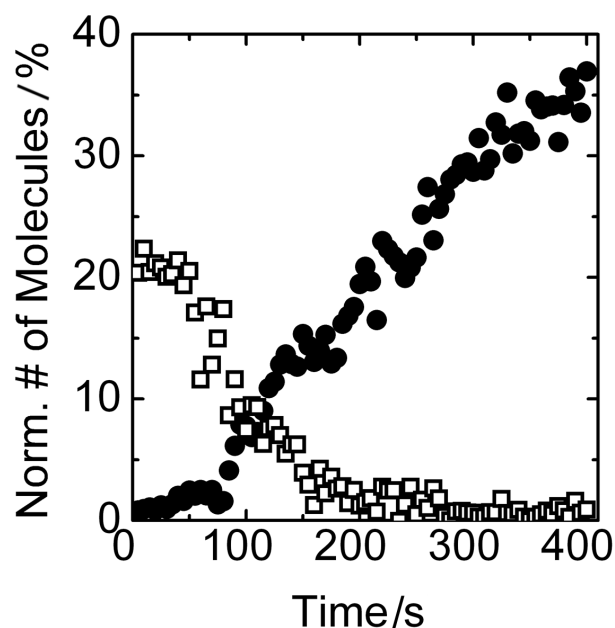


Figure 7.32. Time evolution of the fraction of red-converted mIrisFP molecules within the images series shown in Fig. 7.31. The decrease of molecules seen in Fig. 7.31a-d is described by the open squares and the increase in Fig. 7.31e-h is quantified by the filled circles.

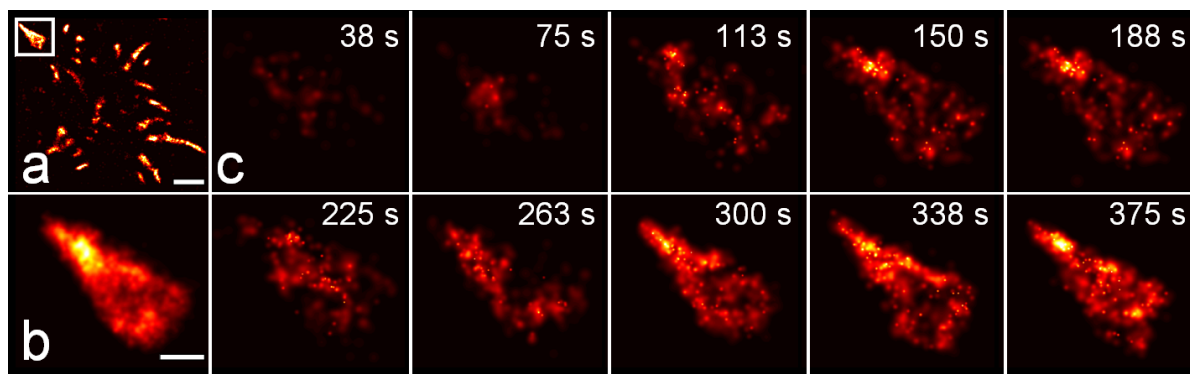


Figure 7.33. (a) PALM image of a region of the cell, shown in Fig. 7.31, into which paxillin-mIrisFP molecules migrated from the conversion area to assemble into adhesion complexes. (b) Expanded view of the area marked with a white frame in panel (a). This PALM image was computed from 12,000 video frames of 50 ms dwell time each. (c) Series of consecutive PALM images 750 frames each. Even at the time resolution of 37.5 s shown here, blurring due to structural changes during data acquisition is sufficiently low. Scale bars, 2 μm (a), 500 nm (b).

the absence of green single-molecule signals confirms the complete disappearance of the focal adhesion.

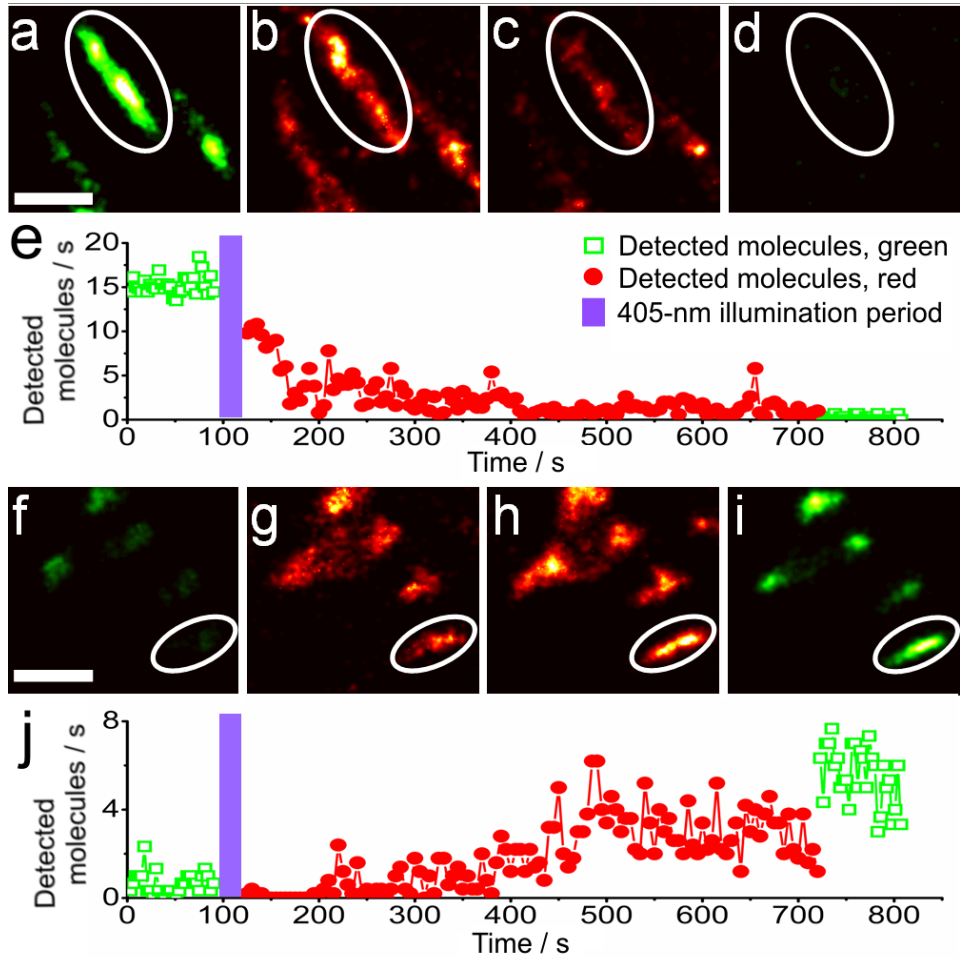


Figure 7.34. (a–e) Dynamics of a disappearing focal adhesion. (a) PALM images were taken by excitation of green mIrisFP molecules for 90 s. After photoconversion, PALM images were acquired by exciting red mIrisFP, covering the intervals (b) 0–300 s and (c,h) 300–600 s after the photoconversion period had ended. (d) Afterwards, PALM images were again taken by exciting green mIrisFP for 90 s. (e) Single molecules registered per second within individual adhesion sites marked by the ellipses in panels a - d, plotted as a function of time. Each data point represents an average over 100 image frames. (f–j) Dynamics of an appearing focal adhesion; panels correspond to (a–e). We note that the number of molecules in the green and the red channels differ slightly because of the different illumination conditions. Scale bar, 1 μm .

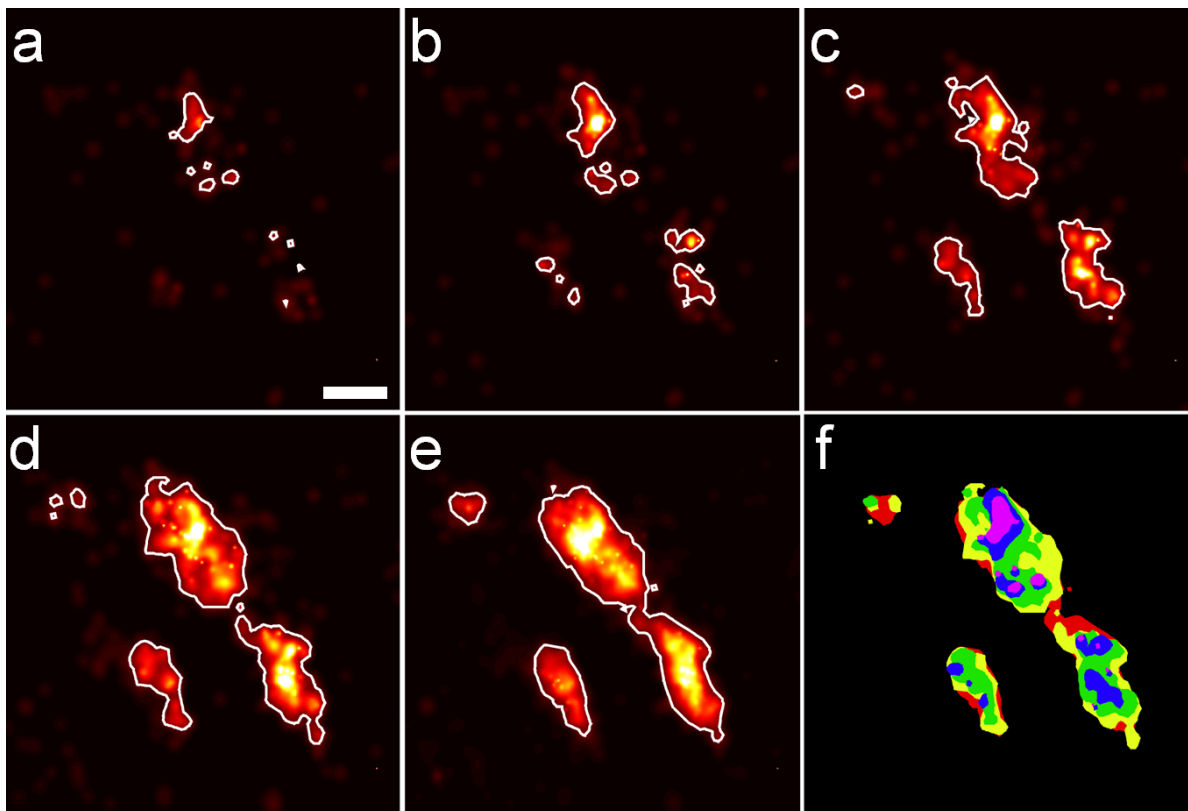


Figure 7.35. To follow the growth of focal adhesions at high resolution, we calculated PALM images acquired with the red form of mIrisFP from (a) 0 – 100 s, (b) 0 – 125 s, (c) 0 – 160 s, (d) 0 – 250 s and (e) 0 – 350 s after photoconversion. (f) Regions with intensities above a set threshold are marked with a white line and overlaid in different colors, 0 - 100 s (purple), 0 - 125 s (blue), 0 - 160 s (green), 0 - 250 s (yellow) and 0 - 350 s (red).

The use of mIrisFP allows simultaneous monitoring of the decomposition of focal adhesions and of the assembly and maturation of newly formed adhesions simultaneously. Because green molecules were initially absent at the site of a newly developing adhesion, the position could not be predicted. Therefore, the entire cell had to be imaged, which is only possible with a widefield, high-resolution method. After photoconversion, a delay of 100 s was observed until the rate of detected red mIrisFP increased for ~300 s, indicating that adhesion assembly took about as long as disassembly. The subsequent plateau indicated a stable adhesion. Both green and red paxillin-mIrisFP molecules migrated into the adhesion, as was evident from the green image taken in the interval 600–700 s after photoconversion and an average rate of single-molecule counting of $\sim 5 \text{ s}^{-1}$ during this interval.

In addition to the temporal analysis, the structural development of single adhesion complexes can be followed with high spatial resolution. Paxillin molecules were observed to initially cluster in isolated spots of <100-nm diameter that grew to form larger patches, which finally fused into the focal adhesion. Similar nucleation behavior has been ob-

7.2. *Imaging Protein Movements with Superresolution*

served on the micrometer scale during assembly and maturation of focal adhesions at the leading edge of migrating cells¹⁶⁴.

7.3. LivePALM

When fluorophores are localized by a full least-squares fit to a 2D Gaussian distribution, the analysis can take up to 4 h on a standard personal computer. The high resolution image can only be inspected long after data acquisition. Therefore, the experimenter relies on experience to choose the proper acquisition conditions such as activation/excitation intensities and acquisition times. A localization algorithm is needed that provides good localization accuracy and, at the same time, is fast enough to keep up with the data acquisition.

A fast image reconstruction software was developed based on the algebraic fluoroBancroft algorithm which exploits the fact that the intensity detected within each image pixel depends on the distance from the point source. With the calculated theoretical form of the PSF or a measured model PSF, the position of the source can thus be calculated from the measured intensities. The localization procedure resembles the one used for the global positioning system (GPS), although GPS is based on triangulation, whereas the fluoroBancroft algorithm uses distances and therefore relies on trilateration.

To evaluate the localization precision in PALM experiments, fluoroBancroft localization was compared to the frequently used algorithm with the highest localization precision in PALM experiments, the full least-squares fit¹⁰⁸. PALM frames taken from actin stress fibers in living Hela cells were analyzed by both algorithms (Fig. 7.36). The stress fibers were labeled with the actin-binding peptide Lifeact fused to d2EosFP. Actin structures are well suited to compare the localization accuracy of different algorithms because they form long straight filaments. At first appearance, no noticeable resolution differences can be seen between the least-squares fit and the fluoroBancroft (Fig. 7.37). We calculated the distribution of fluorophores around the mean contour line for a more exact evaluation. The distribution represents the thickness of the actin fiber broadened by the bound Lifeact constructs and the intrinsic image resolution. The full widths at half maximum of distributions yielded 78 nm and 91 nm for the full least-squares fit and the fluoroBancroft algorithms, respectively. The higher uncertainty of 12 % for the fluoroBancroft algorithm is probably due to the assumption of a fixed width of the point spread function. In a real sample, the width of the detected point spread functions is distributed around the theoretical value, which is more accurately described by the full least-squares algorithm.

The minimal loss in localization precision is more than overcompensated by the gain in evaluation time, and the recorded data are still available for more precise analysis at a later point. After evaluation of the localization accuracy, computation times were compared for both algorithms. PALM analysis consists of two steps, a searching step and a localization step. The complete evaluation algorithm and the localization step alone were compared. To give a hardware platform-independent measure, we calculated the relative performance of the two algorithms on the same computer system (Fig. 7.38a). Fluorophore localization can, in the best case, be more than 100 times faster using the fluoroBancroft algorithm. During typical PALM experiments, between 10 and 100 molecules were activated per frame. In this range, the fluoroBancroft algorithm provides

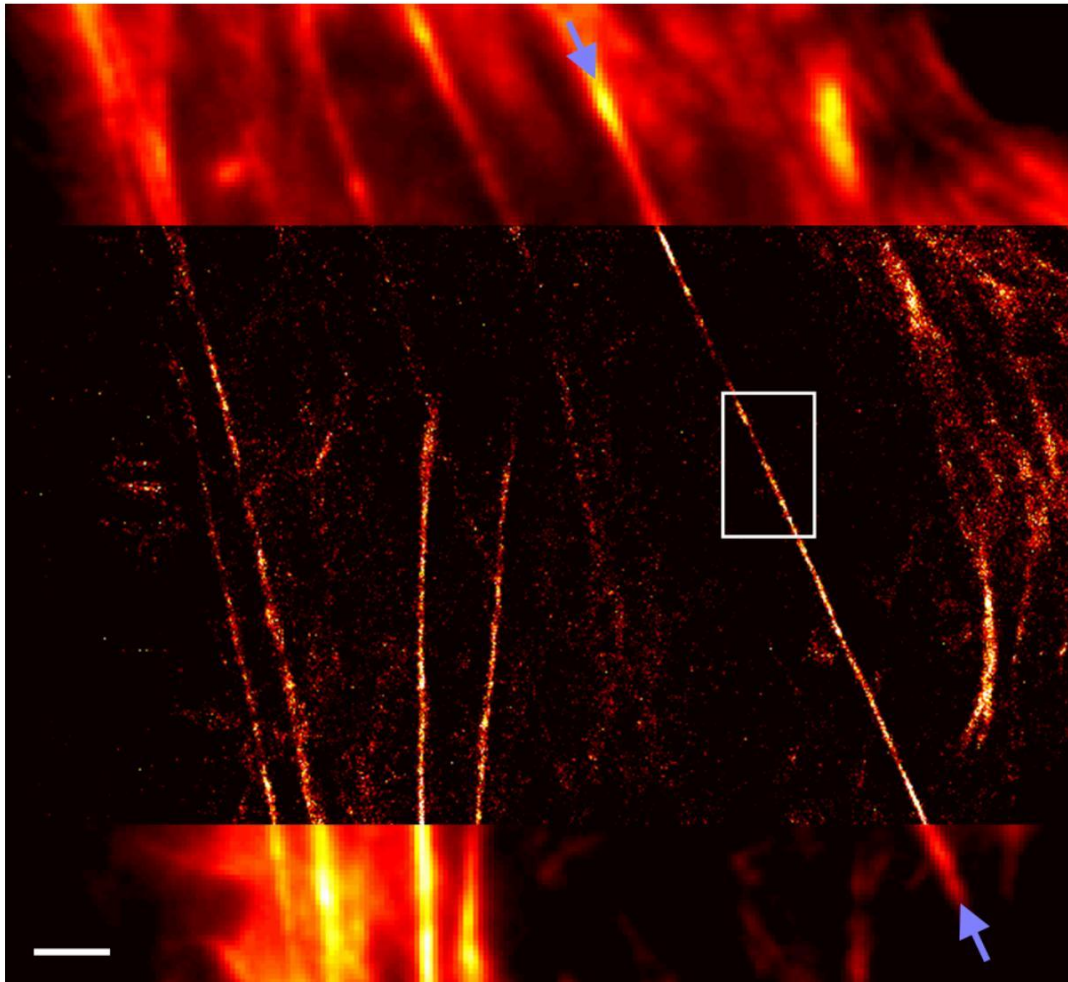


Figure 7.36. TIRFM (top and bottom) and PALM (middle) overlay image of stress fibers (actin bundles) in a live HeLa cell. The white frame marks the region shown in Fig.1a–c. Scale bar, 2 μm .

a performance enhancement of the full analysis routine of up to 20-fold. For a smaller number of activated FPs per frame, the localization process uses a smaller fraction of the total computational time, and the difference in the evaluation time decreases. The fluoroBancroft algorithm permitted analysis of up to 100 molecules per frame with parallel data acquisition at a frame rate of 10 Hz (Fig. 7.38b). With the Gaussian least-squares fitting, only three molecules per frame could be analyzed without slowing the analysis so that it could not keep up with the data acquisition. The fluoroBancroft algorithm, on the other hand, enables real time PALM data acquisition.

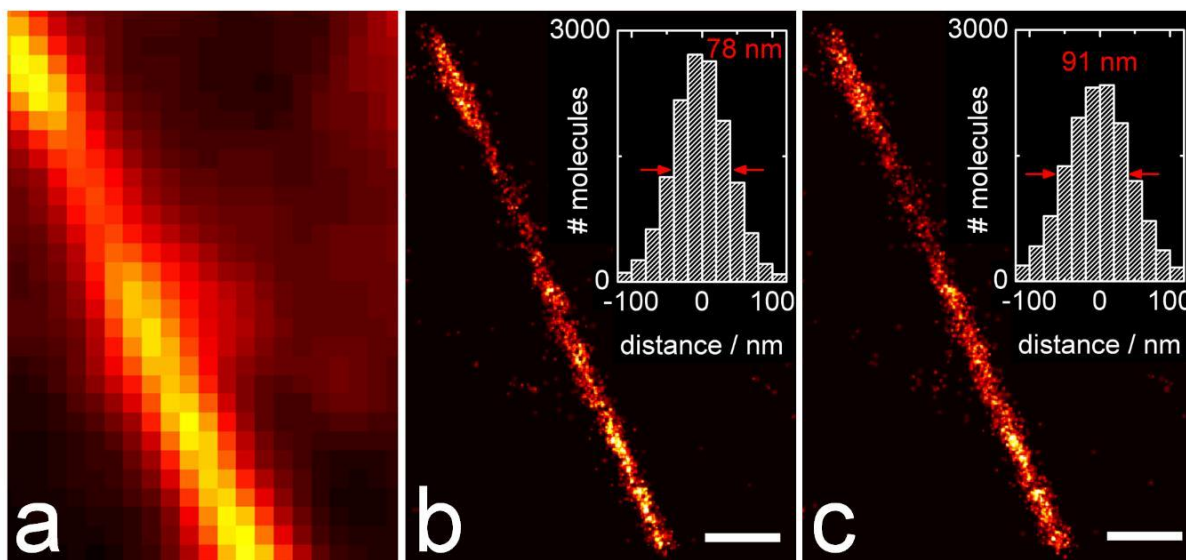
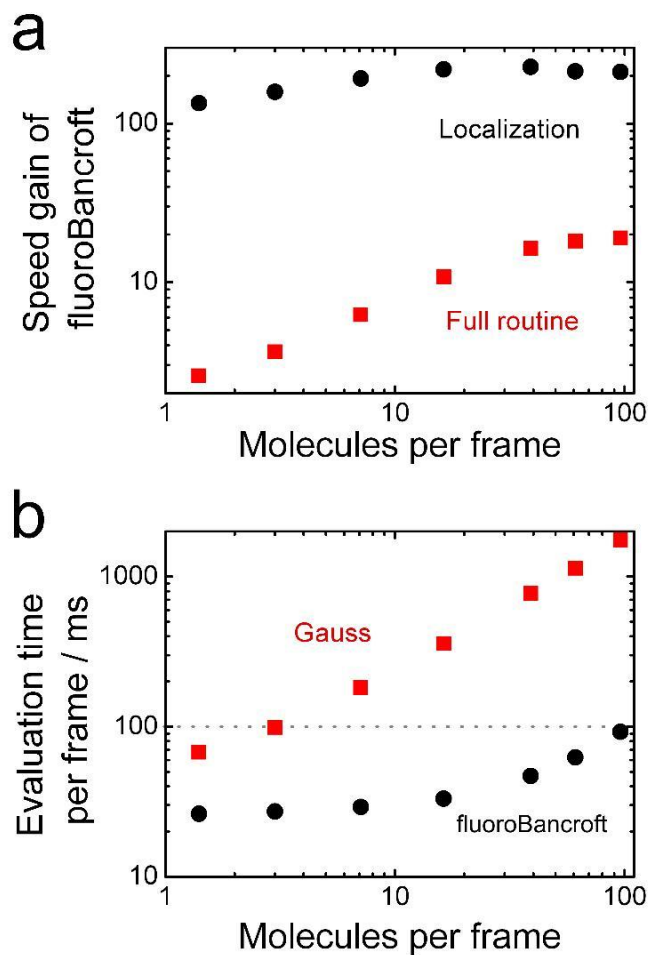


Figure 7.37. The TIRFM image (a) and PALM images (b,c) of an actin fiber labeled with a Lifeact-d2EosFP construct. The PALM images were calculated using the Gaussian least squares fitting (b) and the fluoroBancroft (c) algorithms. Insets in panels b,c show the contributions of detected molecules along a contour line. Scale bar, 500 nm (b,c).



110 **Figure 7.38.** Performance of the image analysis software based on Gaussian least squares fit and fluoroBancroft algorithms, as a function of detected molecules per frame. (a) The ratio of execution times is given for the full routine (signal search plus localization) and the localization step. Overall execution times on a standard personal computer (Intel Core 2 Quad 3.0 GHz) are given for both algorithms.

7.4. Nyquist-Shannon sampling theorem

The resolution of structures in PALM images is determined by two parameters: First, the localization precision of the single molecules and, second, the molecular label density. According to the Nyquist-Shannon theorem, the resolution is given by twice the distance between neighboring molecules. The condition can be visualized by drawing a circle around each detected molecule with increasing radius. A resolution which corresponds to twice the radius is reached as soon as the circles start to overlap. For example, the adhesion complexes studied in the pulse-chase experiments with mIrisFP can be resolved with a resolution of <100 nm (7.39). In densely labeled regions, the resolution is higher than in less densely labeled areas. The number of detected molecules increases in PALM experiments with time and, simultaneously, the resolution according to Nyquist increases (7.39e–h).

When presenting PALM images, molecules above a certain localization precision can be selected. This leads to crisper images. However, at the same time, the molecular density decreases, information about the spatial distribution of the target protein is lost and the data set no longer fulfills the Nyquist criterion (Fig. 7.40). Images displaying molecules with localization accuracies better than 60 nm, 50 nm and 40 nm (Fig. 7.40 c–e) are given together with the image that includes all molecules and a PALM image rendered from all molecules (Fig. 7.40 b,a). The images have a mean localization accuracy of 54 nm (all), 41 nm, 36 nm and 30 nm, respectively, and the positions are shown as blue circles with 7.5 nm radius. Only regions with overlapping blue circles satisfy a combination of localization accuracy and Nyquist criterion of 30 nm.

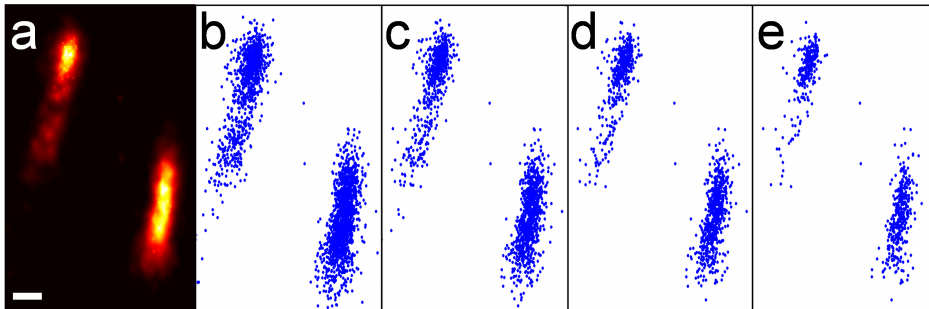


Figure 7.40. (a) Rendered PALM image of paxillin-mIrisFP in focal adhesions including all detected molecules. (b) Positions of all molecules (position error 54 nm) are shown as blue circles with 7.5 nm radius. In overlapping regions, the Nyquist criterion for a resolution of 30 nm is fulfilled. Molecules with a better localization accuracy than 60 nm (c), 50 nm (d) and 40 nm (e) are plotted. The calculated mean localization accuracy is 41 nm (c), 36 nm (d) and 30 nm (e). The mean localization accuracy and the Nyquist criterion for a resolution of 30 nm is only fulfilled in the overlapping regions in (e). Scale bar, 200 nm.

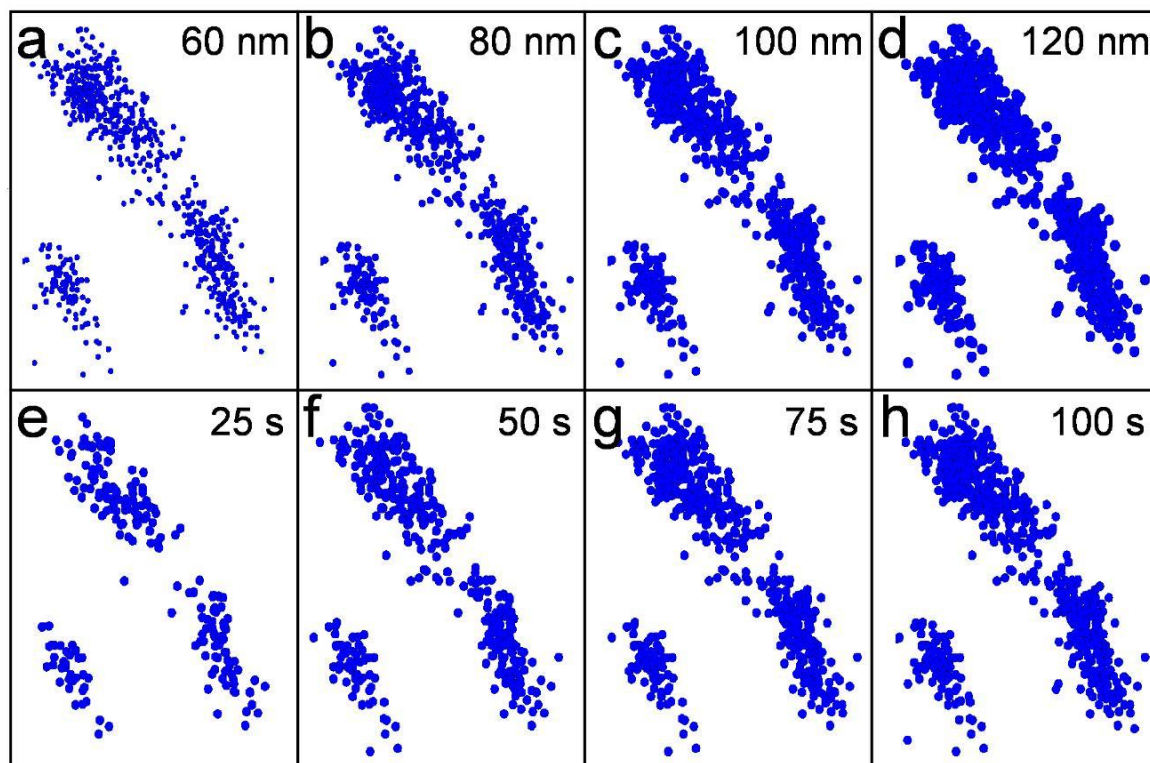


Figure 7.39. Visualization of the Nyquist criterion. Circles with radius 15 nm (a), 20 nm (b), 25 nm (c) and 30 nm (d) are drawn around detected molecule positions for two focal adhesion complexes detected during the paxillin-mIrisFP experiment. In regions, where the blue circles overlap, the Nyquist criterion is fulfilled and a resolution of 60 nm, 80 nm, 100 nm and 120 nm is achieved. The resolution according to Nyquist depends on local marker density and increases in a PALM experiment with time (e–h).

7.5. Light perturbation and cell vitality

PALM imaging requires relatively high illumination intensities to provide a good signal to noise ratio for single molecule detection. Constant high laser illumination might damage cells or at least could negatively influence cellular processes. By taking a DIC image before and after a complete imaging cycle for pulse chase experiments, cell growth, motility and morphology can be observed. The complete imaging cycle included a PALM image of the cell by imaging the green form of mIrisFP with 473-nm illumination (16 W cm^{-2}) for 3,000 frames of 30 ms exposure time. Subsequently, mIrisFP molecules inside the violet box in figure 7.41b were photoconverted to the red form using 405-nm light (56 W cm^{-2}) for 15 s. Then, a PALM image of the red form of mIrisFP was recorded with 561-nm excitation (230 W cm^{-2}) and 473-nm activation light (1 W cm^{-2}) for 7,000 frames of 50 ms exposure time each. A second green PALM image was recorded under the same conditions as the first one. Upon examination no adverse effects from laser exposure during PALM imaging were found. The cell showed no tendency to retract

Method	Power density (laser wavelength)
PALM(This work)	20, 50, 50–250 W cm ⁻² (473 nm, 405 nm, 561 nm)
PALM ³⁵	500 W cm ⁻² (488 nm, 561 nm), 10–200 W cm ⁻² (405 nm)
PALM ¹²⁹	1 kW cm ⁻² (561 nm), 50 W cm ⁻² (405 nm)
PALM ¹²⁸	0.1–1 kW cm ⁻² (514 nm), 1–10 kW cm ⁻² (407 nm)
PALMIRA ⁶³	20 kW cm ⁻² (561 nm)
STED ⁹⁸	400 MW cm ⁻² (635 nm, 750 nm)
STED ³⁹	80–800 MW cm ⁻² peak intensity (595 nm)
STORM ¹⁸⁸	18 kW cm ⁻² (532 nm, 647 nm)
FRAP ¹⁸⁹	640 kW cm ⁻² (488 nm)
FRAP ¹⁹⁰	640 kW cm ⁻² (488 nm)
FRAP ¹⁹¹	3 kW cm ⁻² (488 nm)
FRAP ¹⁹²	19 kW cm ⁻² (488 nm)

Table 7.1. Light intensities used in high resolution and dynamic light microscopy experiments.

from the laser illumination. This is also true for all other PALM experiments described in this theses. Therefore, we can conclude, that live-cell PALM illumination conditions are non-perturbative to living cells. Compared to other high resolution experiments, the laser intensities used in this work are rather low (Table 7.1) to prevent laser damage of the living cells. The laser illumination in other PALM experiments is usually one or even several orders of magnitude higher (Table 7.1). In general, the power densities are low with 20–250 W cm⁻² compared to STED experiments, which use power intensities in the 80–800 MW cm⁻² range. The comparison to other optical methods such as fluorescence recovery after photobleaching (FRAP)(3–640 kW cm⁻²), which are used to measure dynamic properties in living cells, confirms that pulse-chase PALM using three orders of magnitude lower power densities, is an extremely low perturbative method (Table 7.1).

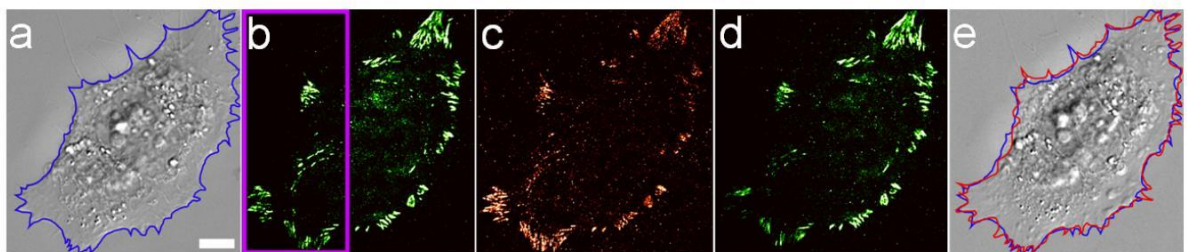


Figure 7.41. A sequence of DIC (**a**, **e**) and PALM (**b-d**) images of a live HeLa cell expressing a paxillin-mIrisFP fusion confirms that the cell morphology is not influenced by the laser illumination intensities typically used for PALM imaging. (**a**) DIC image of a live HeLa cell prior to PALM imaging, cell contour outlined in blue. (**b**) PALM image of the same cell acquired by using the green form of mIrisFP. Subsequently, mIrisFP molecules inside the violet box were photoconverted to the red form. (**c**) PALM image of the red form of mIrisFP. (**d**) Green PALM image recorded under the same conditions as for the image in panel (**b**). (**e**) DIC image taken after PALM image acquisition. The cell contour is marked by a red line; the contour from panel (**a**) is shown in blue for comparison. Scale bar, 10 μm .

8. Discussion PALM

8.1. Improvements of the PALM Method

PALM is excellently suited to answer questions on the molecular level in living organisms and cells. The PALM based methods, together with STED and SSIM, can cover the resolution range between 20–200 nm in light microscopy that is not accessible by conventional methods. A high localization accuracy can only be achieved for single molecule data with a high signal to noise ratio, which can be a problem for the inhomogeneous background found in living cells. We have solved this problem by introducing a local background correction that allows the analysis of single molecule data acquired under difficult background conditions. Our methods avoid errors resulting from assuming a constant background over the complete image or from calculating the background after photobleaching of the molecule. Therefore, our algorithm provides better data with higher localization accuracy

A second important improvement is the development of an on-line analysis software that decreased the data evaluation time from hours to minutes and allowed evaluating the acquired data in real time. This new software enables parallel data acquisition and tracking of nanometer-scale structures inside living cells. Multiple cellular reactions to environmental conditions, nanoparticles and pharmaceutical agents can be visualized with nanometer resolution as they happen within the PALM time resolution limit of a few tens of seconds. The on-line analysis software also improves cellular imaging experiments significantly because it offers the possibility of automatically optimizing key parameters such as activation laser intensity and acquisition time to achieve an optimal number of fluorescent markers per frame, thereby reducing the localization error and wasting of markers due to overlapping point spread functions, as well as the total acquisition time. Altogether, the development of the on-line analysis software makes the PALM method more efficient and user-friendly. It has triggered, together with other publications¹⁹³, the development of advanced algorithms using parallel computing on the Graphics Processing Unit (GPU) combined with the maximum likelihood algorithm^{194, 195} and fast 3D localization¹⁹⁶. Further optimization of imaging evaluation speed is still desirable for analysis of data acquired with faster cameras and brighter molecules. Single molecule localization is one of the basic components of PALM, therefore, it is necessary to think about more precise localization algorithms that take radiation characteristics of single fluorophores into account. Depending on the protein fusion, FPs might not emit light isotropically but rather with a fixed dipole, altering the point spread function considerably, which has to be considered during data evaluation¹⁹⁷.

8.2. Evaluation of new FPs as PALM Markers in Living Cells

We have examined the properties of four new FPs, psRFP, mcavRFP, mRuby(N143C) and mIrisFP in PALM experiments. The suitability of fluorescent proteins for super-resolution microscopy is usually judged by one of the following criteria. (1) The super-resolution image is compared to the diffraction limited image, and the increase in structural detail is judged by visible inspection. (2) The widths of certain structures are determined in both the diffraction limited image and the high resolution representation. (3) The methods based on single molecule detection provide additional parameters such as the number of photons per molecule and the localization accuracy of each molecule. We have applied all three criteria to the FPs studied during this work.

The PALM images created from data acquired with psRFP, mcavRFP, mRuby(N143C), d2EosFP and mIrisFP all show enhanced details and finer structures compared with conventional light microscopy images and thus prove the suitability of all studied FPs for PALM. A more advanced step is the analysis of structures with known size. We compare the measured diameter of microtubule fibers to the value obtained from electron microscopy (25 nm in HeLa cells). Assuming an overall diameter of 35 nm for the FP labeled Rita protein bound to the fibers we calculated an error of 15–25 nm for the psRFP, 30 nm for mcavRFP and 25 nm for mRuby(N143C) for the determined diameters. These results demonstrate that we can determine the size of cellular structures with our new proteins about ten times better in PALM experiments than with conventional light microscopy. We determined the FWHM of microtubule fibers to 50–65 nm with our red FPs. The FWHM of isolated microtubules labeled with EGFP was determined from a SIM reconstruction image to ~ 100 nm¹⁹⁸ and in PALMIRA experiments on fixed cells the size of single fibers labeled with the synthetic dye 5-NHSS were determined to 55–70 nm¹³⁴. STORM experiments with synthetic Cy dyes in fixed cells yielded a similar size of 56 nm with a localization error of 22 nm¹¹⁷. Using the comparable FP asFP595 distances of 100 nm could be resolved with a RESOLFT experiment in a non-cellular environment¹⁹⁹. This comparison of our results with the results obtained from other optical high resolution experiments and labels, show that the values obtained with our PALM measurements are better or comparable.

Along with the high resolution images, the number of photons per molecule and the localization accuracy for individual molecules can be compared. The emission and localization properties of the red FPs studied are quite similar. For all FPs, a mean (median) of about 600 (mean), 300 (median) photons per molecule were detected on average and could be localized with a 2D error of about 30 nm which makes all red FPs competitive to other state-of-the-art photoactivatable FPs. For example, the irreversibly photoconvertible PAmCherry1 with around 700 (mean) and 300 (median) detected photons and a localization accuracy of 15–20 nm is in the same range⁴⁴. Unfortunately, it was not stated whether the 2D or 1D error was calculated. The 2D error calculated for the studied red FPs is higher (30 nm), but the 1D error would be exactly in the same range (15–20 nm). With about 400 (mean) and 250 (median), the number of detected photons

for the reversibly switchable rsCherry and rsCherryRev is lower, but the localization error of 24 nm is still comparable⁴⁴. Also in the same range as PAmCherry1 is PAtagRFP. Unfortunately, statistics from a single frame are given, which does not allow a direct comparison¹⁸⁷. The number of detected photons, 500 (mean), 250 (median) for d2EosFP in fixed cells was surprisingly low. Nevertheless the 2D localization error was 20 nm, still very good due to low background. The photon number and localization accuracy in living cells is for mIrisFP slightly lower. With ~200 (mean) detected photons in the green and 350 (mean) photons in the red channel, and 2D localization errors of 50 nm and 40 nm, mIrisFP is an excellent marker for superresolution imaging and, in the green spectral range, better than Dronpa³⁴, which has a 1D localization error of 30 nm compared to 25 nm for green mIrisFP. In general, the irreversibly green-to-red converting FPs perform a little better than the reversibly switchable FPs due to reduced background. For example, the best FP so far, EosFP was measured with 2600 (mean) and 490 (median) detected photons and a 1D localization accuracy of 10 nm³⁴. In general, we realized that fixation has a strong influence on the number of detected photons. For fixed samples, the photon counts were always lower than for living cells. A comparison of the examined red FPs to synthetic dyes show that the localization accuracies are in the same range 20–25 nm^{200, 117, 188}, although one would expect a better localization due to the overall higher numbers of detected photons (3000–6000)¹¹⁷. Synthetic dyes are engineered or illuminated such that they are in the emitting state for only a very short time so that the number of photons detected per-on-time is restricted to ~130 photons¹⁸⁸ or 300–500 photons per imaging cycle²⁰¹. Overall, it is important to state that statistical parameters are not very useful for determining the localization properties of FPs because the number of photons emitted and the localization accuracy of a FP is influenced by the coupled fusion protein and the detection threshold chosen during PALM analysis. The resolution can be increased by selecting only molecules with high signal photon numbers and low background. The statistical data are useful to judge the quality of a PALM image but can only give a raw estimate of the performance of the FPs used. Even for identical evaluation conditions, protein properties that influence localization such as expression level and cellular background might vary from cell to cell. Keeping this in mind, we can clearly state that the proteins studied during this work are excellent superresolution markers comparable to other state-of-the-art markers. Among the studied FPs, psRFP and mRuby are particularly interesting because these two red FPs do not require short wavelength, blue or violet light, which may be more cytotoxic for high resolution imaging. This makes them ideal markers for live cell and tissue imaging. Combined with green switchable FPs, they are excellently suited for simultaneous two-color superresolution applications. The bright red reversibly photo-switchable FP psRFP is also potentially suited for RESOLFT and SSIM imaging. The closely related asFP595 has already been used to visualize structures with 50–100 nm resolution in a RESOLFT experiment¹⁹⁹. The authors mentioned that the low quantum yield of asFP595 was a problem for RESOLFT imaging. The orders of magnitude higher quantum yield of psRFP should help to overcome these problems. Besides their advantages for high resolution microscopy, both FPs are also excellent markers for conventional light microscopy, due to their slow fading over long time periods. Data can

be collected with a constant signal to noise ratio from the beginning to the end of the recording period. This allows reliable measurement of dynamic information over long time spans and the detection of rare events that may occur only for a short period during dynamic processes and therefore could be missed by time-lapse experiments. Another field of application for reversibly photoswitchable fluorescent proteins are innovative protein tracking strategies, as shown in this work, and fluorescence correlation spectroscopy at high molar concentrations²⁰². Additionally, there exist numerous applications for which the oligomeric nature of psRFP is entirely irrelevant, including tissue imaging, monitoring of gene activity and highlighting of cells and cellular compartments.

8.3. Live Cell Imaging

One of the biggest advantages of fluorescence microscopy, the ability to visualize specific cell components, is restricted because important information about the overall cell shape and localization of the specific cellular structures within the cell are missing. We have overcome this problem by combining PALM with differential interference contrast (DIC) microscopy, which provides the missing information and completes our view on cellular processes.

Cellular structures undergo continuous changes, and proteins, the building blocks for cellular structures are permanently produced, modified and decomposed. Photoconvertible FPs are powerful tools to image these processes and can even visualize protein exchange in structures that appear as static with conventional fluorescence markers. The in- and outflow of proteins are observable for equilibrium cell structures and protein trafficking patterns, inter-organelle exchange, signaling pathways, membrane dynamics, protein transport as well as many other interesting dynamic processes can be studied by selectively highlighting protein subpopulations and following these proteins over time²⁰³. This approach, called pulse-chase, has shown that lysosomes actively communicate with each other through membrane transport pathways⁴¹. Dynamics of mitochondria has been studied as well as separation of chromosomes during mitosis and cell movements during embryonic development of *X. laevis*⁵⁴. These are only a few examples that demonstrate how much we can learn from pulse-chase experiments about dynamics in living cells. By utilizing the multiple phototransformations of mIrisFP, we have extended pulse-chase experiments into the low nanometer regime, which offers the potential of observing static structures and, more importantly, dynamic cellular processes such as protein complex formation, protein-protein interaction and structural changes on the nanometer scale, a length scale that has not been accessible for dynamic studies on living cells so far. The example of focal adhesion maturation shows that small adhesion patches <100 nm in diameter are formed first, which grow out into larger focal adhesions. After observations on the micrometer scale, there was speculation about the existence of such nucleation centers and the sequential recruitment of individual, or classes of, adhesion components¹⁶⁴. We showed that adhesions are not homogeneous clusters of proteins, but instead contain sub-domains rich in specific focal-adhesion components and might display hot spots of enzymatic activity. Due to the red conversion of mIrisFP we can see, in addition to

the inhomogeneous growth and disassembly of adhesions, the otherwise invisible protein fluxes in and out of already existing focal adhesions. The acquisition of a PALM image had previously taken 2–12 hours³⁷. In contrast, we were able to reconstruct images from data recorded for only 40 s, which makes PALM a method fast enough to monitor dynamics on the minute scale. The single molecule detection in PALM experiments offers a quantitative way to analyze protein turnover, focal adhesion formation and disintegration. By counting the amount of molecules detected, which is proportional to the actual number of molecules, we are able to give a more precise measure of protein populations than values obtained from intensity measurements.

8.4. Low Intensity PALM

The phototoxic effects of light during live-cell imaging are often underestimated. Power densities of just a few hundred W cm^{-2} can lead to decreased cell viability²⁰⁴. The main source of photodamage in fluorescently labeled cells is the production of reactive oxygen species. These activated oxygen species react with a large number of cellular components such as proteins, nucleic acids and membrane lipids. Singlet oxygen, which is responsible for most of the physiological damage, is synthesized in a photochemical reaction. Fluorescent proteins are presumably less phototoxic because the chromophore is buried in the center of a hydrophobic protein environment whereas a synthetic dye chromophore is directly exposed to the environment. As the word phototoxicity already implies, photons are necessary for inducing toxicity in fluorescently labeled specimens, and the phototoxicity increases with light intensity. For thick specimens, the wavelength of the excitation light can also be a factor because stronger incident illumination is needed for comparable excitation of shorter wavelength fluorophores due to increased tissue scattering at shorter wavelengths. As the high resolution microscopy field is moving towards live cell imaging, it is interesting to compare the employed laser intensities for different methods. The light intensities used for PALM experiments during this work are lower or comparable to these of other PALM experiments^{35, 129, 128}. The short acquisition times of PALMIRA already require two orders of magnitude higher intensities⁶³. The excitation intensities for STORM are also in the 20 kW cm^{-2} range¹⁸⁸ but still far below the intensities used for STED, with six orders of magnitude higher peak intensities^{98, 39}. In fluorescence recovery after photobleaching (FRAP) experiments, which also yield dynamic information, intensities in the $3\text{--}640 \text{ kW cm}^{-2}$ range are used for photobleaching^{189, 190, 191, 192}. The comparison shows that PALM is the least invasive high resolution technique, a fact of great interest for live cell imaging.

8.5. Resolution

The classical concept of resolution does not apply to PALM. Instead, we can give an uncertainty for every localized molecule and, altogether, an average uncertainty for the localized structure, which is about ten times better than the resolution of conventional

8. Discussion PALM

light microscopes. A second criterion is the Nyquist-Shannon theorem, which helps to judge the information in an image independent of the method. The presented FPs, which allow a 2D localization accuracy of better 30 nm paired with high labeling densities in mammalian cells, provide excellent imaging conditions, as demonstrated on nanoscale structures.

9. Conclusion and Outlook

New microscopy methods such as PALM or STED, with so far unmatched resolution, have revolutionized the field of light microscopy. Because our understanding of cellular processes has been particularly dependent on imaging, the emergence of new imaging modalities will lead to new insights and discoveries in cell biology. The development of these techniques is based on the remarkable properties of optical markers such as photoactivatable fluorescent proteins. The application of FPs in high resolution microscopy requires a detailed understanding of the mechanisms that determine fluorescence emission and photoswitching. We analyzed the chromophore populations of psRFP at different pH, which helped us to understand the optical properties of the FP. By studying the chromophore-protein interactions, we were able to identify important amino acids that influence the chromophore conformation and switching properties. This knowledge can be used to design advanced FPs for imaging applications. It is also helpful for a better understanding of FPs that contain the chromophoric moieties similar to psRFP such as asFP595, Dronpa or mRuby.

We were able to propose a model, which explains all photoswitching processes and the slow bleaching behavior. The deeper understanding of these processes helps performing better conventional long term diffraction-limited microscopy and super-resolution experiments.

Low fluorescence quantum yields were reported for all reversibly switchable red FPs were considered as a problem for imaging applications. By analyzing the chromophore populations of psRFP, we were able to show that the overlapping of the absorption spectra of different chromophore conformations lead to a low apparent fluorescence quantum yield. We could, additionally, determine the quantum yield of the fluorescence chromophore conformation. The obtained value is comparable to other state-of-the-art non-switchable FPs, which renders psRFP an interesting marker for live cell imaging applications.

We confirmed the suitability of psRFP as superresolution marker in PALM experiments. Good results with excellent localization accuracy were demonstrated for the reversibly photoswitchable psRFP, the photoconvertible mcavRFP, the red mRuby(N143C) and multifunctional mIrisFP with different fusion proteins. All studied red FPs can be combined with green photoactivatable FPs for two-color superresolution live cell experiments. Colocalization experiments for example will yield interesting new results about bigger protein complexes on the nanoscale.

The big advantage of optical high resolution techniques compared to other high resolution microscopy methods is the possibility to observe living cells and tissue. We demonstrated pulse-chase experiments for dynamic superresolution microscopy in live cell imaging by employing the multiple phototransformations of mIrisFP. Biologists will be able to visualize the dynamics of structures and processes in living cells at the

9. Conclusion and Outlook

molecular level.

At the same time, technical improvements such as online image analysis, make the new methods easier to use for life scientists and help to optimize data acquisition.

An exciting new era in light microscopy has just begun!

Bibliography

1. Feynman, R. P., Leighton, R. B., Sands, M., and Hafner, E. M. *The Feynman Lectures on Physics*, volume I, Addison Wesley. (1965).
2. Shimomura, O., Johnson, F. H., and Saiga, Y. Extraction, purification and properties of aequorin, a bioluminescent protein from the luminous hydromedusan, *Aequorea*. *J. Cell Comp. Physiol.* **59**, 223–239 (1962).
3. Prasher, D. C., Eckenrode, V. K., Ward, W. W., Prendergast, F. G., and Cormier, M. J. Primary structure of the *Aequorea victoria* green-fluorescent protein. *Gene* **111**, 229–233 (1992).
4. Chalfie, M., Tu, Y., Euskirchen, G., Ward, W. W., and Prasher, D. C. Green fluorescent protein as a marker for gene expression. *Science* **263**, 802–805 (1994).
5. Heim, R., Prasher, D. C., and Tsien, R. Y. Wavelength mutations and posttranslational autooxidation of green fluorescent protein. *Proc. Natl Acad. Sci. USA* **91**, 12501–12504 (1994).
6. Wiedenmann, J. Die Anwendung eines orange fluoreszierenden Proteins und weiterer farbiger Proteine und der zugehörigen Gene aus der Artengruppe *Anemonia* sp. (*sulcata*) Pennant, (Cnidaria, Anthozoa, Actinaria) in Gentechnologie und Molekularbiologie. Patent DE 197.
7. Matz, M. V., Fradkov, A. F., Labas, Y. A., Savitsky, A. P., Zaraisky, A. G., Markelov, M. L., and Lukyanov, S. A. Fluorescent proteins from nonbioluminescent Anthozoa species. *Nat. Biotechnol.* **17**, 969–973 (1999).
8. Wiedenmann, J., Elke, C., Spindler, K. D., and Funke, W. Cracks in the β -can: fluorescent proteins from *Anemonia sulcata* (Anthozoa, Actinaria). *Proc. Natl Acad. Sci. USA* **97**, 14091–14096 (2000).
9. Nienhaus, G. U. and Wiedenmann, J. Structure, dynamics and optical properties of fluorescent proteins: perspectives for marker development. *ChemPhysChem* **10**, 1369–1379 (2009).
10. Hell, S. W. Microscopy and its focal switch. *Nat. Methods* **6**, 24–32 (2008).
11. Wachter, R. M. Chromogenic cross-link formation in green fluorescent protein. *Acc. Chem. Res.* **40**, 120–127 (2007).

Bibliography

12. Sniegowski, J. A., Lappe, J. W., Patel, H. N., Huffman, H. A., and Wachter, R. M. Base catalysis of chromophore formation in Arg96 and Glu222 variants of green fluorescent protein. *J. Biol. Chem.* **280**, 26248–26255 (2005).
13. Sniegowski, J. A., Phail, M. E., and Wachter, R. M. Maturation efficiency, trypsin sensitivity, and optical properties of Arg96, Glu222, and Gly67 variants of green fluorescent protein. *Biochem. Biophys. Res. Commun.* **332**, 657–663 (2005).
14. Henderson, J. N. and Remington, S. J. The kindling fluorescent protein: a transient photoswitchable marker. *Physiology* **21**, 162–170 (2006).
15. Kummer, A. D., Kompa, C., Niwa, H., Hirano, T., Kojima, S., and Michel-Beyerle, M. E. Viscosity-dependent fluorescence decay of the GFP chromophore in solution due to fast internal conversion. *J. Phys. Chem. B* **106**, 7554–7559 (2002).
16. Chattoraj, M., King, B. A., Bublitz, G. U., and Boxer, S. G. Ultra-fast excited state dynamics in green fluorescent protein: multiple states and proton transfer. *Proceedings of the National Academy of Sciences of the United States of America* **93**, 8362 (1996).
17. Lossau, H., Kummer, A., Heinecke, R., Pöllinger-Dammer, F., Kompa, C., Bieser, G., Jonsson, T., Silva, C. M., Yang, M. M., Youvan, D. C., and Michel-Beyerle, M. E. Time-resolved spectroscopy of wild-type and mutant green fluorescent proteins reveals excited state deprotonation consistent with fluorophore-protein interactions. *Chemical physics* **213**, 1–16 (1996).
18. Stoner-Ma, D., Jaye, A. A., Matousek, P., Towrie, M., Meech, S. R., and Tonge, P. J. Observation of excited-state proton transfer in green fluorescent protein using ultrafast vibrational spectroscopy. *J. Opt. Soc. Am.* **127**, 2864–2865 (2005).
19. Piatkevich, K. D., Malashkevich, V. N., Almo, S. C., and Verkhusha, V. V. Engineering ESPT pathways based on structural analysis of LSSmKate red fluorescent proteins with large Stokes shift. *Journal of the American Chemical Society* **132**, 741–746 (2010).
20. Henderson, J. N., Osborn, M. F., Koon, N., Gepshtein, R., Huppert, D., and Remington, S. J. Excited state proton transfer in the red fluorescent protein mKeima. *Journal of the American Chemical Society* **131**, 13212–13213 (2009).
21. Thor, J. J. Photoreactions and dynamics of the green fluorescent protein. *Chem. Soc. Rev.* **38**, 2935–2950 (2009).
22. Gross, L. A., Baird, G. S., Hoffman, R. C., Baldrige, K. K., and Tsien, R. Y. The structure of the chromophore within DsRed, a red fluorescent protein from coral. *Proc. Natl Acad. Sci. USA* **97**, 11990–11995 (2000).

23. Mizuno, H., Mal, T. K., Tong, K. I., Ando, R., Furuta, T., Ikura, M., and Miyawaki, A. Photo-induced peptide cleavage in the green-to-red conversion of a fluorescent protein. *Mol. Cell* **12**, 1051–1058 (2003).
24. Strack, R. L., Strongin, D. E., Mets, L., Glick, B. S., and Keenan, R. J. Chromophore Formation in DsRed Occurs by a Branched Pathway. *J. Am. Chem. Soc.* **132**, 8496–8505 (2010).
25. Subach, O. M., Malashkevich, V. N., Zencheck, W. D., Morozova, K. S., Piatkevich, K. D., Almo, S. C., and Verkhusha, V. V. Structural Characterization of Acylimine-Containing Blue and Red Chromophores in mTagBFP and TagRFP Fluorescent Proteins. *Chem. Biol.* **17**, 333–341 (2010).
26. Pletnev, S., Subach, F. V., Dauter, Z., Wlodawer, A., and Verkhusha, V. V. Understanding Blue-to-Red Conversion in Monomeric Fluorescent Timers and Hydrolytic Degradation of Their Chromophores. *J. Am. Chem. Soc.* **132**, 2243–2253 (2010).
27. Deliolanis, N. C., Kasmieh, R., Wurdinger, T., Tannous, B. A., Shah, K., and Ntziachristos, V. Performance of the red-shifted fluorescent proteins in deep-tissue molecular imaging applications. *Journal of biomedical optics* **13**, 044008 (2008).
28. Wiedenmann, J., Vallone, B., Renzi, F., Nienhaus, K., Ivanchenko, S., Röcker, C., and Nienhaus, G. U. Red fluorescent protein eqFP611 and its genetically engineered dimeric variants. *Journal of biomedical optics* **10**, 014003 (2005).
29. Wolff, M., Wiedenmann, J., Nienhaus, G. U., Valler, M., and Heilker, R. Novel fluorescent proteins for high-content screening. *Drug discovery today* **11**, 1054–1060 (2006).
30. Peyker, A., Rocks, O., and Bastiaens, P. I. H. Imaging activation of two Ras isoforms simultaneously in a single cell. *Chembiochem* **6**, 78–85 (2005).
31. Fradkov, A. F., Verkhusha, V. V., Staroverov, D. B., Bulina, M. E., Yanushevich, Y. G., Martynov, V. I., Lukyanov, S., and Lukyanov, K. A. Far-red fluorescent tag for protein labelling. *Biochemical Journal* **368**, 17 (2002).
32. Van der Krogt, G. N., Ogink, J., Ponsioen, B., and Jalink, K. A comparison of donor-acceptor pairs for genetically encoded FRET sensors: application to the Epac cAMP sensor as an example. *PLoS One* **3**, e1916 (2008).
33. Kaplan, R. N., Riba, R. D., Zacharoulis, S., Bramley, A. H., Vincent, L., Costa, C., MacDonald, D. D., Jin, D. K., Shido, K., Kerns, S. A., Zhu, Z., Hicklin, D., Wu, Y., Port, J., Altorki, N., Port, E. R., Ruggero, D., Shmelkov, S. V., Jensen, K. K., Rafii, S., and D., L. VEGFR1-positive haematopoietic bone marrow progenitors initiate the pre-metastatic niche. *Nature* **438**, 820–827 (2005).

Bibliography

34. Shroff, H., Galbraith, C. G., Galbraith, J. A., White, H., Gillette, J., Olenych, S., Davidson, M. W., and Betzig, E. Dual-color superresolution imaging of genetically expressed probes within individual adhesion complexes. *Proc. Natl Acad. Sci. USA* **104**, 20308–20313 (2007).
35. Manley, S., Gillette, J. M., Patterson, G. H., Shroff, H., Hess, H. F., Betzig, E., and Lippincott-Schwartz, J. High-density mapping of single-molecule trajectories with photoactivated localization microscopy. *Nat. Methods* **5**, 155–157 (2008).
36. Adam, V., Mizuno, H., Grichine, A., Hotta, J., Yamagata, Y., Moeyaert, B., Nienhaus, G. U., Miyawaki, A., Bourgeois, D., and Hofkens, J. Data storage based on photochromic and photoconvertible fluorescent proteins. *J. Biotechnol.* **149**, 289–298 (2010).
37. Betzig, E., Patterson, G. H., Sougrat, R., Lindwasser, O. W., Olenych, S., Bonifacio, J. S., Davidson, M. W., Lippincott-Schwartz, J., and Hess, H. F. Imaging intracellular fluorescent proteins at nanometer resolution. *Science* **313**, 1642–1645 (2006).
38. Hess, S. T., Girirajan, T. P. K., and Mason, M. D. Ultra-high resolution imaging by fluorescence photoactivation localization microscopy. *Biophys. J.* **91**, 4258–4272 (2006).
39. Hein, B., Willig, K. I., and Hell, S. W. Stimulated emission depletion (STED) nanoscopy of a fluorescent protein-labeled organelle inside a living cell. *Proc. Natl Acad. Sci. USA* **105**, 14271–14276 (2008).
40. Henderson, J. N., Gepshtein, R., Heenan, J. R., Kallio, K., Huppert, D., and Remington, S. J. Structure and mechanism of the photoactivatable green fluorescent protein. *J. Am. Chem. Soc.* **131**, 4176–4177 (2009).
41. Patterson, G. H. and Lippincott-Schwartz, J. A photoactivatable GFP for selective photolabeling of proteins and cells. *Science* **297**, 1873–1877 (2002).
42. Chudakov, D. M., Verkhusha, V. V., Staroverov, D. B., Souslova, E., Lukyanov, S., and Lukyanov, K. A. Photoswitchable cyan fluorescent protein for protein tracking. *Nat. Biotechnol.* **22**, 1435–1439 (2004).
43. Verkhusha, V. V. and Sorkin, A. Conversion of the monomeric red fluorescent protein into a photoactivatable probe. *Chem. Biol.* **12**, 279–285 (2005).
44. Subach, F. V., Patterson, G. H., Manley, S., Gillette, J. M., Lippincott-Schwartz, J., and Verkhusha, V. V. Photoactivatable mCherry for high-resolution two-color fluorescence microscopy. *Nat. Methods* **6**, 153–159 (2009).
45. Subach, F. V., Malashkevich, V. N., Zencheck, W. D., Xiao, H., Filonov, G. S., Almo, S. C., and Verkhusha, V. V. Photoactivation mechanism of PAmCherry

- based on crystal structures of the protein in the dark and fluorescent states. *Proc. Natl Acad. Sci. USA* **106**, 21097–21102 (2009).
46. Wiedenmann, J., Ivanchenko, S., Oswald, F., Schmitt, F., Röcker, C., Salih, A., Spindler, K. D., and Nienhaus, G. U. EosFP, a fluorescent marker protein with UV-inducible green-to-red fluorescence conversion. *Proc. Natl Acad. Sci. USA* **101**, 15905–15910 (2004).
 47. Labas, Y. A., Gurskaya, N. G., Yanushevich, Y. G., Fradkov, A. F., Lukyanov, K. A., Lukyanov, S. A., and Matz, M. V. Diversity and evolution of the green fluorescent protein family. *Proc. Natl Acad. Sci. USA* **99**, 4256–4261 (2002).
 48. Ando, R., Hama, H., Yamamoto-Hino, M., Mizuno, H., and Miyawaki, A. An optical marker based on the UV-induced green-to-red photoconversion of a fluorescent protein. *Proc. Natl Acad. Sci. USA* **99**, 12651–12656 (2002).
 49. Chudakov, D. M., Lukyanov, S., and Lukyanov, K. A. Tracking intracellular protein movements using photoswitchable fluorescent proteins PS-CFP2 and Dendra2. *Nat. Protoc.* **2**, 2024–2032 (2007).
 50. Tsutsui, H., Karasawa, S., Shimizu, H., Nukina, N., and Miyawaki, A. Semi-rational engineering of a coral fluorescent protein into an efficient highlighter. *EMBO reports* **6**, 233–238 (2005).
 51. Nienhaus, K., Nienhaus, G. U., Wiedenmann, J., and Nar, H. Structural basis for photo-induced protein cleavage and green-to-red conversion of fluorescent protein EosFP. *Proc. Natl Acad. Sci. USA* **102**, 9156–9159 (2005).
 52. Hayashi, I., Mizuno, H., Tong, K. I., Furuta, T., Tanaka, F., Yoshimura, M., Miyawaki, A., and Ikura, M. Crystallographic evidence for water-assisted photo-induced peptide cleavage in the stony coral fluorescent protein Kaede. *J. Mol. Biol.* **372**, 918–926 (2007).
 53. Lelimosin, M., Adam, V., Nienhaus, G. U., Bourgeois, D., and Field, M. J. Photoconversion of the Fluorescent Protein EosFP: A Hybrid potential simulation study reveals intersystem crossings. *J. Am. Chem. Soc.* **131**, 16814–16823 (2009).
 54. Nienhaus, G. U., Nienhaus, K., Hölzle, A., Ivanchenko, S., Renzi, F., Oswald, F., Wolff, M., Schmitt, F., Röcker, C., Vallone, B., Weidemann, W., Heilker, R., Nar, H., and Wiedenmann, J. Photoconvertible fluorescent protein EosFP: Biophysical properties and cell biology applications. *Photochem. Photobiol.* **82**, 351–358 (2006).
 55. Ivanchenko, S., Glaschick, S., Röcker, C., Oswald, F., Wiedenmann, J., and Nienhaus, G. U. Two-photon excitation and photoconversion of EosFP in dual-color 4Pi confocal microscopy. *Biophys. J.* **92**, 4451–4457 (2007).

Bibliography

56. Hedde, P. N., Fuchs, J., Oswald, F., Wiedenmann, J., and Nienhaus, G. U. Online image analysis software for photoactivation localization microscopy. *Nat. Methods* **6**, 689–690 (2009).
57. McKinney, S. A., Murphy, C. S., Hazelwood, K. L., Davidson, M. W., and Looger, L. L. A bright and photostable photoconvertible fluorescent protein. *Nat. Methods* **6**, 131–133 (2009).
58. Oswald, F., Schmitt, F., Leutenegger, A., Ivanchenko, S., D'Angelo, C., Salih, A., Maslakova, S., Bulina, M., Schirmbeck, R., Nienhaus, G. U., Matz, M. V., and J., W. Contributions of host and symbiont pigments to the coloration of reef corals. *FEBS J.* **274**, 1102–1122 (2007).
59. Ando, R., Mizuno, H., and Miyawaki, A. Regulated fast nucleocytoplasmic shuttling observed by reversible protein highlighting. *Science* **306**, 1370–1373 (2004).
60. Andresen, M., Stiel, A. C., Fölling, J., Wenzel, D., Schönle, A., Egner, A., Eggeling, C., Hell, S. W., and Jakobs, S. Photoswitchable fluorescent proteins enable monochromatic multilabel imaging and dual color fluorescence nanoscopy. *Nat. Biotechnol.* **26**, 1035–1040 (2008).
61. Lukyanov, K. A., Fradkov, A. F., Gurskaya, N. G., Matz, M. V., Labas, Y. A., Savitsky, A. P., Markelov, M. L., Zaraisky, A. G., Zhao, X., Fang, Y., Tan, W., and Lukyanov, S. A. Natural animal coloration can be determined by a nonfluorescent green fluorescent protein homolog. *J. Biol. Chem.* **275**, 25879–25882 (2000).
62. Chudakov, D. M., Belousov, V. V., Zaraisky, A. G., Novoselov, V. V., Staroverov, D. B., Zorov, D. B., Lukyanov, S., and Lukyanov, K. A. Kindling fluorescent proteins for precise in vivo photolabeling. *Nat. Biotechnol.* **21**, 191–194 (2003).
63. Stiel, A. C., Andresen, M., Bock, H., Hilbert, M., Schilde, J., Schönle, A., Eggeling, C., Egner, A., Hell, S. W., and Jakobs, S. Generation of monomeric reversibly switchable red fluorescent proteins for far-field fluorescence nanoscopy. *Biophys. J.* **95**, 2989–2997 (2008).
64. Andresen, M., Wahl, M. C., Stiel, A. C., Gräter, F., Schäfer, L. V., Trowitzsch, S., Weber, G., Eggeling, C., Grubmüller, H., Hell, S. W., et al. Structure and mechanism of the reversible photoswitch of a fluorescent protein. *Proc. Natl Acad. Sci. USA* **102**, 13070–13074 (2005).
65. Andresen, M., Stiel, A. C., Trowitzsch, S., Weber, G., Eggeling, C., Wahl, M. C., Hell, S. W., and Jakobs, S. Structural basis for reversible photoswitching in Dronpa. *Proc. Natl Acad. Sci. USA* **104**, 13005–13009 (2007).
66. Petersen, J., Wilmann, P. G., Beddoe, T., Oakley, A. J., Devenish, R. J., Prescott, M., and Rossjohn, J. The 2.0-Å crystal structure of eqFP611, a far red fluorescent protein from the sea anemone *Entacmaea quadricolor*. *J. Biol. Chem.* **278**, 44626–44631 (2003).

67. Adam, V., Lelimosin, M., Boehme, S., Desfonds, G., Nienhaus, K., Field, M. J., Wiedenmann, J., McSweeney, S., Nienhaus, G. U., and Bourgeois, D. Structural characterization of IrisFP, an optical highlighter undergoing multiple photo-induced transformations. *Proc. Natl Acad. Sci. USA* **105**, 18343–18348 (2008).
68. Fuchs, J., Böhme, S., Oswald, F., Hedde, P. N., Krause, M., Wiedenmann, J., and Nienhaus, G. U. A photoactivatable marker protein for pulse-chase imaging with superresolution. *Nat. Methods* **7**, 627–630 (2010).
69. Wiedenmann, J., Schenk, A., Röcker, C., Girod, A., Spindler, K. D., and Nienhaus, G. U. A far-red fluorescent protein with fast maturation and reduced oligomerization tendency from *Entacmaea quadricolor* (Anthozoa, Actinaria). *Proc. Natl Acad. Sci. USA* **99**, 11646–11651 (2002).
70. Kredel, S., Oswald, F., Nienhaus, K., Deuschle, K., Röcker, C., Wolff, M., Heilker, R., Nienhaus, G. U., and Wiedenmann, J. mRuby, a bright monomeric red fluorescent protein for labeling of subcellular structures. *PLoS One* **4**, 4391 (2009).
71. Nienhaus, K., Nar, H., Heilker, R., Wiedenmann, J., and Nienhaus, G. U. Trans-Cis Isomerization is Responsible for the Red-Shifted Fluorescence in Variants of the Red Fluorescent Protein eqFP611. *J. Am. Chem. Soc.* **130**, 12578–12579 (2008).
72. Ram, S., Ward, E. S., and Ober, R. J. Beyond Rayleigh’s criterion: A resolution measure with application to single-molecule microscopy. *Proc. Natl Acad. Sci. USA* **103**, 4457–4462 (2006).
73. McDermott, G., Le Gros, M. A., Knoechel, C. G., Uchida, M., and Larabell, C. A. Soft X-ray tomography and cryogenic light microscopy: the cool combination in cellular imaging. *Trends Cell Biol.* **19**, 587–595 (2009).
74. Koster, A. J. and Klumperman, J. Electron microscopy in cell biology: integrating structure and function. *Nat. Rev. Mol. Cell Biol.* **4**, 6–10.
75. Larabell, C. A. and Le Gros, M. A. X-ray tomography generates 3-D reconstructions of the yeast, *Saccharomyces cerevisiae*, at 60-nm resolution. *Mol. Biol. Cell* **15**, 957–962 (2004).
76. Leis, A., Rockel, B., Andrees, L., and Baumeister, W. Visualizing cells at the nanoscale. *Trends Biochem. Sci.* **34**, 60–70 (2009).
77. Kuzmenkina, E. V., Heyes, C. D., and Nienhaus, G. U. Single-molecule Förster resonance energy transfer study of protein dynamics under denaturing conditions. *Proc. Natl Acad. Sci. USA* **102**, 15471–15476 (2005).
78. Clegg, R. M. Fluorescence resonance energy transfer. *Curr. Opin. Biotechnol.* **6**, 103–110 (1995).

Bibliography

79. Lippincott-Schwartz, J., Snapp, E., and Kenworthy, A. Studying protein dynamics in living cells. *Nat. Rev. Mol. Cell Biol.* **2**, 444–456 (2001).
80. Sekar, R. B. and Periasamy, A. Fluorescence resonance energy transfer (FRET) microscopy imaging of live cell protein localizations. *J. Cell Biol.* **160**, 629–633 (2003).
81. Park, P. S. H. and Palczewski, K. Imaging G protein-coupled receptor islands. *Nat. Chem. Biol.* **1**, 184–185 (2005).
82. Höppener, C., Siebrasse, J. P., Peters, R., Kubitscheck, U., and Naber, A. High-resolution near-field optical imaging of single nuclear pore complexes under physiological conditions. *Biophys. J.* **88**, 3681–3688 (2005).
83. Pendry, J. Negative refraction makes a perfect lens. *Phys. Rev. Lett.* **85**, 3966–3969 (2000).
84. Liu, Z., Lee, H., Xiong, Y., Sun, C., and Zhang, X. Far-field optical hyperlens magnifying sub-diffraction-limited objects. *Science* **315**, 1686 (2007).
85. Minsky, M. Microscopy Apparatus. US Patent 3,013,467.
86. Wilson, T. and Sheppard, C. J. R. *Theory and practice of scanning optical microscopy*. Academic, New York, (1984).
87. Pawley, J. B. *Handbook of biological confocal microscopy*. Springer Verlag, New York, (2006).
88. Hell, S. W. *Single Molecule Spectroscopy in Chemistry, Physics and Biology*. Springer Verlag, Berlin, (2009).
89. Hell, S. W. and Stelzer, E. H. K. Fundamental improvement of resolution with a 4Pi-confocal fluorescence microscope using two-photon excitation. *Opt. Commun.* **93**, 277–282 (1992).
90. Gustafsson, M. G. L., Agard, D. A., and Sedat, J. W. Sevenfold improvement of axial resolution in 3D wide-field microscopy using two objective lenses. In *Proc. SPIE Int. Soc. Opt.*, volume 2412, 147–156, (1995).
91. Gugel, H., Bewersdorf, J., Jakobs, S., Engelhardt, J., Storz, R., and Hell, S. W. Cooperative 4Pi excitation and detection yields sevenfold sharper optical sections in live-cell microscopy. *Biophys. J.* **87**, 4146–4152 (2004).
92. Egner, A., Verrier, S., Goroshkov, A., Söling, H. D., and Hell, S. W. 4Pi-microscopy of the Golgi apparatus in live mammalian cells. *J. Struct. Biol.* **147**, 70–76 (2004).
93. Perinetti, G., Müller, T., Spaar, A., Polishchuk, R., Luini, A., and Egner, A. Correlation of 4Pi and electron microscopy to study transport through single Golgi stacks in living cells with super resolution. *Traffic* **10**, 379–391 (2009).

94. Hell, S. W. and Wichmann, J. Breaking the diffraction resolution limit by stimulated emission: stimulated-emission-depletion fluorescence microscopy. *Opt. Lett.* **19**, 780–782 (1994).
95. Klar, T. A., Jakobs, S., Dyba, M., Egner, A., and Hell, S. W. Fluorescence microscopy with diffraction resolution barrier broken by stimulated emission. *Proc. Natl Acad. Sci. USA* **97**, 8206–8210 (2000).
96. Schmidt, R., Wurm, C. A., Jakobs, S., Engelhardt, J., Egner, A., and Hell, S. W. Spherical nanosized focal spot unravels the interior of cells. *Nat. Methods* **5**, 539–544 (2008).
97. Rittweger, E., Han, K. Y., Irvine, S. E., Eggeling, C., and Hell, S. W. STED microscopy reveals crystal colour centres with nanometric resolution. *Nat. Photonics* **3**, 144–147 (2009).
98. Westphal, V., Rizzoli, S. O., Lauterbach, M. A., Kamin, D., Jahn, R., and Hell, S. W. Video-rate far-field optical nanoscopy dissects synaptic vesicle movement. *Science* **320**, 246–249 (2008).
99. Eggeling, C., Ringemann, C., Medda, R., Schwarzmann, G., Sandhoff, K., Polyakova, S., Belov, V., Hein, B., Von Middendorff, C., Schönle, A., and Hell, S. W. Direct observation of the nanoscale dynamics of membrane lipids in a living cell. *Nature* **457**, 1159–1162 (2008).
100. Gustafsson, M. G. L. Surpassing the lateral resolution limit by a factor of two using structured illumination microscopy. *J. Microsc.* **198**, 82–87 (2000).
101. Schermelleh, L., Carlton, P. M., Haase, S., Shao, L., Winoto, L., Kner, P., Burke, B., Cardoso, M. C., Agard, D. A., Gustafsson, M. G. L., Leonhardt, H., and W., S. J. Subdiffraction multicolor imaging of the nuclear periphery with 3D structured illumination microscopy. *Science* **320**, 1332–1336 (2008).
102. Shao, L., Isaac, B., Uzawa, S., Agard, D. A., Sedat, J. W., and Gustafsson, M. G. L. I5S: Wide-field light microscopy with 100-nm-scale resolution in three dimensions. *Biophys. J.* **94**, 4971–4983 (2008).
103. Heintzmann, R., Jovin, T. M., and Cremer, C. Saturated patterned excitation microscopy a concept for optical resolution improvement. *J. Opt. Soc. Am.* **19**, 1599–1609 (2002).
104. Gustafsson, M. G. L. Nonlinear structured-illumination microscopy: Wide-field fluorescence imaging with theoretically unlimited resolution. *Proc. Natl Acad. Sci. USA* **102**, 13081–13086 (2005).
105. Rust, M. J., Bates, M., and Zhuang, X. Sub-diffraction-limit imaging by stochastic optical reconstruction microscopy (STORM). *Nat. Methods* **3**, 793–796 (2006).

Bibliography

106. Yildiz, A., Forkey, J. N., McKinney, S. A., Ha, T., Goldman, Y. E., and Selvin, P. R. Myosin V walks hand-over-hand: single fluorophore imaging with 1.5-nm localization. *Science* **300**, 2061–2065 (2003).
107. Pertsinidis, A., Zhang, Y., and Chu, S. Subnanometre single-molecule localization, registration and distance measurements. *Nature* **466**, 647–651 (2010).
108. Cheezum, M. K., Walker, W. F., and Guilford, W. H. Quantitative comparison of algorithms for tracking single fluorescent particles. *Biophys. J.* **81**, 2378–2388 (2001).
109. Thompson, R. E., Larson, D. R., and Webb, W. W. Precise nanometer localization analysis for individual fluorescent probes. *Biophys. J.* **82**, 2775–2783 (2002).
110. Lemmer, P., Gunkel, M., Baddeley, D., Kaufmann, R., Urich, A., Weiland, Y., Reymann, J., Müller, P., Hausmann, M., and Cremer, C. SPDM: light microscopy with single-molecule resolution at the nanoscale. *Applied Physics B: Lasers and Optics* **93**, 1–12 (2008).
111. Egner, A., Geisler, C., Von Middendorff, C., Bock, H., Wenzel, D., Medda, R., Andresen, M., Stiel, A. C., Jakobs, S., Eggeling, C., Schnle, A., and Hell, S. W. Fluorescence nanoscopy in whole cells by asynchronous localization of photoswitching emitters. *Biophys. J.* **93**, 3285–3290 (2007).
112. Fölling, J., Bossi, M., Bock, H., Medda, R., Wurm, C. A., Hein, B., Jakobs, S., Eggeling, C., and Hell, S. W. Fluorescence nanoscopy by ground-state depletion and single-molecule return. *Nat. Methods* **5**, 943–945 (2008).
113. Sharonov, A. and Hochstrasser, R. M. Wide-field subdiffraction imaging by accumulated binding of diffusing probes. *Proc. Natl Acad. Sci. USA* **103**, 18911–18916 (2006).
114. Heilemann, M., van de Linde, S., Schüttelpeiz, M., Kasper, R., Seefeldt, B., Mukherjee, A., Tinnefeld, P., and Sauer, M. Subdiffraction-resolution fluorescence imaging with conventional fluorescent probes. *Angew. Chem. Int. Ed.* **47**, 6172–6176 (2008).
115. Lemmer, P., Gunkel, M., Weiland, Y., Müller, P., Baddeley, D., Kaufmann, R., Urich, A., Eipel, H., Amberger, R., Hausmann, M., and CREMER, C. Using conventional fluorescent markers for far-field fluorescence localization nanoscopy allows resolution in the 10-nm range. *J. Microsc.* **235**, 163–171 (2009).
116. Jerri, A. J. The Shannon sampling theoremIts various extensions and applications: A tutorial review. *Proc. IEEE* **65**, 1565–1596 (2005).
117. Bates, M., Huang, B., Dempsey, G. T., and Zhuang, X. Multicolor super-resolution imaging with photo-switchable fluorescent probes. *Science* **317**, 1749–1753 (2007).

118. Bock, H., Geisler, C., Wurm, C. A., Von Middendorff, C., Jakobs, S., Schönle, A., Egner, A., and Hell, S. W. Two-color far-field fluorescence nanoscopy based on photoswitchable emitters. *Appl. Phys. B* **88**, 161–165 (2007).
119. Gunkel, M., Erdel, F., Rippe, K., Lemmer, P., Kaufmann, R., Hörmann, C., Amberger, R., and Cremer, C. Dual color localization microscopy of cellular nanostructures. *Biotechnol. J.* **4**, 927–938 (2009).
120. Ribeiro, S. A., Vagnarelli, P., Dong, Y., Hori, T., McEwen, B. F., Fukagawa, T., Flors, C., and Earnshaw, W. C. A super-resolution map of the vertebrate kinetochore. *Proc. Natl Acad. Sci. USA* **107**, 10484–10489 (2010).
121. Juette, M. F., Gould, T. J., Lessard, M. D., Mlodzianoski, M. J., Nagpure, B. S., Bennett, B. T., Hess, S. T., and Bewersdorf, J. Three-dimensional sub-100 nm resolution fluorescence microscopy of thick samples. *Nat. methods* **5**, 527–529 (2008).
122. Huang, B., Jones, S. A., Brandenburg, B., and Zhuang, X. Whole-cell 3D STORM reveals interactions between cellular structures with nanometer-scale resolution. *Nat. Methods* **5**, 1047–1052 (2008).
123. Huang, B., Wang, W., Bates, M., and Zhuang, X. Three-dimensional super-resolution imaging by stochastic optical reconstruction microscopy. *Science* **319**, 810–813 (2008).
124. Pavani, S. R. P., Thompson, M. A., Biteen, J. S., Lord, S. J., Liu, N., Twieg, R. J., Piestun, R., and Moerner, W. E. Three-dimensional, single-molecule fluorescence imaging beyond the diffraction limit by using a double-helix point spread function. *Proc. Natl Acad. Sci. USA* **106**, 2995–2999 (2009).
125. Shtengel, G., Galbraith, J. A., Galbraith, C. G., Lippincott-Schwartz, J., Gillette, J. M., Manley, S., Sougrat, R., Waterman, C., Kanchanawong, P., Davidson, M. W., Fetter, R. D., and Hess, H. F. Interferometric fluorescent super-resolution microscopy resolves 3D cellular ultrastructure. *Proc. Natl Acad. Sci. USA* **106**, 3125–3130 (2009).
126. Tang, J., Akerboom, J., Vaziri, A., Looger, L. L., and Shank, C. V. Near-isotropic 3D optical nanoscopy with photon-limited chromophores. *Proc. Natl Acad. Sci. USA* **107**, 10068–10073 (2010).
127. Hess, S. T., Gould, T. J., Gudheti, M. V., Maas, S. A., Mills, K. D., and Zimmerberg, J. Dynamic clustered distribution of hemagglutinin resolved at 40 nm in living cell membranes discriminates between raft theories. *Proc. Natl Acad. Sci. USA* **104**, 17370–17375 (2007).
128. Biteen, J. S., Thompson, M. A., Tselentis, N. K., Bowman, G. R., Shapiro, L., and Moerner, W. E. Super-resolution imaging in live *Caulobacter crescentus* cells using photoswitchable EYFP. *Nat. Methods* **5**, 947–949 (2008).

Bibliography

129. Shroff, H., Galbraith, C. G., Galbraith, J. A., and Betzig, E. Live-cell photoactivated localization microscopy of nanoscale adhesion dynamics. *Nat. Methods* **5**, 417–423 (2008).
130. Cang, H., Labno, A., Lu, C., Yin, X., Liu, M., Gladden, C., Liu, Y., and Zhang, X. Probing the electromagnetic field of a 15-nanometre hotspot by single molecule imaging. *Nature* **469**, 385–388 (2011).
131. Nie, S. and Emory, S. R. Probing single molecules and single nanoparticles by surface-enhanced Raman scattering. *Science* **275**, 1102–1106 (1997).
132. Donnert, G., Keller, J., Medda, R., Andrei, M. A., Rizzoli, S. O., Lührmann, R., Jahn, R., Eggeling, C., and Hell, S. W. Macromolecular-scale resolution in biological fluorescence microscopy. *Proc. Natl Acad. Sci. USA* **103**, 11440–11445 (2006).
133. Lin, W., Margolskee, R., Donnert, G., Hell, S. W., and Restrepo, D. Olfactory neurons expressing transient receptor potential channel M5 (TRPM5) are involved in sensing semiochemicals. *Proc. Natl Acad. Sci. USA* **104**, 2471–2476 (2007).
134. Fölling, J., Belov, V., Kunetsky, R., Medda, R., Schönle, A., Egner, A., Eggeling, C., Bossi, M., and Hell, S. Photochromic rhodamines provide nanoscopy with optical sectioning. *Angew. Chem. Int. Ed.* **46**, 6266–6270 (2007).
135. Fukaminato, T., Umemoto, T., Iwata, Y., Yokojima, S., Yoneyama, M., Nakamura, S., and Irie, M. Photochromism of diarylethene single molecules in polymer matrices. *J. Am. Chem. Soc* **129**, 5932–5938 (2007).
136. Vogelsang, J., Cordes, T., Forthmann, C., Steinhauer, C., and Tinnefeld, P. Controlling the fluorescence of ordinary oxazine dyes for single-molecule switching and superresolution microscopy. *Proc. Natl Acad. Sci. USA* **106**, 8107–8112 (2009).
137. Mitchison, T. J., Sawin, K. E., Theriot, J. A., Gee, K., and Mallavarapu, A. [4] Caged fluorescent probes. *Methods Enzymol.* **291**, 63–78 (1998).
138. Lord, S. J., Conley, N. R., Lee, H. D., Samuel, R., Liu, N., Twieg, R. J., and Moerner, W. A photoactivatable Push- Pull fluorophore for single-molecule imaging in live cells. *J. Am. Chem. Soc.* **130**, 9204–9205 (2008).
139. Griffin, B. A., Adams, S. R., and Tsien, R. Y. Specific covalent labeling of recombinant protein molecules inside live cells. *Science* **281**, 269–272 (1998).
140. Lata, S., Gavutis, M., Tampé, R., and Piehler, J. Specific and stable fluorescence labeling of histidine-tagged proteins for dissecting multi-protein complex formation. *J. Am. Chem. Soc* **128**, 2365–2372 (2006).
141. Nonaka, H., Tsukiji, S., Ojida, A., and Hamachi, I. Non-enzymatic covalent protein labeling using a reactive tag. *J. Am. Chem. Soc* **129**, 15777–15779 (2007).

142. McCann, C. M., Bareyre, F. M., Lichtman, J. W., and Sanes, J. R. Peptide tags for labeling membrane proteins in live cells with multiple fluorophores. *Biotechniques* **38**, 945–952 (2005).
143. Marks, K. M., Braun, P. D., and Nolan, G. P. A general approach for chemical labeling and rapid, spatially controlled protein inactivation. *Proc. Natl Acad. Sci. USA* **101**, 9982–9987 (2004).
144. Miller, L. W., Cai, Y., Sheetz, M. P., and Cornish, V. W. In vivo protein labeling with trimethoprim conjugates: a flexible chemical tag. *Nat. Methods* **2**, 255–257 (2005).
145. Keppler, A., Gendreizig, S., Gronemeyer, T., Pick, H., Vogel, H., and Johnsson, K. A general method for the covalent labeling of fusion proteins with small molecules in vivo. *Nat. Biotechnol.* **21**, 86–89 (2002).
146. Popp, M. W., Antos, J. M., Grotenbreg, G. M., Spooner, E., and Ploegh, H. L. Sortagging: a versatile method for protein labeling. *Nat. Chem. Biol.* **3**, 707–708 (2007).
147. Howarth, M., Takao, K., Hayashi, Y., and Ting, A. Y. Targeting quantum dots to surface proteins in living cells with biotin ligase. *Proc. Natl Acad. Sci. USA* **102**, 7583–7588 (2005).
148. Klein, T., Löschberger, A., Proppert, S., Wolter, S., van de Linde, S., and Sauer, M. Live-cell dSTORM with SNAP-tag fusion proteins. *Nat. Methods* **8**, 7–9 (2010).
149. Dertinger, T., Colyer, R., Iyer, G., Weiss, S., and Enderlein, J. Fast, background-free, 3D super-resolution optical fluctuation imaging (SOFI). *Proc. Natl Acad. Sci. USA* **106**, 22287–22292 (2009).
150. Pollard, T. D. and Cooper, J. . Actin, a central player in cell shape and movement. *Science* **326**, 1208–1212 (2009).
151. Pollard, T. D. and Borisy, G. G. Cellular motility driven by assembly and disassembly of actin filaments. *Cell* **112**, 453–465 (2003).
152. Riedl, J., Crevenna, A. H., Kessenbrock, K., Yu, J. H., Neukirchen, D., Bista, M., Bradke, F., Jenne, D., Holak, T. A., Werb, Z., et al. Lifeact: a versatile marker to visualize F-actin. *Nat. Methods* **5**, 605–607 (2008).
153. Sjoblom, B., Salmazo, A., and Djinovic-Carugo, K. α -Actinin structure and regulation. *Cell. Mol. Life Sci.* **65**, 2688–2701 (2008).
154. Otey, C. A. and Carpen, O. α -actinin revisited: A fresh look at an old player. *Cell Motil. Cytoskel.* **58**, 104–111 (2004).

Bibliography

155. Li, H., DeRosier, D. J., Nicholson, W. V., Nogales, E., and Downing, K. H. Microtubule structure at 8 Å resolution. *Structure* **10**, 1317–1328 (2002).
156. Wendell, K. L., Wilson, L., and Jordan, M. A. Mitotic block in HeLa cells by vinblastine: ultrastructural changes in kinetochore-microtubule attachment and in centrosomes. *J. Cell Sci.* **104**, 261–274 (1993).
157. Kopan, R., Ilagan, M., and Xenia, G. The canonical Notch signaling pathway: unfolding the activation mechanism. *Cell* **137**, 216–233 (2009).
158. Wacker, S. A., Alvarado, C., von Wichert, G., Knippschild, U., Wiedenmann, J., Clauß, K., Nienhaus, G. U., Hameister, H., Baumann, B., Borggrefe, T., Knchel, W., and Oswald, F. RITA, a novel modulator of Notch signalling, acts via nuclear export of RBP-J. *EMBO J.* **30**, 43–56 (2010).
159. Turner, C. E. Paxillin interactions. *J. Cell Sci.* **113**, 4139–4140 (2000).
160. Zaidel-Bar, R., Itzkovitz, S., Ma'ayan, A., Iyengar, R., and Geiger, B. Functional atlas of the integrin adhesome. *Nat. Cell Biol.* **9**, 858–867 (2007).
161. Deakin, N. O. and Turner, C. E. Paxillin comes of age. *J. Cell Sci.* **121**, 2435–2444 (2008).
162. Ballestrem, C., Hinz, B., Imhof, B. A., and Wehrle-Haller, B. Marching at the front and dragging behind. *J. Cell Biol.* **155**, 1319–1332 (2001).
163. Laukaitis, C. M., Webb, D. J., Donais, K., and Horwitz, A. F. Differential dynamics of $\alpha 5$ integrin, paxillin, and α -actinin during formation and disassembly of adhesions in migrating cells. *J. Cell Biol.* **153**, 1427–1440 (2001).
164. Webb, D. J., Parsons, J. T., and Horwitz, A. F. Adhesion assembly, disassembly and turnover in migrating cells—over and over and over again. *Nat. Cell Biol.* **4**, E97–E100 (2002).
165. Wiseman, P. W., Brown, C. M., Webb, D. J., Hebert, B., Johnson, N. L., Squier, J. A., Ellisman, M. H., and Horwitz, A. F. Spatial mapping of integrin interactions and dynamics during cell migration by image correlation microscopy. *J. Cell Sci.* **117**, 5521–5534 (2004).
166. Digman, M. A., Brown, C. M., Horwitz, A. R., Mantulin, W. W., and Gratton, E. Paxillin dynamics measured during adhesion assembly and disassembly by correlation spectroscopy. *Biophys. J.* **94**, 2819–2831 (2008).
167. Ezratty, E. J., Partridge, M. A., and Gundersen, G. G. Microtubule-induced focal adhesion disassembly is mediated by dynamin and focal adhesion kinase. *Nat. Cell Biol.* **7**, 581–590 (2005).

168. Williams, A. T. R., Winfield, S. A., and Miller, J. N. Relative fluorescence quantum yields using a computer-controlled luminescence spectrometer. *Analyst* **108**, 1067–1071 (1983).
169. Hendler, R. W. and Shrager, R. I. Deconvolutions based on singular value decomposition and the pseudoinverse: a guide for beginners. *J. Biochem. Biophys. Methods* **28**, 1–33 (1994).
170. Müller, J. D., McMahon, B. H., Chien, E. Y. T., Sligar, S. G., and Nienhaus, G. U. Connection between the taxonomic substates and protonation of histidines 64 and 97 in carbonmonoxy myoglobin. *Biophys. J.* **77**, 1036–1051 (1999).
171. Axelrod, D. Total Internal Reflection Fluorescence Microscopy in Cell Biology. *Traffic* **2**, 764–774 (2001).
172. Geisler, C., Schönle, A., Von Middendorff, C., Bock, H., Eggeling, C., Egner, A., and Hell, S. W. Resolution of $\lambda/10$ in fluorescence microscopy using fast single molecule photo-switching. *Appl. Phys. A* **88**, 223–226 (2007).
173. Funatsu, T., Harada, Y., Tokunaga, M., Saito, K., and Yanagida, T. Imaging of single fluorescent molecules and individual ATP turnovers by single myosin molecules in aqueous solution. *Nature* **374**, 555–559 (1995).
174. Stout, A. L. and Axelrod, D. Evanescent field excitation of fluorescence by epillumination microscopy. *Appl. Opt.* **28**, 5237–5242 (1989).
175. Lidke, K. A., Rieger, B., Lidke, D. S., and Jovin, T. M. The role of photon statistics in fluorescence anisotropy imaging. *IEEE Trans. Image Process.* **14**, 1237–1245 (2005).
176. Andersson, S. Localization of a fluorescent source without numerical fitting. *Opt. Express* **16**, 18714–18724 (2008).
177. Bancroft, S. An algebraic solution of the GPS equations. *IEEE Trans. Aerosp. Electron. Syst.* , 56–59 (2007).
178. Nienhaus, K., Renzi, F., Vallone, B., Wiedenmann, J., and Nienhaus, G. U. Exploring Chromophore- Protein Interactions in Fluorescent Protein cmFP512 from *Cerianthus membranaceus*: X-ray Structure Analysis and Optical Spectroscopy. *Biochemistry* **45**, 12942–12953 (2006).
179. Wilmann, P. G., Petersen, J., Devenish, R. J., Prescott, M., and Rossjohn, J. Variations on the GFP chromophore. *J. Biol. Chem.* **280**, 2401–2404 (2005).
180. Quillin, M. L., Anstrom, D. M., Shu, X., O’Leary, S., Kallio, K., Chudakov, D. M., and Remington, S. J. Kindling Fluorescent Protein from *Anemonia sulcata*: Dark-State Structure at 1.38 Å Resolution,. *Biochemistry* **44**, 5774–5787 (2005).

Bibliography

181. Kredel, S., Nienhaus, K., Oswald, F., Wolff, M., Ivanchenko, S., Cymer, F., Jeromin, A., Michel, F. J., Spindler, K. D., Heilker, R., Nienhaus, G. U., and J., W. Optimized and far-red-emitting variants of fluorescent protein eqFP611. *Chem. Biol.* **15**, 224–233 (2008).
182. He, X., Bell, A. F., and Tonge, P. J. Ground state isomerization of a model green fluorescent protein chromophore. *FEBS Lett.* **549**, 35–38 (2003).
183. Schäfer, L. V., Groenhof, G., Boggio-Pasqua, M., Robb, M. A., and Grubmüller, H. Chromophore protonation state controls photoswitching of the fluoroprotein asFP595. *PLoS Comput. Biol.* **4**, e1000034 (2008).
184. Shaner, N. C., Lin, M. Z., McKeown, M. R., Steinbach, P. A., Hazelwood, K. L., Davidson, M. W., and Tsien, R. Y. Improving the photostability of bright monomeric orange and red fluorescent proteins. *Nat. Methods* **5**, 545–551 (2008).
185. Marriott, G., Mao, S., Sakata, T., Ran, J., Jackson, D. K., Petchprayoon, C., Gomez, T. J., Warp, E., Tulyathan, O., Aaron, H. L., sacoff, E. Y., and Yan, Y. Optical lock-in detection imaging microscopy for contrast-enhanced imaging in living cells. *Proc. Natl Acad. Sci. USA* **105**, 17789–17794 (2008).
186. Schüttrigkeit, T. A., Feilitzsch, T., Kompa, C. K., Lukyanov, K. A., Savitsky, A. P., Voityuk, A. A., and Michel-Beyerle, M. E. Femtosecond study of light-induced fluorescence increase of the dark chromoprotein asFP595. *Chem. Phys.* **323**, 149–160 (2006).
187. Subach, F. V., Patterson, G. H., Renz, M., Lippincott-Schwartz, J., and Verkhusha, V. V. Bright Monomeric Photoactivatable Red Fluorescent Protein for Two-Color Super-Resolution sptPALM of Live Cells. *J. Am. Chem. Soc.* **132**, 6481–6491 (2010).
188. Steinhauer, C., Forthmann, C., Vogelsang, J., and Tinnefeld, P. Superresolution microscopy on the basis of engineered dark states. *J. Am. Chem. Soc.* **130**, 16840–16841 (2008).
189. Cheutin, T., McNairn, A. J., Jenuwein, T., Gilbert, D. M., Singh, P. B., and Misteli, T. Maintenance of stable heterochromatin domains by dynamic HP1 binding. *Science* **299**, 721–725 (2003).
190. Phair, R. D. and Misteli, T. High mobility of proteins in the mammalian cell nucleus. *Nature* **404**, 604–609 (2000).
191. Paulick, M. G., Forstner, M. B., Groves, J. T., and Bertozzi, C. R. A chemical approach to unraveling the biological function of the glycosylphosphatidylinositol anchor. *Proc. Natl Acad. Sci. USA* **104**, 20332–20337 (2007).

192. Chen, D. and Huang, S. Nucleolar Components Involved in Ribosome Biogenesis Cycle between the Nucleolus and Nucleoplasm in Interphase Cells. *J. Biol. Chem.* **153**, 169–176 (2001).
193. Wolter, S., Schüttpelz, M., Tscherepanow, M., van de Linde, S., Heilemann, M., and Sauer, M. Real-time computation of subdiffraction-resolution fluorescence images. *J. Microsc.* **237**, 12–22 (2010).
194. Quan, T., Li, P., Long, F., Zeng, S., Luo, Q., Hedde, P. N., Nienhaus, G. U., and Huang, Z. L. Ultra-fast, high-precision image analysis for localization-based super resolution microscopy. *Opt. Express* **18**, 11867–11876 (2010).
195. Smith, C. S., Joseph, N., Rieger, B., and Lidke, K. A. Fast, single-molecule localization that achieves theoretically minimum uncertainty. *Nat. Methods* **7**, 373–375 (2010).
196. Henriques, R., Lelek, M., Fornasiero, E. F., Valtorta, F., Zimmer, C., and Mhlanga, M. M. QuickPALM: 3D real-time photoactivation nanoscopy image processing in ImageJ. *Nat. Methods* **7**, 339–340 (2010).
197. Mortensen, K. I., Churchman, L. S., Spudich, J. A., and Flyvbjerg, H. Optimized localization analysis for single-molecule tracking and super-resolution microscopy. *Nat. Methods* **7**, 377–381 (2010).
198. Kner, P., Chhun, B. B., Griffis, E., Winoto, L., and Gustafsson, M. G. L. Super-resolution video microscopy of live cells by structured illumination. *Nat. Methods* **6**, 339–342 (2009).
199. Hofmann, M., Eggeling, C., Jakobs, S., and Hell, S. W. Breaking the diffraction barrier in fluorescence microscopy at low light intensities by using reversibly photoswitchable proteins. *Proc. Natl Acad. Sci. USA* **102**, 17565–17569 (2005).
200. Wombacher, R., Heidbreder, M., van de Linde, S., Sheetz, M. P., Heilemann, M., Cornish, V., and Sauer, M. Live-cell super-resolution imaging with trimethoprim conjugates. *Nat. Methods* **7**, 717–719 (2010).
201. Heilemann, M., van de Linde, S., Schüttpelz, M., Kasper, R., Seefeldt, B., Mukherjee, A., Tinnefeld, P., and Sauer, M. Fluoreszenzmikroskopie unterhalb der optischen Auflösungsgrenze mit konventionellen Fluoreszenzsonden. *Angew. Chem. Int. Ed.* **120**, 6266–6271 (2008).
202. Eggeling, C., Hilbert, M., Bock, H., Ringemann, C., Hofmann, M., Stiel, A. C., Andresen, M., Jakobs, S., Egner, A., Schönle, A., and Hell, S. W. Reversible photoswitching enables single-molecule fluorescence fluctuation spectroscopy at high molecular concentration. *Microsc. Res. Tech.* **70**, 1003–1009 (2007).

Bibliography

203. Lippincott-Schwartz, J. and Patterson, G. H. Photoactivatable fluorescent proteins for diffraction-limited and super-resolution imaging. *Trends Cell Biol.* **19**, 555–565 (2009).
204. Carlton, P. M., Boulanger, J., Kervrann, C., Sibarita, J. B., Salamero, J., Gordon-Messer, S., Bressan, D., Haber, J., Haase, S., Shao, L., Winoto, L., Matsuda, A., Kner, P., Uzawa, S., Gustafsson, M., Kam, Z., Agardk, D. A., and Sedata, J. W. Fast live simultaneous multiwavelength four-dimensional optical microscopy. *Proc. Natl Acad. Sci. USA* **107**, 16016–16022 (2010).

A. Publications

Parts of this thesis have already been published in scientific journals

- J. Fuchs, S. Böhme, F. Oswald, P.N. Hedde, M. Krause, J. Wiedenmann, G. U. Nienhaus, "Imaging protein movement in live cells with super-resolution using mIrisFP," *Nat. Methods* **7**, 627-630 (2010).
- P. N. Hedde, J. Fuchs, F. Oswald, J. Wiedenmann, and G. U. Nienhaus, "Online image analysis software for photoactivation localization microscopy," *Nat. Methods* **6**, 689-690 (2009).

and at conferences (posters and talks)

- J. Fuchs, R. Rieger, C. Röcker, D. Ortman, A. Plettl, and G. U. Nienhaus, "Advanced fluorescence techniques for the study of the dynamics of individual biomolecules," in "Trends in Nanosciences (Irsee, Germany)," poster (2005)
- J. Fuchs and G. U. Nienhaus, "Fluorescent proteins studied by advanced spectroscopy," in "Jahrestagung Deutsche Gesellschaft für Biophysik (Mainz, Germany)," poster (2006)
- J. Fuchs and G. U. Nienhaus, "Fluorescent proteins studied with new spectroscopy techniques," in "Sektionstagung Deutsche Gesellschaft für Biophysik (Hühnfeld, Germany)," poster (2007)
- J. Fuchs and G. U. Nienhaus, "Optical properties of fluorescent proteins in controlled environments," in "Hot Topics in Molecular Imaging (Les Houches, France)," talk (2008)
- J. Fuchs, S. Gundel, J. Wiedenmann and G. U. Nienhaus, "Photoswitching mechanism and application of a new red fluorescent protein," in "Jahrestagung Deutsche Gesellschaft für Biophysik (Berlin, Germany)," poster (2008)
- J. Fuchs, P. N. Hedde, S. Gundel, J. Wiedenmann and G. U. Nienhaus, "A new red fluorescent protein for high resolution microscopy," in "Sektionstagung Deutsche Gesellschaft für Biophysik (Hühnfeld, Germany)," poster (2009)

A. Publications

Additional work on related topics has been published in:

- T. Grossmann, S. Schleede, M. Hauser, M. B. Christiansen, C. Vannahme, C. Eschenbaum, S. Klinkhammer, T. Beck, J. Fuchs, G. U. Nienhaus, U. Lemmer, A. Kristensen, T. Mappes, H. Kalt, "Low-threshold conical microcavity dye lasers," *Appl. Phys. Lett.* **97**, 063304 (2010)
- T. Grossmann, S. Schleede, M. Hauser, M. B. Christiansen, C. Vannahme, C. Eschenbaum, S. Klinkhammer, T. Beck, J. Fuchs, G. U. Nienhaus, U. Lemmer, A. Kristensen, T. Mappes, H. Kalt, "Lasing in dye-doped high-Q conical polymeric microcavities," *Proc. of SPIE* **7913**, 79130Y (2011)

B. Acknowledgements

I would like to thank my Ph.D. supervisor Prof. Uli Nienhaus for giving me the opportunity to work on this interesting topic. I'm deeply thankful for his supported during my entire academic career. I learned a lot from him about biophysics and how to do a good job.

Moreover, I would like to thank Prof. Wolfgang Wenzel for kindly agreeing to co-referee this Thesis. I really appreciate his interest in my work.

I am also grateful to Prof. Dagmar Gerthsen for being my mentor during this work.

I would like to express my gratitude to the following co-investigators:

- Per Niklas Hedde for perfect teamwork. He has stimulated my work with his ideas and his commitment.
- Susan Gayda for numerous insightful discussions and for sharing her biochemical knowledge and mIrisFP with me.
- Silke Gundel for a great collaboration. She built the basis for this thesis with her previous work on psRFP.
- Jörg Wiedenmann for his beautiful fluorescent proteins and helpful discussions on this topic.
- Franz Oswald for sharing his expertise in cell biology. He has stimulated this work with many interesting ideas. Big thanks to him and his girls for providing excellent samples.
- Karin Nienhaus for many interesting discussions that helped me doing the right experiments and ask the right questions.
- Uwe Theilen for help with protein purification and for sharing his knowledge and samples from the field of alcoholic transformed fruits .
- Hans Bartunik and Galina Kachalova for unforgettable experiments at DESY.
- Andrei Kobitski for his help in technical and programming questions.

B. Acknowledgements

I also like to thank people

- Charly Röcker for sharing his knowledge on microscopy. I'm deeply thankful for his help on so many problems.
- Robert Rieger for being a friend for many years. His ideas and discussions in many fields have always been inspiring.
- Tobias Grossmann for a great collaboration.
- Karin Nienhaus, Dave Evans, Per Niklas Hedde and Andrei Kobitstki for reading this manuscript. Their comments and numerous hints really improved the readability and quality of this manuscript.
- Heinz Hoffmann, Helmut Lay, Thomas Ahnert and Bernhard Gruchmann for help with computer problems.
- the secretaries Renate Helfen, Monika Brenkmann, Renate Bender, Ursula Mösle and Heidi Kohn.

I would like to thank all former and present colleagues in the Nienhaus group in Karlsruhe and Ulm. I'm not mentioning all the names, but I enjoyed working with each of them and I had a really great time. I want to thank the people in Karlsruhe especially the Kalt group and the Wegener group for a warm welcome and helping us with the start in Karlsruhe.

I'm deeply grateful to my parents Ursula and Josef. Their support has always encouraged me to go my own way.

This work is dedicated to my big love Johanna, who has always been understanding and supportive, more than I could expect.

C. Curriculum Vitae

Contact Information

Name Jochen Fuchs
Address Kasernstr. 60
89231 Neu-Ulm
Germany
email jochen-fuchs (at) web.de

Personal Data

Date and place of birth July 12, 1978 in Ellwangen/Jagst, Germany
Citizenship German

Professional experience

since 03/2011 **Carl Zeiss AG**
Corporate Research and Technology
Research Scientist

10/09 – 12/10 **Karlsruhe Institute of Technology (KIT) and**
Center for Functional Nanostructures (CFN)
Research Scientist

06/06 – 09/09 **University of Ulm**
Department of Biophysics
Research Scientist

08/03 – 08/04 **University of Illinois at Urbana-Champaign, USA**
Department of Physics, Research group of Prof. T. Ha
Research Assistant

Education

- 05/06 – 12/10 Karlsruhe Institute of Technology (KIT)
and University of Ulm**
Ph.D Student (physics)
Subject: Characterization and Application of Photoswitchable
Fluorescent Proteins for Nanoscopy
Research advisor: Prof. G. U. Nienhaus
- 10/99 – 05/06 University of Ulm**
Physics Department
Diploma Student
Thesis topic: Fluoreszenzspektroskopische Untersuchungen zur
Dynamik einzelner Biomoleküle
Research advisor: Prof. G. U. Nienhaus
- 07/98 – 04/99 Military Service**
FmBt 230, Dillingen
- 06/98 Abitur**, Peutinger Gymnasium, Ellwangen, Germany

Awards and Honors

- Scholar of the Baden-Württemberg Program (08/03–08/04)
- Teaching award of University of Ulm (2000)